SYNTHESIS AND STUDY OF BORON AND ANTIMONY LEWIS ACIDS AS SMALL ANION RECEPTORS AND LIGANDS TOWARDS TRANSITION METALS

A Dissertation

by

CASEY ROBERT WADE

Submitted to the Office of Graduate Studies of
Texas A&M University
in partial fulfillment of the requirements for the degree of

DOCTOR OF PHILOSOPHY

December 2011

Major Subject: Chemistry

Synthesis and Study of Boron and Antimony Lewis Acids as Small Anion Receptors and Ligands Towards Transition Metals

Copyright 2011 Casey Robert Wade

SYNTHESIS AND STUDY OF BORON AND ANTIMONY LEWIS ACIDS AS SMALL ANION RECEPTORS AND LIGANDS TOWARDS TRANSITION METALS

A Dissertation

by

CASEY ROBERT WADE

Submitted to the Office of Graduate Studies of
Texas A&M University
in partial fulfillment of the requirements for the degree of

DOCTOR OF PHILOSOPHY

Approved by:

Chair of Committee,	François P. Gabbaï
Committee Members,	Donald J. Darensbourg
	Timothy R. Hughbanks
	Michael D. Manson
Head of Department,	David H. Russell

December 2011

Major Subject: Chemistry

ABSTRACT

Synthesis and Study of Boron and Antimony Lewis Acids as Small Anion Receptors and Ligands Towards Transition Metals. (December 2011)

Casey Robert Wade, B.S., University of Nebraska-Lincoln

Chair of Advisory Committee: Dr. François P. Gabbaï

Although fluoride is used at low concentrations in drinking water as a means of promoting dental health, it poses a danger at high exposure levels where it can lead to skeletal fluorosis or other adverse effects. Cyanide is notoriously toxic, and its large scale use in industrial processes warrants the need for close monitoring to remain aware of potential contamination of water sources and other environmental resources. Based on these considerations, it is critical to continue to develop improved methods of monitoring fluoride and cyanide concentrations in water. However, molecular recognition of these anions in water poses considerable challenges. For fluoride, this is due largely to its high hydration enthalpy (ΔH^o = -504 kJ mol^{-1}), which drastically reduces its reactivity in water. Additionally, the strong basicity of cyanide (pKa of (HCN) = 9.3) may obscure its detection in neutral water due to protonation. In addition to achieving detection of these anions in water, it is most desirable to have information of the detection event relayed in the form of a positive, rather than negative, response (i.e., turn-on vs turn-off).

The general strategy of appending cationic groups to triarylboranes imparts beneficial Coulombic, inductive, and sometimes chelate effects that have allowed a number of these Lewis acidic receptors to sense fluoride and cyanide in aqueous environments. With the goal of developing new triarylborane-based receptors that show enhanced affinities for these anions, as well as turn-on responses to detection, a series of pyridinium boranes were synthesized and studied. Having recognized that the inherent Lewis acidity of antimony(V) species might be exploited for anion sensing, we also describe initial studies on the ability of tetraorganostibonium ions (R_4Sb^+) and cationic transition metal-triarylstibine complexes (R_3SbM^+) to complex fluoride. Finally, the electropositivity of antimony and its ability to form stable compounds in both the +3 and +5 oxidation states have led us to begin investigations into the bonding and redox reactivity of novel metal stibine/stiborane complexes.

DEDICATION

For Mom

ACKNOWLEDGEMENTS

I would like to thank my undergraduate research advisor, Dr. John Belot, for all of his mentorship and giving me the opportunity to get my feet wet in his lab. In addition, a special thanks goes to Prof. Victor Day, who helped guide my way to Texas A&M. I would also like to acknowledge Prof. Don Darensbourg, Prof. Timothy R. Hughbanks, and Prof. Mike Manson for sitting on my committee. A special thanks goes to Prof. Manson for many enlightening discussions about science in general.

I am extremely grateful to the members of the Gabbaï group, past and present, who have been both friends and wonderful colleagues: Dr. Mitsukimi Tsunoda, Dr. Tom Taylor, Dr. Chammi Gamage, Dr. Ching-Wen Chiu, Dr. Mieock Kim, Dr. Youngmin Kim, Dr. Takeshi Matsumoto, Dr. Zureima Garcia Hernandez, Haiyan Zhao, Tzu-Pin Lin, Iou-sheng Ke, James Jones, Lauren Leamer, Masato Hirai, Kantapat Chansaenpak, Adriana Hampton, James Bondi, Pawel Jewula, Dan Gardner, Ivan Lenov, Sirinan Kulchat, and Merid Haile. I would especially like to thank Dr. Todd Hudnall and Dr. Chris Dorsey for their guidance in my early years in the Gabbaï Lab and for teaching me about balance in graduate school.

I would like to acknowledge the staff members who gave me a great deal of advice and assistance including: Dr. Nattamai Bhuvanesh, Dr. Joseph H. Reibenspies, Dr. Vladimir Bakhmoutov, Dr. K. P. Sarathy, Steve Silber, Lisa Perez, and Sandy Manning. I would also like to acknowledge the NSF and the Welch Foundation for research

funding, as well as the Texas A&M Department of Chemistry and Office of Graduate Studies for Travel Grants.

I'd like to thank Christine Thomas for her love, patience, and support while I finished my Ph.D.

Finally, my greatest thanks goes to my research advisor, Prof. François P. Gabbaï. I am extremely grateful to him for giving me the opportunity to join his research lab and for his enduring patience and enthusiasm. Thanks Boss!

TABLE OF CONTENTS

CHAPTER Page

CHAPTER Page

CHAPTER Page

LIST OF FIGURES

Page

Page

Page

Page

Page

Page

Page

Page

Page

Page

Page

LIST OF TABLES

Page

Page

Page

CHAPTER I

INTRODUCTION TO TRIARYLBORANE AND TETRAORGANOSTIBONIUM-BASED LEWIS ACIDS FOR THE MOLECULAR RECOGNITION OF FLUORIDE AND CYANIDE*

1.1 Introduction

Fluoride is often added to drinking water and toothpaste because of its beneficial effects in dental health. It is also administered in the treatment of osteoporosis.[1] While the beneficial effects of fluoride are well documented, chronic exposure to high levels of this anion can lead to dental or even skeletal fluorosis.[2-4] A great deal of attention has therefore been devoted to the discovery of improved analytical methods for the detection of fluoride, especially in water. This field of research has also been stimulated by the potential use of such methods for the detection of phosphorofluoridate nerve agents such as sarin or the uranium enrichment reagent UF_6 which release fluoride upon hydrolysis. In addition to these applications, the capture of fluoride, especially in water, is a stimulating academic challenge because of the high hydration enthalpy of this anion (ΔH^o = -504 kJ mol^{-1}).

Efficient analytical methods have been developed, and are currently employed, for measuring fluoride concentrations in water. These methods rely on ion-selective

---

This dissertation follows the style and format of the Journal of the American Chemical Society.

*Reprinted in part with permission from, "Fluoride ion complexation and sensing using organoboron compounds"; Wade, C. R.; Broomsgrove, A. E. J.; Aldridge, S.; Gabbaï, F. P. *Chem. Rev.* **2010**, *110*, 3958-3984. Copyright 2010 American Chemical Society.

electrodes or colorimetric assays based on the fluoride-induced displacement of a dye from a fluorophilic metal ion.[3,4] These molecular-based colorimetric methods, which are appealing from a practical and economic point of view, suffer from a number of drawbacks, including interferences from other anions.[3-5] As a result, a great deal of current research has been devoted to the discovery of alternative molecular-based strategies.

Organic receptors that interact with the fluoride anion via formation of hydrogen bonds have been at the forefront of this effort.[6] In most cases, the binding sites of the sensors consist of amide, urea, thiourea, guanidinium, or pyrrole functionalities that are capable of hydrogen bonding with the anionic guest.[7-26] Implementation of this strategy has led to the design of very selective fluoride receptors and sensors which sometimes tolerate aqueous environments.[27-29] However, as recently noted, fluoride recognition by these derivatives mostly takes place in organic solvents, which greatly limits the scope of their use.[30] Faced with these limitations, alternative strategies based on the use of Lewis acidic compounds have attracted an increasing attention.[31-44]

In addition to fluoride, there is heightened interest in developing methods for the detection of the highly toxic cyanide anion.[45-47] This anion is used in a number of industrial processes as well as produced naturally by some plants as a protection against predators.[48-50] Consequently, cyanide contamination of water sources and other environmental resources is a legitimate fear that warrants further development of analytical methods to monitor levels of this anion.[51]

A number of current cyanide detection methods rely on the nucleophilicity of the anion and the formation of covalent bonds with electrophilic organic compounds.[52-65] However, only a few of these receptors are capable of detecting cyanide in water and, of these, some are limited by the requirement for basic conditions and high cyanide concentrations.[53,61,62,64-66] Strategies for the detection of cyanide based on coordination of the anion to a Lewis acidic metal have also been adopted and used for successful determinations down to the ppm level.[67-76] Similar to fluoride, triarylboranes have been investigated as cyanide receptors in an effort to overcome the limitations posed by some of the current methods. An impressive body of work has been directed toward the development of triarylboranes as superior fluoride and cyanide anion receptors.[6,47,77-89] Although this work includes a large number of neutral boranes that have been successfully employed for this task, the majority of this introduction will focus on systems that implement either a cationic group or transition metal moiety to enhance the anion affinity and/or response of triarylboranes to anion binding.

1.2 Reaction of triarylboranes with fluoride and cyanide

Because of their intrinsic Lewis acidity, triarylboranes react with small nucleophilic anions, including fluoride and cyanide, to generate tetrahedral borate anions. This reaction is traditionally described as an addition reaction that occurs via donation of an electron pair of the anion into the p_z-orbital of the boron center (Figure 1). Although anion coordination relieves the inherent unsaturation of the boron center, it occurs at the expense of any stabilizing π-interactions between the boron center and the aryl ligand. It is also important to point out that anion coordination induces a notable pyramidalization

of the boron center that is accompanied by an increase in repulsive steric interaction between the aryl substituents. Based on these simple considerations, it is evident that the fate of this reaction will depend on the electronic properties of the aryl substituents as well as their steric bulk. The latter consideration plays a role in governing the selectivity of triarylborane receptors for small anions such as fluoride and cyanide. In the absence of steric protection of the boron center, larger and less basic anions may interact and interfere in the detection.

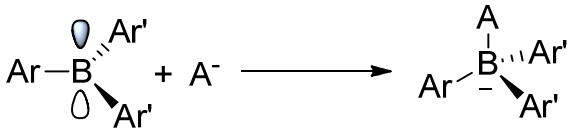

Ar, Ar' = Aryl group, A^- = F^- or CN^-

Figure 1. Reaction of a triarylborane with F^- or CN^-.

Table 1. Computed thermodynamic and metrical parameters for the reaction shown in Figure 1 with A- = F-. (Ph = phenyl, Mes = mesityl).

Ar	Ar'	ΔH (kJ mol^{-1})	*d*(B-F) (Å)	Σ(C-B-C)
Ph	Ph	-344.7	1.465	333
Mes	Ph	-268.7	1.491	340.5°

Cyanide complexation by the simple triarylborane, Ph_3B, has long been used as a means of precipitating cesium ions as cyanoborate salts.[90] Similarly, complexation of fluoride by Ph_3B has been observed, but the thermodynamics of this reaction have not

been experimentally explored.[91] However, theoretical calculations carried out for the reaction between Ph_3B and F^- show that the gas-phase reaction is exothermic by ΔH = -342 or -344.7 kJ mol^{-1}, depending on the level of theory used (Table 1).[92,93]. These calculations also indicate that the C-B-C angles decrease from 120° in Ph_3B to 111° in $[Ph_3BF]^-$.[92] While these thermodynamic and geometric parameters are indicative of the formation of a strong bond in the gas phase, it should be kept in mind that solvation effects may significantly reduce the exothermicity of this reaction in solution. Comparable calculations have been carried out for the reaction of F^- with Mes_2PhB (**1**) affording ΔH = -268.7 kJ mol^{-1} (Table 1).[94] These results indicate that the fluoride ion affinity (FIA = $-\Delta H$) of **1** is significantly lower than that obtained for Ph_3B, thus demonstrating that an increase in the bulk of the substituents is detrimental to fluoride binding. Presumably, steric repulsions impede tetrahedralization at boron, thereby weakening the boron-fluoride interaction.[94] This view is further supported by the length of the B-F bond, which increases from 1.465 Å in $[Ph_3BF]^-$ to 1.491 Å in [**1**-F]$^-$. A notable effect is also detected in the extent of pyramidalization at the boron atom, as indicated by the sum of the C-B-C angles (Σ(C-B-C)) of 340.5° in [**1**-F]$^-$ versus 333° in $[Ph_3BF]^-$. These metrical data for [**1**-F]$^-$ are given added weight by their similarity to the recent experimentally determined structural data for the $[n\text{-}Bu_4N]^+$ salt [d(B-F) = 1.481(2) Å, Σ(C-B-C) = 339.8°] (Figure 2).[95]

The pyramidalization of the boron center in [**1**-F]$^-$ is essentially identical to that found in the related cyanide adduct [K(18-crown-6)]$^+$[**1**-CN]$^-$ (340.9°) (Figure 2).[95] The structure of [**1**-CN]$^-$ shows a very linear B-C-N bond angle (173.4(2)°) and a B-C_{CN}

distance of 1.631(3) Å, longer than the B-F distance in [**1**-F]$^-$. This B-C_{CN} bond distance is comparable to that measured for [Ph_3BCN]$^-$ (1.65(2) Å) although, the boron is slightly more pyramidalized ($\Sigma(C_{Ph}\text{-B-}C_{Ph}) = 336°$).[96]

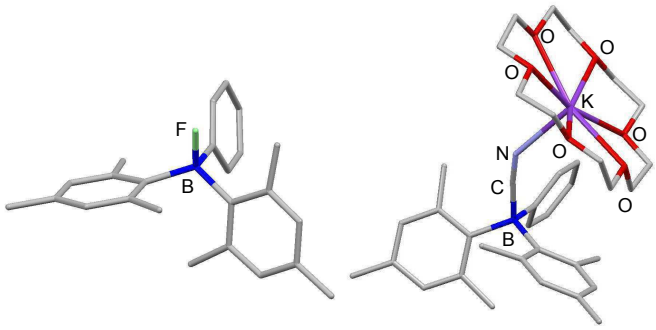

Figure 2. Crystal structure of [**1**-F]$^-$ in the [^{n}Bu$_4$N]$^+$ salt (left) and [K(18-crown-6)]$^+$[**1**-CN]$^-$ (right).

From a spectroscopic point of view, fluoride or cyanide binding to the boron center of a triarylborane has been studied by a number of methods. For example, the ^{11}B NMR resonance of triarylboranes, which is typically detected in the 60 to 75 ppm range, is shifted upfield to the -15 to + 10 ppm range in cyanoborate and fluoroborate species. These upfield shifts reflect the change in coordination number and geometry of the boron atom. The ^{19}F NMR resonance of the boron-bound fluorine nucleus typically appears as a broad signal in the -150 to -180 ppm range, shifted significantly upfield from free fluoride anions, which usually appear in the -120 to -130 ppm range. IR spectroscopy has also been used to qualitatively confirm cyanoborate formation. Upon cyanide binding, the C≡N stretching frequency is shifted to higher wavenumber versus

'free' cyanide (ν_{CN} = 2080 cm^{-1}). This effect is evidenced by the C≡N stretching frequency of [**1**-CN]$^-$ which appears at 2167 cm^{-1}.[95]

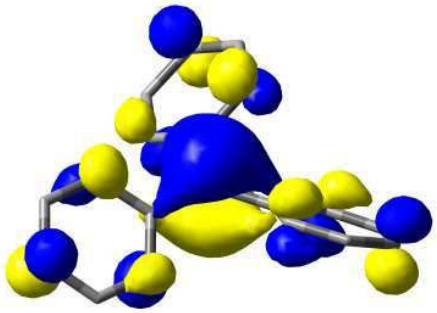

Figure 3. DFT LUMO of Ph_3B (b3lyp/6-31g(d)).

The low-energy edge of the UV-vis absorption spectrum of triarylboranes is typically dominated by electronic transitions from filled molecular orbitals into the lowest occupied molecular orbital (LUMO), an orbital often dominated by the boron p_z-orbital (Figure 3).[97] Anion binding, which leads to population of the boron p_π-orbital, induces a quenching of all transitions involving the LUMO. As a result, titration experiments can often be carried out by monitoring this quenching as a function of anion concentration and used to determine the anion binding constant for the triarylborane. This method has been used to determine the fluoride affinity of triarylboranes such as Mes_2PhB (**1**),[98] Mes_3B (**2**),[99] and Ant_3B(**3**)[97] (Ant = 9-anthryl), as well as numerous others (Figure 4). These boranes complex fluoride ions in THF with binding constants (K_F = [Ar_3BF^-]/([Ar_3B][F^-]) of 5 × 10^6 M^{-1}, 3.3 (±0.3) × 10^5 M^{-1} and 2.8 (±0.3) × 10^5 M^{-1}, respectively, at room temperature.[97,99] The lower binding constants of **2** and **3** can be assigned to the

steric protection provided by the three mesityl and 9-anthryl substituents to the boron center of these derivatives.

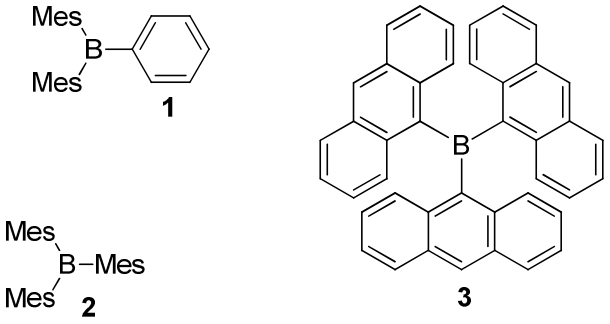

Figure 4. Triarylborane fluoride receptors **1**-**3**.

A similar spectrophotometric titration of **1** with F^- in CH_2Cl_2 (AN = 20.4 with AN = acceptor number as defined by Gutmann[100]), a more electrophilic and more competing solvent than THF (AN = 8), afforded a lower binding constant of $K_F = 8.9(1.9) \times 10^4$ M^{-1}.[95] The cyanide binding constant (K_{CN}) of **1** in the same solvent was found to be $1.9(0.5) \times 10^5$ M^{-1}, suggesting that this borane exhibits a higher affinity for cyanide over fluoride. Further evidence for this premise was given by competition experiments. When excess CN^- was added to a solution of [**1**-F]$^-$ in CH_2Cl_2, conversion to the cyanoborate [**1**-CN]$^-$ was observed by multinuclear NMR, whereas the reverse reaction, addition of F^- to a solution of [**1**-CN]$^-$, resulted in no reaction.

Despite the competitive binding of F^- and CN^-, boranes such as **1**-**3** show a high selectivity for these anions over other common anions such as Cl^-, Br^-, I^-, NO_3^-, and PO_4^{3-}. This selectivity has been assigned to the steric protection of the boron atom and is

most acute in triarylboranes featuring at least two mesityl or anthryl groups, which prevent coordination of larger anions. Some interference can, however, be observed in the case of other small anions including hydroxide, azide, and sometimes acetate.

Although the fluoride binding constants given for **1**-**3** in organic solvents are quite elevated, several studies indicate that the fluoroborates dissociate in the presence of water. This process has been confirmed in the case of $[Ant_3BF]^-$ ($[\mathbf{3}\text{-}F]^-$), which reverts to Ant_3B by the addition of water to a THF solution of the fluoroborate. Analogously, the fluoride binding constant of **2** in THF is reduced from 3.3 (±0.3) x 10^5 M^{-1} to about 1 (±0.3) M^{-1} when 10 % of water is added to the THF solution.[99] This drastic reduction of the binding constant in the presence of water can be attributed to the high hydration enthalpy of the fluoride anion (ΔH_{hyd} = -504 kJ mol^{-1}). Likewise, cyanide complexation in water is challenged by competitive protonation (p*K*a (HCN) = 9.3).

1.3 Enhancing the anion affinity of triarylboranes with cationic substituents

Several strategies have been identified to increase the fluoride and cyanide affinity of triarylboranes. One of the most successful strategies for achieving recognition of these anions in aqueous environments has relied on decoration of triarylboranes with pendant cationic functionalities. The presence of cationic groups introduces Coulombic and inductive effects that enhance the Lewis acidity of the boron center and improve the solubility of these receptors in water. An early example of such a compound is the cationic borane $[\mathbf{4}]^+$, which was isolated as a triflate salt (Figure 5). This cationic borane is compatible with protic environments and binds fluoride in THF/MeOH (3/1 vol.) with a K_F of 5.0 (±0.5) × 10^6 M^{-1}. In comparison, Mes_3B does not form a fluoride adduct

under these conditions, thus pointing to the favorable influence of the ammonium group on the anion affinity of [**4**]$^+$. Unlike Mes_3B, [**4**]$^+$ also reacts with aqueous fluoride ions under biphasic conditions ($H_2O/CHCl_3$) to form the corresponding zwitterion **4**-F.[101] Structural and computational studies indicate that **4**-F is stabilized by an intramolecular CH···FB hydrogen bond (Figure 5). Despite the presence of a cationic functionality, this borane retains a high selectivity for the fluoride anion over less basic anions. It does, however, react with cyanide to form the corresponding cyanoborate adduct.[102] Titration experiments carried out in THF show that the cyanide binding constant (K_{CN} = 8.0 (±0.5) × 10^5 M^{-1}) is significantly lower than the fluoride binding constant (K_F > 10^8 M^{-1} in THF). Presumably, steric crowding around the boron center hampers coordination of the larger cyanide anion.

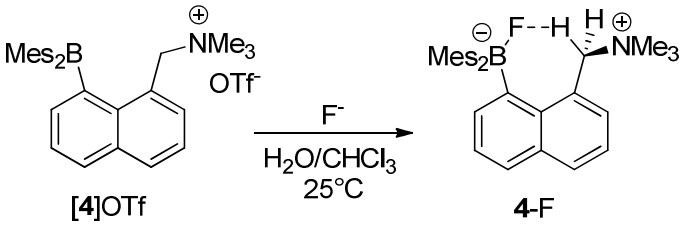

Figure 5. Reaction of [**4**]$^+$ with F^- to form **4**-F.

The proximity of the cationic moiety to the boron binding site is also thought to be responsible for the differing anion affinities of the isomeric ammonium-functionalized ferrocenyldimesitylboranes [1,1'-**5**]$^+$ and [1,2-**5**]$^+$ (Figure 6**)**.[103] The 1,1' isomer has a fluoride binding constant of 9.4(3.6) × 10^5 M^{-1} in CH_2Cl_2, which is only marginally greater than that of charge-neutral $FcBMes_2$ (**6**) (K_F = 7.8(1.2) x 10^4 M^{-1}). The

corresponding 1,2 isomer, despite having a very similar Fe(II/III) redox couple (+367 mV with respect to ferrocene/ferrocenium, cf. +314 mV for [1,1'-**5**]$^+$), binds fluoride nearly four orders of magnitude more strongly (K_F = 5.6(2.3) × 10^9 M^{-1} in CH_2Cl_2). The same trend is observed in the cyanide binding affinities, which are 5.7(1.7) × 10^5 M^{-1} and 5.6(2.4) × 10^9 M^{-1} for [1,1'-**5**]$^+$ and [1,2'-**5**]$^+$, respectively. Additionally, the ^{1}H and ^{1}H{^{19}F} NMR data for 1,2-**5**-F are consistent with the presence of a supplementary CH···FB hydrogen bond in solution.

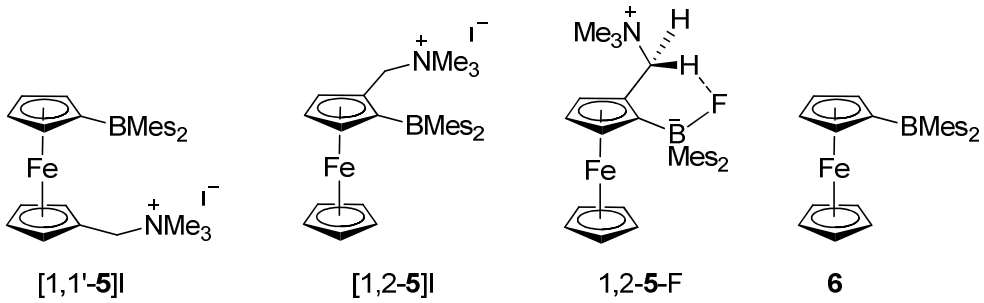

Figure 6. Ferrocenyldimesitylboranes [1,1'-**5**]$^+$, [1,2-**5**]$^+$, 1,2-**5**-F and **6**.

The cationic ammonium boranes [*o*-**7**]$^+$ and [*p*-**7**]$^+$ have also been synthesized as their triflate salts (Figure 7).[104] Both of these cations react quantitatively with F^- and CN^- in organic solvents to afford the corresponding ammonium fluoroborate (*o*-**7**-F and *p*-**7**-F) and cyanoborate (*o*-**7**-CN and *p*-**7**-CN) zwitterions. The behavior of these two isomers becomes drastically different in aqueous solution. In H_2O/DMSO 60:40 vol. (HEPES 6 mM, pH 7), [*p*-**7**]$^+$ reacts with CN^- to afford a K_{CN} of 3.9(±0.1) × 10^8 M^{-1} but is not affected by F^-. On the other hand, [*o*-**7**]$^+$ reacts exclusively with F^- under these conditions with a K_F of 910 (±50) M^{-1}, showing no affinity for CN^-. The contrasting

behavior of [*o*-**7**]$^+$ and [*p*-**7**]$^+$ can be explained by invoking a combination of inductive and steric effects. Theoretical calculations indicate that the LUMO of [*o*-**7**]$^+$ has a lower energy than that of [*p*-**7**]$^+$, which should lead to an increased Lewis acidity and account for the ability of this compound to bind the less nucleophilic F^-. However, the proximity of the ammonium group to the boron binding site in [*o*-**7**]$^+$ is thought to prevent coordination of the larger cyanide anion to this receptor. Although not explicitly stated in the original report, the zwitterion *o*-**7**-F may also be stabilized by CH···FB hydrogen bonding interactions involving the nitrogen-bound methyl groups (Figure 8).

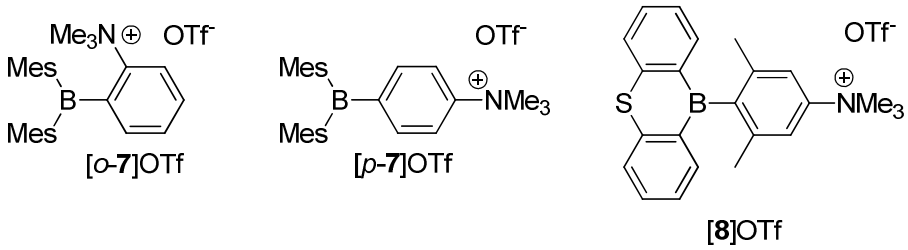

Figure 7. Ammonium boranes [*o*-**7**]OTf, [*p*-**7**]OTf, and [**8**]OTf.

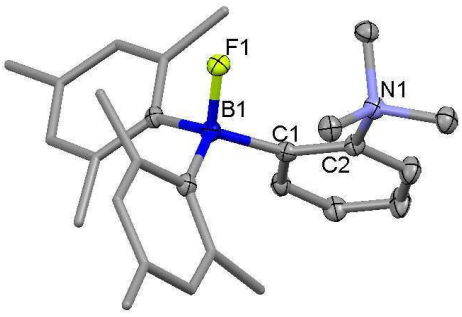

Figure 8. Crystal structure of *o*-**7**-F.

The cationic ammonium borane $[\mathbf{8}]^+$, featuring a 9-thia-10-boraanthracene group, has also been synthesized.[105] This borane binds F^- and CN^- quanitatively in THF, but slowly decomposes in water. Nevertheless, $[\mathbf{8}]^+$ reacts selectively with aqueous CN^- under $H_2O/MeNO_2$ biphasic conditions but shows no affinity for F^- under similar conditions. The lack of steric protection of the boron center due to the use of the the 9-thia-10-boraanthracene, versus the dimesitylboryl group typically employed, also allows $[\mathbf{8}]^+$ to form an adduct with the neutral donor 4-dimethylaminopyridine.

The effect of multiple cationic groups on the Lewis acidity and anion affinity of ammonium boranes has also been examined. The mono-, di-, and tri-cationic ammonium boranes $[\mathbf{9}]^+$, $[\mathbf{10}]^{2+}$, and $[\mathbf{11}]^{3+}$ were synthesized as the triflate salts (Figure 9).[106] Cyclic voltammetry experiments in CH_3CN showed reversible boron reduction potentials (*vs* Fc/Fc^+) at $E_{1/2}$ = -2.33 V for $[\mathbf{9}]^+$ and -2.09 V for $[\mathbf{10}]^{2+}$ and an irreversible reduction wave at -1.86 V for $[\mathbf{11}]^{3+}$. These reduction potentials are more positive than the reduction process measured for Mes_3B ($E_{1/2}$ = -2.63 V *vs* Fc/Fc^+). The gradual shift to higher potential with an increasing number of ammonium groups is in agreement with an increased electron deficiency at the boron centers. Although the monocation $[\mathbf{9}]^+$ was found to be insoluble in water, $[\mathbf{10}]^{2+}$ and $[\mathbf{11}]^{3+}$ were both soluble and stable in pure water, prompting a study of the F^- and CN^- affinities of these two boranes. Neither $[\mathbf{10}]^{2+}$ nor $[\mathbf{11}]^{3+}$ showed any affinity for F^- in D_2O, as determined by ^1H NMR. However, cyanide was found to react slowly with $[\mathbf{11}]^{3+}$ in pure water, and formation of the cyanoborate was confirmed by both ^{11}B NMR (δ = -12.6 ppm) and IR spectroscopy (ν(CN) = 2172 cm^{-1}). The decreased reactivity of $[\mathbf{10}]^{2+}$ and $[\mathbf{11}]^{3+}$ versus $[p\text{-}\mathbf{7}]^+$ has

been ascribed to increased protection of the boron center by the addition of two *ortho*-methyl groups.

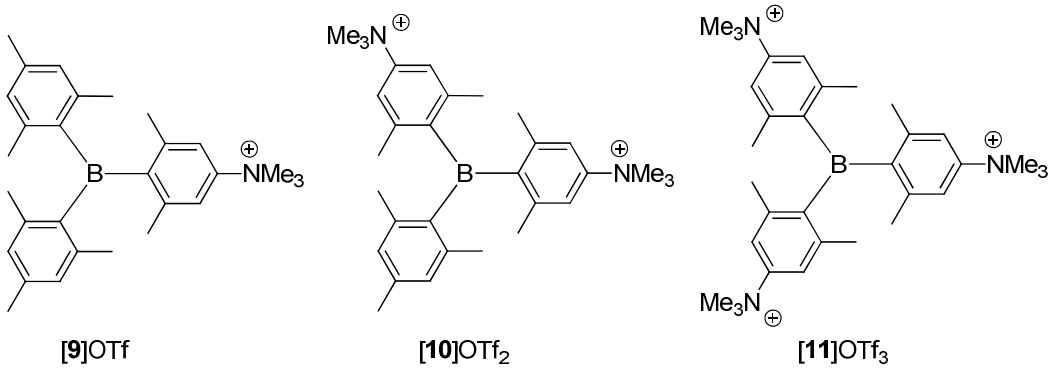

Figure 9. Ammonium boranes [**9**]OTf, [**10**]OTf_2, and [**11**]OTf_3.

In parallel to the study of ammonium boranes as fluoride receptors, a series of related phosphonium boranes of general formula [*p*-Mes_2B-C_6H_4-PPh_2R]$^+$ with R = Me ([**12**]$^+$), Et ([**13**]$^+$), Pr ([**14**]$^+$), and Ph ([**15**]$^+$) were also investigated.[107,108] These boranes are stable in water but undergo conversion to the corresponding zwitterionic hydroxide species (**12**-OH to **15**-OH) upon elevation of the pH. This process can be easily followed by monitoring the absorbance of the boron-centered chromophore as a function of pH. The resulting data can be modeled on the basis of Eq. 1 to calculate the pK_R^+ values shown in Table 2. These pK_R^+ values indicate that the Lewis acidity of the boranes increases with their hydrophobicity. A similar trend is observed in the fluoride affinity of these compounds as shown by the fluoride binding constant of [**15**]$^+$, which exceeds that of [**12**]$^+$ by more than one order of magnitude (Figure 10, Table 2).[108] Presumably, the increased hydrophobicity and decreased solvation of [**15**]$^+$ facilitates the

covalent ion pairing process that occurs upon reaction with fluoride (or hydroxide). Like $[o\text{-}\mathbf{7}]^+$, none of these phosphonium boranes interact with other commonly encountered anions, such as Cl^-, Br^-, I^-, OAc^-, NO_3^-, $H_2PO_4^-$, and HSO_4^-. From an applied perspective, these hydrophobic effects are significant as $[\mathbf{15}]^+$ is capable of detecting fluoride ions in water below the maximum contaminant level of 4 ppm set by the US Environmental Protection Agency.

$$[R_3B]^+ + 2\,H_2O \underset{}{\overset{K_{R+}}{\rightleftharpoons}} R_3B\text{-}OH + H_3O^+ \qquad \text{(Eq. 1)}$$

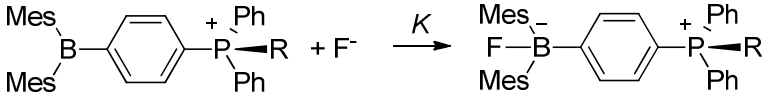

$[\mathbf{12}]^+$ $[\mathbf{13}]^+$ $[\mathbf{14}]^+$ $[\mathbf{15}]^+$
R = Me Et Pr Ph

Figure 10. Reaction of phosphonium boranes $[\mathbf{12}]^+$,$[\mathbf{13}]^+$,$[\mathbf{14}]^+$, and $[\mathbf{15}]^+$ with F^-.

Table 2. pK_R^+ values and fluoride binding constants for phosphonium boranes.

R	Cpd	pK_R^+	K_F $(M^{-1})^a$
Me	$[\mathbf{12}]^+$	7.3	840
Et	$[\mathbf{13}]^+$	6.9	2500
Pr	$[\mathbf{14}]^+$	6.6	4000
Ph	$[\mathbf{15}]^+$	6.1	10500

[a] H_2O/MeOH,9/1 vol.; 9 mM pyridine buffer, pH 4.6 – 4.9

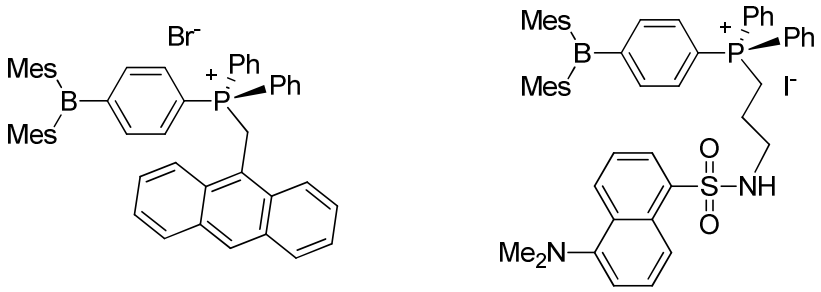

[**16**]Br [**17**]I

Figure 11. Phosphonium triarylboranes [**16**]Br and [**17**]I.

Although the cyanide affinity of phosphonium boranes $[\mathbf{12}]^+$-$[\mathbf{15}]^+$ was not investigated, two analogs of these receptors, $[\mathbf{16}]^+$ and $[\mathbf{17}]^+$, functionalized with anthryl and dansyl groups, were shown to bind cyanide in MeOH with cyanide binding constants > 10^6 M^{-1} (Figure 11).[109] Fluoride binding constants of 340(±40) M^{-1} for $[\mathbf{16}]^+$ and 500(±50) M^{-1} for $[\mathbf{17}]^+$ were also measured in this solvent, pointing to a selectivity for CN^- by these receptors. Although $[\mathbf{16}]^+$ quickly decomposed in H_2O/MeOH (6:4, v/v) at pH 7, $[\mathbf{17}]^+$ was found to be stable under these conditions and capable of detecting cyanide at concentrations as low as 26 ppb, responding with a turn-on of green fluorescence emission from the dansyl chromophore.

The diphosphonium azaborine $[\mathbf{18}]^{2+}$ has also been investigated (Figure 12).[110] Despite its dicationic character, which should lead to a notable enhancement of the fluoride binding constant, this derivative displays only a moderate affinity for fluoride anions in H_2O/DMSO 1/3 vol with a K_F of 190(±30) M^{-1}. Formation of the fluoride complex can no longer be observed when the volumetric fraction of water is greater than 1/3. However, $[\mathbf{18}]^{2+}$ binds CN^- with a K_{CN} of 1.2(±0.4) × 10^4 M^{-1} in H_2O/DMSO 6/4

vol. at pH 7. The lower F^- and CN^- affinities of this receptor versus other cationic boranes may be due to the large bulk of the Tip (2,4,6-triisopropylphenyl) ligand, which sterically passivates the boron center. It is also probable that the aromaticity of the azaborine ring reduces the electron deficiency of the boron atom. In principle, the aromatic stabilization affecting the Lewis acidity of such compounds could be reduced, if not eliminated, upon substitution of the nitrogen atom by a heavier group 15 congener. Such congeners include the phosphaborine **19**, which was alkylated to afford the phosphonium derivatives $[\mathbf{20}]^+$ and $[\mathbf{21}]^+$.[111] Although cyanide was not investigated, fluoride titrations carried out in CH_2Cl_2 indicate a drastic increase in the fluoride binding constant on going from **19** to $[\mathbf{20}]^+$ which is caused by the inductive and Coulombic influence of the phosphonium center. Analogous results have been obtained with P-methylated phosphonioborins $[\mathbf{21}]^+$ and $[\mathbf{22}]^+$.[107,112] The high fluorophilicity of these derivatives is reflected by their ability to transport fluoride from water into organic phases. Cation $[\mathbf{22}]^+$ is also able to scavenge fluoride ions as a solid in water.

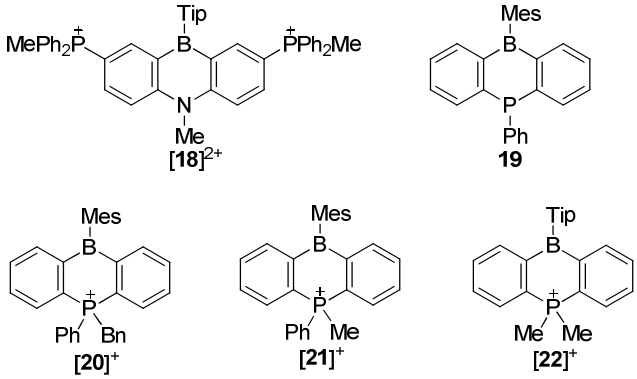

Figure 12. Diphosphonium azaborine $[\mathbf{18}]^{2+}$ and phosphonioborins **19**, $[\mathbf{20}]^+$, $[\mathbf{21}]^+$, and $[\mathbf{22}]^+$.

1.4 Enhancing the anion affinity of cationic triarylboranes via cooperative effects

Early studies in the chemistry of polydentate Lewis acids have shown that anion complexation can be enhanced via chelation. This strategy has been applied to increasing the fluoride affinity of boron-based Lewis acids,[113] with a great deal of attention being devoted to 1,8-diborylnaphthalenes.[94,99,114-119] Fluoride ion chelation has also been observed in heteronuclear bidentate systems combining a boryl group with another Lewis acidic moiety. Such systems have effectively incorporated secondary fluorosilane,[120] chlorostannane,[121] and arylmercury[119,122,123] Lewis acid binding sites for chelation of fluoride. Based on the premise that chelate effects could be combined with Coulombic effects to further enhance the fluoride and cyanide affinity of boron-based receptors, recent efforts have been devoted to the synthesis of triarylboranes with cationic substituents at a position adjacent to the boron binding site. Clues to enhanced Lewis acidity in such complexes via cooperative effects with an adjacent cationic group can be seen from the ammonium boranes [**4**]$^+$, [1,2'-**5**]$^+$, and [*o*-**7**]$^+$, which exhibit high fluoride affinities that are likely assisted by H-F hydrogen bonding interactions with the nearby ammonium group.

The heteronuclear B/Hg compound [**24**]$^+$ has been synthesized by methylation of its neutral amino precursor **23** (Figure 13).[123] Fluoride titration experiments carried out in THF/water (9:1 vol) mixtures showed that the fluoride binding constant of [**24**]$^+$ (K_F = 6.2 (±0.2) × 10^4 M^{-1}) is substantially higher than that of its neutral precursor **23** (K_F = 1.3 (±0.1) × 10^2 M^{-1}).

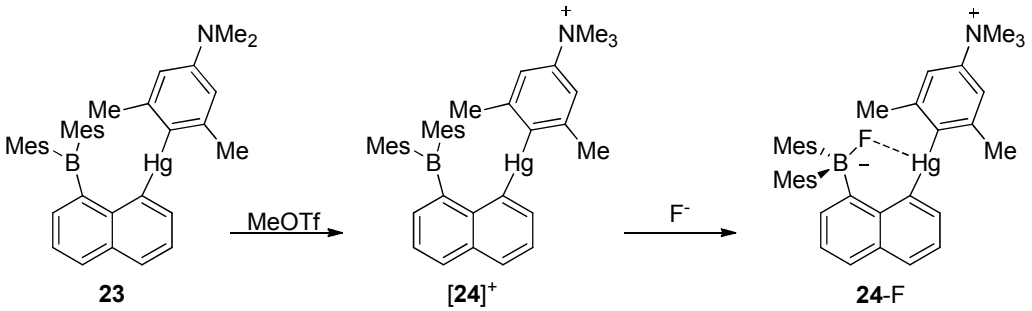

Figure 13. Synthesis of [**24**]$^+$ and its reaction with F^- to form the B-F-Hg chelate complex **24**-F.

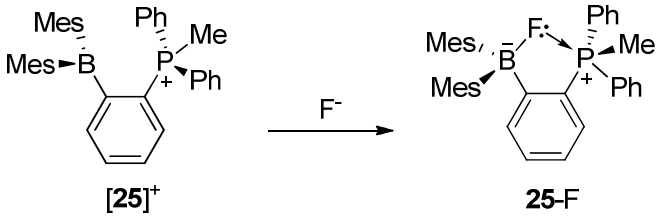

Figure 14. Reaction of [**25**]$^+$ with F^- to form zwitterionic P-F-B chelate complex **25**-F.

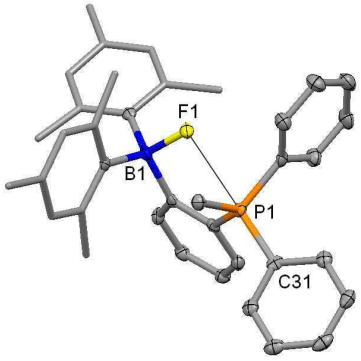

Figure 15. Crystal structure of **25**-F. The mesityl groups are represented by thin lines for clarity.

Phosphonium borane [**25**]$^+$, the ortho isomer of [**12**]$^+$ (Figure 14), exemplifies the advantage of combining cationic and chelate effects.[124,125] Unlike [**12**]$^+$ (pK_R^+ = 7.3),

[**25**]$^+$ is not stable in water at neutral pH. It can be observed by UV-vis spectroscopy at pH 2.3 in water, but the absorption band associated with the cationic borane quickly disappears above pH 3.5. These experiments indicate that the pK_{R+} of [**25**]$^+$ is in the 3-4 range. Because of its elevated acidity, the fluoride binding constant of this compound has been evaluated in methanol rather than water. Under these conditions, its fluoride binding constant exceeds 10^6 M^{-1} and is at least four orders of magnitude higher than that measured for the para isomer [**12**]$^+$ (K = 400 (±50) M^{-1}). Although an increase in inductive effects can be invoked fpr [**25**]$^+$ when compared to the para isomer [**12**]$^+$, a structural analysis of **25**-F shows that the phosphonium center acts as a Lewis acid and engages the fluoride anion in a B−F→P donor-acceptor interaction with a P-F distance of 2.66 Å (Figure 15). A Natural Bond Orbital (NBO) analysis indicates that this interaction, which involves donation of a fluorine lone pair into a P-C σ*-orbital, contributes 5.0 kcal/mol to the stability of the complex.

The fluoride and cyanide affinities of sulfonium boranes [**26**]$^+$ and [**27**]$^+$ have also been investigated (Figure 16).[126] These boranes were found to be stable up to pH 7.0 and 9.5, respectively, in H_2O/MeOH (95:5 v/v). While [**27**]$^+$ showed no affinity for F^- or CN^- in H_2O/MeOH (95:5 v/v) at pH 7, [**26**]$^+$ provided a weak response to F^- and quickly began precipitating the cyanide adduct **26**-CN upon addition of as little as 0.2 equiv. of CN^-. The cyanide titration of [**26**]$^+$ could be carried out in a 60:40 v/v H_2O/MeOH mixture at pH 7 without precipitation to yield a K_{CN} of > 10^8 M^{-1}. Moreover, [**26**]$^+$ was shown to be capable of detecting concentrations of CN^- as low as 50 ppb, the European Union (EU) maximum allowable concentration for this anion in drinking water.[127].

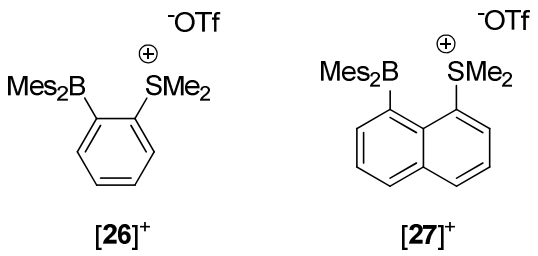

[**26**]$^+$ [**27**]$^+$

Figure 16. Sulfonium boranes [**26**]$^+$ and [**27**]$^+$.

The difference in anion affinities between [**26**]$^+$ and [**27**]$^+$ can be traced back to a combination of steric effects and the presence of lp(S) → p(B) bonding interactions. For [**27**]$^+$, the narrow bite angle of the 1,8-napthalenediyl backbone results in steric congestion around the boron binding site and allows a B-S separation of 3.07 Å, slightly shorter than that measured for the o-phenylene derivative [**26**]$^+$ (3.12 Å). NBO analysis confirms the presence of lp(S) → p(B) donor-acceptor interactions, which result in a greater stabilization energy for [**27**]$^+$ (E_{del} = 6.8 kcal mol^{-1}) than for [**26**]$^+$ (E_{del} = 2.3 kcal mol^{-1}). The stronger interaction of the sulfonium lone pair with the boron p-orbital in [**27**]$^+$ accounts for the lower anion affinity of this receptor. The structure of **26**-CN shows that the centroid of the boron-bound cyanide anion resides 3.03 Å from the sulfonium center. NBO analysis of the DFT-optimized structure revealed that this short contact results in a π(C≡N) → σ*(S-C) donor-acceptor interaction, as well as a back-bonding lp(S) → π*(C≡N) interaction. Concomitant deletion of these interactions leads to an increase in the energy of the molecule by E_{del} = 4.1 kcal mol^{-1}. These results suggest that weak chelate effects due to these sulfonium-cyanide interactions should serve to enhance the cyanide affinity of [**26**]$^+$.

The fluoride binding properties of a pair of sulfonium and telluronium boranes $[\mathbf{28}]^+$ and $[\mathbf{29}]^+$, very similar to $[\mathbf{27}]^+$ except for the substitution of a chalcogen Me substituent for Ph, have also been investigated (Figure 17).[128] Analogous to $[\mathbf{27}]^+$, both compounds exhibit short Ch-B separations (Ch = S, Te; 3.129(3) Å for $[\mathbf{28}]^+$ and 3.244(6) Å for $[\mathbf{29}]^+$) and lp(Ch) → p(B) donor acceptor interactions (E_{del} = 8.2 kcal mol^{-1} for $[\mathbf{28}]^+$ and 10.8 kcal mol^{-1} for $[\mathbf{29}]^+$). Although $[\mathbf{29}]^+$ selectively binds fluoride in MeOH with a fluoride binding constant of 750(±50) M^{-1}, the sulfonium analog $[\mathbf{28}]^+$ shows little to no affinity for this anion in the same solvent. This behavior has been attributed to the greater polarizability and electropositivity of the tellurium atom versus sulfur, which results in the formation of stronger B−F→Ch (Ch = S, Te) donor-acceptor interactions in the former case. Indeed, the crystal structures of the fluoride adducts showed that the Te-F distance in **29**-F (2.506(2) Å) is slightly shorter than the S-F distance in **28**-F (2.548(1) Å), despite the larger size of Te. A NBO analysis also found that the lp(F) → σ*(Ch-C) interactions in these molecules provided a greater stabilization energy for **29**-F (E_{del} = 22.8 kcal mol^{-1}) than for **28**-F (E_{del} = 9.2 kcal mol^{-1}).

$[\mathbf{28}]^+$ $[\mathbf{29}]^+$

Figure 17. Sulfonium borane $[\mathbf{28}]^+$ and telluronium borane $[\mathbf{29}]^+$.

1.5 Triarylborane fluoride receptors incorporating transition metal groups

Fluoride and cyanide binding to the boron center of borylated ligands in transition metal complexes has also been investigated. The major impetus for designing sensors containing transition metal moieties has been to improve the nature of the photophysical or electrochemical response to anion binding. As explained in the first part of this introduction, the low energy edge of the UV-vis absorption spectrum of triarylboranes is typically dominated by electronic transitions from filled molecular orbitals into the LUMO. Since the boron p_π-orbital contributes largely to the LUMO of most boranes, these transitions are quenched upon coordination of fluoride to the boron center. For many boranes containing simple aryl substituents, these transitions remain in the UV region such that no visible color change can be detected with the naked eye upon fluoride coordination. However, visible colorimetric responses have been achieved by the use of highly delocalized aryl substituents, which push the low energy edge of the borane absorption into the visible range.[97,99,129,130]

Colorimetric responses have also been obtained when fluoride binding to the boron center of borylated ligands in transition metal complexes influences intramolecular charge transfer (CT) processes, including metal-to-ligand charge transfer (MLCT). The color change from yellow to orange induced by fluoride binding to the iridium complex [**30**]$^+$ has been attributed to an intramolecular charge transfer (CT) process involving the dimesitylfluoroborate moiety as the donor and the pyridinium moiety as the acceptor (Figure 18).[131] Comparison of the K_{F1} (the constant associated with binding of the first equivalent of fluoride, K_{F2} would denote the second equivalent) measured for [**30**]$^+$ in

MeCN with the fluoride binding constant of the free ligand **31** indicates a substantial increase in the fluoride affinity in $[\mathbf{30}]^+$, presumably due to favorable Coulombic effects.

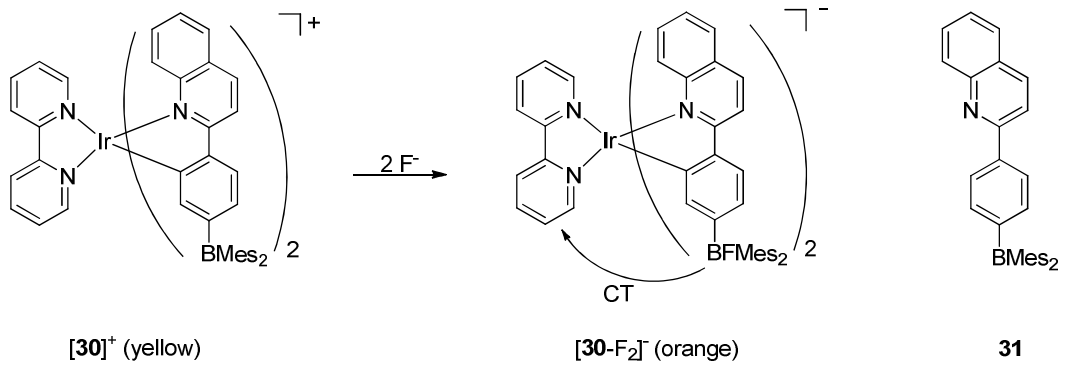

Figure 18. Reaction of $[\mathbf{30}]^+$ with fluoride resulting in formation of $[\mathbf{30}\text{-}F_2]^-$ which exhibits intramolecular CT.

In complex **32**,[132] fluoride binding to the boron center effectively increases the electron releasing properties of the borylated ligand, leading to a more electron-rich metal center (Figure 19). The observed color change of solutions of **32** in MeCN from yellow to red upon F^- binding to this complex is thus ascribed to a red shift of the MLCT band due to increased energy of the filled metal orbitals, whereas the energy of the accepting orbital on the diimine chelate ligand remains largely unaffected (Figure 19). Despite the neutral charge and electron rich nature of the boron substituents in **32**, the complex exhibits a high fluoride affinity (K_F = 4.2(±1.5) x 10^4 M^{-1}, MeCN).

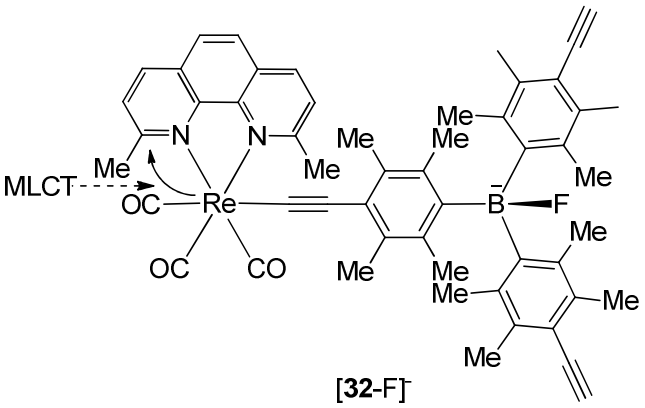

Figure 19. Depiction of MLCT mechanism in [**32**-F]$^-$.

The diborane **33** displays a very high fluoride affinity in CH_2Cl_2, with K_{F1} estimated to be equal or greater than 10^8 M^{-1} (Figure 20).[133] The second binding constant is also very high and comparable to that measured for simple triarylboranes. The high Lewis acidity of this compound makes it a viable receptor in more competing protic environments. For example, **33** captures fluoride in THF/ethanol (7/3) with a binding constant in the 10^4-10^5 M^{-1} range. Further tuning of the fluoride binding properties of **33** has been achieved by its coordination to transition metals, as in **33**-$PtPh_2$ and [**33**-$Cu(PPh_3)_2$]$^+$ (Figure 20 and Figure 21).[133,134] Cyclic voltammetry measurements suggest that metal coordination leads to a significant increase in the electron accepting abilities of the boron centers when compared to the free ligand **33**. Although exact fluoride binding constants for these metal complexes have not been determined, they display a high affinity for fluoride anions. For example, [**33**-$Cu(PPh_3)_2$]$^+$ precipitates as a monofluoride adduct when mixed with fluoride ions in methanol (Figure 21).[133] Complex **33**-$PtPh_2$ binds two equivalents of fluoride in CH_2Cl_2 with $K_{F1} \geq 10^9$ M^{-1} and $K_{F2} \sim 10^6$ M^{-1}.

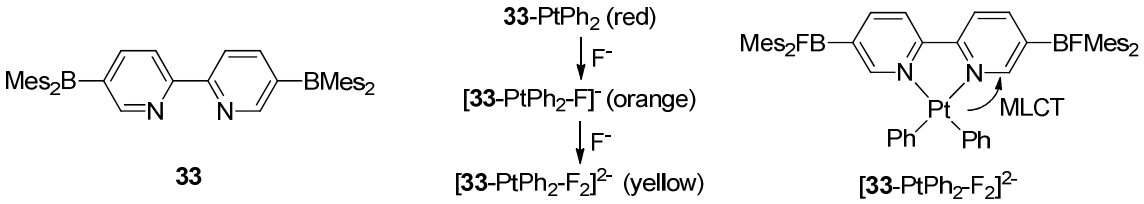

Figure 20. Observed color change of **33**-$PtPh_2$ solutions upon sequential F^- binding and depiction of the responsible MLCT process.

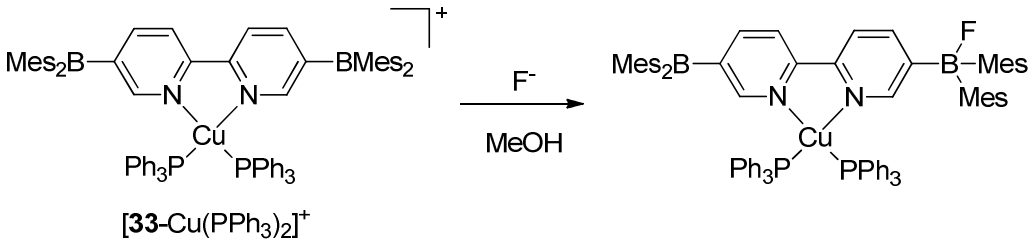

Figure 21. Reaction of [**33**-$Cu(PPh_3)_2$]$^+$ with F^-.

The red color of **33**-$PtPh_2$, which results from a MLCT band at 542 nm in CH_2Cl_2, is blueshifted to about 435 nm upon binding of the first fluoride anion to produce an orange monofluoride complex (Figure 20).[133] Binding of a second fluoride anion induces a further shift of the band to below 380 nm. These observations are in line with an increased MLCT energy gap upon fluoride binding as the ligand π–based LUMO goes up in energy, representing the reverse scenario of the charge transfer process in **32**.

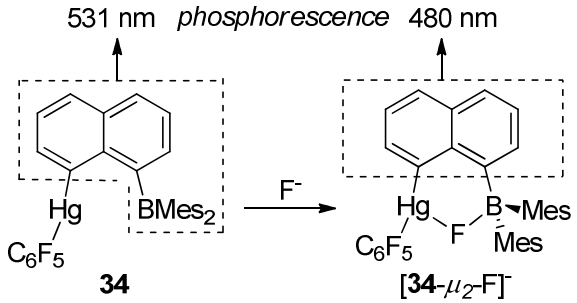

Figure 22. Reaction of **34** with F^- and depiction of phosphorescent response.

Because of spin-orbit coupling imparted by the presence of a heavy atom, many complexes containing elements such as iridium, platinum, and mercury are phosphorescent. Since the phosphorescence of such complexes usually arises from ligand-centered excited states, borylated examples of such complexes have emissive properties that can be modulated by addition of fluoride. One of the earliest examples of such a complex includes **34**, in which the spin-orbit perturbation provided by the mercury atom induces a red phosphorescence of the dimesitylborylnaphthalene chromophore with λ_{max} = 531 nm (Figure 22).[122] Upon fluoride binding to the boron center, conjugation of the naphthalenediyl and mesityl substituents is interrupted. As a result, the naphthalene moiety of [**34**-μ_2-F]$^-$ behaves as an isolated chromophore that emits a characteristic green phosphorescence (λ_{max} = 480 nm).

The high fluoride binding constant of **34** (K_F = 4.2(±1.5) x 10^4 M^{-1}, 9/1 THF/H_2O) can be assigned to the electron withdrawing properties of the C_6F_5 group. This fluoride binding constant is similar to that measured for the cationic ammonium Hg/B complex [**24**]$^+$ (K_F = 6.2 (±0.2) × 10^4 M^{-1}, 9/1 THF/H_2O) and is greater than that of the neutral amino precursor **23** (K_F = 1.3 (±0.1) × 10^2 M^{-1}, 9/1 THF/H_2O). Like [**24**]$^+$, the increased

Lewis acidity of the mercury center in **34** results in the formation of B-F-Hg chelate motif in [**34**-μ_2-F]$^-$ (Figure 22). The crystal structure of [S(NMe$_2$)$_3$][**34**-μ_2-F]$^-$ shows that the bridging fluorine atom forms a short bond of 1.483(4) Å with a boron atom and a longer one of 2.589(2) Å with the mercury atom. The latter is well within the sum of the van der Waals radii of the two elements and is, in fact, comparable to the distances observed in a fluoride adduct of a tetranuclear mercuracarborand (2.56 and 2.65 Å).[40]

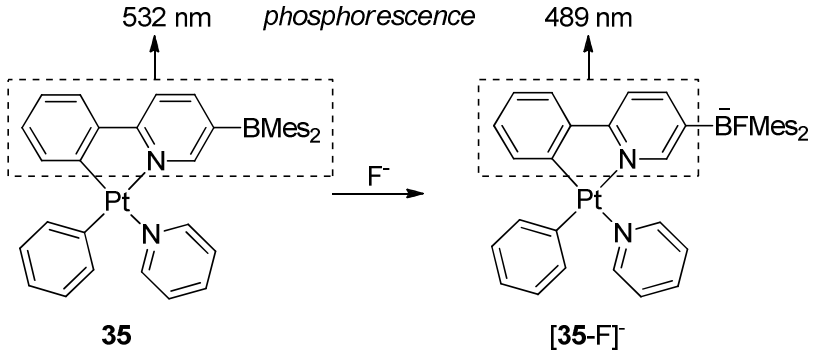

Figure 23. Reaction of **35** with F$^-$ and depiction of phosphorescent response.

Phosphorescence switching has also been observed in several platinum complexes.[135-137] For example, under an atmosphere of nitrogen fluoride binding to the boron atom in **35** switches the dimesitylboryl-phenylpyridyl-based phosphorescence at λ_{max} = 532 nm to a phenylpyridyl-based phosphorescence at λ_{max} = 489 nm in CH_2Cl_2 (Figure 23).[136] The fluoride binding constants for this and similar complexes fall in the range 10^5-10^8 M^{-1} in CH_2Cl_2, although no titrations were reported in more competitive solvents or under aqueous conditions.

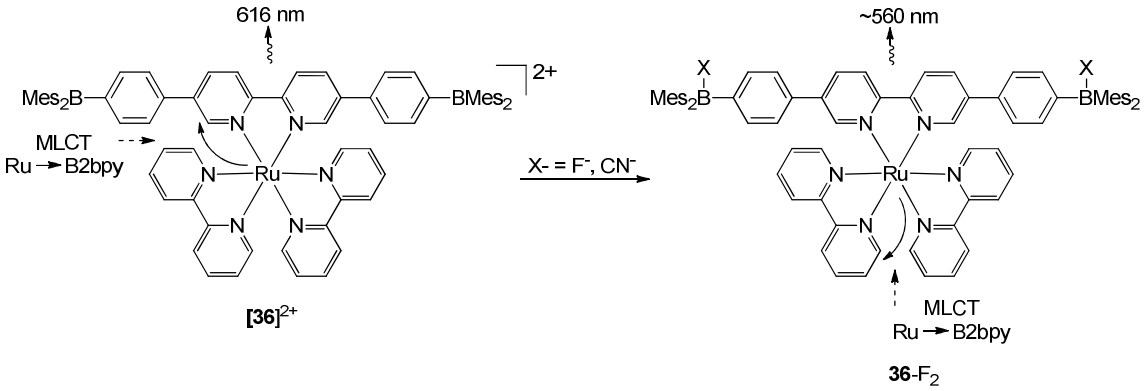

Figure 24. Reaction of [**36**]$^{2+}$ with F^- or CN^- and depiction of the MLCT switching and phosphorescent response.

A series of dicationic Ru complexes, such as [**36**]$^{2+}$, containing diborylated 2,2'-bipyridine ligands also exhibit phosphorescence switching due to chromophore isolation (Figure 24).[138] A red MLCT phosphorescence emission is observed for these receptors in CH_2Cl_2, appearing in the range λ_{max} = 600-630 nm. Fluoride or cyanide binding to the boron center of these complexes is accompanied by a blueshift of the phosphorescence and the appearance of orange emission. This change in phosphorescence is the result of a switch from Ru → B2bpy-based to Ru → bpy-dominated MLCT transitions upon anion complexation to the borylated ligand (Figure 24). The fluoride and cyanide binding constants of these complexes in CH_2Cl_2 were estimated to be $>10^8$ M^{-2} .

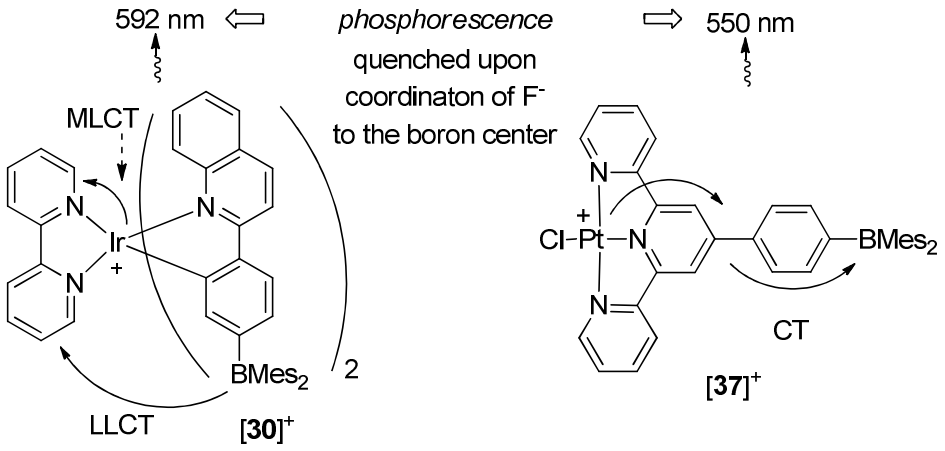

Figure 25. Depiction of MLCT and LLCT mechanisms in [**30**]$^+$ and [**37**]$^+$.

A slightly different phosphorescence response is observed for [**30**]$^+$.[131] In this case, red phosphorescence observed at λ_{max} = 592 nm and assigned to a mixed ^{3}MLCT/^{3}LLCT excited state is quenched upon titration with fluoride anions (Figure 25). Unlike the previous examples, there is no appearance of emission associated with the isolated chromophores. The exact origin of the response has not been firmly delineated and is assigned to "changes of the excited-state property of the complex" upon fluoride binding. A similar behavior is displayed by the platinum complexes [**37**]$^+$and **38**a-b which bear triarylborane-functionalized ligands.[139,140] In the case of [**37**]$^+$, the emitting triplet excited state is thought to arise from a MLCT transition that is relayed by a ligand-to-boron CT transition (Figure 25). For **38**a and **38**b (Figure 26), emission bands at 541 nm and 498 nm, respectively, in THF are attributed to MLCT and ligand-centered phosphorescence, respectively. Addition of fluoride or cyanide to all of these compounds leads to a complete quenching of the phosphorescence due to population of the empty boron p-orbital.

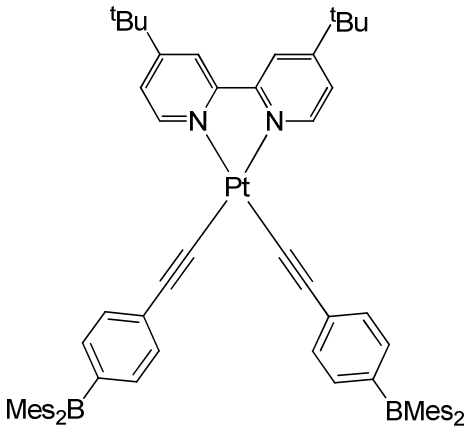

38a

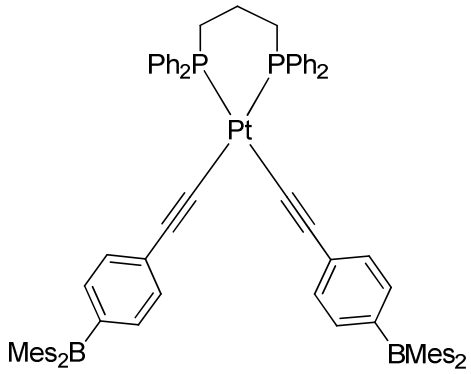

38b

Figure 26. Platinum complexes **38**a and **38**b.

In some instances, anion binding can also result in a drastic increase of the phosphorescence of platinum complexes. This is, for example, the case with **39** whose emission spectrum displays a heavy-atom induced phosphorescence from the N-(2'-pyridyl)-7-azaindolyl (NPA) ligand at 494 nm and a fluorescence emission at 399 nm originating from the triarylborane chromophore (Figure 27).[137] Remarkably, coordination of the fluoride to the boron atom annuls the extended triarylborane chromophore, which no longer competes for photoexcitation with the NPA chromophore. In turn, the excited-state population of the NPA chromophore is increased, leading to an increase of its triplet emission at 494 nm.

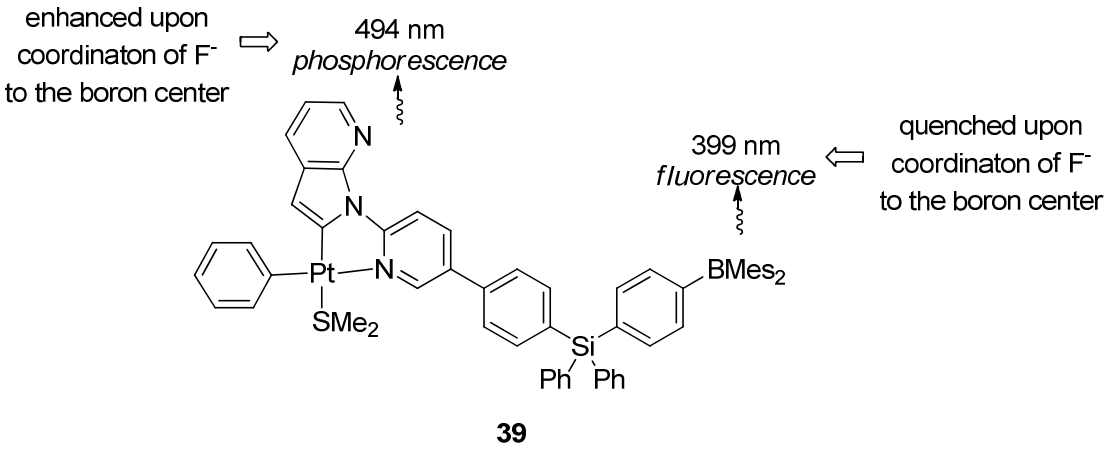

39

Figure 27. Depiction of phosphoresence response in **39**.

The effects of fluoride and cyanide binding on the $Fe^{II/III}$ redox couple of dimesitylboryl functionalized ferrocene derivatives have also been studied. Ferrocenyldimesitylborane (**6**) binds both fluoride and cyanide in CH_2Cl_2, with binding constants of K_F = 7.8 (1.2) x 10^4 M^{-1} and K_{CN} = 8.3(2.0) x 10^4 M^{-1}, respectively.[141] The $Fe^{II/III}$ redox couple of **6** occurs at $E_{1/2}$ = +181 mV with respect to ferrocene/ferrocenium. Fluoride binding results in a -550 mV shift of this potential to $E_{1/2}$ = -369 mV, consistent with the formation of an anionic four coordinate borate (Table 3). A similar shift of -564 mV from $E_{1/2}$ = +181 mV to $E_{1/2}$ = -383 mV is observed upon cyanide complexation to the boron center of this receptor. Such shifts are not without precedent in the Lewis acid/base chemistry of ferrocenylboranes, with a similar shift being reported by Piers for the coordination of trimethylphosphine to $FcB(C_6F_5)_2$.[142] The related pentamethylcyclopentadienyl derivative **40** undergoes oxidation at $E_{1/2}$ = -176 mV, with shifts of *ca.* -550 mV upon binding of either fluoride or cyanide (Table 3).[141] The

difference in the absolute values of these potentials with respect to **6** ($\Delta E_{1/2} \approx$ -350 mV) reflects the electron donating nature of the five methyl groups of the Cp* ring.

Table 3. Changes observed in the potential of the $Fe^{II/III}$ couples of **6** and **40** upon fluoride and cyanide binding.

	$E_{1/2}(Ar_3B)$ (mV)	$\Delta E_{1/2}(Ar_3BF)$ (mV)	$\Delta E_{1/2}(Ar_3BCN)$ (mV)	Solvent
6	+181	-550	-564	MeCN
40	-176	-550	-550	MeCN

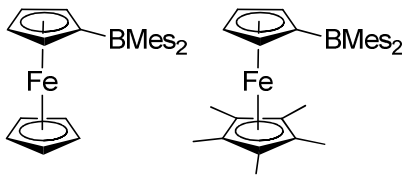

6 **40**

1.6 Reaction of antimony(V)-based Lewis acids with fluoride

The Lewis acidity of antimony(V) compounds has been well documented. One of the most prominent examples of this behavior is found in the reaction of SbF_5 with inorganic Bronsted acids to produce superacids.[143-145] For instance, superacids derived from HF/SbF_5 mixtures rely on the potent Lewis acidity SbF_5 to form exceptionally stable and weakly coordinating SbF_6^- or $Sb_2F_{11}^-$ anions.[146,147] In addition, pentacoordinate stiboranes of the form R_nSbX_{5-n} (R = alkyl or aryl, X = halide) have been shown to form stable hexacoordinate species via adduct formation with neutral donor molecules.[148-153]

The Lewis acidity of tetraorganostibonium cations (R_4Sb^+) has also been studied. These cations adopt ionic, tetrahedral structures in the presence of common, weakly

coordinating counteranions such as BF_4^-, I_3^-, ClO_4^-, and BPh_4^-.[154-157] On the other hand, the crystal structures of the tetraphenylstibonium halides (Ph_4SbX, X = F, Cl, Br, I) show that each of these compounds forms a covalent Sb-X bond and trigonal bipyramidal structure in the solid state.[156,158-161] Analysis of these structures indicates increasing elongation of the Sb-X bonds in the order I > Br > Cl > F when compared to the sum of the covalent radii of the two elements.[156,158] A combination of the ionic and covalent resonance forms was used to explain this phenomenon, in which an increasing contribution from the ionic form leads to Sb-X bond elongation (Figure 28). Not suprisingly, this trend in the Sb-X bond lengths correlates with the basicity of the corresponding halide anion, suggesting that smaller, more basic anions should form stronger bonds with the Ph_4Sb^+ cations.

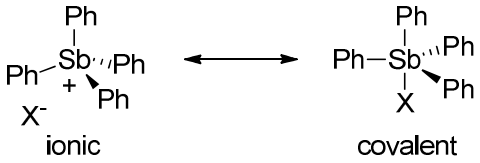

Figure 28. The ionic and covalent resonance forms of tetraphenylstibonium halides.

Conductivity measurements also indicate that Ph_4SbF and Ph_4SbCl are weakly or non-conducting in MeCN, whereas Ph_4SbBr and Ph_4SbI exhibit intermediate to strong electrolyte behavior.[156,162] This behavior would suggest that the Sb-F and Sb-Cl covalent bonds are retained, at least to some extent, in solution. This behavior by Ph_4SbX species is in contrast to the lighter P and As analogs which tend to remain ionic both in solution and in the solid state. Due to the formation of a strong covalent bond in

Ph_4SbF, the sulfate salt of Ph_4Sb^+ has been used for the biphasic extraction of F^- from water into CCl_4 or $CHCl_3$ (Figure 29).[163-165] This behavior is reminiscent of several cationic boranes, which have been shown to extract F^- under similar conditions.[101,105,166]

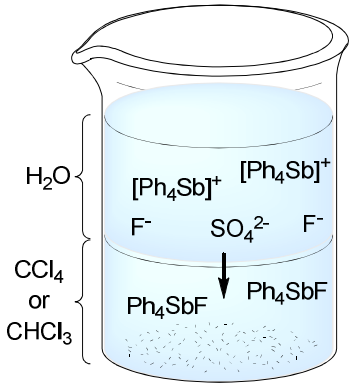

Figure 29. Biphasic extraction of F^- from water into CCl_4 or $CHCl_3$ using Ph_4Sb^+.

1.7 Objectives

Based on the effectiveness of pendant cationic groups to enhance the anion affinity of triarylboranes, we proposed to study the synthesis and the anion binding properties of pyridinium-functionalized cationic boranes. In addition to targeting *N*-methyl pyridinium cations, we considered the coordination of the pyridyl group to cationic transition metal fragments as a means of introducing cationic charge and turn-on photophysical or electrochemical responses to anion sensing. The ability of adjacent cationic groups to stabilize the boron-bound fluoride anion in triarylboranes also prompted us to adopt this strategy for the stabilization of aryltrifluoroborates against hydrolysis. Consequently, we initiated a study of the synthesis and hydrolytic stability of

zwitterionic ammonium and phosphonium aryltrifluoroborates, which are potentially useful as ^{18}F carriers in PET imaging.

We also sought to exploit the inherent Lewis acidity of antimony(V) species for anion sensing. For this reason, the synthesis and anion affinity of a stibonium borane was studied. This concept also led to initial studies on the ability of tetraorganostibonium ions (R_4Sb^+) and cationic transition metal-triarylstibine complexes (R_3SbM^+) to complex fluoride with antimony as the sole receptor site.

Finally, we have initiated a new research project exploring the structure, bonding, and reactivity of transition metal complexes bearing organoantimony(V)-based ligands. This class of ligands has been relatively unexplored, but holds the potential to stabilize catalytically relevant transition metal species and may be capable of supporting new heterobimetallic redox processes.

CHAPTER II

PYRIDYL/PYRIDINIUM TRIARYLBORANES*

2.1 Introduction

Triarylboranes are receiving a great deal of interest as receptors for small nucleophilic anions[78,82] including fluoride[167] and the highly toxic cyanide anion.[102,104,106,110,126,141,168-170] Simple triarylboranes, such as tris(9-anthryl)borane (**3**)[97] or trimesitylborane,[99] complex fluoride in non-polar organic solvents to form the corresponding fluoroborate anions, whose stability constants range from 10^5 to 10^6 M^{-1}. In the case of cationic boranes,[110-112,131,133,171-173] such as [**12**]$^+$,[108] fluoride binding is assisted by favorable Coulombic attractions and occurs in aqueous solutions where fluoride is highly hydrated (Figure 30).[78,101,102,104,106-108,123-126] Similar effects allow cationic boranes such as [*p*-**7**]$^+$ and [**26**]$^+$ to complex cyanide anions in neutral water at concentrations as low as 50 ppb.[104,126]

In most cases, the aromatic substituents of triarylboranes are conjugated via the vacant boron p-orbital, leading to the formation of a chromophore whose absorption and emission are red-shifted when compared to that of the individual aromatic substituents.[97] Fluoride binding leads to population of the boron p-orbital, interrupting conjugation and, as a result, providing a turn-off response both in the absorption and emission spectra of

---

* Reprinted in part from: "Colorimetric turn-on sensing of fluoride ions in $H_2O/CHCl_3$ mixtures by pyridinium boranes″; Wade, C. R.; Gabbaï, F. P. *Dalton Trans.* **2009**, 9169-9175. - Reproduced by permission of the Royal Society of Chemistry; and "Cyanide anion binding by a triarylborane at the outer rim of a cyclometalated ruthenium(II) cationic complex″; Wade, C. R.; Gabbaï, F. P. *Inorg. Chem.* **2010**, *49*, 714-720. Copyright 2010 American Chemical Society.

the borane. The turn-off, rather than turn-on, nature of the observed response inherently limits the sensitivity of triarylborane-based anion sensors.

Realizing this limitation, Wang recently reported a series of bifunctional molecules containing both a triarylborane and triarylamine moiety. In such systems, the emission of the triarylamine moiety is quenched by an intramolecular electron transfer process.[174,175] Because the emission of the triarylamine moiety can be revived upon addition of fluoride to the boron center, such derivatives behave as turn-on fluoride sensors.[176] However, these derivatives are neutral and can only be expected to be compatible with organic solvents.

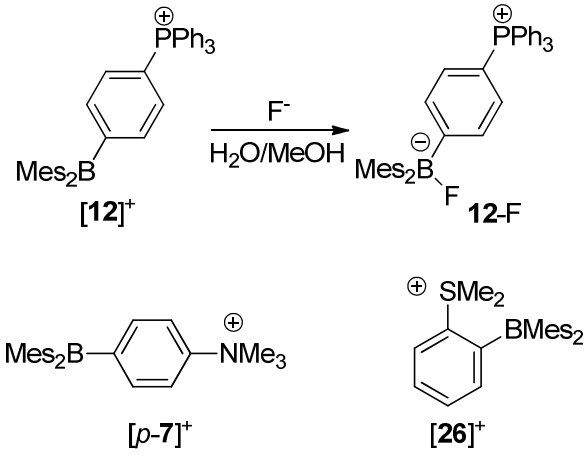

Figure 30. Reaction of the phosphonium borane [**12**]$^+$ with F^- and the cationic borane-based cyanide receptors [*p*-**7**]$^+$ and [**26**]$^+$.

Arylboronic acids such as **41**[177] have also been considered as fluoride sensors. In the case of **41**, formation of the corresponding fluoroborate species is accompanied by the appearance of an intramolecular charge transfer band involving the borate moiety as a

donor and the electron deficient aryl group as the acceptor (Figure 31).[177] Appearance of this charge transfer band results in an intense turn-on colorimetric response. Although this strategy has proved quite general,[131,178] it has not been applied to the case of simple triorganoborane fluoride receptors.

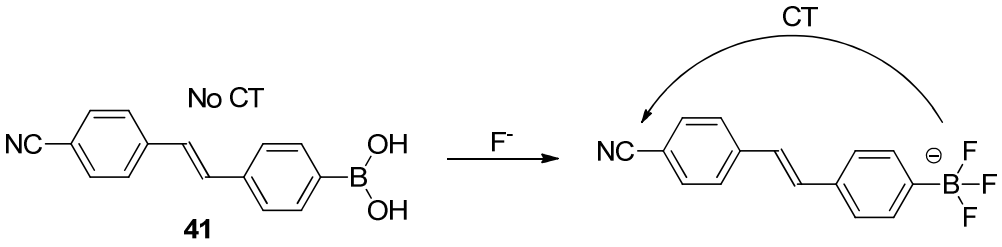

Figure 31. Reaction of arylboronic acid **41** with F^-.

In parallel to these developments, an increasing amount of attention has been devoted to the synthesis and anion binding properties of boron derivatives containing a transition metal moiety.[121,131-137,139,141,179-186] The study of such compounds has been motivated by the unusual physicochemical properties imparted by the presence of the transition metal and their response to anion binding at the boron center. Efforts in this area have yielded cationic derivatives such as [**30**]$^+$, [**37**]$^+$, [**33**]$^+$, and [**42**]$^+$ (Figure 32).[131,133,135,139] Although these complexes have been well characterized, relatively little is known about their affinity for anions other than fluoride, and the structure of the fluoride adducts remain unknown. On the other hand, ferrocenyl borane **6** has been reported to act as an electrochemical reporter for cyanide, with anion complexation to the boron center resulting in a 560 mV cathodic shift of the ferrocene/ferrocenium redox couple.[141]

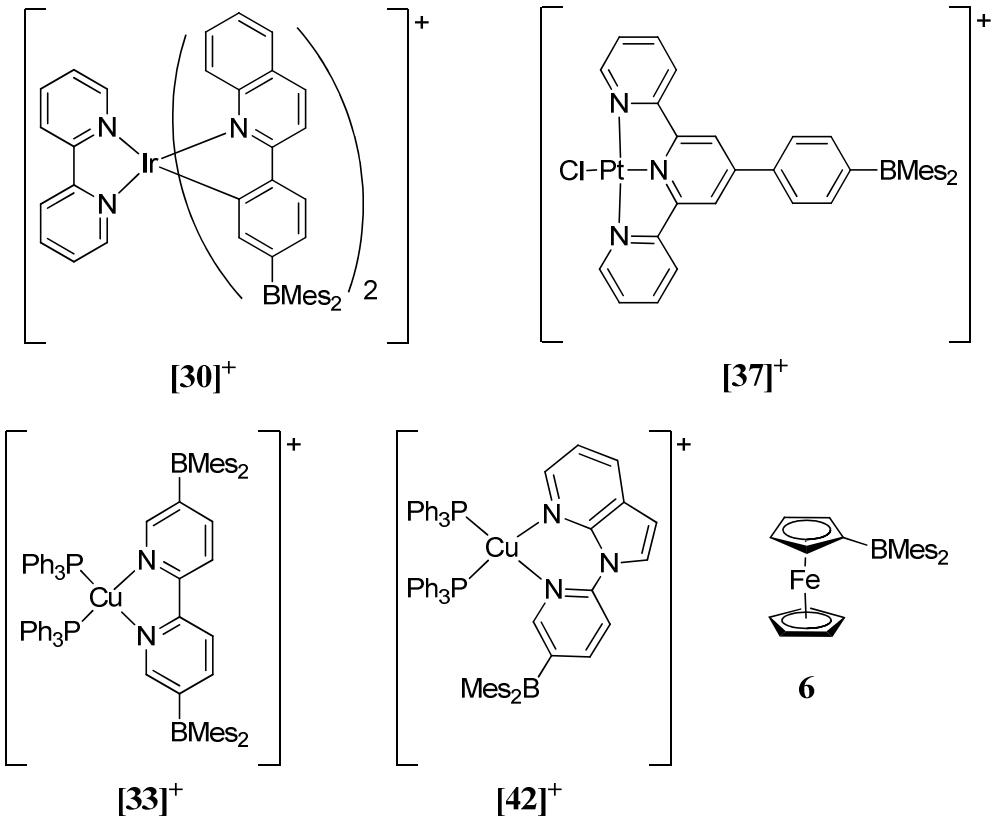

Figure 32. Cationic triarylboranes containing transition metal moieties.

With the goal of achieving turn-on type fluoride/cyanide sensing in water, we turned our attention to the investigation of cationic boranes bearing electron deficient pyridinium moieties. These moieties were hypothesized to provide desirable Coulombic effects which bolster the anion affinity of the borane. They also provide versatility in quaternization of the pyridine nitrogen, which can be achieved via methylation or coordination to a transition metal center. This chapter describes our efforts in this area including the synthesis, structural characterizaton, and study of the fluoride/cyanide receptor properties of such complexes.

2.2 Synthesis, structure, and fluoride binding studies of N-methyl pyridinium boranes

The reaction of 2-(4'-lithiophenyl)pyridine and 2-(5'-lithiothiophen-2'-yl)pyridine with dimesitylboron fluoride (Mes_2BF) afforded boranes **43**[136,181] and **44** in moderate yields (Figure 33). Subsequent treatment of **43** and **44** with MeOTf in Et_2O yielded the new cationic boranes [**45**]OTf and [**46**]OTf, which have been fully characterized. These salts dissolve in polar solvents such as acetone, acetonitrile, and DMSO but are insoluble in hydrocarbon solvents and diethyl ether. The ^{1}H NMR spectra of [**45**]OTf and [**46**]OTf in acetone-d_6 feature all expected resonances for the aromatic C*H* groups of the aryl, pyridinium, and mesityl groups. The proton resonance of the *N*-methyl groups in [**45**]OTf and [**46**]OTf appear at 4.43 ppm and 4.59 ppm, respectively. The broad ^{11}B NMR signals at 76 ppm for [**45**]OTf and 68 ppm for [**46**]OTf indicate that the boron atom of these derivatives adopts a trigonal planar geometry in solution. Broad UV absorption bands are observed at 319 nm and 355 nm for [**45**]OTf and [**46**]OTf, respectively, in $CHCl_3$ solution and are assigned to the absorbance of the boron-centered chromophore.

Both [**45**]OTf and [**46**]OTf are quantitatively converted into the zwitterionic fluoroborate adducts **45**-F and **46**-F upon addition of TBAF (*n*-tetrabutylammonium fluoride) in $CDCl_3$ (Figure 34). These zwitterions have been characterized by multinuclear NMR spectroscopy and single crystal X-ray diffraction. In both cases, the ^{11}B NMR signal is in the expected range for a four-coordinate boron center (5.6 ppm for **45**-F, 4.9 ppm for **46**-F). The ^{19}F NMR signals, which appear at -173 ppm for **45**-F and -

168 ppm for **46**-F, indicate the presence of fluoroborate moieties.[97,99,107,187] The structures of **45**-F (Figure 35) and **46**-F (Figure 36) confirm the presence of a fluorine atom coordinated to the boron center via B(1)-F(1) bond lengths of 1.482(3) and 1.460(5) Å, respectively, which are comparable to those found in other triarylfluoroborate anions (1.47 Å).[97,107]

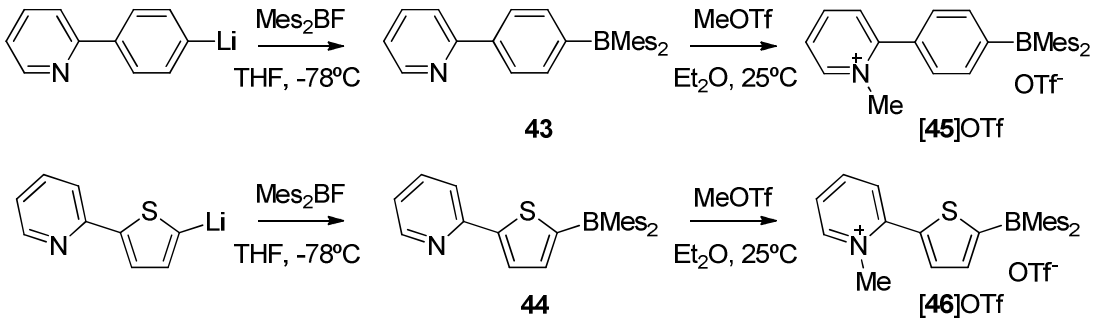

Figure 33. Synthesis of cationic boranes [**45**]OTf and [**46**]OTf.

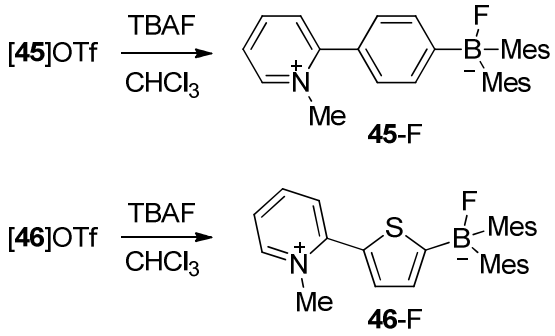

Figure 34. Synthesis of cationic boranes **45**-F and **46**-F.

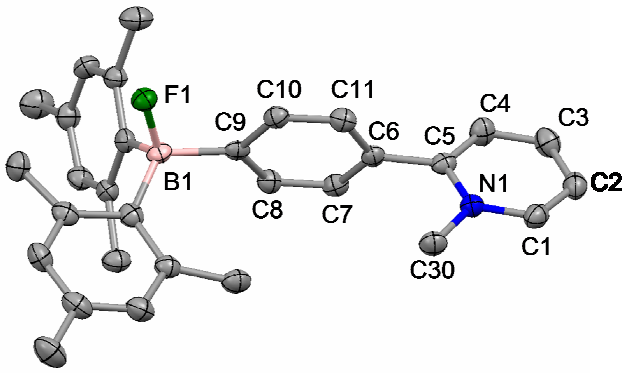

Figure 35. Crystal structure of fluoroborates **45**-F. Displacement ellipsoids are scaled to the 50% probability level.

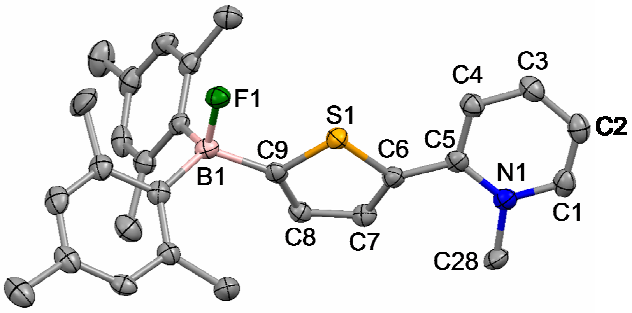

Figure 36. Crystal structure of fluoroborate **46**-F. Displacement ellipsoids are scaled to the 50% probability level.

Notably, conversion of [**45**]OTf and [**46**]OTf into **45**-F and **46**-F is accompanied by the appearance of an intense yellow color in the solutions of the compounds (Figure 37). These colorimetric changes indicate that both [**45**]OTf and [**46**]OTf act as turn-on sensors for fluoride. In order to understand the origin of this turn-on response, the UV-spectra of these compounds in $CHCl_3$ solutions were monitored upon incremental addition of *n*-tetrabutylammonium fluoride (TBAF). In both cases, addition of fluoride results in a quenching of the borane absorption band, indicating a break in conjugation

due to fluoride binding to the boron center (Figure 38 and Figure 39).[97,99] However, in each case, this quenching is also accompanied by the appearance of a new absorption band (at 368 nm for **45**-F and 430 nm for **46**-F), which is responsible for the observed visible color changes. The shape of the fluoride binding isotherms suggests that the fluoride binding constants of these cationic boranes are above the 10^7-10^8 M^{-1} range. Addition of chloride, bromide, or iodide anions does not affect the UV-Vis spectra of the cationic boranes, indicating that these anions do not bind to the borane. Although [**45**]OTf and [**46**]OTf are soluble in up to 9:1 H_2O:MeOH solvent mixtures, addition of fluoride to these solutions does not result in the formation of the fluoroborates, indicating that these cationic boranes do not have sufficient Lewis acidity to overcome the high hydration energy of the fluoride anion. Similarly, NMR measurements in the same deuterated solvent mixture show no indication of formation of the fluoroborate species.

Figure 37. Observed color change of solutions of $[\mathbf{45}]^+$ and $[\mathbf{46}]^+$ (0.017M, $CHCl_3$) upon addition of TBAF.

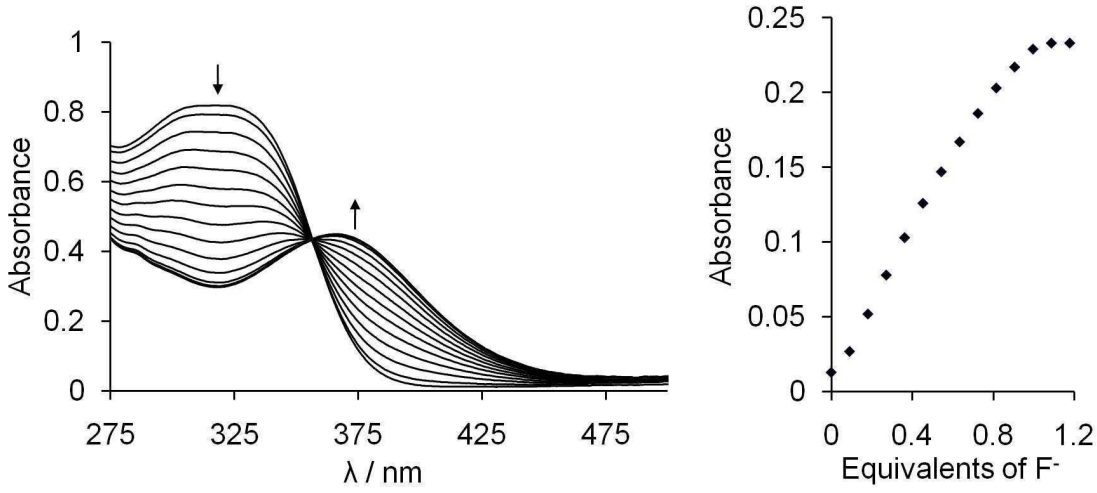

Figure 38. Spectral changes in the UV-Vis absorption spectra of [**45**]OTf (6.3 x 10^{-5} M) monitored at 406 nm in $CHCl_3$ upon incremental addition of a TBAF solution (3.4 x 10^{-3} M in $CHCl_3$).

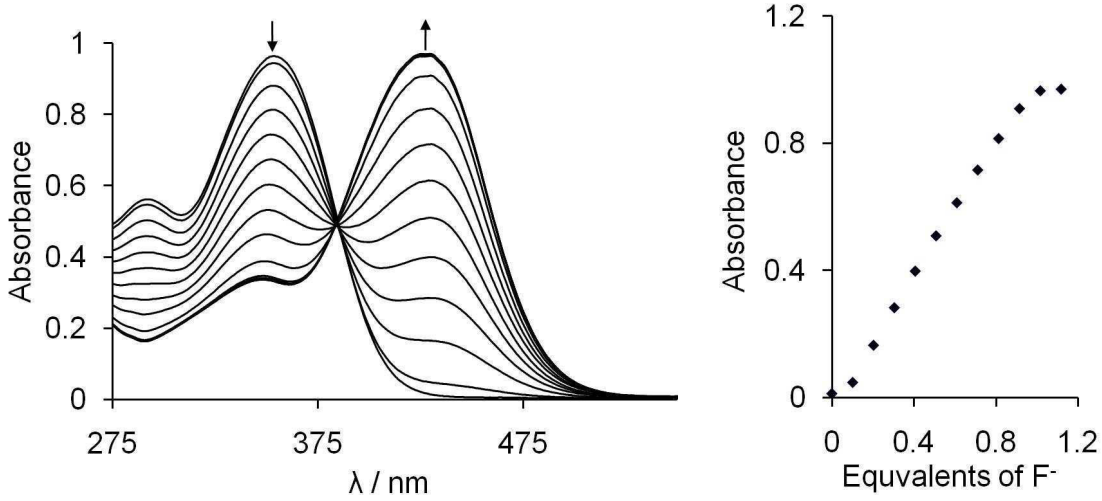

Figure 39. Spectral changes in the UV-Vis absorption spectra of [**46**]OTf (5.6 x 10^{-5} M) monitored at 430 nm in $CHCl_3$ upon incremental addition of a TBAF solution (3.4 x 10^{-3} M in $CHCl_3$).

Despite the inability of these compounds to complex fluoride directly in aqueous media, we investigated their capacity to extract fluoride from aqueous solutions into a less polar solvent where binding might be more favorable. When $CDCl_3$ solutions of [**45**]OTf and [**46**]OTf (0.5 mL, 0.07 M) were layered with solutions of TBAF in D_2O (0.125 mL, 0.28 M, 1 eq.), the organic layers quickly developed a yellow color indicative of formation of the fluoroborate species. Changes in both the ^1H and ^{19}F NMR spectra were consistent with the formation of the corresponding zwitterionic fluoride adducts **45**-F and **46**-F. Conversion to the fluoroborate species was monitored by integration of ^1H NMR signals corresponding to the aromatic C*H* groups of the mesityl substituents, which undergo an upfield shift (*ca.* 0.4 ppm) upon fluoride binding (Figure 40). Based on integration of the ^1H NMR spectra, [**45**]OTf was converted to **45-**F in 50% yield, and [**46**]OTf underwent full conversion to **46**-F. The greater fluoride affinity of $[\mathbf{46}]^+$ when compared to $[\mathbf{45}]^+$ can be assigned to the well-documented electron withdrawing properties of the thienyl group,[188] which are further enhanced by the pyridinium ring. By layering the solution of [**45**]OTf in $CDCl_3$ with a total of four equivalents of TBAF in D_2O (0.500 mL), the conversion to **45**-F increased to 74%. We performed similar experiments by layering the $CDCl_3$ solutions of [**45**]OTf or [**46**]OTf with a NaF/D_2O (0.125 mL, 0.27 M, 1 eq.) solution. Under these conditions, only 5% conversion to **45**-F and 30% conversion to **46-**F was observed, suggesting that the *n*-tetrabutylammonium cation acts as a phase transfer agent for fluoride anions. The percent conversion to **45-**F remained low when the solution of [**45**]OTf was layered with a total of four equivalents of NaF/D_2O (0.500 mL), whereas [**46**]OTf was converted to

46-F in a 42% yield with four equivalents of NaF/D_2O (Figure 40). In the experiments performed with NaF, a slight upfield shift of the pyridinium C*H* signals is observed for the remaining [**46**]OTf. Similar changes were observed in the spectra of [**45**]OTf upon layering with NaF/D_2O and are attributed to the changing ionic strength of the organic layer.

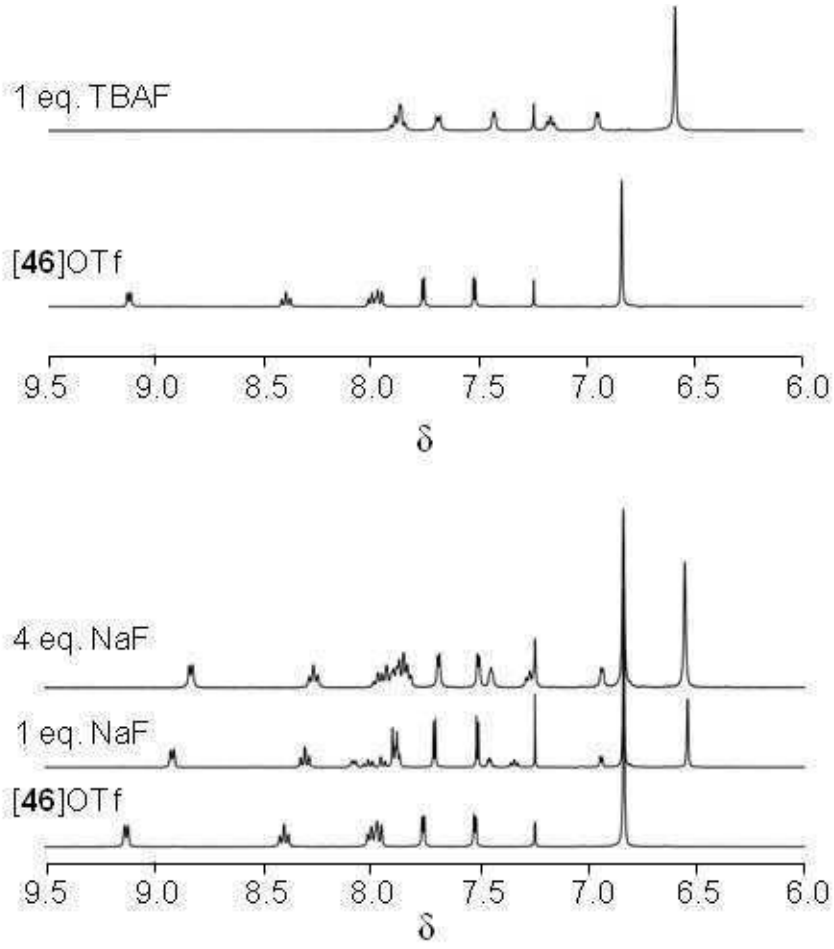

Figure 40. ^1H NMR spectra of [**46**]OTf in $CDCl_3$ upon layering with a D_2O solution of TBAF (top) or NaF (bottom).

The structures of [**45**]$^+$, [**46**]$^+$, **45**-F and **46**-F have been optimized using DFT methods (B3LYP, 6-31+g(d') for all atoms) and subjected to single point energy calculations using the Polarizable Continuum Model[189,190] (PCM) and chloroform as a solvent. Inspection of the frontier orbitals shows that the lowest unoccupied molecular orbital (LUMO) of each molecule is localized on the pyridinium group and the highest occupied molecular orbital (HOMO) is localized exclusively on the mesityl rings (Figure 41 and Figure 42). Although common TD-DFT methods cannot be used to study such chromophores,[191] it appears reasonable to assume that the lowest energy absorption band of these compounds is dominated by a HOMO-LUMO transition. Because of the localization of the frontier orbitals, these transitions can be regarded as intramolecular charge transfer transitions involving the boron moiety as the donor and the pyridinium moiety as the acceptor. In agreement with this assumption, we note that the HOMO-LUMO energy gap undergoes a noticeable decrease upon going from the cationic boranes [**45**]$^+$ and [**46**]$^+$ to the corresponding fluoroborate species **45**-F and **46**-F, respectively. Presumably, this fluoride-induced decrease of the HOMO-LUMO gaps is responsible for the experimentally observed red-shift in the electronic spectra, thus explaining the turn-on response given by [**45**]$^+$ and [**46**]$^+$ in the presence of fluoride.

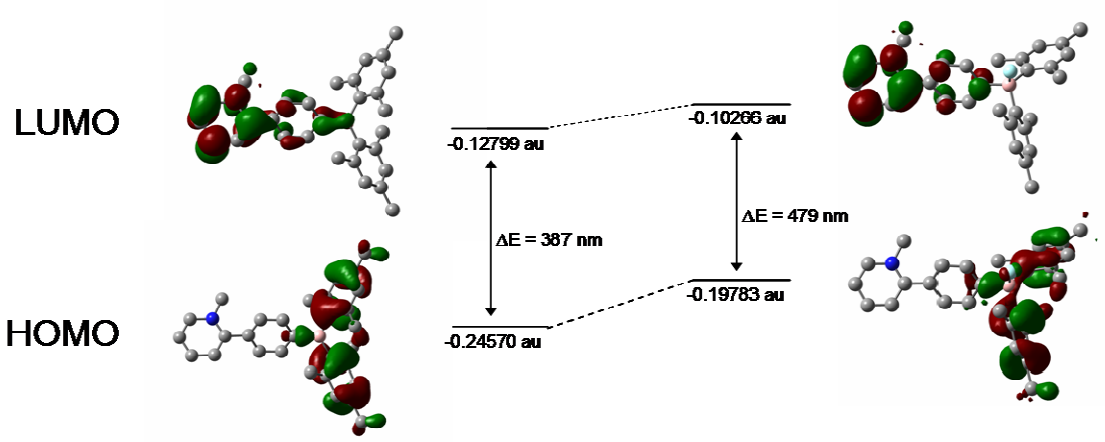

Figure 41. Rendering of the HOMOs and LUMOs of [**45**]$^+$ (left) and [**45**]F (right) and the relative orbital and HOMO-LUMO gap energies. Isovalues are set at 0.03.

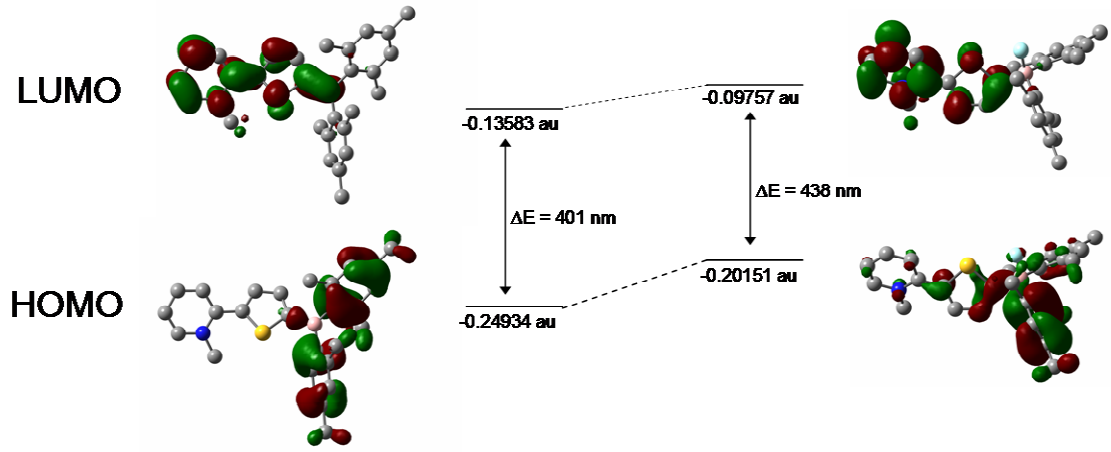

Figure 42. Rendering of the HOMOs and LUMOs of [**46**]$^+$ (left) and [**46**]F (right) along with relative orbital and HOMO-LUMO gap energies. Isovalues are set at 0.03.

2.3 Synthesis, structure, and fluoride binding studies of Pd(II) and Pt(II) cyclometalated pyridyl triarylboranes

The reaction of **44** with $Pd(OAc)_2$ in refluxing CH_2Cl_2 afforded the cyclometalated acetate dimer **47** in 66% yield (Figure 43). The identity of **47** was confirmed by ^1H NMR and single crystal X-ray diffraction. The ^1H NMR of **47** ($CDCl_3$) displays all of the expected resonances for the thienylpyridine and -$BMes_2$ groups. The presence of a singlet resonance at 7.07 ppm, corresponding to the remaining C*H* of the thiophene group, implies C-H activation by Pd at the adjacent position and a κ-*C*,*N* coordination mode of the ligand. The formation of a dimer was inferred by the presence of a singlet resonance at 2.05 ppm, which can be assigned to the bridging acetate . The X-ray crystal structure of **47** confirmed that the ligand **44** coordinates to each Pd atom in a κ-*C*,*N* fashion, with the two ligands in a trans arrangement in the acetate-bridged dimer (Figure 44). The coordination geometry around the Pd atoms is square planar with trans N-Pd-O and C-Pd-O angles in the range 171.13(19)-175.6(2)°. In addition, the short Pd1-Pd2 distance (2.8147(12) Å) enforced by the bridging acetate ligands suggests the presence of a d^8-d^8 metallophilic interaction in this complex.

Subsequent treatment of **47** with LiCl in THF followed by AgOTf and TMEDA produced the cationic palladium complex [**48**]$^+$ as the triflate salt (Figure 43). The ^1H NMR spectrum ($CDCl_3$) of [**48**]OTf displays all of the expected resonances for the thienylpyridine and -$BMes_2$ groups as well as for the TMEDA ligand. The thiophene *CH* resonance appears as a singlet at 7.31 ppm, shifted downfield from the resonance observed for **47**. The resonances corresponding to the metal-coordinated TMEDA N-

CH$_3$ and N-*CH*$_2$ groups appear as broad singlets at 2.88 and 2.96 ppm, respectively. No ^{11}B NMR signal could be observed, even after extended acquisition times.

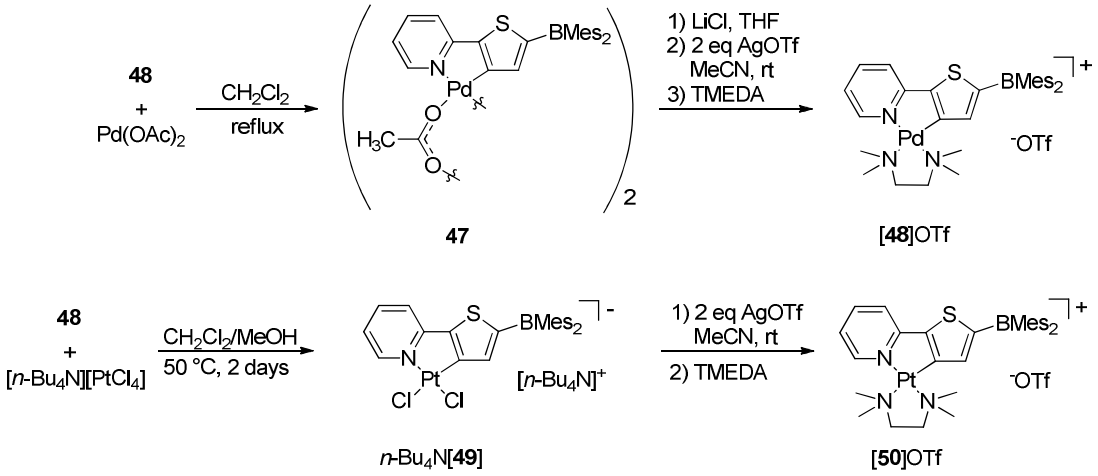

Figure 43. Synthesis of compounds **47,** [**48**]OTf, (*n*-Bu)$_4$N[**49**], and [**50**]OTf.

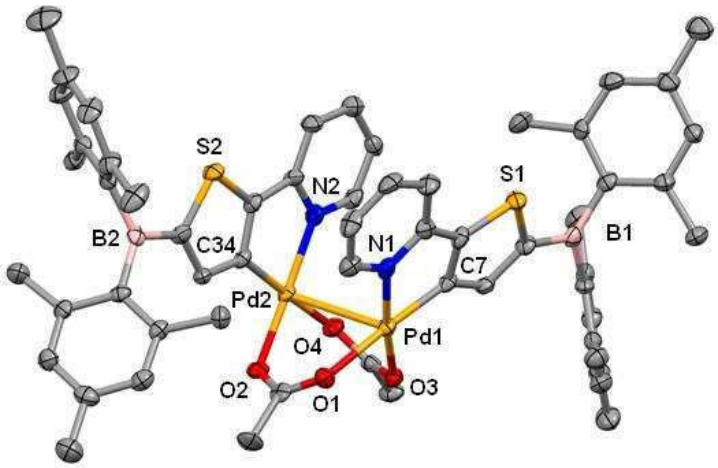

Figure 44. Crystal structure of **47**. Displacement ellipsoids are scaled to the 50% probability level. Hydrogen atoms have been omitted for clarity. Selected bond lengths (Å) and angles (˚): Pd(1)-Pd(2) 2.8147(12); Pd(1)-C(7) 1.935(7); Pd(2)-C(34) 1.951(6); Pd(1)-N(1) 2.030(5); Pd(2)-N(2) 2.027(5); Pd(1)-O(1) 2.132(5); Pd(1)-O(3) 2.041(4); Pd(2)-O(2) 2.038(4); Pd(2)-O(4) 2.144(4); N(1)-Pd(1)-O(3) 171.34(19); C(7)-Pd(1)-O(1) 173.5(2); N(2)-Pd(2)-O(2) 171.13(19); C(34)-Pd(2)-O(4) 175.6(2).

A mixture of **44** and $[(n\text{-Bu})_4N]_2PtCl_4$ in CH_2Cl_2/MeOH (2/1 vol.) was heated at 50 ˚C for 2 days to generate the dichloroplatinate complex [**49**]$^-$ as the $[(n\text{-Bu})_4N]^+$ salt. $(n\text{-Bu})_4N$[**49**] was characterized by ^{1}H NMR and used without further purification. The reaction of [**49**]$^-$ with AgOTf in acetonitrile, followed by an excess of TMEDA, afforded the cationic platinum complex [**50**]$^+$ as the triflate salt (Figure 43). The ^{1}H NMR spectrum ($CDCl_3$) of [**50**]OTf displays all of the expected resonances. The thiophene *CH* resonance (7.30 ppm) appears in the same range as that observed for [**48**]OTf, whereas the signals corresponding to the metal-coordinated TMEDA N-CH_3 (3.08 ppm) and N-CH_2 (3.17 ppm) groups are shifted downfield relative to [**48**]OTf. The ^{11}B NMR spectrum displays a broad signal around +68 ppm, within the expected range for a triarylborane.

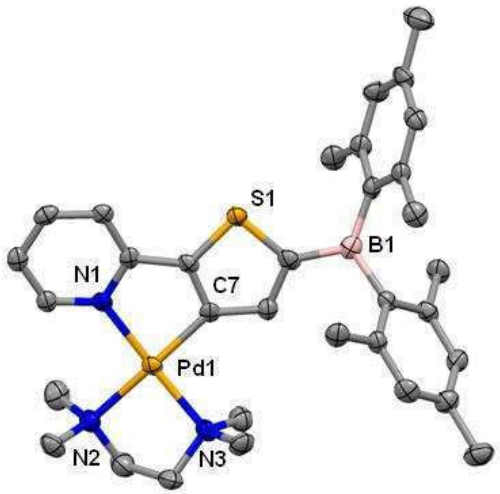

Figure 45. Crystal structure of [**48**]OTf. Displacement ellipsoids are scaled to the 50% probability level. Hydrogen atoms and triflate anions have been omitted for clarity. Selected bond lengths (Å) and angles (˚): Pd(1)-C(7) 1.992(6); Pd(1)-N(1) 2.074(5); Pd(1)-N(2) 2.193(5); Pd(1)-N(3) 2.084(5); C(7)-Pd(1)-N(2) 173.6(2); N(1)-Pd(1)-N(3) 172.6(2).

The crystal structures of [**48**]OTf (Figure 45) and [**50**]OTf (Figure 46) have been determined. Both molecules crystallize in the space group P-1 as MeCN and Et_2O solvates. The Pd and Pt atoms in these structures are in square planar coordination environments with chelating κ-*C*,*N*-2-(dimesitylborylthienyl)pyridinato and κ-*N*,*N*-TMEDA ligands in the coordination sphere. A noteworthy feature of this coordination environment is the strong trans influence of the carbanion ligand (C7), which results in a slight elongation of the Pd1-N2 (2.193(5) Å) and Pt1-N2 (2.196(10) Å) bonds compared to the Pd1-N3 (2.084(5) Å) and Pt1-N3 (2.065(11) Å) bonds trans to the pyridyl N donor. Furthermore, the boron center in both complexes is trigonal planar (Σ C-B-C = 360˚ for both [**48**]OTf and [**50**]OTf) and does not form any short contacts with the triflate anion.

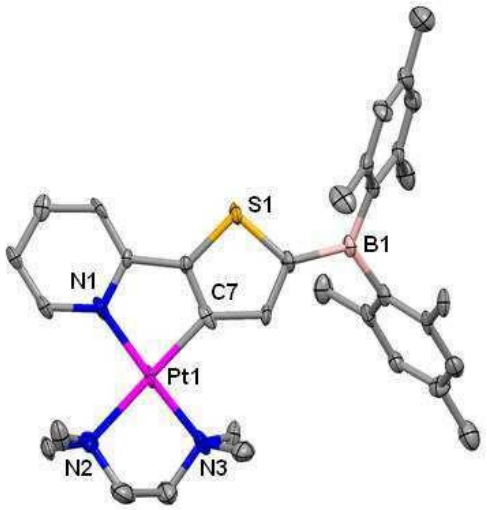

Figure 46. Crystal structure of [**50**]OTf. Displacement ellipsoids are scaled to the 50% probability level. Hydrogen atoms and triflate anions have been omitted for clarity. Selected bond lengths (Å) and angles (˚): Pt(1)-C(7) 2.023(12); Pt(1)-N(1) 2.032(11); Pt(1)-N(3) 2.065(11); Pt(1)-N(2) 2.196(10); C(7)-Pt(1)-N(2) 173.3(4); N(1)-Pt(1)-N(3) 173.8(4).

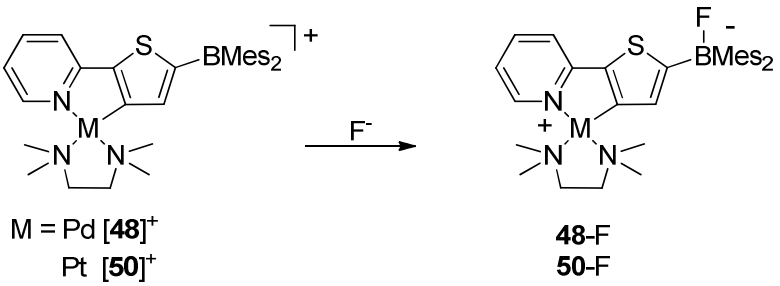

Figure 47. Reaction of [**48**]$^+$ and [**50**]$^+$ with F^-.

Addition of TBAF to solutions of [**48**]$^+$ and [**50**]$^+$ in dmso-d_6, resulted in changes in the ^{1}H NMR spectra that were consistent with the formation of the fluoride adducts **48**-F and **50**-F (Figure 47). Additionally, the ^{19}F NMR spectra of these complexes showed the appearance of two new signals at -169.2 ppm for **48**-F and -168.3 ppm for **50**-F, corresponding to the formation of a fluoroborate species. Although no ^{11}B NMR signal could be observed for **48**-F, the appearance of a relatively sharp signal at +4.51 ppm in the spectrum of **50**-F is also in agreement with the formation of a tetrahedral fluoroborate.

The formation of **48**-F and **50**-F from [**48**]OTf and [**50**]OTf is accompanied by the appearance of an increasingly intense yellow color, similar to that observed upon fluoride complexation by [**46**]OTf. The UV-Vis spectra of these compounds in THF were monitored upon incremental addition of KF in MeOH (Figure 48 and Figure 49). The UV-Vis spectra of [**48**]OTf and [**50**]OTf display broad absorption bands in the 380-420 nm and 400-450 nm range, respectively, which are assigned to a mixture of metal-to-ligand charge transfer and π-π^* transitions.[192] In both cases, addition of fluoride results in quenching of these bands and the appearance of lower energy absorption bands

centered around 425 nm for **48**-F and 450 nm for **50**-F. These spectra were fitted to a 1:1 binding model, which showed that the fluoride binding constants for both [**48**] $^{+}$ and [**50**]$^{+}$ exceed 10^{6} M^{-1}. Despite the high fluoride affinity of [**48**]$^{+}$ and [**50**]$^{+}$ observed in THF, these receptors show no measurable affinity for fluoride in THF/MeOH or THF/H_2O mixtures. Additionally, [**48**]$^{+}$ and [**50**]$^{+}$ are subject to interference from other common anions such as Cl^{-}, Br^{-}, and I^{-} in THF solution. Presumably, the presence of the bulky mesityl substituents precludes complexation of these anions to the boron center, and the interference is the result of ligand substitution at the Pd and Pt centers. This possibility was confirmed by the reaction of [**50**]OTf with an excess of TBACl in $CDCl_3$, which resulted in changes in the ^{1}H NMR spectrum that were consisent with loss of the TMEDA ligand and formation of [**49**]$^{-}$.

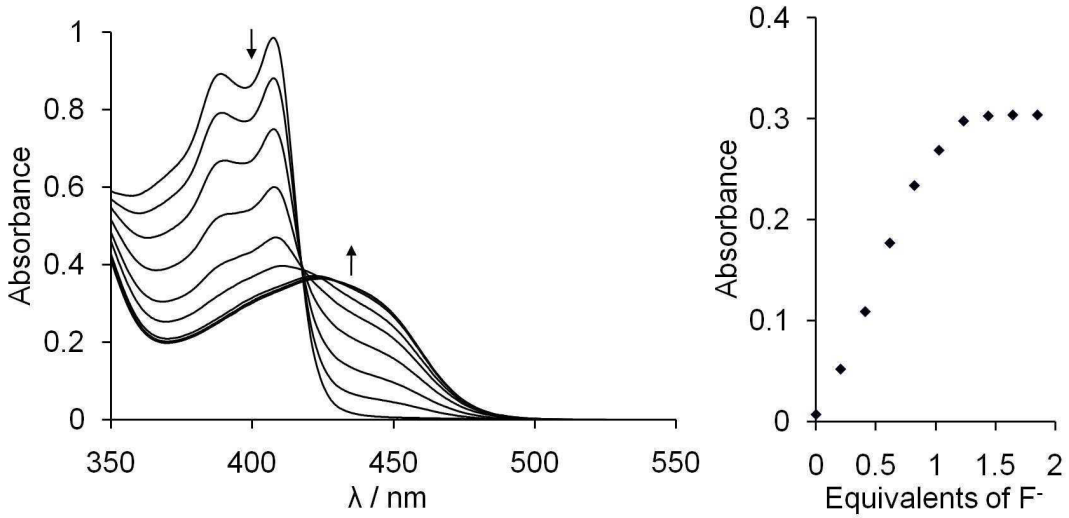

Figure 48. Spectral changes in the UV-Vis absorption spectra of [**48**]OTf (4.9×10^{-5} M) in THF upon incremental addition of a KF solution (6.0×10^{-3} M in MeOH). The isotherms are plotted based on the absorbance measured at 445 nm.

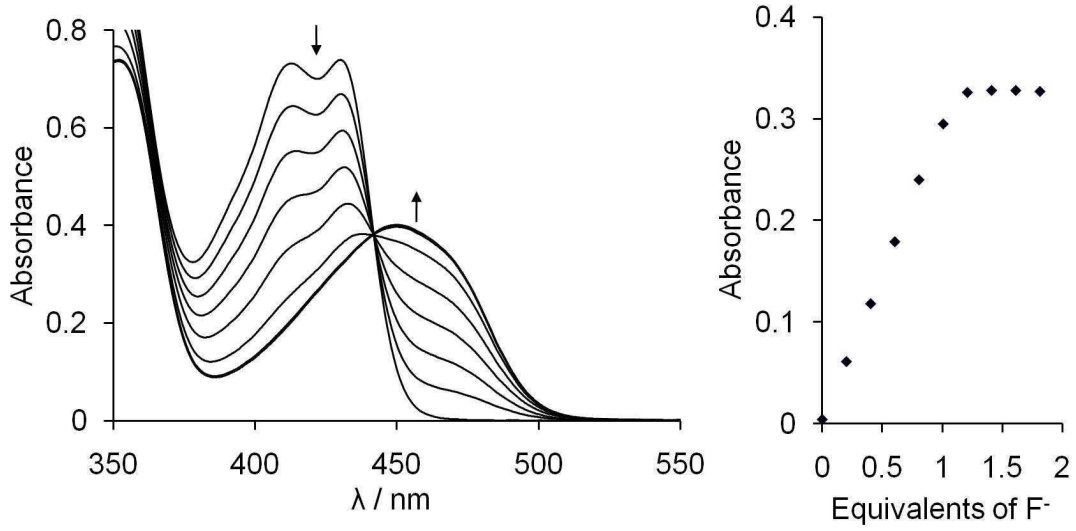

Figure 49. Spectral changes in the UV-Vis absorption spectra of [**50**]OTf (5.0×10^{-5} M) in THF upon incremental addition of a KF solution (6.0×10^{-3} M in MeOH). The isotherms are plotted based on the absorbance measured at 470 nm.

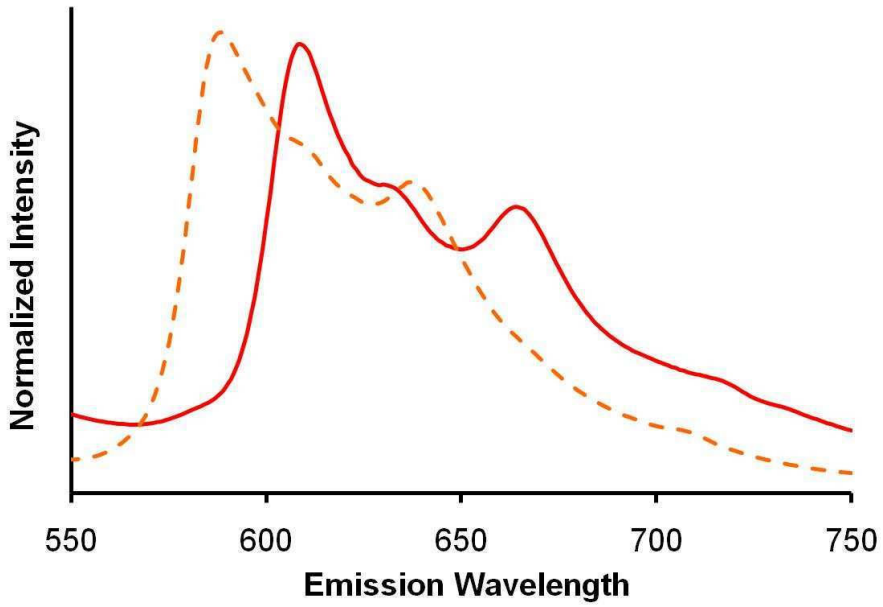

Figure 50. Normalized solid-state emission spectra of [**50**]OTf (—)and **50**-F (- - -).

Notably, the platinum complexes [**50**]OTf and **50**-F display visible red and orange luminescence, respectively, in the solid state under a handheld UV lamp, whereas the palladium complexes [**48**]OTf and **48**-F are nonemissive. The solid-state emission spectra of [**50**]OTf and **50**-F were measured at room temperature (Figure 50). Both complexes displayed similar emission band features, although the emission was blueshifted *ca.* 20 nm for **50**-F (λ_{em} = 588 nm) versus [**50**]OTf (λ_{em} = 608 nm). The measured microsecond emission lifetime for [**50**]OTf (τ = 6.788(9) μs) and the structured emission for both [**50**]OTf and **50**-F suggest a mixed ^{3}LC and MLCT origin.[193-195] The observed increase in energy of the emission upon formation of **50**-F is consistent with decreased ligand delocalization due to fluoride coordination to the boron center.[136]

2.4 Cyclometalation of pyridyl triarylboranes with Ru(II)

Coordinatively saturated, cyclometalated ruthenium complexes such as [(2,2'-bpy)$_2$Ru(2-ppy)]$^+$ (2-ppy = κ-*C*,*N*-2-phenylpyridinato) have been previously studied and shown to possess a relatively inert metal core.[196-201] Moreover, such complexes possess well-understood electrochemical and photophysical properties.[196-201] Encouraged by these precedents, we decided to investigate the synthesis and anion binding properties of a borylated analogue of such a complex. Consequently, **43** was allowed to react with (2,2'-bpy)$_2$RuCl$_2$ in refluxing CH_2Cl_2/MeOH in the presence of AgOTf (Figure 51) to afford [**51**]OTf as dark purple needles in 52% yield after recrystallization from CH_2Cl_2/Et_2O.[201] Salt [**51**]OTf has been fully characterized, and its crystal structure determined. It displays moderate solubility in polar organic solvents such as THF,

CH_2Cl_2, DMSO, acetone, and pyridine but is insoluble in H_2O and less polar solvents such as Et_2O and pentane. The ^1H NMR spectrum of [**51**]OTf (pyridine-d_5) displays distinct resonances for each of the aryl C*H* groups of the 2,2'-bpy and phenylpyridyl ligands. The presence of single mesityl aromatic C*H* and ortho- and meta- CH_3 resonances indicates equivalency of boron mesityl substituents at room temperature. The broad signal observed at 74 ppm in the ^{11}B NMR spectrum (CD_2Cl_2) is characteristic of a triarylborane.

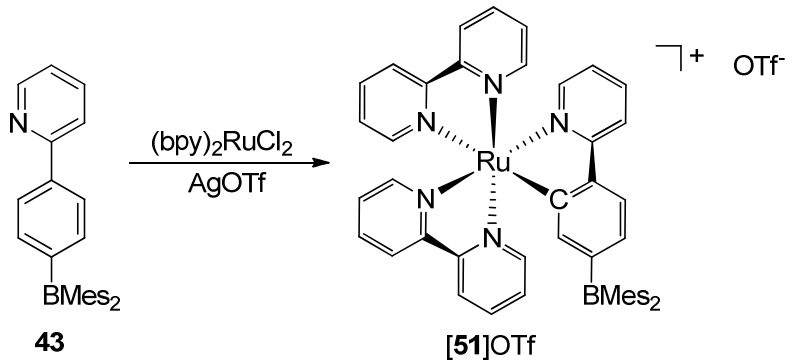

Figure 51. Synthesis of [**51**]OTf.

The UV-Vis spectrum of [**51**]OTf (THF/DMF, 9/1 vol.) displays two prominent features: a sharp band at 335 nm (ε = 33460), assigned to absorption of the triarylborane-based chromophore, and a broad metal-to-ligand-charge-transfer (MLCT) band with λ_{max} = 550 nm (ε = 11650) spanning the 450-625 nm range. This MLCT band appears in the same range as that reported for the non-borylated cation $[(bpy)_2Ru(2\text{-}ppy)]^+$.[197,198] Cyclic voltammetry experiments performed on [**51**]OTf show that it undergoes a fully reversible $Ru^{II/III}$ redox couple at $E_{1/2}$ = +0.051 V *vs* Fc/Fc^+ (1 mM, 0.1 M $TBAPF_6$,

DMF, glassy carbon electrode, 200 mV scan rate). In order to understand the effects, if any, of the pendant dimesitylboryl group on the $Ru^{II/III}$ redox couple, the cyclic voltammogram of the non-borylated complex, $[(bpy)_2Ru(2\text{-}ppy)]OTf$, was recorded. Under the same conditions, this complex undergoes oxidation at $E_{1/2}$ = +0.025 V *vs* Fc/Fc^+, indicating that decoration of the phenylpyridyl ligand with a dimesitylboryl moiety has only a limited influence on the redox properties of the complex.

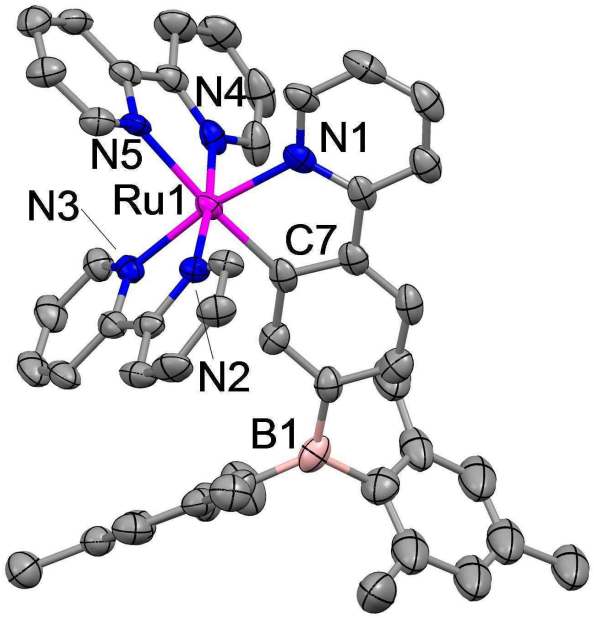

Figure 52. X-ray crystal structure of [**51**]$^+$. Displacement ellipsoids are scaled to the 50% probability level. Hydrogens and triflate anion have been omitted for clarity. Selected bond lengths (Å) and angles (˚): Ru(1)-C(7) 2.038(5)Å; Ru(1)-N(1) 2.068(4)Å; Ru(1)-N(2) 2.035(3)Å; Ru(1)-N(3) 2.035(4)Å; Ru(1)-N(4) 2.070(4)Å; Ru(1)-N(5) 2.152(4)Å; C(7)-Ru(1)-N(1) 79.80(18)˚; N(2)-Ru(1)-N(3) 79.24(15)˚; N(4)-Ru(1)-N(5) 77.38(15); B(1)-C(9) 1.587(8)Å; B(1)-C(12) 1.556(8)Å; B(1)-C(21) 1.564(8)Å; C(12)-B(1)-C(21) 123.4(5)˚; C(12)-B(1)-C(9) 115.4(5)˚; C(21)-B(1)-C(9) 121.2(4)˚.

The crystal structure of [**51**]OTf confirms the presence of the cyclometalated ligand bearing a dimesitylboryl group (Figure 52). The Ru-N bond distances are all within the 2.035(4)-2.070(4) Å range, with the exception of the Ru(1)-N(5) bond trans to the Ru(1)-C(7) bond which is somewhat elongated (2.152(4) Å) due to the strong trans effect of the carbanionic ligand. The Ru(1)-C(7) bond was measured to be 2.038(5) Å, in the range of Ru-C distances observed for similar complexes.[196,201-203] The boron atom displays B-C distances in the range 1.556(8)-1.587(8) Å, comparable to those observed in similar triarylboranes.[136,181]

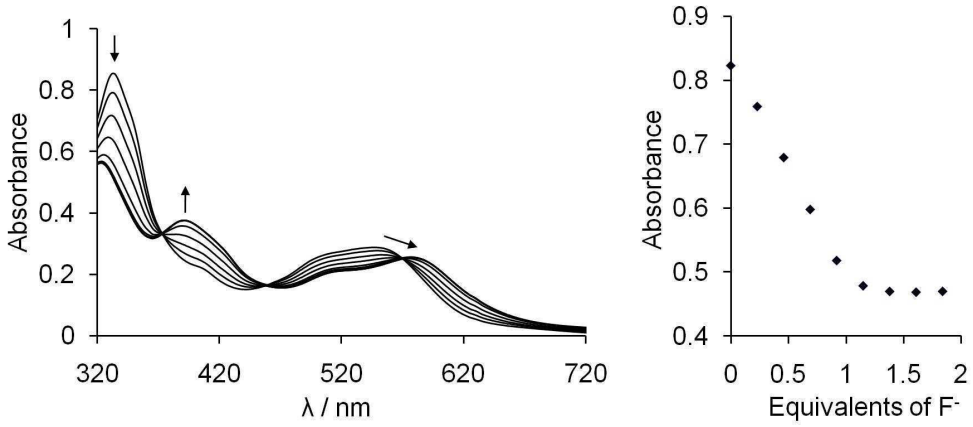

Figure 53. Spectral changes in the UV-Vis absorption spectra of [**51**]OTf (2.5×10^{-5} M) in 9/1 THF/ DMF upon incremental addition of a TBAF solution (3.5×10^{-3} M in DMF). The isotherms are plotted based on the absorbance measured at 338 nm.

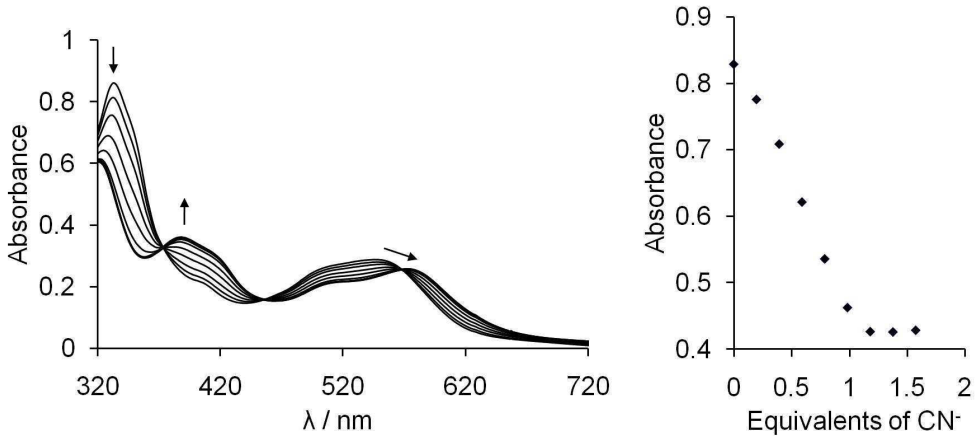

Figure 54. Spectral changes in the UV-Vis absorption spectra of [**51**]OTf (2.5×10^{-5} M) in 9/1 THF/ DMF upon incremental addition of a TEACN solution (3.0×10^{-3} M in DMF). The isotherms are plotted based on the absorbance measured at 338 nm.

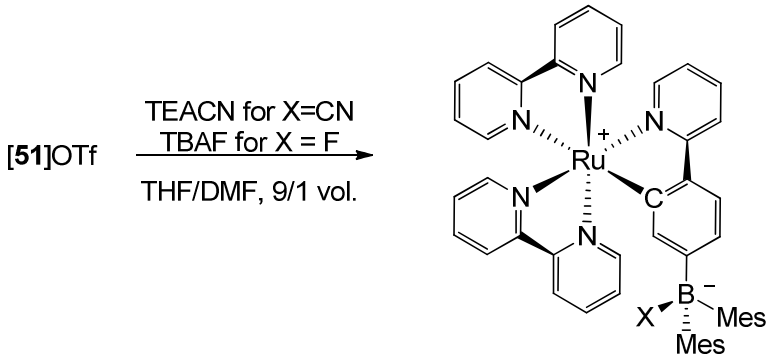

Figure 55. Reaction of [**51**]OTf with F^- and CN^-.

Addition of fluoride or cyanide anions to solutions of $[\mathbf{51}]^+$ in acetone resulted in a color change from deep purple to nearly black. To understand the origin of this color change, the reactions were monitored using UV-Vis spectroscopy. The UV-Vis spectrum of [**51**]OTf (3.0 mL, 2.5 x 10^{-5} M, THF/DMF, 9/1 vol.) was monitored upon incremental addition of either tetrabutylammonium fluoride (TBAF, 3.5 x 10^{-3} M, DMF) or

tetraethylammonium cyanide (TEACN, 3.0 x 10^{-3} M, DMF) (Figure 53 and Figure 54). Similar spectral changes observed for both titrations suggest a similar mode of interaction-namely, fluoride and cyanide coordination to the boron center of [**51**]$^{+}$. The absorption band at 335 nm, assigned to the absorbance of the triarylborane chromophore, is quenched upon addition of the first equivalent of fluoride or cyanide ions. This phenomenon results from a loss of conjugation in the boron-centered chromophore, indicating formation of **51**-F and **51**-CN (Figure 55).[97,99] Formation of these complexes is also accompanied by the appearance of a broad band spanning the 360 – 450 nm range with λ_{max} = 390 nm (ε = 14 200) for both **51**-F and **51**-CN. This behavior is reminiscent of that observed upon addition of fluoride anions to the *N*-methylated pyridinium cation [**45**]$^{+}$ and is tentatively assigned to a charge transfer transition involving the dimesitylfluoroborate as the donor and the metallated pyridyl ring or 2,2'-bpy ligands as the acceptor. Formation of **51**-F and **51**-CN also results in a bathochromic shift of the Ru(II) $d_{\pi} \rightarrow$ 2,2'-bpy MLCT band with a shift of the lowest energy edge of the band from 550 nm to 580 nm. This bathochromic shift can be rationalized by invoking the increased energy and donor ability of the borylated ligand in **51**-F and **51**-CN (*vs* [**51**]$^{+}$), which leads to a more electron rich Ru(II) center.

The spectral changes induced by fluoride binding to [**51**]$^{+}$ in THF/DMF (9/1 vol.) can be fitted to a 1:1 binding isotherm to provide a fluoride binding constant K_F of 8.0(± 2.0) × 10^{6} M^{-1} (Figure 54). Encouraged by the magnitude of these binding constants, similar titrations were carried out in chloroform, whose elevated acceptor number[100] (AN = 23.1 for $CHCl_3$ vs. 8.9 for THF and 16.0 for DMF) makes it a more competitive solvent for

anion binding.[188] Accordingly, this experiment provided a substantially lower K_F of 1.1(± 0.1) × 10^4 M^{-1} (Figure 56). A lower binding constant K_F of 7.5(± 0.5) × 10^2 M^{-1} was obtained for the free ligand **43** in $CHCl_3$ (Figure 57), thus providing evidence for the beneficial influence of the cationic Ru(II) moiety, which increases the anion affinity of the boron center both through inductive and Coulombic effects. The observed fluoride binding constant is, however, notably smaller than the value of 6.5(± 0.5) × 10^6 M^{-1} measured for the phosphonium borane [*p*-(Mes_2B-C_6H_4-PPh_2Me)]$^+$ in $CHCl_3$.[99] Presumably, the cationic charge of the Ru(II) moiety is largely dissipated on the two 2,2'-bpy ligands, leading to a decrease of its inductive influence on the borylated phenylpyridine ligand. The bulk of the Ru(II) moiety may also hamper the anion-induced tetrahedralization of the boron center.

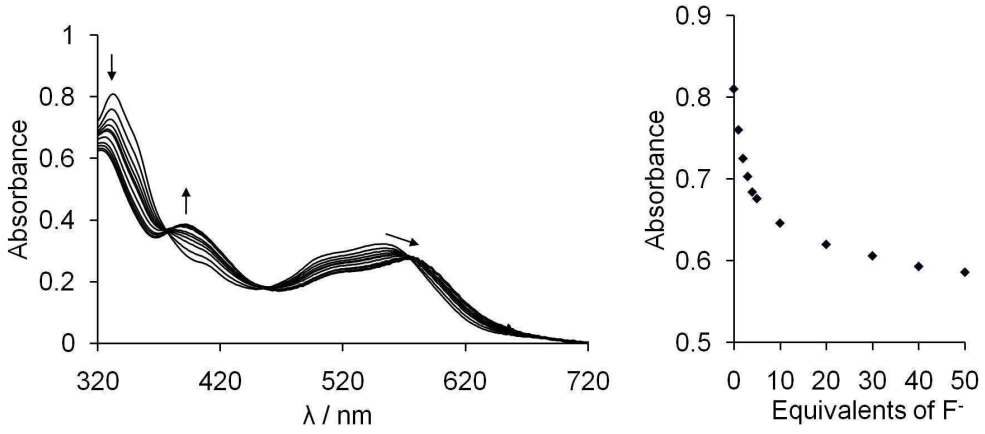

Figure 56. Spectral changes in the UV-Vis absorption spectra of [**51**]OTf (2.6 × 10^{-5} M) in 9/1 $CHCl_3$/ DMF upon incremental addition of a TBAF solution (2.6 × 10^{-2} M in $CHCl_3$). The isotherms are plotted based on the absorbance measured at 332 nm.

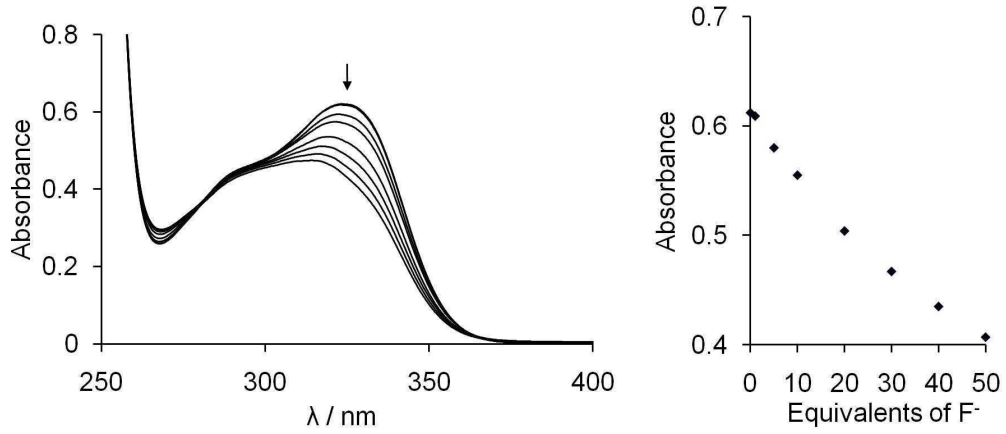

Figure 57. Spectral changes in the UV-Vis absorption spectra of **43** (2.6×10^{-5} M) in 9/1 $CHCl_3$/DMF upon incremental addition of a TBAF solution (2.6×10^{-2} M in $CHCl_3$). The isotherms are plotted based on the absorbance measured at 328 nm.

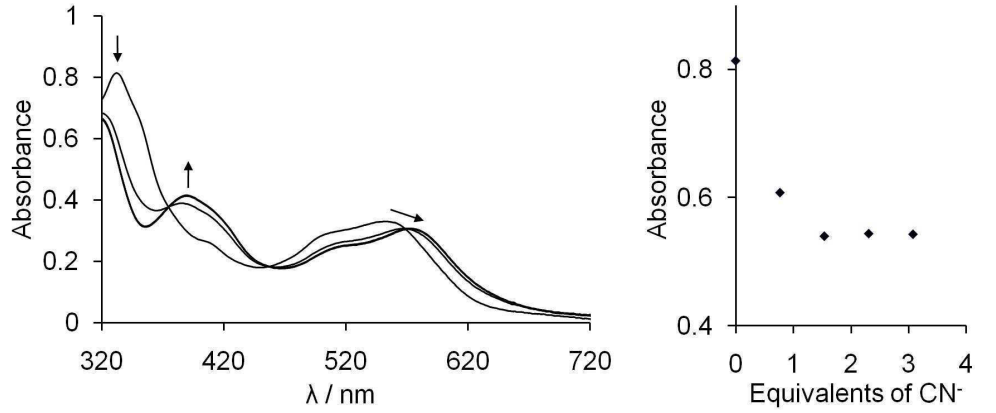

Figure 58. Spectral changes in the UV-Vis absorption spectra of [**51**]OTf (2.6×10^{-5} M) in 9/1 $CHCl_3$/DMF upon incremental addition of a TEACN solution (2.0×10^{-2} M in $CHCl_3$). The isotherms are plotted based on the absorbance measured at 332 nm.

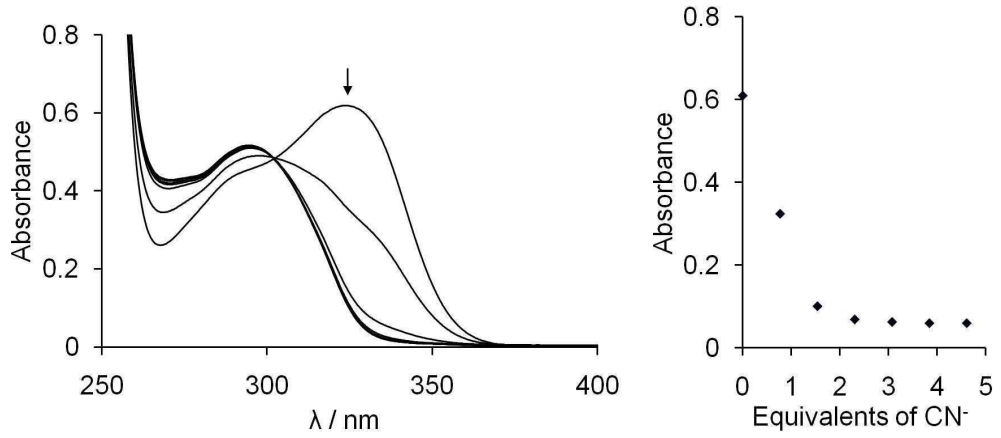

Figure 59. Spectral changes in the UV-Vis absorption spectra of **43** (2.6×10^{-5} M) in 9/1 $CHCl_3$/DMF upon incremental addition of a TEACN solution (2.0×10^{-2} M in $CHCl_3$). The isotherms are plotted based on the absorbance measured at 328 nm.

Next, the affinity of $[\mathbf{51}]^+$ for cyanide ions was investigated under conditions analogous to those used for fluoride. These experiments afforded $K_{CN} > 10^7$ M^{-1} in THF/DMF (9/1 vol.) (Figure 54) and $K_{CN} = 3.0(\pm 1.0) \times 10^6$ M^{-1} in $CHCl_3$ (

Figure **58**), indicating that $[\mathbf{51}]^+$ has a higher affinity for cyanide than fluoride in these solvent mixtures. The binding constant measured in $CHCl_3$ for $[\mathbf{51}]^+$ is also significantly higher than that measured for **43** in the same solvent ($K_{CN} = 4.0(\pm 2.0) \times 10^5$ M^{-1}, Figure 59), once again pointing to the favorable influence of the cationic Ru(II) moiety. Addition of Cl^-, Br^-, I^-, or NO_3^- resulted in no changes in the UV-Vis spectrum of [**51**]OTf, indicating that these anions do not bind to boron or react at the metal center, as was observed for $[\mathbf{48}]^+$ and $[\mathbf{50}]^+$. In addition, the reversible nature of fluoride binding to the boron center was confirmed by reappearance of the absorption bands corresponding $[\mathbf{51}]^+$ upon addition of a small amount of the fluoride ion scavenger $Al(NO_3)_3$ to solutions of **51**-F (Figure 60).

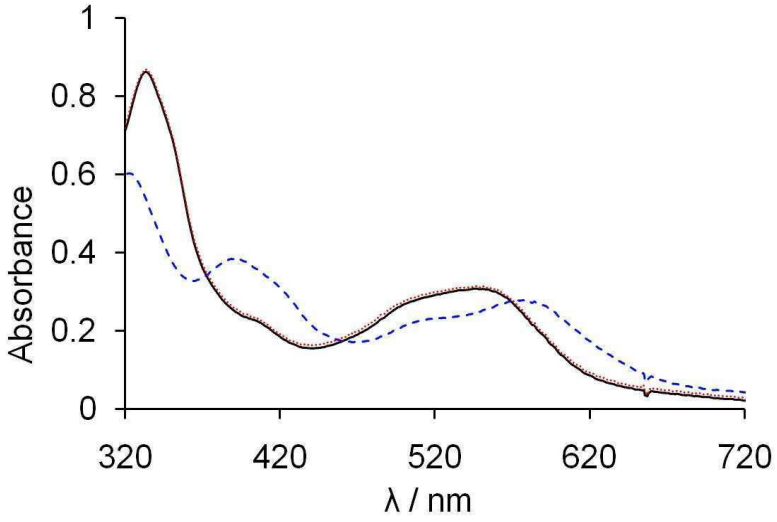

Figure 60. Regeneration of the UV-Vis spectrum of [**51**]$^+$ from **51**-F by addition of $Al(NO_3)_3$. A solution of [**51**]OTf (3.0 mL, 2.6×10^{-5} M, 9/1 dmso/THF) (—) was treated with 1 eq. of TBAF in THF to generate **51**-F *in situ* (----). Subsequent addition of a small amount of solid $Al(NO_3)_3$ resulted in the regeneration of the spectrum corresponding to [**51**]$^+$ (····).

The structures of [**51**]$^+$, **51**-F, and **51**-CN have been optimized using DFT methods (B3LYP, Stuttgart RSC 1997 ECP basis set for Ru and 6-31+g(d') for all other atoms) and subjected to single point energy calculations using the Polarizable Continuum Model[189,190] (PCM) with THF as the solvent. Inspection of the frontier orbitals shows that the lowest unoccupied molecular orbital (LUMO) is localized on the 2,2'-bpy ligands and a Ru d_π orbital in each of the molecules (Figure 61). It is worth noting that, in the case of [**51**]$^+$, the empty p-orbital of boron contributes to the LUMO+2 rather than the LUMO, as is typically observed for triarylboranes. The highest occupied molecular orbital (HOMO) is also similar in each of the three cases, with electron density residing primarily on a Ru d_π orbital and the phenylpyridine ligand. The effects of anion binding

are reflected in the marked decrease of the HOMO-LUMO gap going from [**51**]$^+$ (2.78 eV) to **51**-F (2.52 eV) and **51**-CN (2.56 eV). This result provides support for the observed redshift in the lowest energy bands of the UV-Vis spectrum.

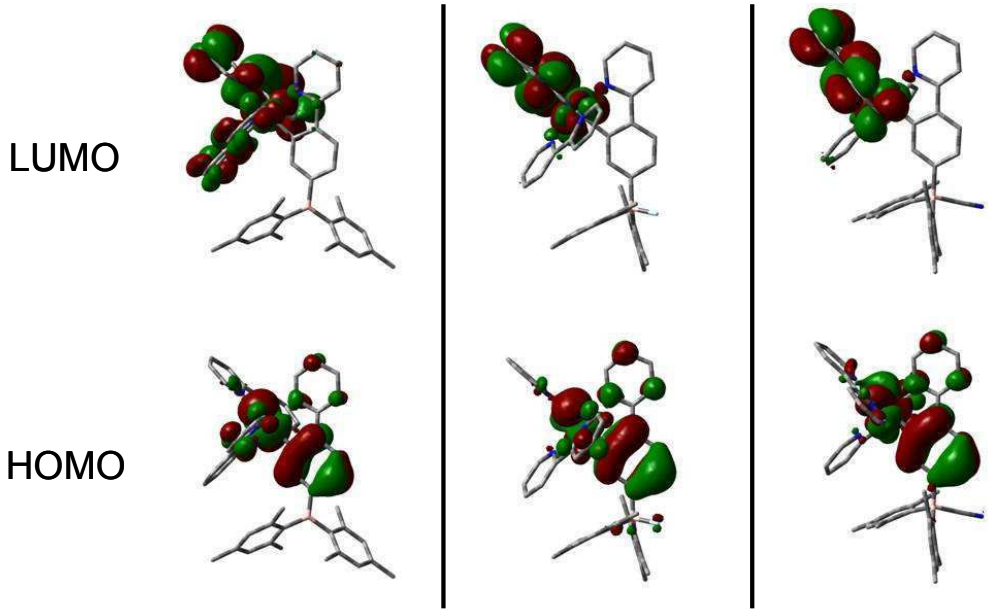

Figure 61. Rendering of the frontier molecular orbitals of [**51**]$^+$ (left), **51**-F (middle), and **51**-CN (right). Isovalues are set at 0.02

In order to confirm the formation of **51**-F and **51**-CN, crystallization experiments were undertaken. Single crystals of **51**-F were obtained by slow evaporation of a pyridine solution of [**51**]OTf and TBAF at room temperature. The structure of **51**-F confirms the presence of a fluorine atom coordinated to the boron center via a B(1)-F(1) length of 1.468(8) Å, which is comparable to that found in other triarylfluoroborate anions (1.47 Å) (Figure 62).[97,107] No significant changes were observed in the Ru(1)-N or Ru(1)-C(7) bond distances when compared to **51** [OTf] (Ru(1)-N, 2.031(5) – 2.138(5) Å; Ru(1)-

C(7), 2.036(6) Å). Crystals of **51**-CN were obtained by slow evaporation of a CH_3OH/acetone solution containing KCN and **51** [OTf]. The structure clearly displays a cyanide anion bound to the boron center with a B(1)-C(50) distance of 1.635(8) Å (Figure 63). The Ru(1)-N bond distances in **51**-CN (Ru(1)-N, 2.033(4) – 2.141 (4) Å) again experience no significant changes versus **51** [OTf] or **51**-F, but the Ru(1)-C(7) bond length is slightly elongated (2.062(5) Å), possibly because of increased interligand steric repulsion caused by pyramidalization of the boron center.

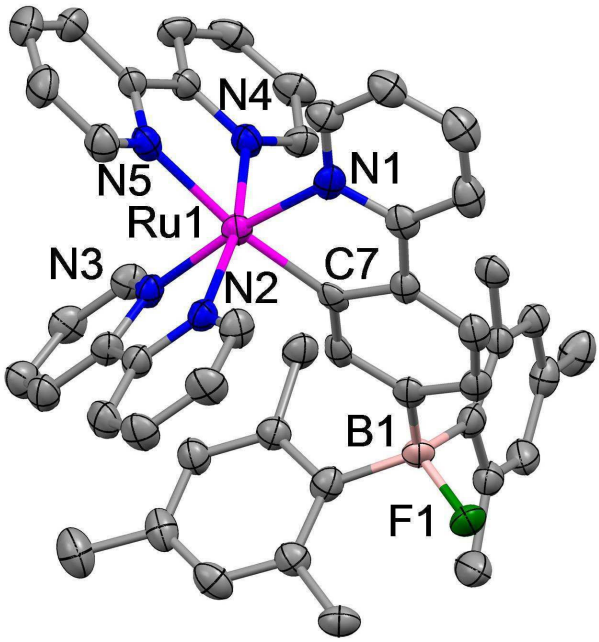

Figure 62. Crystal structure of **51**-F. Displacement ellipsoids are scaled to the 50% probability level. Selected bond lengths (Å) and angles (˚): Ru(1)-C(7) 2.036(6)Å; Ru(1)-N(1) 2.068(5)Å; Ru(1)-N(2) 2.031(5)Å; Ru(1)-N(3) 2.043(5)Å; Ru(1)-N(4) 2.055(5)Å; Ru(1)-N(5) 2.138(5)Å; C(7)-Ru(1)-N(1) 79.6(2)˚; N(2)-Ru(1)-N(3) 78.65(19)˚; N(4)-Ru(1)-N(5) 77.76(19)˚; B(1)-F(1) 1.468(8)Å; B(1)-C(9) 1.651(10)Å; B(1)-C(12) 1.652(10)Å; B(1)-C(21) 1.675(9)Å; F(1)-B(1)-C(9) 103.6(5)˚; F(1)-B(1)-C(12) 111.4(5)˚; C(9)-B(1)-C(12) 109.4(5)˚; F(1)-B(1)-C(21) 102.9(5)˚; C(9)-B(1)-C(21) 119.0(5)˚; C(12)-B(1)-C(21) 110.1(5)˚.

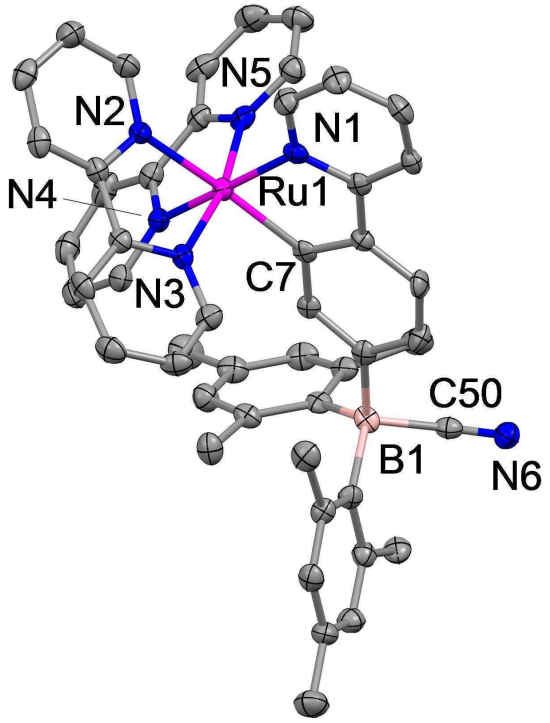

Figure 63. Crystal structure of **51**-CN. Displacement ellipsoids are scaled to the 50% probability level. Selected bond lengths (Å) and angles (˚): Ru(1)-C(7) 2.062(5)Å; Ru(1)-N(1) 2.076(4)Å; Ru(1)-N(2) 2.141(4)Å; Ru(1)-N(3) 2.063(4)Å; Ru(1)-N(4) 2.053(4)Å; Ru(1)-N(5) 2.033(4)Å; C(7)-Ru(1)-N(1) 80.08(17)˚; N(2)-Ru(1)-N(3) 76.89(16)˚; N(4)-Ru(1)-N(5) 78.33(17)˚; B(1)-C(50) 1.635(8)Å; B(1)-C(9) 1.648(7)Å; B(1)-C(12) 1.659(7)Å; B(1)-C(21) 1.675(7)Å; C(9)-B(1)-C(12) 108.3(4)˚; C(9)-B(1)-C(21) 118.9(4)˚; C(12)-B(1)-C(21) 112.0(4)˚; C(50)-B(1)-C(9) 103.2(4)˚; C(50)-B(1)-C(12) 114.6(4)˚; C(50)-B(1)-C(21) 99.4(4)˚.

The formation of **51**-F and **51**-CN was also studied by ^{1}H NMR. Addition of TBAF to a solution of **51**[OTf] in acetone-d_6 resulted in the appearance of a new set of ^{1}H NMR signals assigned to **51**-F. Significant broadening of many of the signals in the ^{1}H NMR spectrum of **51**-F suggests restricted molecular motion caused by pyramidalization of the boron atom. Nonetheless, addition of $Al(NO_3)_3$ to the NMR sample leads to a restoration of the original purple color as well as of the sharp resonances assigned to

[**51**]$^+$. The ^{19}F NMR spectrum of **51**-F is dominated by a resonance at around -174 ppm, which is in the expected range for a fluoroborate species. Despite extended acquisition times, the ^{11}B NMR signal of **51**-F could not be detected. The ^{1}H NMR spectrum of **51**-CN displays two distinct sets of Mes-C*H* signals at 6.64 and 6.75 ppm as well as two *ortho*-Mes-CH_3 (2.14 and 2.45 ppm) and *para*-Mes-CH_3 (2.24 and 2.29 ppm) resonances. This observation suggests a diasterotopic relationship between the two mesityl groups, likely caused by hindered rotation of the substituents around the boron atom. The^{11}B NMR spectrum of **51**-CN displays a sharp signal at -12.7 ppm, which is in the typical range for a triaryl cyanoborate.

2.5 Electrochemical response to anion binding

Encouraged by the high affinity that [**51**]$^+$ displays for cyanide and fluoride, we decided to determine if the readily accessible $Ru^{II/III}$ redox couple could be used to report anion binding events occurring at the boron center. The cyclic voltammogram of [**51**]$^+$ (1 mM, 0.1 M $TBAPF_6$, DMF) displays a reversible oxidation wave for the $Ru^{II/III}$ redox couple at $E_{1/2}$ = 0.051 V *vs* Fc/Fc^+. Addition of one equivalent of TBAF to [**51**]$^+$ in the electrochemical cell resulted in the appearance of a new wave at $E_{1/2}$ = -0.191 V (*vs* Fc/Fc^+), which is assigned to the formation of **51**-F (Figure 64). This cathodic shift of the $Ru^{II/III}$ redox process is in agreement with an increase in the donor strength of the cyclometalating ligand induced by anion binding and a decrease in the overall charge of the complex. Appearance of the new wave at $E_{1/2}$ = -0.191 V was accompanied by a decrease in the intensity of the oxidation wave of [**51**]$^+$ (Figure 64). Increasing the fluoride ion concentration resulted in net decrease of both oxidation waves

corresponding to [**51**]$^+$ and **51**-F. This unexpected phenomenon is assigned to increased conversion of [**51**]$^+$ to **51**-F and subsequent precipitation of the latter at higher fluoride concentration. In agreement with this interpretation, addition of the fluoride ion scavenger $Al(NO_3)_3$ to the electrochemical cell led to the nearly full reappearance of the oxidation wave at $E_{1/2}$ = +0.051 V vs Fc/Fc^+, indicating regeneration of the cationic species [**51**]$^+$.

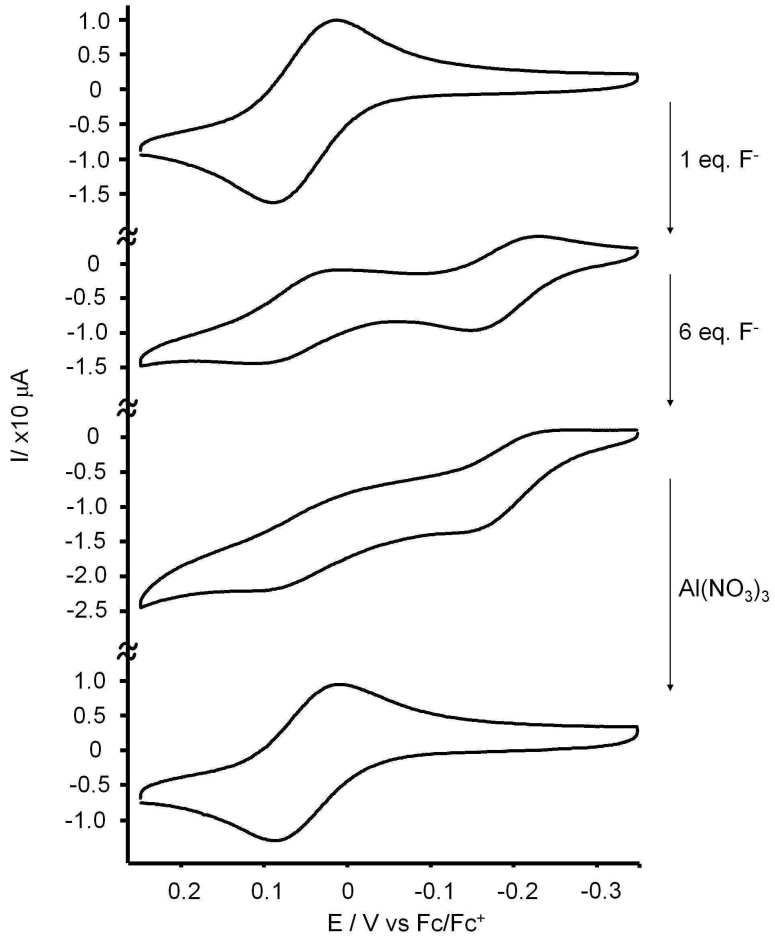

Figure 64. Cyclic voltammograms of [**51**]OTf before and after addition 1 eq. and 6 eq. of F^- in DMF and, subsequently, $Al(NO_3)_3$ ([**51**]OTf] = 1 mM, [*n*-Bu_4NPF_6] = 0.1 M, ν = 200 mV s^{-1}).

Addition of cyanide ions to a solution of [**51**]$^+$ in the electrochemical cell triggered formation of **51**-CN, as evidenced by the detection of a new oxidation wave at $E_{1/2}$ = -0.147 V *vs* Fc/Fc$^+$ (Figure 65). Conversion of [**51**]$^+$ into **51**-CN was not complicated by precipitation; moreover, the conversion appeared quantitative, in agreement with the elevated cyanide binding constant displayed by [**51**]$^+$.

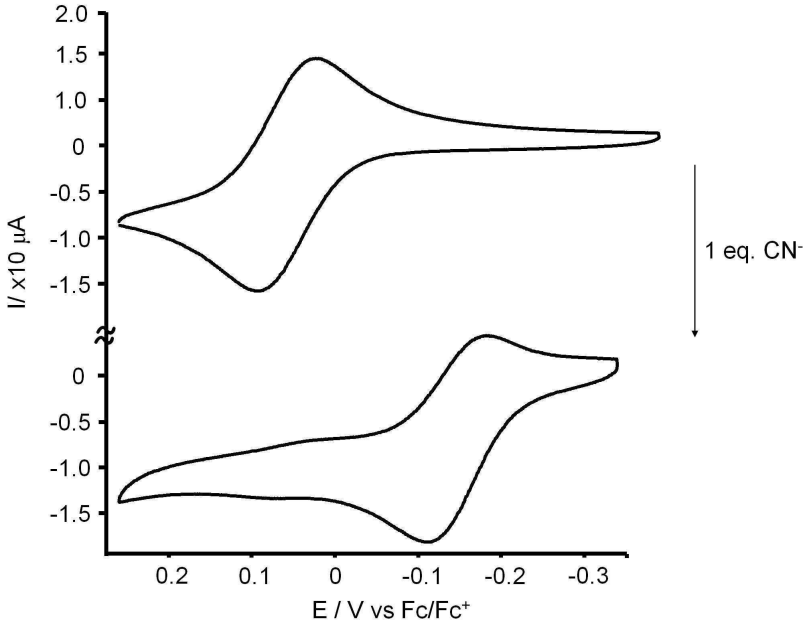

Figure 65. Cyclic voltammograms of [**51**]OTf before and after addition of 1 eq. of CN^- in DMF ([**51**]OTf] = 1 mM, [*n*-Bu_4NPF_6] = 0.1 M, ν = 200 mV s^{-1}).

2.6 Conclusions

In conclusion, we have investigated a series of novel triarylborane-based anion receptors bearing cationic pyridinium moieties. The *N*-methyl pyridinium derivatives [**45**] $^+$ and [**46**]$^+$ show a high affinity for fluoride in organic solvents. These results

suggest that the *N*-methyl pyridinium group provides Coulombic effects that enhance the Lewis acidity of the boron center. However, these effects are not sufficient to allow fluoride complexation directly in aqueous conditions. Nonetheless, the presence of the pyridinium moiety imparts intramolecular charge transfer behavior that results in a desirable turn-on colorimetric response upon fluoride binding in organic solvents. A similar turn-on response was observed for the Pd^{2+} and Pt^{2+} cyclometalated complexes $[\mathbf{48}]^+$ and $[\mathbf{50}]^+$, although these receptors are hampered by the susceptibility of the metal centers to attack by common anions such as Cl^-, Br^-, I^-, and CN^-. These results led us to investigate a coordinatively saturated Ru^{2+} complex $[\mathbf{51}]^+$ that binds both fluoride and cyanide anions in organic solvents without interference from other common anions. Although anion sensing could not be achieved in aqueous environments, $[\mathbf{51}]^+$ exhibits both photophysical and electrochemical changes upon fluoride and cyanide binding in organic solvents.

2.7 Experimental

General Considerations. 2-(4'-Bromophenyl)pyridine[204] and $RuCl_2(2,2'\text{-bpy})_2$[205] were synthesized by published procedures. NaF and dimesitylboron fluoride were purchased from Aldrich. *n*-$Bu_4NF{\cdot}3H_2O$ (TBAF), 2-(2-thienyl)pyridine, and $Pd(OAc)_2$ were purchased from Alfa Aesar and used as received. K_2PtCl_4 was purchased from Pressure Chemical, Inc. and converted to $[n\text{-}Bu_4N]_2[PtCl_4]$ using a published procedure.[206] Solvents were dried by passing through an alumina column (*n*-hexane, CH_2Cl_2) or refluxing under N_2 over Na/K (Et_2O and THF). Air-sensitive compounds were handled under a N_2 atmosphere using standard Schlenk and glovebox techniques.

UV-vis spectra were recorded on either an HP8453 spectrophotometer or an Ocean Optics USB4000 spectrometer with an Ocean Optics ISS light source. Elemental analyses were performed at Atlantic Microlab (Norcross, GA). NMR spectra were recorded on Varian Unity Inova 400 FT NMR (399.59 MHz for ^{1}H, 375.99 MHz for ^{19}F, 128.19 MHz for ^{11}B, 100.45 MHz for ^{13}C) spectrometer at ambient temperature unless otherwise stated. Chemical shifts δ are given in ppm, and are referenced against external Me_4Si (^{1}H, ^{13}C) and $BF_3 \cdot Et_2O$ (^{11}B, ^{19}F).

Crystallography. Single crystals of **45**-F were obtained by slow evaporation of a solution of [**45**]OTf and TBAF in CH_3CN/acetone. Single crystals of **46**-F were obtained by cooling a concentrated acetone-d_6 solution of [**46**]OTf and TBAF. The details of the data collection and structure refinement for **45**-F and **46**-F are included in Table 4. Single crystals of **47** were obtained by slow diffusion of hexanes into a solution of the compound in benzene. Single crystals of [**48**]OTf and [**50**]OTf were obtained by cooling solutions of the compounds in 1/2 MeCN/Et_2O to -40 ˚C. The details of the data collection and structure refinement for **47**, [**48**]OTf, and [**50**]OTf are included in Table 5. Single crystals of [**51**]OTf were obtained by slow diffusion of Et_2O into a solution of the compound in CH_2Cl_2. Single crystals of **51-**F were obtained by slow evaporation of a mixture of [**51**]OTf and TBAF in pyridine-d_5. Single crystals of **51**-CN were obtained by slow evaporation of a mixture of [**51**]OTf and KCN in 1/1 acetone/MeOH. The details of the data collection and structure refinement for [**51**]OTf, **51-**F, and **51**-CN are included in Table 6.

The crystallographic measurements were performed using a Bruker-AXS APEX-II CCD area detector diffractometer, with a graphite-monochromated Mo-Kα radiation (λ = 0.71069 Å). A specimen of suitable size and quality was selected and mounted onto a nylon loop. The semiempirical method SADABS[207] was applied for absorption correction. The structures were solved by direct methods using SHELXTL/PC package (version 6.1)[208] which successfully located most of the non-hydrogen atoms. Subsequent refinement on F^2 allowed location of the remaining non-hydrogen atoms. All H atoms were geometrically placed and refined in a riding model approximation.

Theoretical Calculations. Density functional theory (DFT) calculations (full geometry optimization) were carried out with *Gaussian03* using the gradient-corrected Becke exchange functional (B3LYP) and the Lee-Yang-Parr correlation functional. A 6-31+g(d') basis set was used for C, H, N, B, F, and S. A Stuttgart RSC 1997 ECP basis set was used for Ru. Frequency calculations were carried out on the optimized structure of each compound. In the case of **46**-F, an imaginary frequency corresponding to low energy rotation of a para-methyl group of a mesityl ligand was observed and ignored. Single point energy calculations were performed using the Polarizable Continuum Model[189,190] (PCM) with chloroform as a solvent for [**45**]$^+$, [**46**]$^+$, **45**-F and **46**-F and THF as a solvent for [**51**]$^+$, **51**-F, and **51**-CN.

Table 4. Crystal data, data collections, and structure refinements for **45**-F and **46**-F.

Crystal data	**45**-F·0.25 C_3H_6O, 0.75 CH_3CN	**46**-F
Formula	$C_{32.24}H_{36.71}BFN_{1.76}O_{0.24}$	$C_{28}H_{31}BFNS$
Mr	482.51	443.41
Crystal size/mm	0.24 x 0.10 x 0.05	0.12 x 0.10 x 0.08
Crystal system	Monoclinic	Tetragonal
Space group	P2(1)/c	I4(1)/a
a/Å	13.924(3)	22.51(3)
b/Å	12.520(3)	22.51(3)
c/Å	15.974(4)	17.90(3)
β/°	101.333(3)	-
V/Å^3	2730.4(11)	9071(22)
Z	4	16
ρ_{calc}/g cm^{-3}	1.174	1.299
μ/mm^{-1}	0.072	0.168
F(000)	1034	3776
T/K	110(2)	110(2)
Scan mode	ω, φ	ω, φ
hkl Range	-15 → +15	-25 → +25
	-14 → +14	-25 → +23
	-18 → +18	-20 → +20
Measd reflns	22904	22185
Unique reflns [R_{int}]	4278 [0.0831]	3557 [0.0956]
Reflns used for refinement	4278	3557
Refined parameters	351	289
GooF	1.001	1.000
$R1$,[a] $wR2$[b] (all data)	0.0986, 0.1433	0.0839, 0.1290
ρ_{fin} (max., min.)/eÅ^{-3}	0.318, -0.272	0.404, -0.365

[a] $R1 = \Sigma||F_o| - |F_c||/\Sigma|F_o|$. [b] $wR2 = ([\Sigma w(F_o^2 - F_c^2)^2]/[\Sigma\, w(F_o^2)^2])^{1/2}$; $w = 1/[\sigma^2(F_o^2) + (ap)^2 + bp]$; $p = (F_o^2 + 2F_c^2)/3$ with $a = 0.0690$ for **45**-F, 0.0715 for **46**-F; and $b = 0$ for **45**-F, 21 for **46**-F.

Table 5. Crystal data, data collections, and structure refinements for **47**, [**48**]OTf and [**50**]OTf.

Crystal data	**47**	[**48**]OTf·CH_3CN,Et_2O	[**50**]OTf·CH_3CN,Et_2O
Formula	$C_{64}H_{66}B_2N_2O_4S_2Pd_2$	$C_{40}H_{56}BF_3N_4O_4S_2Pd$	$C_{40}H_{56}BF_3N_4O_4S_2Pt$
Mr	1225.73	895.22	983.91
Crystal size/mm	0.15 x 0.10 x 0.05	0.10 x 0.06 x 0.03	0.12 x 0.04 x 0.03
Crystal system	Triclinic	Triclinic	Triclinic
Space group	P-1	P-1	P-1
a/Å	13.762(5)	7.986(4)	8.009(7)
b/Å	15.018(6)	14.733(7)	14.814(13)
c/Å	15.933(6)	18.586(9)	18.626(16)
α /°	80.051(6)	96.092(6)	95.975(14)
β/°	77.834(6)	91.966(5)	92.108(15)
γ /°	65.528(5)	91.065(6)	90.336(15)
V/Å^3	2916.3(19)	2172.6(17)	2196(3)
Z	2	2	2
ρ_{calc}/g cm^{-3}	1.396	1.368	1.488
μ/mm^{-1}	0.737	0.579	3.345
F(000)	1260	932	996
T/K	110(2)	110(2)	110(2)
Scan mode	ω, φ	ω, φ	ω, φ
hkl Range	-16 → +16	-9 → +9	-9 → +9
	-18 → +18	-17 → +17	-17 → +17
	-19 → +19	-22 → +22	-22 → +22
Measd reflns	28732	20612	15554
Unique reflns [Rint]	10790 [0.0977]	7640 [0.0784]	7684 [0.1021]
Reflns used for refinement	10790	7640	7684
Refined parameters	685	500	445
GooF	1.007	1.031	1.013
R1,[a] *w*R2[b] (all data)	0.1107, 0.1596	0.0989, 0.1750	0.1338, 0.1693
ρ_{fin} (max., min.)/eÅ^{-3}	0.685, -1.032	1.061, -1.101	3.338, -2.701

[a] $R1 = \Sigma||F_o| - |F_c||/\Sigma|F_o|$. [b] $wR2$ $([\Sigma w(F_o^2 - F_c^2)^2]/[\Sigma w(F_o^2)^2])^{1/2}$; $w = 1/[\sigma^2(F_o^2) + (ap)^2 + bp]$; $p = (F_o^2 + 2F_c^2)/3$ with a = 0.0586 for **47**, 0.0924 for [**48**]OTf, and 0.068for [**50**]OTf; and b = 0 for **47**, 0.2015 for [**48**]OTf, and 0 for [**50**]OTf.

Table 6. Crystal data, data collections, and structure refinements for [**51**]OTf, **51**-F, and **51**-CN.

Crystal data	**51** [OTf]	**51**-F·C_6H_5N	**51**-CN·CH_3OH
Formula	$C_{50}H_{45}BF_3N_5O_3SRu$	$C_{55}H_{50}BFN_6Ru$	$C_{51}H_{49}BN_6ORu$
Mr	964.85	917.91	873.84
Crystal size/mm	0.17 x 0.12 x 0.08	0.18 x 0.15 x 0.10	0.35 x 0.08 x 0.06
Crystal system	Monoclinic	Monoclinic	Tetragonal
Space group	P2(1)/c	P2(1)/c	P4(3)
a/Å	14.3700(4)	14.003(4)	11.2355(10)
b/Å	21.1565(7)	23.236(7)	11.2355(10)
c/Å	14.8607(5)	16.816(4)	32.768(3)
β/°	103.511(2)	128.800(15)	-
V/Å^3	4392.9(2)	4381.2(19)	4136.5(6)
Z	4	4	4
ρ_{calc}/g cm^{-3}	1.459	1.392	1.392
μ/mm^{-1}	0.467	0.408	0.426
F(000)	1984	1912	1812
T/K	110(2)	110(2)	110(2)
Scan mode	ω, φ	ω, φ	ω, φ
hkl Range	-16 → +16	-16 → +16	-13 → +13
	-24 → +21	-26 → +26	-14 → +14
	-16 → +16	-19 → +19	-37 → +43
Measd reflns	32052	45426	30058
Unique reflns [R_{int}]	6657 [0.0585]	6856 [0.0888]	9663 [0.0836]
Reflns used for refinement	6657	6856	9663
Refined parameters	614	568	543
GooF	1.001	1.000	1.000
$R1$,[a] $wR2$[b] (all data)	0.0809, 0.1281	0.0908, 0.1715	0.0775, 0.1073
ρ_{fin} (max., min.)/eÅ^{-3}	0.921, -1.111	2.051, -1.010	0.528, -0.576

[a] $R1 = \Sigma||F_o| - |F_c||/\Sigma|F_o|$. [b] $wR2 = ([\Sigma w(F_o^2 - F_c^2)^2]/[\Sigma w(F_o^2)^2])^{1/2}$; $w = 1/[\sigma^2(F_o^2) + (ap)^2 + bp]$; $p = (F_o^2 + 2F_c^2)/3$ with a = 0.0694 for [**51**]OTf, 0.0710 for **51**-F, and 0.0362 for **51**-CN; and b = 0 for [**51**]OTf, 21 for **51**-F, and 0 for **51**-CN.

Synthesis of 43. *n*-BuLi (0.790 mL, 2.5 M in hexanes, 1.97 mmol) was added to a THF (10 mL) solution of 2-(4'-bromophenyl)pyridine (0.440 g, 1.88 mmol) at -78 ºC. The resulting reaction mixture was stirred at -78 ºC for 1 hr and mixed with a solution of Mes_2BF (0.529 g, 1.97 mmol) in THF (10mL). The reaction was stirred overnight at room temperature before removing the solvent *in vacuo*. The solids were extracted with CH_2Cl_2 (20 mL) and filtered through Celite to remove LiF. The filtrate was evaporated to dryness and the residue recrystallized from Et_2O/pentane to afford 2-(4'-dimestylborylphenyl)pyridine (**43**) (0.400 g, 53% yield). ^{1}H NMR (399.9 MHz, $CDCl_3$): δ 2.04 (s, 12H, Mes-C*H*$_3$), 2.33 (s, 6H, Mes-C*H*$_3$), 6.85 (s, 4H, Mes-C*H*), 7.25-7.28 (m, 1H, Pyr-C*H*), 7.64 (d, $^3J_{H\text{-}H}$ = 8.42 Hz, 2H, Ph-C*H*), 7.75-7.81 (m, 2H, Pyr-C*H*), 7.98 (d, $^3J_{H\text{-}H}$ = 7.98 Hz, 2H, Ph-C*H*), 8.72 (d, $^3J_{H\text{-}H}$ = 4.58 Hz, 1H, Pyr-C*H*). ^{11}B NMR (128.2 MHz, $CDCl_3$): δ 75.10.

Synthesis of 44. *n*-BuLi (1.30 mL, 2.5 M in hexanes, 3.26 mmol) was added to a THF (10 mL) solution of 2-(2-thienyl)pyridine (0.500 g, 3.1 mmol) at -78ºC. The resulting reaction mixture was stirred at -78ºC for 1 hr and mixed with a solution of Mes_2BF (0.873 g, 3.26 mmol) in THF (10 mL). The reaction was stirred overnight at room temperature before removing the solvent *in vacuo*. The crude product was extracted with CH_2Cl_2 (20 mL) and filtered through Celite to remove LiF. The filtrate was evaporated to dryness and the residue was recrystallized from Et_2O/pentane to afford the crude product 2-(2-pyridyl)-5-dimesitylboryl-thiophene (**44)** (0.70 g, 55% yield). ^{1}H NMR (399.9 MHz, $CDCl_3$): δ 2.16 (s, 12H, Mes-C*H*$_3$), 2.32 (s, 6H, Mes-C*H*$_3$), 6.84 (s, 4H, Mes-C*H*), 7.16-7.21 (m, 1H, Pyr-C*H*), 7.46 (d, $^3J_{H\text{-}H}$ = 3.85 Hz, 1H, Thioph-C*H*), 7.69-

7.72 (m, 2H, Pyr-C*H*), 7.74 (d, $^{3}J_{H\text{-}H}$ = 3.58 Hz, 1H, Thioph-C*H*), 8.58 (d, 1H, Pyr-C*H*, $^{3}J_{H\text{-}H}$ = 4.67 Hz). ^{11}B NMR (128.2 MHz, acetone-d_6): δ 67.35.

Synthesis of [45]OTf. Without further purification, **43** (0.100 g, 0.248 mmol) was treated with MeOTf (0.100 mL, 0.420 mmol) in 10 mL Et_2O at room temperature. A white solid precipitated upon standing overnight. The solid was filtered, washed with Et_2O (3 × 5 mL) and pentane (3 × 5 mL), and dried under vacuum to afford [**45**]OTf (0.115g, 82% yield). ^{1}H NMR (399.9 MHz, acetone-d_6): δ 2.03 (s, 12H, Mes-CH_3), 2.30 (s, 6H, Mes-CH_3), 4.43 (s, 3H, N-CH_3), 6.89 (s, 4H, Mes-C*H*), 7.71 (d, $^{3}J_{H\text{-}H}$ = 7.88 Hz, 2H, Ph-C*H*), 7.82 (d, $^{3}J_{H\text{-}H}$ = 7.88 Hz, 2H, Ph-C*H*), 8.25-8.27 (m, 2H, Pyr-C*H*), 8.78 (t, $^{3}J_{H\text{-}H}$ = 8.06 Hz, 1H, Pyr-C*H*), 9.24 (d, $^{3}J_{H\text{-}H}$ = 6.05 Hz, 1H, Pyr-C*H*). ^{13}C NMR (100.5 MHz, $CDCl_3$): δ 21.22 (*p*-Mes-*C*H_3), 23.47 (*o*-Mes-*C*H_3), 47.48 (pyr-*C*H_3), 118.92, 122.11, 127.25, 128.21, 128.43, 129.50, 133.55, 136.45, 139.50, 140.72, 141.05, 145.26, 147.63, 149.42, 155.67. ^{11}B NMR (128.2 MHz, acetone-d_6): δ 76.3. ^{19}F NMR (375.97 MHz, acetone-d_6): δ -77.8 (OTf). Anal. Calcd for $C_{31}H_{33}BNSF_3O_3$: C, 65.61; H, 5.86. Found: C, 65.71; H, 5.92.

Synthesis of [46]OTf. Without further purification, **44** (0.100 g, 0.240 mmol) was treated with MeOTf (0.10 mL, 0.420 mmol) in 10mL Et_2O at room temperature. A white solid precipitated upon standing overnight. The solid was filtered, washed with Et_2O (3 × 5 mL) and pentane (3 × 5 mL), and dried under vacuum to afford [**46**]OTf (0.125 g, 89% yield). ^{1}H NMR (399.9 MHz, acetone-d_6): δ 2.14 (s, 12H, Mes-CH_3), 2.29 (s, 6H, Mes-CH_3), 4.59 (s, 3H, N-CH_3), 6.89 (s, 4H, Mes-C*H*), 7.60 (d, $^{3}J_{H\text{-}H}$ = 3.85 Hz, 1H, Thiophene-C*H*), 8.00 (d, $^{3}J_{H\text{-}H}$ = 3.85 Hz, 1H, Thiophene-C*H*), 8.24 (t, $^{3}J_{H\text{-}H}$ = 6.41 Hz,

1H, Pyr-C*H*), 8.37 (d, $^{3}J_{H\text{-}H}$ = 8.06 Hz, 1H, Pyr-C*H*), 8.72 (t, 1H, Pyr-C*H*, $^{3}J_{H\text{-}H}$ = 7.88 Hz), 9.24 (d, 1H, Pyr-C*H*, $^{3}J_{H\text{-}H}$ = 6.23 Hz). ^{13}C NMR (100.5 MHz, acetone-d_6): δ 21.20 (Mes-*p*-*C*H$_3$), 23.61 (Mes-*o*-*C*H$_3$), 48.64 (pyr-*C*H$_3$), 128.08, 129.24, 131.62, 135.86, 140.31, 140.79, 141.33, 141.54, 143.02, 146.43, 148.56, 150.28, 156.43. ^{11}B NMR (128.2 MHz, acetone-d_6): δ 68.4. ^{19}F NMR (375.97 MHz, acetone-d_6): δ -77.6 (OTf). Anal. Calcd for $C_{29}H_{31}BNS_2F_3O_3$: C, 60.73; H, 5.45. Found: C, 60.89; H, 5.53.

Generation of 45-F and 46-F. 45-F and **46**-F were prepared and characterized by multinuclear NMR spectroscopy *in situ* by addition of TBAF to solutions of [**3**]OTf and [**4**]OTf in acetone-d_6. Data for **45**-F: ^{1}H NMR (399.9 MHz, acetone-d_6): δ 1.94 (s, 12H, Mes-C*H*$_3$), 2.08 (s, 6H, Mes-C*H*$_3$), 4.34 (s, 3H, N-C*H*$_3$), 6.45 (s, 4H, Mes-C*H*), 7.10-7.30 (bm, 3H), 8.03-8.07 (m, 3H), 8.59 (t, $^{3}J_{H\text{-}H}$ = 8.06 Hz, 1H, Pyr-C*H*), 9.00 (d, $^{3}J_{H\text{-}H}$ = 6.05 Hz 1H, Pyr-C*H*). ^{13}C NMR (100.5 MHz, dmso-d_6): δ 20.56 (Mes-*o*-*C*H$_3$), 24.90 (Mes-*o*-*C*H$_3$), 46.96 (pyr-*C*H$_3$), 125.34, 125.99, 126.35, 128.03, 129.72, 130.60, 133.51, 140.60, 144.81, 146.30, 154.12, 157.08, 169.42. ^{11}B NMR (128.2 MHz, acetone-d_6): δ 5.64. ^{19}F NMR (375.97, MHz, acetone-d_6): δ -176.0. Data for **46**-F: ^{1}H NMR (399.9 MHz, acetone-d_6): δ 2.03 (s, 12H, Mes-C*H*$_3$), 2.09 (s, 6H, Mes-C*H*$_3$), 4.51 (s, 3H, N-C*H*$_3$), 6.47 (s, 4H, Mes-C*H*), 6.90 (d, $^{3}J_{H\text{-}H}$ = 3.48 Hz, 1H, Thioph-C*H*), 7.66 (dd, $^{3}J_{H\text{-}H}$ = 3.66 Hz, $^{4}J_{H\text{-}F}$ = 2.56 Hz, 1H, Thioph-C*H*), 7.74 (t, $^{3}J_{H\text{-}H}$ = 6.31 Hz, 1H, Pyr-C*H*), 8.18 (d, $^{3}J_{H\text{-}H}$ = 8.24 Hz, 1H, Pyr-C*H*), 8.36 (t, $^{3}J_{H\text{-}H}$ = 7.78 Hz, 1H, Pyr-C*H*,), 8.81 (d, $^{3}J_{H\text{-}H}$ = 6.23 Hz 1H, Pyr-C*H*). ^{13}C NMR (100.5 MHz, acetone-d_6): δ 20.92 (Mes-*p*-*C*H$_3$), 24.90 (Mes-*o*-*C*H$_3$), 48.67 (pyr-*C*H$_3$), 120.68, 123.58, 123.88, 129.13, 129.39, 130.15, 131.44,

132.22, 135.62, 141.60, 144.28, 146.72, 152.38. ^{11}B NMR (128.2 MHz, acetone-d_6): δ 4.93. ^{19}F NMR (375.97, MHz, acetone-d_6): δ -167.5.

Synthesis of 47. A CH_2Cl_2 solution (15 mL) of $Pd(OAc)_2$ (0.120g, 0.54mmol) and **44** (0.200g, 0.49mmol) was heated to reflux overnight. The reaction mixture was filtered over Celite and concentrated *in vacuo*. The product precipitated as a yellow powder upon addition of pentane and was recrystallized from benzene/hexane mixture (185 mg, 66%). The product was characterized by ^{1}H NMR and used without further purification. ^{1}H NMR (399.9 MHz, $CDCl_3$): δ 2.05 (s, 6H, C*H*$_3$CO$_2$), 2.15 (s, 24H, Mes-C*H*$_3$), 2.28 (s, 12H, Mes-C*H*$_3$), 6.40 (t, 2H, Pyr-C*H*, $^3J_{H\text{-}H}$ = 6.54 Hz), 6.80-6.84 (s + d, 10H, Mes-C*H* + Pyr-C*H*), 7.07 (s, 2H, Thiophene-C*H*), 7.39 (t, 2H, Pyr-C*H*, $^3J_{H\text{-}H}$ = 7.85 Hz), 7.77 (d, 2H, Pyr-C*H*, $^3J_{H\text{-}H}$ = 5.67 Hz).

Synthesis of [48]OTf. LiCl (18 mg, 0.42 mmol) was added to a THF (15 mL) solution of **47** (215 mg, 0.19mmol), and the resulting mixture was allowed to stir at room temperature for 2 days. The reaction mixture was filtered over Celite and concentrated to *ca.* 5 mL *in vacuo*. Addition of benzene (10 mL) resulted in precipitation of a pale yellow powder that was filtered and washed with H_2O (3 × 5 mL) and benzene (3 × 5 mL). The product was dried overnight *in vacuo* overnight to yield 156 mg (70 %) of crude [(κ-*C,N*-**44**)PdCl]$_2$, which was used without further purification.

AgOTf (76 mg, 0.29 mmol) was added as a solid to a solution of crude [(κ-*C,N*-**44**)PdCl]$_2$ (156 mg, 0.14 mmol) in MeCN (10mL). The yellow suspension was stirred overnight before filtering over Celite. TMEDA (0.15mL, 1.0mmol) was added to the filtrate, and the yellow solution was allowed to stir for 2 days in a sealed flask. The

solvent was removed *in vacuo* and the resulting orange residue was extracted with CH_2Cl_2 (5 mL), and filtered over Celite. Removal of the solvent *in vacuo* and recrystallization of the resulting yellow solid from MeCN/Et_2O (2 mL/5 mL) at -40 ˚C yielded 64 mg (29 %) of [**48**]OTf. ^{1}H NMR (399.9 MHz, $CDCl_3$): δ 2.09 (s, 12H, Mes-C*H*$_3$), 2.30 (s, 6H, Mes-C*H*$_3$), 2.88 (br s, 12H, N-C*H*$_3$), 2.96 (br s, 4H, N-C*H*$_2$), 6.82 (s, 4H, Mes-C*H*), 7.31 (s, 1H, Thiophene-C*H*), 7.34 (t, 1H, $^3J_{H\text{-}H}$ = 6.6 Hz, Pyr-C*H*), 7.44 (d, 1H, $^3J_{H\text{-}H}$ = 7.8 Hz, Pyr-C*H*), 7.79 (t, 1H, $^3J_{H\text{-}H}$ = 7.8 Hz, Pyr-C*H*), 8.31 (d, 1H, $^3J_{H\text{-}H}$ = 5.5 Hz, Pyr-C*H*). ^{13}C NMR (100.5 MHz, $CDCl_3$): δ 21.26 (Mes-*o*-*C*H$_3$), 23.46 (Mes-*p*-*C*H$_3$), 49.20 (N-*C*H$_3$), 52.54 (N-*C*H$_3$), 61.19 (N-*C*H$_2$), 64.34 (N-*C*H$_2$), 120.09, 122.70, 128.31, 139.15, 140.50, 140.87, 141.88, 148.89, 151.29, 152.63, 153.36, 160.15. ^{11}B NMR (128.2 MHz, $CDCl_3$): No signal was observed. Anal. Calcd. for $PdC_{34}H_{43}S_2N_3O_3F_3B$: C, 52.35; H, 5.56. Found: C, 51.72; H, 5.59.

Synthesis of (*n*-Bu)$_4$N[49]. A solution of [*n*-Bu$_4$N]$_2$PtCl$_4$ (0.830g, 1.0mmol) and **44** (0.414g, 1.0mmol) in CH_2Cl_2/MeOH (20mL/10 mL) was heated to 50 ˚C for 2 days. The reaction mixture was concentrated to *ca* 10mL *in vacuo*, and H_2O (10mL) was added. The resulting sticky, brown solid was filtered and washed with H_2O (3 × 10mL). The product was triturated in Et_2O (20 mL) and filtered to afford (*n*-Bu)$_4$N[**49**] (0.445g, 48%) as a fine brown/yellow powder was that was used without further purification. ^{1}H NMR (399.9 MHz, $CDCl_3$): δ 0.88 (t, 12H, $NCH_2CH_2CH_2$-*C*H$_3$, $^3J_{H\text{-}H}$ = 7.23 Hz), 1.34 (m, 8H, NCH_2CH_2-*C*H$_2$-CH_3), 1.58 (m, 8H, NCH_2-*C*H$_2$-CH_2CH_3), 2.10 (s, 12H, Mes-C*H*$_3$), 2.26 (s, 6H, Mes-C*H*$_3$), 3.31 (m, 8H, N-*C*H$_2$-$CH_2CH_2CH_3$), 6.75 (s, 4H, Mes-C*H*),

6.87 (t, 1H, Pyr-C*H*, $^{3}J_{H\text{-}H}$ = 6.62 Hz), 7.26 (d, 1H, Pyr-C*H*), 7.61 (t, 1H, Pyr-C*H*, $^{3}J_{H\text{-}H}$ = 7.73 Hz), 7.74 (s, 1H, Thiophene-C*H*), 9.69 (d, 1H, Pyr-C*H*, $^{3}J_{H\text{-}H}$ = 5.84 Hz).

Synthesis of [50]OTf. AgOTf (0.257g, 1.0mmol) was added as a solid to a solution of (*n*-Bu)$_4$N[**49**] (0.436 g, 0.48 mmol) in MeCN (10mL). The yellow suspension was stirred overnight before filtering over Celite. TMEDA (0.15mL, 1.0mmol) was added to the filtrate, and the yellow solution was allowed to stir for 2 days in a sealed flask. The solvent was removed *in vacuo* and the resulting orange residue was extracted with CH_2Cl_2 (10 mL) and filtered over Celite. Removal of the solvent *in vacuo* and recrystallization of the resulting yellow solid from MeCN/Et_2O (3 mL/10 mL) at -40 ˚C afforded 0.175 g (42 %) of [**50**]OTf. ^{1}H NMR (399.9 MHz, $CDCl_3$): δ 2.09 (s, 12H, Mes-C*H*$_3$), 2.30 (s, 6H, Mes-C*H*$_3$), 3.08 (br s, 12H, N-C*H*$_3$), 3.17 (br s, 4H, N-C*H*$_2$), 6.82 (s, 4H, Mes-C*H*), 7.28-7.32 (s + t, 2H, Thiophene-C*H,* Pyr-C*H*), 7.45 (d, 1H, $^{3}J_{H\text{-}H}$ = 7.8 Hz, Pyr-C*H*), 7.79 (t, 1H, $^{3}J_{H\text{-}H}$ = 7.8 Hz, Pyr-C*H*), 8.45 (d, 1H, $^{3}J_{H\text{-}H}$ = 6.1 Hz, Pyr-C*H*). ^{13}C NMR (100.5 MHz, $CDCl_3$): δ 21.28 (Mes-*o*-*C*H$_3$), 22.33 (Mes-*p*-*C*H$_3$), 50.58 (N-*C*H$_3$), 54.15 (N-*C*H$_3$), 63.58 (N-*C*H$_2$), 65.86 (N-*C*H$_2$), 119.77, 122.48, 128.31, 139.14, 140.66, 140.70, 140.88, 141.97, 148.85, 155.23, 161.95. Two B-*C*ipso not observed. ^{11}B NMR (128.2 MHz, acetone-d_6): δ 68.0 (broad). Anal. Calcd. for $PtC_{34}H_{43}S_2N_3O_3F_3B$: C, 47.01; H, 4.99. Found: C, 46.58; H, 5.03.

Generation of 48-F and 50-F. 48-F and **50**-F were prepared and characterized by multinuclear NMR *in situ* by addition of a slight excess of TBAF to solutions of [**48**]OTf and [**50**]OTf in dmso-d_6. Data for **48**-F: ^{1}H NMR (399.9 MHz, dmso-d_6): δ 1.92 (s, 12H, Mes-C*H*$_3$), 2.07 (s, 6H, Mes-C*H*$_3$), 2.73 (br s, 12H, N-C*H*$_3$), 2.87 (br s, 4H, N-C*H*$_2$), 6.40

(s, 4H, Mes-C*H*), 6.83 (bs, 1H, Thiophene-C*H*), 6.57 (t, 1H, $^{3}J_{H\text{-}H}$ = 6.59 Hz, Pyr-C*H*), 7.25 (d, 1H, $^{3}J_{H\text{-}H}$ = 7.69 Hz, Pyr-C*H*), 7.77 (t, 1H, $^{3}J_{H\text{-}H}$ = 6.96 Hz, Pyr-C*H*), 8.16 (d, 1H, $^{3}J_{H\text{-}H}$ = 5.67 Hz, Pyr-C*H*). ^{13}C NMR (100.5 MHz, dmso-d_6): δ 20.59 (Mes-*o*-*C*H$_3$), 24.31 (Mes-*p*-*C*H$_3$), 47.96 (N-*C*H$_3$), 51.30 (N-*C*H$_3$), 60.02 (N-*C*H$_2$), 63.04 (N-*C*H$_2$), 117.76, 118.58, 128.09, 130.82, 131.48, 137.81, 140.27, 140.35, 148.68, 152.99, 154.94, 161.21, 174.45. ^{19}F NMR (375.97 MHz, dmso-d_6): δ -169.2. ^{11}B NMR (128.2 MHz, dmso-d_6): δ No signal was observed. Data for **50**-F: ^{1}H NMR (399.9 MHz, dmso-d_6): δ 1.94 (s, 12H, Mes-C*H*$_3$), 2.07 (s, 6H, Mes-C*H*$_3$), 2.92 (br s, 12H, N-C*H*$_3$), 3.09 (br s, 4H, N-C*H*$_2$), 6.40 (s, 4H, Mes-C*H*), 6.81 (bs, 1H, Thiophene-C*H*), 6.90 (t, 1H, $^{3}J_{H\text{-}H}$ = 6.59 Hz, Pyr-C*H*), 7.23 (d, 1H, $^{3}J_{H\text{-}H}$ = 7.88 Hz, Pyr-C*H*), 7.74 (t, 1H, $^{3}J_{H\text{-}H}$ = 7.60 Hz, Pyr-C*H*), 8.29 (d, 1H, $^{3}J_{H\text{-}H}$ = 5.86 Hz, Pyr-C*H*). ^{13}C NMR (100.5 MHz, dmso-d_6): δ 20.60 (Mes-*o*-*C*H$_3$), 24.34 (Mes-*p*-*C*H$_3$), 49.31 (N-*C*H$_3$), 53.14 (N-*C*H$_3$), 62.41 (N-*C*H$_2$), 64.84 (N-*C*H$_2$), 117.05, 118.18, 128.10, 130.78, 132.12, 139.52, 140.40, 143.70, 148.73, 153.13, 153.39, 163.12, 176.55. ^{19}F NMR (375.97 MHz, dmso-d_6): δ -168.3. ^{11}B NMR (128.2 MHz, dmso-d_6): δ +4.51.

Synthesis of [51]OTf. AgOTf (0.102 g, 0.400 mmol) was added as a solid to a solution of bpy$_2$RuCl$_2$·2H$_2$O (0.100 g, 0.2 mmol) and **43** (0.400 g, 1.00 mmol) in 3mL CH_2Cl_2 and 10mL MeOH. The mixture was heated to reflux for 2 hrs, and the solvent was removed *in vacuo*. The resulting purple solid was extracted with 20 mL CH_2Cl_2 and filtered over Celite. The solvent was again removed, and the residue was washed with 3 × 10mL Et_2O and 5mL cold acetonitrile. Recrystallization of the crude product by slow diffusion of Et_2O into a CH_2Cl_2 solution gave the pure product in 52% yield as dark

purple needles. ^{1}H NMR (399.9 MHz, pyridine-d_5): δ 2.01 (s, 12H, Mes-CH_3), 2.31 (s, 6H, Mes-CH_3), 6.72 (s, 1H, Ph-C*H*), 6.81 (s, 4H, Mes-C*H*), 6.94 (t, $^{3}J_{H\text{-}H}$ = 7.08 Hz, 1H, Pyr-C*H*), 7 (t, $^{3}J_{H\text{-}H}$ = 7.14 Hz, 1H, Pyr-C*H*), 7.05-7.09 (m, 2H, Pyr-C*H*), 7.34 (d, $^{3}J_{H\text{-}H}$ = 7.88 Hz, 1H, Pyr-C*H*), 7.40 (t, $^{3}J_{H\text{-}H}$ = 6.41 Hz, 1H, Pyr-C*H*), 7.54 (t, $^{3}J_{H\text{-}H}$ = 8.06 Hz, 1H, Pyr-C*H*), 7.58 (t, $^{3}J_{H\text{-}H}$ = 7.33 Hz, 1H, Pyr-C*H*), 7.65 (t, $^{3}J_{H\text{-}H}$ = 8.06 Hz, 1H, Pyr-C*H*), 7.68 (d, $^{3}J_{H\text{-}H}$ = 7.68 Hz, 1H, Pyr-C*H*), 7.72 (d, $^{3}J_{H\text{-}H}$ = 6.04 Hz 1H, Pyr-C*H*), 7.82 (d, $^{3}J_{H\text{-}H}$ = 5.67 Hz 1H, Pyr-C*H*), 7.89 (d, $^{3}J_{H\text{-}H}$ = 8.24 Hz, 1H, Pyr-C*H*), 8.01 (d, $^{3}J_{H\text{-}H}$ = 5.67 Hz, 1H, Pyr-C*H*), 8.05 (d, $^{3}J_{H\text{-}H}$ = 7.87 Hz, 1H, Pyr-C*H*), 8.12 (d, $^{3}J_{H\text{-}H}$ = 5.31 Hz, 1H, Pyr-C*H*), 8.16 (d, $^{3}J_{H\text{-}H}$ = 8.24 Hz, 1H, Pyr-C*H*), 8.32-8.29 (m, 2H, Pyr-C*H*), 8.46 (d, $^{3}J_{H\text{-}H}$ = 8.42 Hz, 1H, Pyr-C*H*), 8.50 (d, $^{3}J_{H\text{-}H}$ = 7.69 Hz, 1H, Pyr-C*H*), 8.61 (d, $^{3}J_{H\text{-}H}$ = 8.24 Hz, 1H, Pyr-C*H*). ^{13}C NMR (100.5 MHz, acetone-d_6): δ 21.07 (Mes-*p*-*C*H$_3$), 23.25 (Mes-*o*-*C*H$_3$), 120.38, 123.50, 123.58, 123.70, 123.93, 124.04, 124.29, 126.59, 126.74, 126.88, 127.89, 128.54, 128.91, 133.94, 134.28, 135.65, 136.44, 137.07, 138.53, 140.70, 142.87, 144.01, 150.00, 150.02, 150.12, 150.84, 151.12, 154.87, 155.96, 157.25, 157.61, 158.63, 167.92, 183.91, 192.04 (Ph-*C*-Ru). ^{11}B NMR (128.2 MHz, CD_2Cl_2): δ 74.

Generation of 51-F and 51-CN. **51**-F and **51**-CN were prepared and characterized by multinuclear NMR *in situ* by addition of a slight excess of TBAF or TEACN, respectively, to solutions of [**51**]OTf in pyridine-d_5 or acetone-d_6. Data for **51**-CN: ^{1}H NMR (399.9 MHz, pyridine-d_5): δ 2.14 (s, 6H, Mes-CH_3), 2.24 (s, 3H, Mes-CH_3), 2.29 (s, 3H, Mes-CH_3), 2.45 (s, 6H, Mes-CH_3), 6.53 (s, 1H, Ph-C*H*), 6.64 (s, 2H, Mes-C*H*), 6.68 (t, $^{3}J_{H\text{-}H}$ = 6.77 Hz, 1H, Pyr-C*H*), 6.75 (s, 2H, Mes-C*H*), 6.84-6.95 (m, 4H, Pyr-C*H*), 7.30 (d, $^{3}J_{H\text{-}H}$ = 7.14 Hz, 1H, Pyr-C*H*), 7.40 (d, $^{3}J_{H\text{-}H}$ = 7.14 Hz, 1H, Pyr-C*H*), 7.48-

7.60 (m, 3H, Pyr-C*H*), 7.82-7.90 (m, 3H, Pyr-C*H*), 7.96 (m, 2H, Pyr-C*H*), 8.07 (m, 2H, Pyr-C*H*), 8.23 (d, 1H, Pyr-C*H*, $^{3}J_{H\text{-}H}$ = 8.06 Hz), 8.34 (d, 1H, Pyr-C*H*, $^{3}J_{H\text{-}H}$ = 7.69 Hz), 8.49 (d, 1H, Pyr-C*H*, $^{3}J_{H\text{-}H}$ = 78.24 Hz), 8.52 (d, 1H, Pyr-C*H*, $^{3}J_{H\text{-}H}$ = 5.5 Hz), 8.62 (d, 1H, Pyr-C*H*, $^{3}J_{H\text{-}H}$ = 8.06 Hz). ^{13}C NMR (100.5 MHz, pyridine-d_5): δ 21.09 (Mes-*p*-*C*H$_3$), 21.12 (Mes-*p*-*C*H$_3$), 25.84 (Mes-*o*-*C*H$_3$), 26.42 (Mes-*o*-*C*H$_3$), 118.04, 120.64, 122.69, 122.75, 123.03, 123.21, 125.56, 125.77, 125.84, 127.17, 129.24, 129.38, 130.93, 131.24, 131.44, 132.42, 133.18, 134.12, 135.27, 140.31, 142.67, 142.76, 143.67, 149.01, 149.12, 155.08, 156.76, 157.13, 158.02, 165.89, 169.50, 189.48 (Ph-*C*-Ru). ^{11}B NMR (128.2 MHz, pyridine-d_5): δ -12.7 Data for **51**-F: ^{1}H NMR (399.9 MHz, acetone- d_6): δ 1.28 (s, 3H, Mes-CH_3), 1.61 (s, 6H, Mes-CH_3), 1.89 (s, 6H, Mes-CH_3), 2.14 (s, 3H, Mes-CH_3), 6.13 (bs, 1H, Ph-C*H*), 6.26 (bs, 2H, Mes-C*H*), 6.33 (bs, 2H, Mes-C*H*), 6.75 (t, 1H, Pyr-C*H*, $^{3}J_{H\text{-}H}$ = 6.52 Hz), 6.94 (br, 1H, Pyr-C*H*), 7.15-7.21 (bm, 3H, Pyr-C*H*), 7.37 (br, 2H, Pyr-C*H*), 7.45 (d, 1H, Pyr-C*H*, $^{3}J_{H\text{-}H}$ = 5.50 Hz), 7.50 (d, 1H, Pyr-C*H*, $^{3}J_{H\text{-}H}$ = 6.4 Hz), 7.55 (t, 1H, Pyr-C*H*, $^{3}J_{H\text{-}H}$ = 7.60 Hz), 7.61 (t, 1H, Pyr-C*H*, $^{3}J_{H\text{-}H}$ = 7.62 Hz), 7.67 (t, 1H, Pyr-C*H*, $^{3}J_{H\text{-}H}$ = 6.8 Hz), 7.83-7.88 (m, 3H, Pyr-C*H*), 8.02-8.07 (m, 3H, Pyr-C*H*), 8.19 (br, 1H, Pyr-C*H*), 8.32 (br, 1H, Pyr-C*H*), 8.70 (d, 1H, Pyr-C*H*, $^{3}J_{H\text{-}H}$ = 8.26 Hz), 8.80 (d, 1H, Pyr-C*H*, $^{3}J_{H\text{-}H}$ = 8.26 Hz). ^{13}C NMR (100.5 MHz, pyridine-d_5): δ 21.27 (Mes-*p*-*C*H$_3$), 21.30 (Mes-*p*-*C*H$_3$) 25.82 (Mes-*o*-*C*H$_3$), 26.22 (Mes-*o*-*C*H$_3$), 117.76, 120.18, 122.69, 122.75, 123.03, 123.12, 124.06, 125.46, 125.68, 125.92, 127.10, 128.79, 128.86, 130.48, 130.78, 132.22, 133.07, 133.98, 135.11, 139.69, 142.35, 148.91, 149.25, 149.37, 155.28, 155.70, 156.89, 157.14, 158.01, 168.60, 169.91, 188.98 (Ph-*C*-Ru). ^{19}F NMR (375.97 MHz, pyridine-d_5): δ -174.39 (90 %), 176.19 (10 %).

Titration of [45]OTf and [46]OTf with Fluoride in $CHCl_3$. Solutions of [**45**]OTf (3.0 mL, 5.6×10^{-5} M, $CHCl_3$) and [**46**]OTf (3.0 mL, 6.2×10^{-5} M, $CHCl_3$) were titrated with incremental (5 μL) amounts of fluoride anions by addition of a 3.4×10^{-3} M solution of TBAF in $CHCl_3$.

Biphasic Fluoride Capture with [45]OTf and [46]OTf. ^{1}H NMR spectra of solutions of [**45**]OTf and [**46**]OTf in $CDCl_3$ (0.500 mL, 0.07 M) were collected after layering and shaking with 0.125 mL (1 eq. F^-) and/or 0.500 mL (4 eq. F^-) of D_2O solutions containing TBAF or NaF (0.28 M). Conversion to the fluoroborate species **45**-F and **46-**F was monitored by integration of the signals corresponding to the mesityl aromatic C*H* groups, which are shifted significantly upfield upon fluoride binding.

Titration of [48]OTf and [50]OTf with Fluoride in THF. Solutions of [**48**]OTf (3.0 mL, 4.9×10^{-5} M, THF) and [**50**]OTf (3.0 mL, 5.0×10^{-5} M, THF) were titrated with incremental amounts of fluoride anions by addition of a 6.0×10^{-3} M solution of KF in MeOH.

Titration of [51]OTf with Fluoride and Cyanide in THF/DMF. Solutions of [**51**]OTf (3.0 mL, 2.5×10^{-5} M, 9/1 DMF/THF) were titrated with incremental (5 μL) amounts of fluoride or cyanide anions by addition of a 3.5×10^{-3} M solution of TBAF in DMF or a 3.0×10^{-3} M solution of TEACN in DMF.

Electrochemistry. Electrochemical experiments were performed with an electrochemical analyzer from CH Instruments (Model 610A) with a glassy carbon working electrode and a platinum auxiliary electrode. The reference electrode was built from a silver wire inserted a small glass tube fitted with a porous vycor frit at the tip and

filled with a THF solution containing (n-Bu)$_4$NPF$_6$ (0.1 M) and $AgNO_3$ (0.005 M). All three electrodes were immersed in a DMF solution (3 mL) containing 0.1 M of supporting electrolyte ((n-Bu)$_4$NPF$_6$) and 0.001 M of [**51**]OTf. **51**-F and **51**-CN were prepared *in situ* in the electrochemical cell by addition of 0.1 mL of 0.03 M TEACN or TBAF solutions in DMF. In all cases, ferrocene was used as an internal standard, and all potentials are reported with respect to the $E_{1/2}$ of the Fc^+/Fc redox couple.

CHAPTER III

STABILIZATION OF ARYLTRIFLUOROBORATES BY PROXIMAL CATIONIC GROUPS*

3.1 Introduction

The discovery of novel fluorination reactions is attracting increasing interest because of their relevance to the preparation of ^{18}F-labeled radiotracers for PET imaging.[209-211] An approach that has gained attention in the past few years involves the functionalization of a biomolecule with an arylboronic acid or ester, which is subsequently converted into a [^{18}F]-aryltrifluoroborate prior to PET imaging.[211-214] Such an approach is appealing because time-consuming synthetic steps can be carried out before introduction of the relatively short-lived ^{18}F radionuclide. Despite its attractive attributes, this method is complicated by: i) the solvolysis of the aryltrifluoroborate at physiological pH, which will lead to deactivation of the radiolabel;[213] ii) the acidic pH needed for the formation of the aryltrifluoroborate, which may limit compatibility with proteins or other biomolecules that would denature under these conditions.

We have recently shown that the fluoride affinity of organoboranes[78,167] can be significantly increased by introduction of a proximal cationic functionality as in [*o*-**7**]$^+$, [**25**]$^+$, and [**26**]$^+$ (Figure 66).[124-126] In addition to favorable inductive and Coulombic

---

* Reprinted in part from, "Stabilization of zwitterionic aryltrifluoroborates against hydrolysis"; Wade, C. R.; Zhao, H.; Gabbaï, F. P. *Chem. Commun.* **2010**,*46*, 6380-6381. -Reproduced by permission of the Royal Society of Chemistry.

effects that promote fluoride ion capture, the resulting complexes are stabilized by hydrogen bonding or donor-acceptor interactions involving the proximal cationic functionality. We hypothesized that these effects could be exploited for the stabilization of trifluoroborate groups against hydrolysis. This chapter describes the implementation of this strategy and encompasses the synthesis and kinetic studies of hydrolysis of zwitterionic *ortho*- ammonium and phosphonium aryltrifluoroborates.

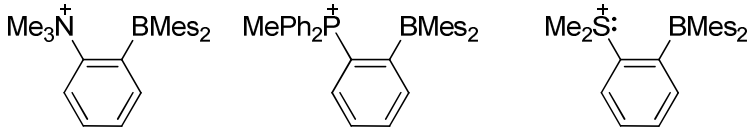

[*o*-**7**]$^+$ [**25**]$^+$ [**26**]$^+$

Figure 66. Triarylborane anion receptors [*o*-**7**]$^+$, [**25**]$^+$, and [**26**]$^+$ bearing proximal cationic groups.

3.2 Synthesis and characterization of zwitterionic aryltrifluoroborates

The *ortho*-functionalized boronic acids 2-(dimethylamino)phenyl boronic acid and 2-(diphenylphosphino)phenyl boronic acid were prepared by modification of literature preparations[215,216] and converted to the pinacol boronate esters prior to methylation. Reaction of the boronate esters with MeOTf afforded the cationic compounds [**52**]$^+$ and [**53**]$^+$ as the triflate salts in good yields (Figure 67). Both compounds are soluble in polar organic solvents such as chloroform, acetonitrile, and methanol. [**52**]$^+$ displays moderate solubility in H_2O whereas [**53**]$^+$ is soluble to a lesser extent because of the greater hydrophobicity of the phenyl substituents.

The zwitterionic aryltrifluoroborates **52**-BF_3 and **53**-BF_3 were prepared by reaction of the boronic ester precursors with KHF_2 in $MeOH/H_2O$ solvent (Figure 67). These compounds have been fully characterized. The ^{11}B NMR spectra of these compounds display a sharp signal around 3 ppm, which is characteristic of an aryltrifluoroborate species. The trifluoroborate functionality of these compounds also gives rise to a sharp ^{19}F NMR resonance which appears around -130 ppm. These spectroscopic features are reminiscent of those of *o*-(*i*-Pr_2PH)(BF_3)C_6H_4, which has been reported.[217]

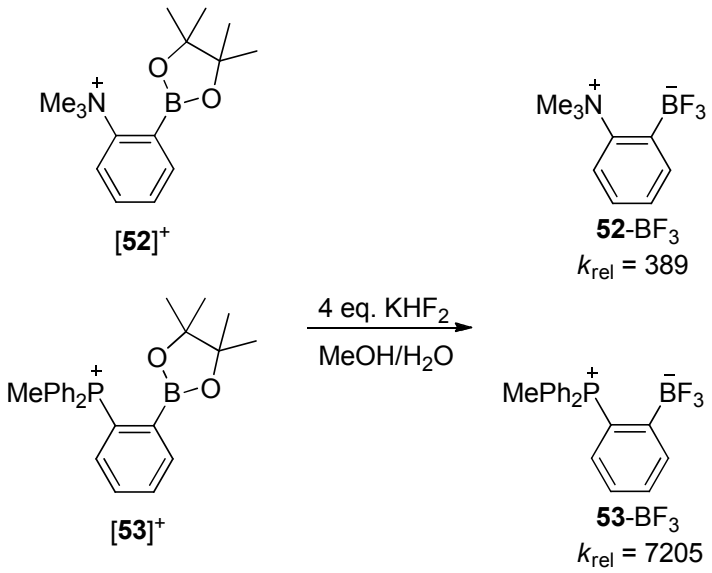

Figure 67. Synthesis of aryltrifluoroborates **52**-BF_3 and **53**-BF_3.

3.3 Kinetic study of aryltrifluoroborate hydrolysis

Although **52**-BF_3 and **53**-BF_3 do not decompose in organic solvents, slow fluoride release is observed in D_2O/CD_3CN (8/2 vol.) at pH 7.5 ([phosphate buffer] = 500 mM,

$[ArBF_3]$ = 20 mM with $ArBF_3$ = **52**-BF_3 and **53**-BF_3). This reaction, which is expected to produce the corresponding $[ArB(OH)_2]^+/ArB(OH)_3$ species, can be easily monitored by ^{19}F NMR spectroscopy. Although the mechanism of fluoride dissociation involves multiple steps, it has been previously demonstrated that dissociation of the first fluoride anion is rate determining.[213] In turn, the kinetics of such reactions can be properly treated by a simple first order rate law ($v = k_{obs}[ArBF_3]$). Treatment of the data on the basis of this equation yields $k_{obs} = 6.3 \times 10^{-5}$ min^{-1} for **52**-BF_3 and 3.4×10^{-6} min^{-1} for **53**-BF_3 (Figure 68). Comparison of these rate constants with that obtained for $PhBF_3^-$ (k_{obs} = 0.0245 min^{-1}) under the same conditions indicates that the presence of the cationic functionality in **52**-BF_3 and **53**-BF_3 passivates these compounds against hydrolysis. This lowering of the reaction rate can be quantified by the relative rate constant $k_{rel} = k_{obs}(PhBF_3^-)/k_{obs}(ArBF_3)$ (Figure 67). Comparison of the data obtained for **52**-BF_3 (k_{rel} = 389) with that of its para isomer (k_{rel} = 16)[213] reveals that the juxtaposition of the cationic and trifluoroborate moieties plays an important stabilizing role. This stabilization is unequivocal in the case of **53**-BF_3, whose hydrolysis is 7205 times slower than that of $[PhBF_3]^-$ and is likely enhanced by the accepting properties of phosphonium center[218] as well as the hydrophobic protection provided by the Ph_2PMe unit.[108,125]

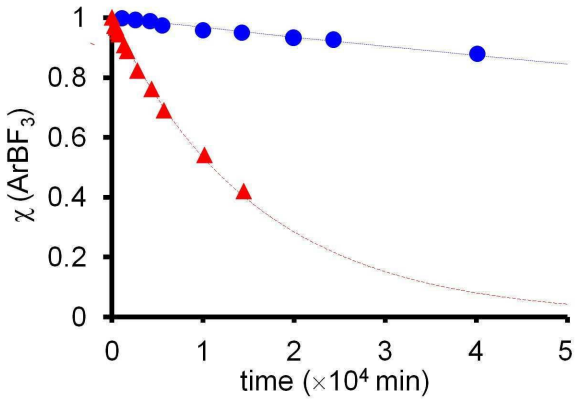

Figure 68. Plot of the mole fraction (χ) of **52**-BF_3 (▲) and **53**-BF_3 (●) (20 mM) in D_2O/CD_3CN (8/2 vol.) at pH 7.5 ([phosphate buffer] = 500 mM) as a function of time.

3.4 Structural features of zwitterionic aryltrifluoroborates

The crystal structures of **52**-BF_3 and **53**-BF_3 have been determined (Figure 69). The asymmetric unit of **53**-BF_3 possesses two independent molecules (molecules A and B), which feature similar structures. Owing to the rigidity of the *ortho*-phenylene backbone, the onium and trifluoroborate moieties present in these structures are held in close proximity as indicated by the B-E separations (E = N, P) of 3.344 Å in **52**-BF_3 and 3.461 Å (molecule A) and 3.381 Å (molecule B) in **53**-BF_3. This proximity induces a strong Coulombic interaction of the onium and trifluoroborate moieties, thereby adding to the stability of these compounds. This view, which is reinforced by a comparison of the behavior of **52**-BF_3 and its para isomer, is also in agreement with the observed increased fluoride ion affinity of $[o\text{-}\mathbf{7}]^+$ and $[\mathbf{25}]^+$ when compared to their respective para isomers $[p\text{-}\mathbf{7}]^+$ and $[\mathbf{12}]^+$.

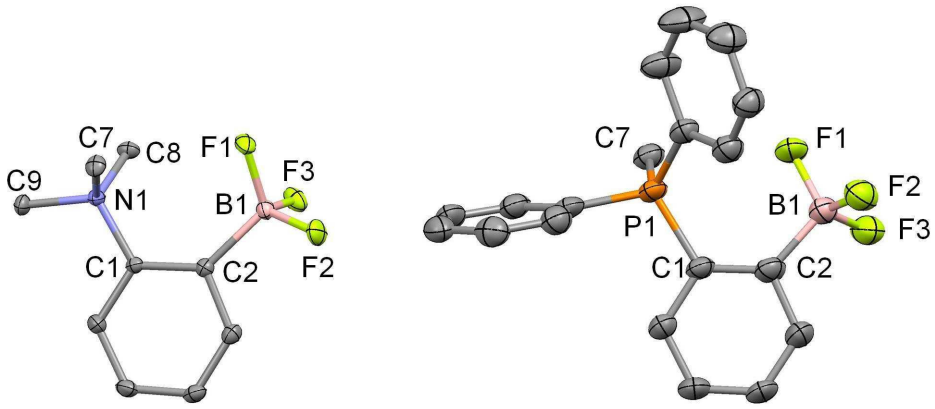

Figure 69. Crystal structures of the zwitterionic aryltrifluoroborates **52**-BF_3 (left) and **53**-BF_3 (right). Ellipsoids are scaled to the 50% probability level and hydrogen atoms have been omitted for clarity. Only one of the two independent molecules of **53**-BF_3 is shown.

In addition to Coulombic effects, these zwitterions can also be stabilized by intramolecular hydrogen-bonding involving the boron-bound fluorine atoms and the hydrogen atoms of the E-bound methyl groups.[103,184,219-221] The F-C_{Methyl} separations in the 2.976-3.041 Å range for **52**-BF_3 and 2.974-3.145 Å range for **53**-BF_3 support the formation of such hydrogen bonding interactions.[101] In the case of **53**-BF_3, additional stability may be added by weak F(lone pair)→P-C(σ*) donor-acceptor interactions, which have been previously observed in compounds such as *o*-(Ph_2PMe)(Mes_2BF)C_6H_4 (**25**-F)[125] and *o*-(*i*-Pr_2PH)(Mes_2BF)C_6H_4.[217] For **53**-BF_3, F(lone pair)→P-C(σ*) interactions can be proposed based on the shortest measured F-P distances of 3.003 Å (molecule A) and 3.105 Å (molecule B), which are within the sum of the van der Waals radii of the elements (r_{vdw} = 1.5 Å for F, 1.95 Å for P).[222] The presence of such interactions is also supported by the linearity of the F-P-C_{trans} angle (174.4˚ av.).

3.5 Conclusions

In conclusion, we have shown that zwitterionic ammonium and phosphonium aryltrifluoroborates are endowed with an exceptional kinetic stability against hydrolysis. This stability arises from the same Coulombic effects and intramolecular interactions that enhance the fluoride affinity of triarylboranes bearing a proximal onium moiety. These effects are most acute in the case of **53**-BF_3, which is almost four orders of magnitude more kinetically stable than $PhBF_3^-$. Overall, the stability observed for these complexes makes them viable candidates for conjugation with biomolecules and ^{18}F-radiolabeling experiments.

3.6 Experimental

General Considerations. 2-bromothioanisole was purchased from TCI America. KHF_2 was purchased from Alfa Aesar. Solvents were dried by passing through an alumina column (*n*-hexane, CH_2Cl_2) or refluxing under N_2 over Na/K (Et_2O and THF). Air-sensitive compounds were handled under a N_2 atmosphere using standard Schlenk and glovebox techniques. Elemental analyses were performed at Atlantic Microlab (Norcross, GA). NMR spectra were recorded on a Varian Unity Inova 400 FT NMR (399.59 MHz for ^1H, 375.99 MHz for ^{19}F, 128.19 MHz for ^{11}B, 100.45 MHz for ^{13}C, 161.75 MHz for ^{31}P) spectrometer at ambient temperature. Chemical shifts (δ) are given in ppm and are referenced against residual solvent signals (^1H, ^{13}C) or external $BF_3 \cdot Et_2O$ (^{11}B, ^{19}F) and H_3PO_4 (^{31}P).

Table 7. Crystal data, data collections, and structure refinements for **52**-BF_3 and **53**-BF_3.

Crystal data	**52**-BF_3	**53**-BF_3
Formula	$C_9H_{13}BF_3N$	$C_{19}H_{17}BF_3P$
Mr	203.02	344.11
Crystal size/mm	0.20 x 0.20 x 0.16	0.27 x 0.12 x 0.08
Crystal system	Monoclinic	Triclinic
Space group	P2(1)/c	P-1
a/Å	7.0647(2)	11.6184(6)
b/Å	13.0809(3)	12.0740(6)
c/Å	10.1994(2)	12.6108(7)
α /°	90	108.737(3)
β/°	95.349(1)	94.921(4)
γ /°	90	90.944(3)
V/Å^3	938.45(4)	1667.30(15)
Z	4	4
ρ_{calc}/g cm^{-3}	1.437	1.371
μ/mm^{-1}	0.125	0.192
F(000)	424	712
T/K	110(2)	110(2)
Scan mode	ω, φ	ω, φ
hkl Range	-10 → +10	-13 → +13
	-19 → +18	-14 → +14
	-15 → +15	-14 → +14
Measd reflns	9940	27166
Unique reflns [Rint]	3254 [0.0303]	5847 [0.0758]
Reflns used for refinement	3254	5847
Refined parameters	127	433
GooF	1.000	1.001
R1,[a] *w*R2[b] (all data)	0.0491, 0.0993	0.0981, 0.2021
ρ_{fin} (max., min.)/eÅ^{-3}	0.380, -0.220	0.780, -0.611

[a] $R1 = \Sigma||F_o| - |F_c||/\Sigma|F_o|$. [b] $wR2\ ([\Sigma w(F_o^2 - F_c^2)^2]/[\Sigma\ w(F_o^2)^2])^{1/2}$; $w = 1/[\sigma^2(F_o^2) + (ap)^2 + bp]$; $p = (F_o^2 + 2F_c^2)/3$ with $a = 0.0563$ for **52**-BF_3, 0.0300 for **53**-BF_3 and $b = 0$ for **52**-BF_3, 8.5 for **53**-BF_3.

Crystallography. Single crystals of **52**-BF_3 were obtained by slow evaporation of a solution of the compound in acetonitrile. Single crystals of **53**-BF_3 were obtained by slow evaporation of solutions of the compounds in acetonitrile/H_2O (5/1). The crystal data for **52**-BF_3 and **53**-BF_3 are included in Table 7. The crystallographic measurements of **52**-BF_3 and **53**-BF_3 were performed using a Bruker-AXS APEX-II CCD area detector diffractometer, with a graphite-monochromated Mo-Kα radiation (λ = 0.71069 Å). A specimen of suitable size and quality was selected and mounted onto a nylon loop. The semiempirical method SADABS[207] was applied for absorption correction. The structures were solved by direct methods using SHELXTL/PC package (version 6.1)[208] which successfully located most of the non-hydrogen atoms. Subsequent refinement on F^2 allowed location of the remaining non-hydrogen atoms. All H atoms were geometrically placed and refined in a riding model approximation.

Synthesis of 52-BF_3. A solution of *ortho*-$(Me_2N)C_6H_4(B(OH)_2)$[215] (0.725 g, 4.39 mmol) and pinacol (0.570 g, 4.83 mmol) in CH_2Cl_2 (10 mL) was stirred for 3 hrs over anhydrous $MgSO_4$. The solution was filtered and the solvent removed *in vacuo* to yield the pinacol borane *o*-$(Me_2N)C_6H_4(BPin_2)$ in 79 % yield (0.860 g). ^{1}H NMR (399.9 MHz, $CDCl_3$): δ 1.35 (s, 12H, pinacol-*CH*$_3$), 2.86 (s, 6H, N- *CH*$_3$), 6.80-6.85 (m, 2H, Ph-*CH*), 7.30 (ddd, 1H, Ph-*CH*, $^3J_{H\text{-}H}$ = 8.24, 7.14 Hz, $^4J_{H\text{-}H}$ = 1.83 Hz), 7.63 (dd, 1H, Ph-*CH*, $^3J_{H\text{-}H}$ = 7.33 Hz, $^4J_{H\text{-}H}$ = 1.83 Hz). ^{11}B NMR (128.2 MHz, $CDCl_3$): δ 32.4. The reaction of *o*-$(Me_2N)C_6H_4(BPin_2)$ (0.284 g, 1.15 mmol) with 2 eq. of methyl triflate (0.26 mL) in Et_2O (10 mL) led to the immediate precipitation of a white solid, which was filtered and washed with Et_2O (3 × 5 mL) to afford [*o*-$(Me_2N)C_6H_4(BPin_2)$]OTf

([**52**]OTf) in 65% yield (0.308 g). ^{1}H NMR (399.9 MHz, $CDCl_3$): δ 1.38 (s, 12H, pinacol-*CH*$_3$), 3.83 (s, 9H, N- *CH*$_3$), 7.50 (t, 1H, Ph-*CH*, $^{3}J_{H\text{-}H}$ = 7.33 Hz), 7.67 (t, 1H, Ph-*CH*, $^{3}J_{H\text{-}H}$ = 8.43 Hz), 7.85 (d, 1H, Ph-*CH*, $^{3}J_{H\text{-}H}$ = 8.43 Hz), 7.98 (d, 1H, Ph-*CH*, $^{3}J_{H\text{-}H}$ = 7.33 Hz). ^{13}C NMR (100.5 MHz, $CDCl_3$): δ 24.61, 57.54, 85.89, 119.72, 122.27, 129.88, 133.30, 139.14, 150.60. ^{11}B NMR (128.2 MHz, $CDCl_3$): δ 31.50. Anal. Calcd. for $C_{16}H_{25}BNO_5F_3S$: C, 46.73; H, 6.31; N, 3.41. Found: C, 47.00; H, 6.03; N, 3.45. A solution of [**52**]OTf (0.05 g, 0.12 mmol) in MeOH (1 mL) was treated with KHF_2 (0.038 g, 0.48 mmol) in H_2O (1 mL). The solution was sonicated for 15 minutes, and the precipitate was collected by filtration. The solid was then extracted with 5 mL hot acetonitrile, the solution was filtered over Celite, and the solvent removed *in vacuo* to yield 0.023 g (93 %) of **52**-BF_3. ^{1}H NMR (399.9 MHz, CD_3CN): δ 3.63 (s, 9H, N- *CH*$_3$), 7.33 (ddd, 1H, Ph-*CH*, $^{3}J_{H\text{-}H}$ = 8.35 Hz, 7.17 Hz, $^{4}J_{H\text{-}H}$ = 2.04 Hz), 7.39 (t, 1H, Ph-*CH*, $^{3}J_{H\text{-}H}$ = 7.16 Hz), 7.55 (d, 1H, Ph-*CH*, $^{3}J_{H\text{-}H}$ = 8.31 Hz), 7.97 (d, 1H, Ph-*CH*, $^{3}J_{H\text{-}H}$ = 5.31 Hz). ^{13}C NMR (100.5 MHz, CD_3CN): δ 57.8 q, (pseudo-q, $^{3}J_{H\text{-}F}$ = 3.90 Hz), 128.46, 129.62, 139.72 (q, $^{3}J_{H\text{-}F}$ = 4.32 Hz), 151.17. ^{11}B NMR (128.2 MHz, CD_3CN): δ 3.2 (q, $^{1}J_{B\text{-}F}$ = 45.5 Hz). ^{19}F NMR (375.97 MHz, CD_3CN): δ -131.5 (q, $^{1}J_{B\text{-}F}$ = 45.5 Hz). Anal. Calcd for $C_9H_{13}BNF_3$: C, 53.25; H, 6.45; N, 6.90. Found: C, 53.18; H, 6.59; N, 6.90.

Synthesis of 53-BF_3. The pinacol borane *ortho*-$(Ph_2P)C_6H_4(Bpin)$[223] (0.175 g, 0.451 mmol) was treated with 2 eq. of MeOTf (0.10 mL) in Et_2O (5 mL), leading to the immediate precipitation of a white solid. This white solid was filtered and washed with Et_2O (3 × 5 mL). Recrystallization by slow diffusion of Et_2O into a CH_2Cl_2 solution (3 mL) yielded 0.180 g (72%) of [*o*-$(Ph_2MeP)C_6H_4(Bpin)$]OTf ([**53**]OTf). ^{1}H NMR (399.9

MHz, $CDCl_3$): δ 0.96 (s, 12H, pinacol-*CH*$_3$), 3.06 (d, 3H, P-*CH*$_3$, $^1J_{H\text{-}P}$ = 13.92 Hz), 7.11 (dd, 1H, Ph-*CH*, $^3J_{H\text{-}P}$ = 15.7 Hz, $^3J_{H\text{-}H}$ = 7.80 Hz), 7.54-7.67 (m, 9H, Ph-*CH*), 7.74 (t, 3H, Ph-CH, , $^3J_{H\text{-}H}$ = 7.51 Hz) 8.22 (dd, 1H, Ph-*CH*, , $^3J_{H\text{-}P}$ = 7.50 Hz, $^3J_{H\text{-}H}$ = 6.87 Hz). ^{13}C NMR (100.5 MHz, $CDCl_3$): δ 9.88 (d, P-CH_3, $^1J_{C\text{-}P}$ = 57.22 Hz), 24.24 (pinacol-CH_3), 85.28 (pinacol-*C*-O), 121.07 (d, $J_{C\text{-}P}$ = 88.5 Hz), 123.95 (d, $J_{C\text{-}P}$ = 84.7 Hz), 130.32 (d, $J_{C\text{-}P}$ = 13.0 Hz), 132.13 (d, $J_{C\text{-}P}$ = 13.73 Hz), 132.7 (d, $J_{C\text{-}P}$ = 9.9 Hz), 133.88 (d, $J_{C\text{-}P}$ = 3.0 Hz), 134.55 (d, $J_{C\text{-}P}$ = 2.3 Hz), 136.84 (d, $J_{C\text{-}P}$ = 13.0 Hz), 139.27 ((d, $J_{C\text{-}P}$ = 13.7 Hz), (ipso C for phenylene-C-B not observed). ^{11}B NMR (128.2 MHz, $CDCl_3$): δ 29.72. ^{31}P NMR (161.75 MHz, $CDCl_3$): δ 25.64. Anal. Calcd. for $C_{26}H_{29}BO_5F_3PS$: C, 56.54; H, 5.29. Found: C, 56.29; H, 5.26. [**53**]OTf (0.050 g, 0.09 mmol) in of MeOH (1 mL) was then treated with a solution of KHF_2 (0.028 g, 0.36 mmol) in H_2O (1 mL). The resulting solution was sonicated for 15 minutes, and the precipitate was collected by filtration. The solid was washed with H_2O (3 × 1 mL) and dried *in vacuo* to yield 0.026 g (97 % yield) of **53**-BF_3. ^{1}H NMR (399.9 MHz, $CDCl_3$): δ 2.89, (d, 3H, P-*CH*$_3$, $^2J_{H\text{-}P}$ = 13.9 Hz), 6.81 (dd, 1H, $^3J_{H\text{-}P}$ = 15.1 Hz, $^3J_{H\text{-}H}$ = 7.8 Hz), 7.19 (tdd, 1H, *J* = 7.69, 3.45, 1.33 Hz), 7.41 (dd, 4H,*m*-phenyl-*CH*, *J* = 12.96, 7.88 Hz), 7.55 (td, 4H, *o*-phenyl-*CH*, *J* = 8.13, 3.17 Hz), 7.59 (td, 1H, phenyl-*CH*, *J* = 7.58, 1.87 Hz), 7.68 (tq, 1H, phenyl-*CH, J* = 7.58, 1.68 Hz), 8.15 (dd, 1H, phenyl-*CH, J* = 6.40, 7.58 Hz). ^{13}C NMR (100.5 MHz, $CDCl_3$): δ 11.50 (d, $^1J_{P\text{-}C}$ = 58.85 Hz), 119.05 (d $J_{P\text{-}C}$ = 86.98 Hz), 123.62 (d $J_{P\text{-}C}$ = 88.50 Hz), 126.67 (d $J_{P\text{-}C}$ = 14.49 Hz), 129.63 (d $J_{P\text{-}C}$ = 12.97 Hz), 132.62 (d $J_{P\text{-}C}$ = 9.91 Hz), 133.43 (d $J_{P\text{-}C}$ = 3.38 Hz), 133.64 (d $J_{P\text{-}C}$ = 3.03 Hz), 134.16 (d $J_{P\text{-}C}$ = 15.26 Hz), 135.84 (dq $^1J_{P\text{-}C}$ =16.77 Hz, $^3J_{F\text{-}C}$ = 3.02 Hz). ^{11}B NMR (128.2 MHz, $CDCl_3$): δ 3.68. ^{19}F NMR

(375.97 MHz, $CDCl_3$): δ -139.0. ^{31}P NMR (161.75 MHz, $CDCl_3$): δ 26.23. Anal. Calcd. for $C_{19}H_{17}BF_3P$: C, 66.32; H, 4.98. Found: C, 65.62; H, 4.83.

Table 8. Kinetic data for the hydrolysis of **52**-BF_3.

Time (min)	$[F^-]$	$[BF_3]$	exp. ratio $[BF_3]/([BF_3]+[F])$	k_{obs}=6.30E-05 calc. ratio $[BF_3]/([BF_3]+[F])$
0	0	100	1.000	1.000
255	2.82	100	0.973	0.984
450	3.47	100	0.966	0.972
595	4.86	100	0.954	0.963
740	5.94	100	0.944	0.954
1330	10.14	100	0.908	0.920
1660	12.57	100	0.888	0.901
2790	21.51	100	0.823	0.839
4350	31.28	100	0.762	0.760
5700	44.78	100	0.691	0.698
10155	84.44	100	0.542	0.527
14460	137.25	100	0.421	0.402
20000				0.284
30000				0.151
40000				0.080
50000				0.043

NMR Spectroscopic Kinetic Analyses. Samples of **52**-BF_3 (5 mg) and **53**-BF_3 (8.5 mg) were each dissolved in 0.2 mL CD_3CN and 1.0 mL D_2O phosphate buffer (pH 7.5, 500 mM). The resulting mixtures were filtered over glass wool to remove any precipitated solids. The ^{19}F NMR spectrum of each sample was collected periodically. Decomposition of the aryltrifluoroborate species was monitored by integration of the decreasing aryltrifluoroborate signal in conjunction with the increasing signal

corresponding to free F^- using VNMRJ Version 2.2 NMR processing software. The rate constants, k_{obs}, were calculated using a method reported in the literature.[213] The data used for these calculations are given in Table 8, Table 9, and Table 10.

Table 9. Kinetic data for the hydrolysis of **53**-BF_3.

Time (min)	$[F^-]$	$[BF_3]$	exp. ratio $[BF_3]/([BF_3]+[F])$	k_{obs} =3.40E-06 calc. ratio $[BF_3]/([BF_3]+[F])$
0	0	100	1	1
1100	0.25	100	0.997506234	0.996266985
2560	0.81	100	0.991965083	0.99133377
4170	1.21	100	0.98804466	0.985922035
5520	2.67	100	0.973994351	0.981407022
9975	4.46	100	0.957304231	0.966653667
14250	5.3	100	0.949667616	0.952704973
19920	7.24	100	0.932487878	0.934514627
24300	7.97	100	0.926183199	0.920700947
40110	13.77	100	0.878966336	0.87251625
50000				0.843664817

Table 10. Kinetic data for the hydrolysis of $K[PhBF_3]$.

Time (min)	$[F^-]$	$[BF_3]$	exp. ratio $[BF_3]/([BF_3]+[F])$	k_{obs} =0.0245 calc. ratio $[BF_3]/([BF_3]+[F])$
0	0	100	1.000	1.000
15	44	100	0.694	0.692
30	105	100	0.488	0.480
45	197	100	0.337	0.332
60	335	100	0.230	0.230
75	531	100	0.158	0.159
90	841	100	0.106	0.110

CHAPTER IV

SYNTHESIS, STRUCTURE, AND ANION BINDING STUDIES OF BIFUNCTIONAL BORON/ANTIMONY LEWIS ACIDS*

4.1 Introduction

Following the seminal contribution of Biallas and Shriver, who first showed that bifunctional Lewis acids could be used for anion chelation,[224] the chemistry of boron-based bidentate Lewis acids has been growing at a steady rate,[25,87,89,114,225] leading to numerous applications in anion sensing[78,167] and organic/organometallic chemistry.[226-228] A key aspect of this chemistry lies in the stability of the chelate complex formed between the bidentate host and the anionic guest.[94,99,115,119,121,122,187,229,230] Through a series of recent studies, it has been shown that anion binding at boron can be assisted by an adjacent onium ion via Coulombic effects.[101,103,124-126,128,228,231] An in-depth analysis of some of the complexes isolated suggested that these favorable Coulombic effects can also be complemented by donor-acceptor interactions involving non-bonding lone pairs of the anion and vacant orbitals at the central atom of the onium group. This situation is illustrated by the structure of **25**–F which features a B-F→P bond of 2.66 Å, estimated to contribute 5 kcal/mol to the stability of complex (Figure 70).[125]

---

* Reprinted in part with permission from: "Fluoride anion chelation by a bidentate stibonium-borane Lewis acid"; Wade, C. R.; Gabbaï F. P. *Organometallics* **2011**, in press, DOI: 10.1021/om200499y. Copyright 2010 American Chemical Society. and "Synthesis and structure of peri-substituted boron/pnictogen napththalene derivatives"; Wade, C. R.; Saber, M. R.; Gabbaï F. P. *Heteroatom Chem.* **2011**, *22*, 500-505. Copyright 2010 by John Wiley & Sons, Inc.

Additional support for the benefits of cooperative binding with onium ions comes from an investigation of the fluoride affinities of the sulfonium and telluronium derivatives [**28**]$^+$ and [**29**]$^+$. The telluronium derivative [**29**]$^+$ was found to have a significantly higher fluoride affinity than the sulfonium borane [**28**]$^+$, which was attributed to the formation of a stronger B-F→Ch interaction (Figure 70).[128] These results, which can be rationalized by invoking the greater size, electropositivity, and polarizability of the chalcogen in [**29**]$^+$, are also in agreement with the stability of halogen-bonded complexes, which increases with the size of the halogen.[232] This theory suggests that the Lewis acidity of other heavy main group onium ions may be exploited for the development of potent heteronuclear bidentate anion receptors. This chapter describes our efforts to expand this approach through the synthesis and investigation of the anion binding properties of antimony analogs of [**25**]$^+$ and [**28**]$^+$/[**29**]$^+$.

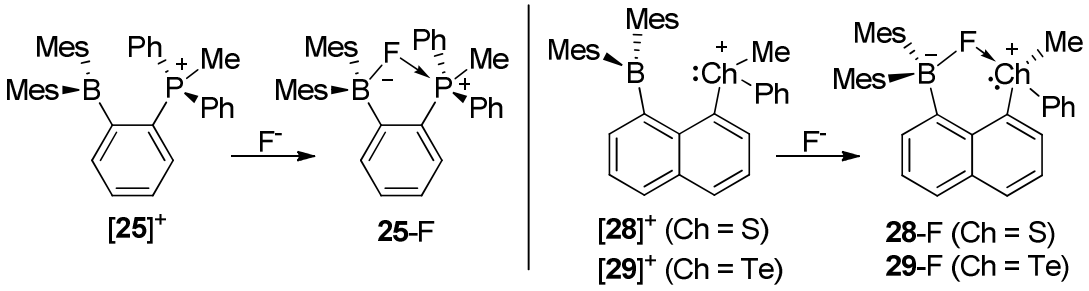

Figure 70. Reaction of [**25**]$^+$ and [**28**]$^+$/[**29**]$^+$ with F^- to form the B-F-P and B-F-Ch bridges species.

4.2 Synthesis, structure, and anion binding studies of a bifunctional boron/antimony Lewis acid with an *ortho*-phenylene backbone

The reaction of *o*-$(Ph_2Sb)BrC_6H_4$[233] with 2 eq. of *t*-BuLi in Et_2O followed by Mes_2BF afforded *o*-$(Ph_2Sb)(Mes_2B)C_6H_4$. Subsequent treatment of this derivative with MeOTf in Et_2O generated the triflate salt of [**54**]$^+$ in moderate yield as a moisture sensitive white powder (Figure 71). Salt [**54**]OTf is soluble in polar organic solvents such as $CHCl_3$, CH_2Cl_2, THF, and methanol, but not in Et_2O or hydrocarbon solvents such as hexanes. The ^{1}H NMR spectrum of [**54**]OTf recorded in $CDCl_3$ displays a signal at 1.91 ppm assigned to the antimony-bound methyl group. The spectrum also shows a series of broad resonances corresponding to the mesityl aromatic *CH* and *ortho-CH₃* groups, which suggests steric crowding and hindered rotation of the boron substituents in solution. A broad signal at +80.2 ppm in the ^{11}B NMR spectrum of [**54**]OTf indicates the presence of a tricoordinate "base-free" boron atom".[125] This is supported by the UV-Vis absorption spectrum of [**54**]OTf in $CHCl_3$, which displays a broad absorption band centered at 334 nm, characteristic of aryldimesitylborane chromophores. The intensity of absorption band decreased significantly over the course of several minutes, an effect attributed to the reaction of [**54**]OTf with adventitious water.

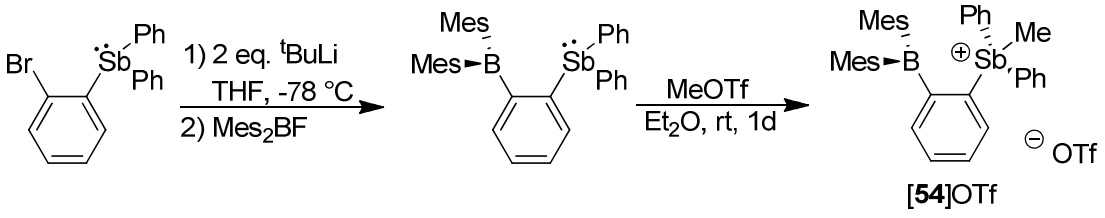

Figure 71. Synthesis of stibonium/borane [**54**]OTf.

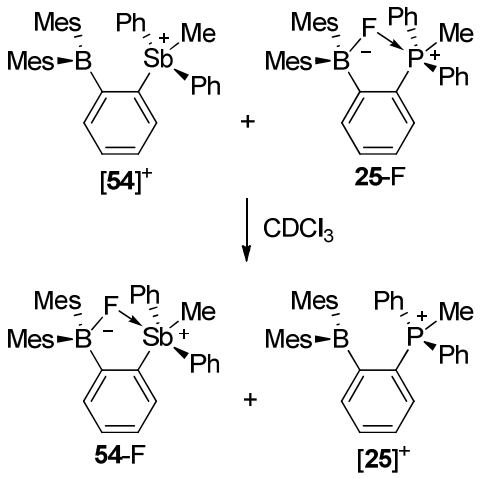

Figure 72. Competition reaction between [**54**]$^+$ and **25**-F.

Because of the moisture sensitive nature of [**54**]$^+$, a fluoride binding constant could not be determined by UV-Vis titration. We therefore decided to compare the relative fluoride affinity of [**54**]$^+$ to that of its phosphonium analog [**25**]$^+$. To this end, we studied the reaction of [**54**]$^+$ with an equimolar amount of **25**-F in $CDCl_3$ and observed the quantitative formation of **54**–F and [**25**]$^+$ using multinuclear NMR spectroscopy (Figure 72). The identity of **54**–F was independently confirmed by the reaction of [**54**]OTf with one equivalent of $[S(NMe_2)_3][Me_3SiF_2]$ (TASF) in $CDCl_3$. The ^{11}B NMR spectrum of **54**–F displays a single sharp signal at 7.51 ppm, indicative of a tetrahedral boron center.[125] Similarly, the ^{19}F NMR spectrum shows a single resonance at –161.4 ppm, in the expected range for a triarylfluoroborate species. The ^1H NMR resonance of the antimony-bound methyl group is shifted upfield to 1.34 ppm and appears as a doublet ($J_{H\text{-}F}$ = 2.38 Hz) because of coupling to the fluorine nucleus. The superior fluoride

affinity of [**54**]$^+$ was confirmed by the observation that **54**–F remained intact when treated with one equivalent of [**25**]$^+$ in $CDCl_3$.

To obtain structural insight into the enhanced fluoride affinity of [**54**]$^+$, the X-ray crystal structure of **54**-F was determined (Figure 73). Examination of this structure indicates the formation of an unprecedented B–F–Sb chelate motif, demonstrating that [**54**]$^+$ can be regarded as a bidentate Lewis acid. In agreement with the formation of this chelate complex and the bridging location of the fluoride anion,[128] we note that the B(1)–F(1) bond (1.521(4) Å) is elongated when compared to terminal B–F bonds found in compounds such as *p*-(Ph_2MeP)C_6H_4($BFMes_2$) (**12**-F, B-F: 1.476(4) Å). It is also longer than the B-F bond observed in the structure of its phosphorus congener **25**-F (1.482(3) Å),[107] suggesting that the antimony atom in **54**-F exerts a stronger pull than the phosphorus atom in **25**-F.[125] Accordingly, the Sb–F distance in **54**-F (2.450(2) Å) is shorter than the P–F distance in **25**-F (2.666(2) Å), despite the larger size of the antimony atom. Owing to the bridging location of the fluorine atom, the Sb–F distance in **54**-F is elongated when compared to that in Ph_3MeSbF (2.069(3) Å)[234] but is comparable to that observed in the Sb-F-Sb bridges of polymeric Me_4SbF (2.369(14) and 2.382(12) Å).[235] As a result of the B-F-Sb bridge, the antimony center adopts a distorted trigonal bipyramidal geometry defined by C(14)-Sb(1)-F(1) = 173.8(1)˚ and Σ(C_{eq}-Sb-C_{eq}) = 348.1˚. Additionally, the Sb-C(14) bond (2.135(4) Å), trans to the fluoride anion, is only marginally longer than the equatorial Sb-C bonds (Sb(1)-C(1) = 2.093(4) Å and Sb(1)-C(8) = 2.092(4) Å).

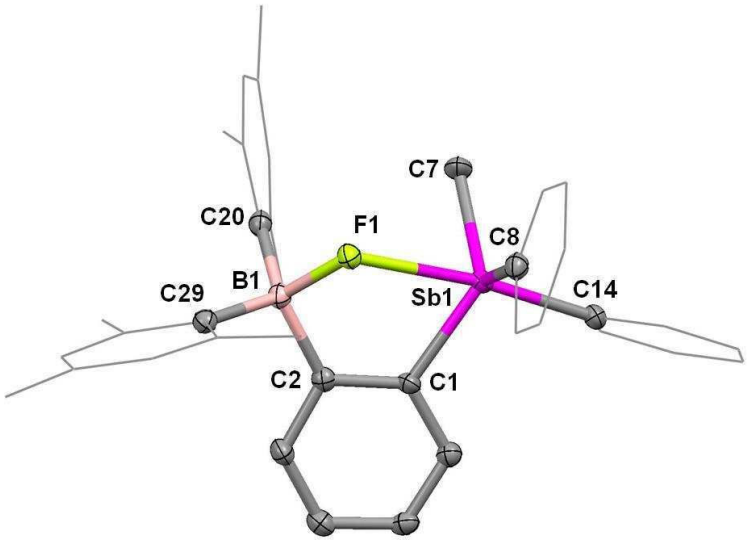

Figure 73. Crystal structure of **54**-F. Displacement ellipsoids are scaled to the 50% probability level. Hydrogen atoms have been omitted for clarity and phenyl and mesityl groups are depicted in wireframe. Selected bond lengths (Å) and angles (˚): Sb(1)-F(1) 2.450(2); F(1)-B(1) 1.521(4); Sb(1)-C(1) 2.093(4); Sb(1)-C(7) 2.107(4); Sb(1)-C(8) 2.092(4); Sb(1)-C(14) 2.135(4); C(8)-Sb(1)-C(1) 115.85(14); C(8)-Sb(1)-C(7) 111.77(16); C(1)-Sb(1)-C(7) 120.50(15); C(14)-Sb(1)-F(1) 173.84(11); C(2)-B(1)-C(20) 118.0(3); C(2)-B(1)-C(29) 108.6(3); C(20)-B(1)-C(29) 116.7(3).

The geometry of **54**–F has been optimized using density functional theory (DFT) methods (B3LYP functional with the mixed basis set: aug-cc-pvTz-pp for Sb, 6-31+g(d') for B, and F, 6-31g for C, H). The resulting geometry closely matches that determined experimentally and corresponds to a true minimum as indicated by the absence of imaginary frequencies. Atoms in Molecules (AIM) calculations carried out at the optimized geometry located a bond path connecting the antimony and fluorine atom of **54**–F. Although bonding orbitals tend to become more diffuse as the size of the atom increases, the value of the electron density at the Sb–F bond critical point (BCP) ($\rho(r)$ = 4.26×10^{-2} e $bohr^{-3}$) is significantly larger than that determined for the P–F bond of **25**-F

($\rho(r)$ = 2.05 × 10^{-2} e $bohr^{-3}$).[125] The greater BCP electron density observed in **54**–F suggests that the Pn–F bond (Pn = P or Sb) in **54**–F is greater than in **25**-F. The Sb–F bond in **54**–F has also been investigated using a Natural Bond Orbital (NBO) analysis. This analysis reveals the presence of a $lp_{(F)} \rightarrow \sigma^*_{(Sb\text{-}C)}$ donor–acceptor interaction which, as indicated by deletion calculations, contributes E_{del} = 15.2 kcal mol^{-1} to the stability of **54**–F (Figure 74). This value greatly exceeds that measured in for the P–F bond of **25**-F (E_{del} = 5.0 kcal mol^{-1}), again corroborating the higher Lewis acidity of the antimony derivative. Finally, we calculated the enthalpy change for the reaction presented in Figure 72 by carrying out single point calculations on [**54**]$^+$, [**25**]$^+$, **54**–F and **25**-F (functional: B3LYP, basis sets: aug-cc-pvTz-pp for Sb/6-311+g(2d,p) for all other atoms). These calculations indicate that the reaction is exothermic (ΔH = −4.9 kcal/mol), thus corroborating the experimental observations as well as the results of the NBO analysis.

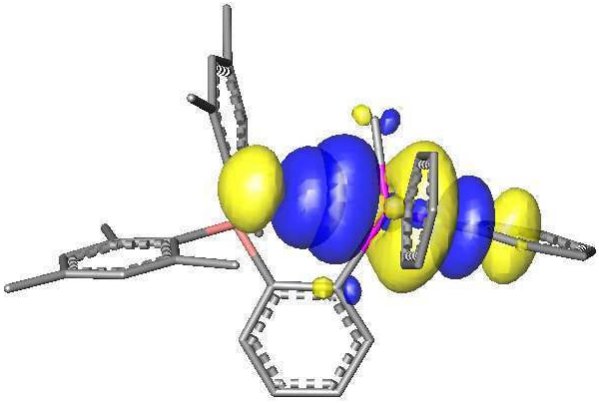

Figure 74. Plot of the NBO $lp_{(F)} \rightarrow \sigma^*_{(Sb\text{-}C)}$ donor-acceptor interaction calculated for **54**-F.

Given that cationic triarylboranes such as [**25**]$^+$ and [**26**]$^+$, with onium ions adjacent to the borane, have also been successfully used as receptors for cyanide or azide, we sought to investigate the reactivity of [**54**]$^+$ with these anions. Addition of 1 equiv. of TBACN or $TBAN_3$ to solutions of [**54**]OTf in dry $CDCl_3$ resulted in quantitative conversion to the adducts **54**-CN and **54**-N_3, as confirmed by multinuclear NMR spectroscopy. The aliphatic region of the ^{1}H NMR of **54**-CN taken at room temperature displayed 3 distinct resonances in a 3:3:6 ratio, corresponding to the mesityl *ortho*-CH_3 groups. A similar pattern is observed for the mesityl aromatic C-H signals, which appear in the 6.6-6.8 ppm range as broad signals in a 1:1:2 ratio. This result indicates inequivalency of the boron mesityl substituents with free rotation of one and hindered rotation of the other on the NMR timescale. The signal corresponding to the antimony-bound methyl group appears as a singlet at 1.56 ppm. The ^{11}B NMR spectrum of **54**-CN displays a single peak at -11.7 ppm, in the expected region for a triarylcyanoborate. The IR spectrum of the **54**-CN, obtained as a colorless microcrystalline solid by precipitation and washing with anhydrous MeOH, shows a CN stretching band at 2160 cm^{-1}, in the same region as that reported for similar triarylcyanoborates.[104,126] The ^{1}H NMR of **54**-N_3 more closely resembles that of **54**-F, exhibiting single resonances for the mesityl *ortho*-CH_3 and CH groups and a singlet at 1.32 ppm corresponding to the antimony-bound methyl group. The ^{11}B NMR of **54**-N_3 displays a single peak at +0.99 ppm.

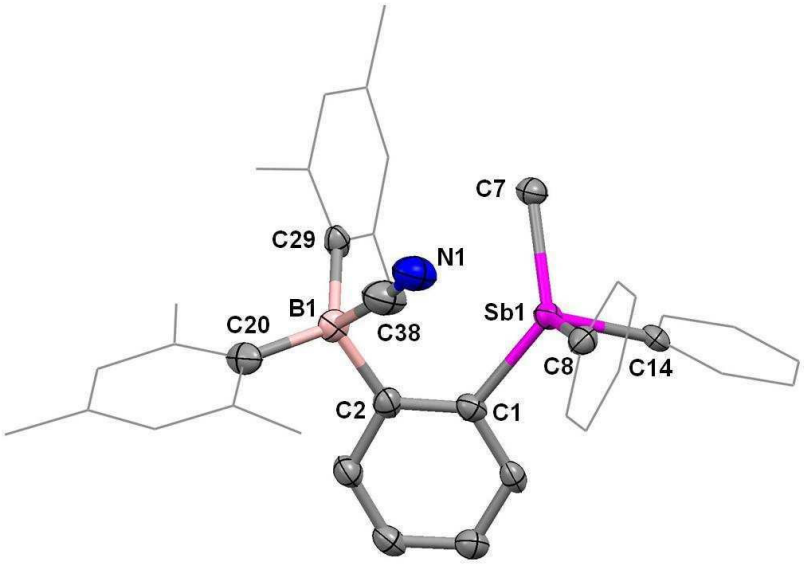

Figure 75. Crystal structure of **54**-CN. Displacement ellipsoids are scaled to the 50% probability level. Hydrogen atoms have been omitted for clarity, and phenyl and mesityl groups are depicted in wireframe. Selected bond lengths (Å) and angles (˚): Sb(1)-C(38) 2.943(7); Sb(1)-N(1) 3.093(5); Sb(1)-C(1) 2.113(5); Sb(1)-C(7) 2.103(5); Sb(1)-C(8) 2.088(5); Sb(1)-C(14) 2.119(5); C(38)-B(1) 1.601(8); N(1)-C(38)-B(1) 173.5(7); C(8)-Sb(1)-C(7) 111.19(19); C(8)-Sb(1)-C(1) 110.11(19); C(7)-Sb(1)-C(1) 125.70(19); C(8)-Sb(1)-C(14) 102.32(18); C(7)-Sb(1)-C(14) 101.77(19); C(1)-Sb(1)-C(14) 102.21(18); C(2)-B(1)-C(20) 108.9(4); C(2)-B(1)-C(29) 116.4(4); C(20)-B(1)-C(29) 117.4(4).

The X-ray crystal structures of **54**-CN and **54**-N_3 have been determined. Examination of the structure of **54**-CN suggests that the boron-bound cyanide anion may form a weak B-CN-Sb bridging interaction. This is indicated by the C(38)-Sb(1) and N(1)-Sb(1) distances of 2.943(7) Å and 3.093(5) Å, respectively, which are longer than the sum of the covalent radii (Sb-C 2.08 Å, Sb-N 2.10 Å),[236] but shorter than the sum of the van der Waals radii (Sb-C 3.9 Å, Sb-N 3.8 Å)[222] (Figure 75). Additionally, the B(1)-C(38) bond distance (1.601(8) Å) is slightly shorter than that measured for *p*-$(Me_3N)C_6H_4(B(CN)Mes_2)$ (*p*-**7**-CN, B-C_{CN} = 1.618(8) Å)[104] or *o*-$(Me_2S)(Mes_2(CN)B)C_6H_4$ (**26**-CN, B-C_{CN} = 1.636(5) Å).[126]

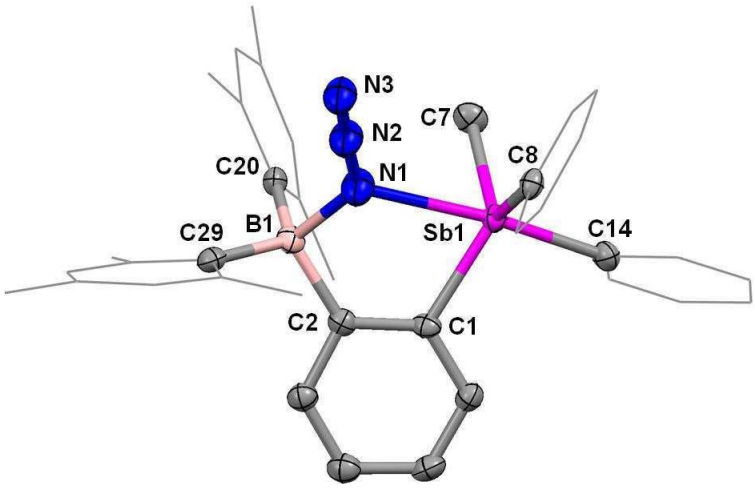

Figure 76. Crystal structure of **54**-N_3. Displacement ellipsoids are scaled to the 50% probability level. Hydrogen atoms have been omitted for clarity and phenyl and mesityl groups are depicted in wireframe. Selected bond lengths (Å) and angles (˚): Sb(1)-C(7) 2.096(5); Sb(1)-C(8) 2.100(4); Sb(1)-C(1) 2.110(4); Sb(1)-C(14) 2.121(4); Sb(1)-N(1) 2.477(4); N(1)-N(2) 1.216(5); N(1)-B(1) 1.623(6); N(2)-N(3) 1.150(5); C(7)-Sb(1)-C(8) 112.01(18); C(7)-Sb(1)-C(1) 120.31(18); C(8)-Sb(1)-C(1) 118.48(16); C(14)-Sb(1)-N(1) 174.10(15); N(2)-N(1)-B(1) 127.6(4); N(2)-N(1)-Sb(1) 122.9(3); C(2)-B(1)-C(20) 116.3(3); C(2)-B(1)-C(29) 109.6(4); C(20)-B(1)-C(29) 116.6(4).

On the other hand, the structure of **54**-N_3 clearly shows that the terminal azide N atom is engaged in a B-N-Sb bridging interaction (Figure 76). The B(1)-N(1) bond distance (1.623(6) Å) in **54**-N_3 is very similar to that measured for the phosphonium analog **25**-N_3 (1.623(4) Å). However, the Sb(1)-N(1) distance (2.477(4) Å) is significantly shorter than the corresponding P-N bond distance (2.790(2) Å)[124] and only marginally longer than the Sb-N distance in $Ph_4Sb(N_3)$ (2.373(3) Å).[237] Similar to **54**-F, the antimony center in **54**-N_3 adopts a distorted trigonal bipyramidal geometry defined by C(14)-Sb(1)-F(1) = 174.10(15)˚ and $\Sigma(C_{eq}–Sb–C_{eq})$ = 350.8˚.

The geometries of **54**-CN and **54**-N_3 were optimized using density functional theory (DFT) methods (B3LYP functional with the mixed basis set: aug-cc-pvTz-pp for Sb, 6-

31+g(d') for B, N, and F, 6-31g for C, H). The resulting geometries closely matched those determined experimentally, and no imaginary frequencies were calculated at the optimized structures. To probe the role of the stibonium group in assisting cyanide and azide anion binding, Atoms in Molecules (AIM) analysis and Natural Bond Order (NBO) calculations were performed at the optimized geometries. For **54**-CN, the AIM calculation located a bond path between Sb and the N atom of the boron-bound cyanide anion with an electron density of $\rho(r) = 1.95 \times 10^{-2}$ e bohr^{-3} at the BCP. In the case of **54**-N_3, the AIM calculation identified the bond path between Sb and the bridging azide N atom with $\rho(r) = 4.31 \times 10^{-2}$ e bohr^{-3} at the BCP. Although the electron density at the BCP of the Sb-N bond in **54**-N_3 is comparable to that calculated for the Sb-F bond in **54**-F (4.26×10^{-2} e bohr^{-3}), these values are a factor of two greater than that calculated at the BCP between Sb and N in **54**-CN. This observation is in line with the long Sb-C_{CN} and Sb-N_{CN} distances observed in the solid state structure of **54**-CN, as well as with the absence of a nonbonding lone pair on the cyanide anion. The presence of a weak $\pi_{(CN)} \rightarrow \sigma^*_{(S\text{-}C)}$ interaction in **26**-F has been proposed to contribute to the high cyanide affinity of the *o*-sulfonium borane [**26**]$^+$, suggesting that the Sb-N_{CN} bond path calculated for **54**-CN may be due to a similar $\pi_{(CN)} \rightarrow \sigma^*_{(Sb\text{-}C)}$ interaction.[126]

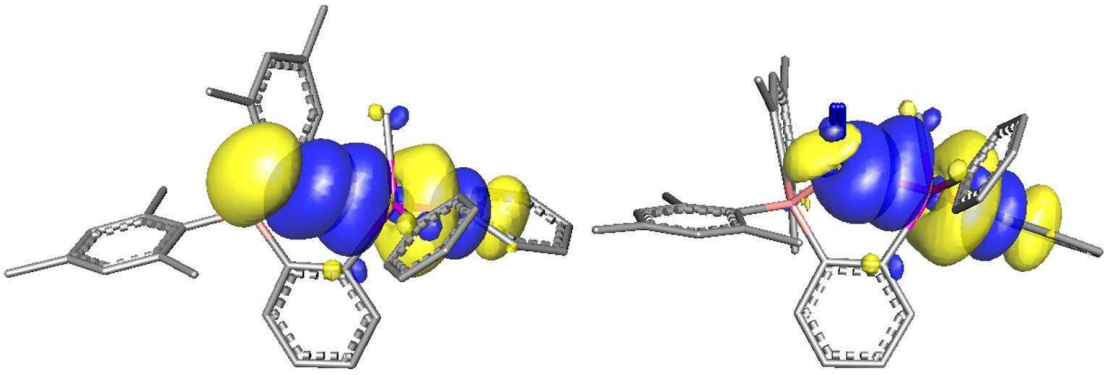

Figure 77. Plots of the NBO donor-acceptor interactions calculated for **54**-CN (left) and **54**-N_3 (right). Density isovalues are set to 0.03, and hydrogen atoms have been omitted for clarity.

An NBO analysis performed on **54**-CN confirms the presence of a weak $\pi_{(CN)} \rightarrow \sigma^*_{(Sb-C)}$ interaction whose deletion affords an increase in the energy of the molecule by 3.54 kcal mol^{-1} (Figure 77). In **54**-N_3, NBO analysis located a $lp_{(N)} \rightarrow \sigma^*_{(Sb-C)}$ donor-acceptor interaction whose deletion resulted in an increase in the total energy of the molecule by 15.15 kcal mol^{-1}. This value is very close to that calculated from deletion of the $lp_{(F)} \rightarrow \sigma^*_{(Sb-C)}$ (E_{del} = 15.18 kcal mol^{-1}) interaction in **54**-F and significantly greater than the $lp_{(N)} \rightarrow \sigma^*_{(P-C)}$ (E_{del} = 5.8 kcal mol^{-1}) donor-acceptor interaction in the phosphonium analog **25**-N_3.[124] Altogether, these results support the notion of an increased Lewis acidity of bifunctional onium/boron anion receptors upon moving to heavier main group onium ions, and this effect can be attributed to a greater energetic/spatial accessibility of the accepting $\sigma^*_{(E-C)}$ orbital.

4.3 Synthesis and structure of a bifunctional boron/antimony Lewis acid with a *peri*-napthalene backbone

Next, we decided to investigate the synthesis a stibonium analog of [**29**]$^+$. The synthesis of the bismuth/boron compound **56** had been previously carried out by Mohammed Saber via the reaction of tetrakis(thf)lithium dimesityl-1,8-naphthalenediylborate with Ph_2BiCl (Figure 78). Consequently, the antimony/boron derivative **55** was synthesized using a similar protocol. The ^1H NMR spectra of both compounds displayed six distinct signals corresponding to the methyl groups of the boron mesityl substituents. The unsymmetrical nature of the mesityl groups suggests significant steric crowding between the dimesityl boryl and diphenyl pnictogen groups brought into close proximity by the 1,8-naphthalenediyl backbone. However, broad signals appearing at 66 and 68 ppm in the ^{11}B NMR spectra of **55** and **56**, respectively, are typical for triarylboranes and suggest that the boron centers remain largely trigonal planar, without significant electron-pair donation from the stibine and bismuthane groups.

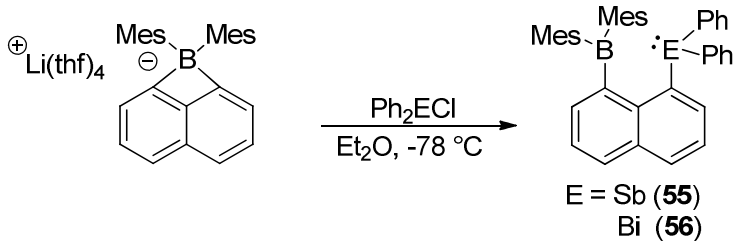

Figure 78. Synthesis of compounds **55** and **56**.

In an effort to obtain the stibonium analog of [**29**]$^+$, we reacted **55** with MeOTf under various conditions. However, these attempts at methylation were unsuccessful and only resulted in decomposition of the compound. Based on the ^{1}H NMR data for **55** and **56**, we surmised that steric crowding due to the close proximity of the bulky dimesitylboryl and diphenylstibine groups prevented the formation of a stable methylated derivative of **55**. However, this did not preclude the possibility that a Sb→B donor-acceptor interaction, enforced by the 1,8-naphthalenediyl backbone, could also play a role in passivating the Sb lone pair. To establish the presence of any unusual E→B (E = Sb, Bi) interactions, the X-ray crystal structures of **55** and **56** were determined (Figure 79 and Figure 80).

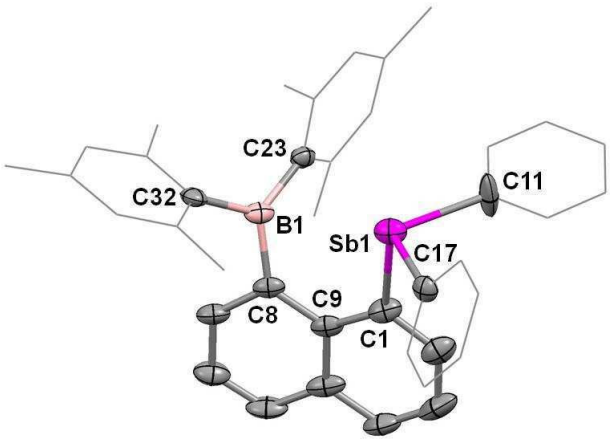

Figure 79. Crystal structure of **55**. Ellipsoids are scaled to the 50% probability level. Phenyl and mesityl groups have been depicted in wireframe, and hydrogen atoms have been omitted for clarity. Selected bond lengths (Å) and angles (°): Sb(1)-C(17) 2.143(4), Sb(1)-C(1) 2.157(6), Sb(1)-C(11) 2.241(3), C(9)-C(1)-Sb(1) 122.5(4), C(9)-C(8)-B(1) 130.2(5), C(32)-B(1)-C(23) 121.3(5), C(32)-B(1)-C(8) 114.9(5), C(23)-B(1)-C(8) 122.5(5).

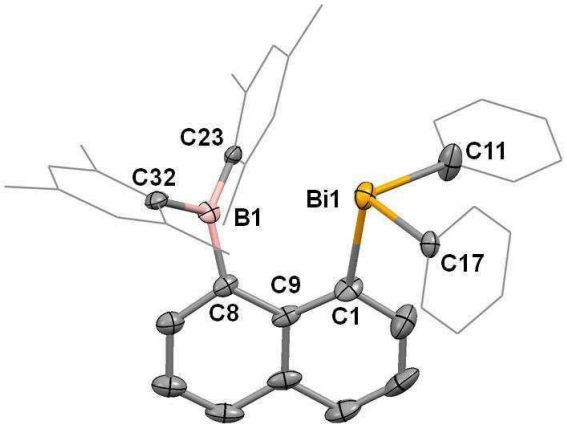

Figure 80. Crystal structure of **56.** Ellipsoids are scaled to the 50% probability level. Phenyl and mesityl groups have been depicted in wireframe, and hydrogen atoms have been omitted for clarity. Selected bond lengths (Å) and angles (˚): Bi(1)-C(17) 2.266(6), Bi(1)-C(1) 2.268(6), Bi(1)-C(11) 2.298(5), C(9)-C(1)-Bi(1) 123.9(4), C(9)-C(8)-B(1) 130.6(5), C(8)-B(1)-C(32) 115.1(5), C(8)-B(1)-C(23) 122.3(5), C(32)-B(1)-C(23) 121.8(5).

Both structures exhibited similar crystal packing, with both compounds crystallizing in the space group P-1 with two molecules of **55** and **56** and one molecule of solvent per unit cell. The E→B (E = Sb, Bi) distances of 3.216 Å for **55** and 3.330 Å for **56** are longer than the sum of the covalent radii (Sb-B 2.23 Å, Bi-B 2.32 Å)[236] but shorter than the sum of the van der Waals radii (Sb-B 4.0 Å, Bi-B 4.1 Å)[222] of the two elements. Despite the short E→B distances, the geometry around the boron centers remains trigonal planar, as indicated by the sum of the C-B-C (C = C8, C23, C32) angles of 358.7˚ for **55** and 359.2˚ for **56**. Evidence for steric crowding between the diphenyl pnictogen and dimesityl boryl substituents in these structures can be seen from the deviation of the E-C1-C9 (E = Sb1, Bi1; 122.5(4)˚ for **55**, 123.9(4)˚ for **56**), B1-C8-C9 (130.2(5)˚ for **55**, 130.6(5)˚ for **56**), and C1-C9-C8 (124.0(5)˚ for **55**, 124.6(5)˚ for **56**) angles from the ideal 120˚. As a last remark on the structure of these compounds, we

note that the E1-C1 bonds of **55** (2.157(6) Å) and **56** (2.268(6) Å) are significantly longer that the C8-B1 bond lengths (1.589(8) Å in **55** and 1.575(9) Å in **56**). In turn, the positioning of the group 15 elements above the naphthalenediyl platform may preclude strong interaction with the boron atom.

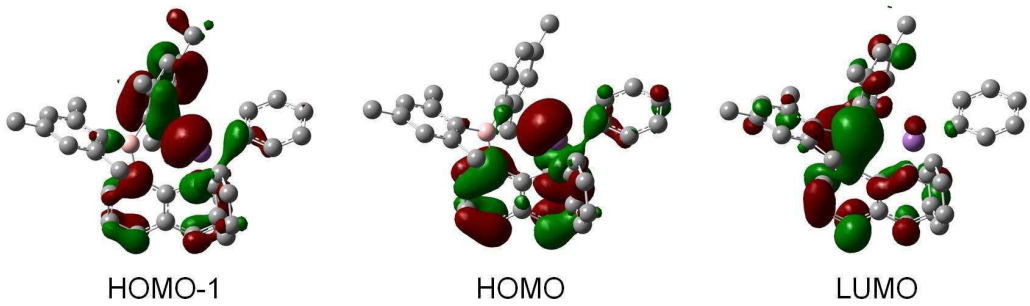

Figure 81. Frontier molecular orbitals of **55**.

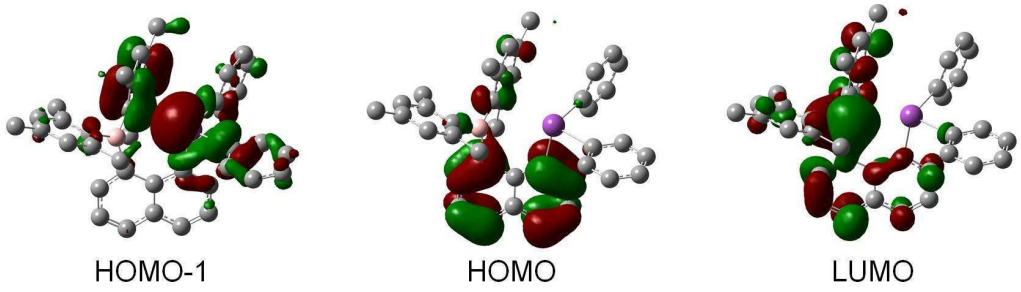

Figure 82. Frontier molecular orbitals of **56**.

In order to fully understand the nature of the E→B interactions present in these compounds, DFT calculations, including full geometry optimization and Natural Bond Order (NBO) analysis, were carried out. All calculations were performed using the Gaussian03 program with B3LYP functional and the mixed basis set: 6-31g for C and H,

6-31+g(d′) basis set for B, and Stuttgart RSC 1997 ECP for Sb and Bi. The results of the geometry optimizations, starting from the crystal structure geometries, were in good agreement with those observed experimentally. The Sb-B and Bi-B distances of 3.410 Å and 3.448 Å, respectively, measured in the optimized structures of **55** and **56** are slightly longer than the distances observed in the crystal structures. Inspection of the frontier molecular orbitals of **55** and **56** shows that, in both cases, the lowest unoccupied molecular orbital (LUMO) bears a significant contribution from the empty B p-orbitals (Figure 81 and Figure 82). The HOMO and HOMO-1 of **55** both contain contributions from the predominantly 5s lone pair of the Sb atom. However, for **56**, the Bi 6s lone pair contribution is found solely in the HOMO-1, whereas the density in the HOMO is localized on the naphthalene π-system. The presence of weak E→B interactions was confirmed by NBO analysis performed at the optimized geometry. This analysis identifies donor-acceptor interactions involving the pnictogen lone-pairs as donors and the empty boron p-orbital as the acceptor in both molecules (Figure 83). Deletion calculations carried out by zeroing the Kohn-Sham matrix elements corresponding to the lp(E)→p(B) interactions using the NBO program led to an increase in the total energy of the molecules by 8.65 kcal/mol for **55** and 6.32 kcal/mol for **56**. For comparison, we attempted a DFT optimization of intermolecular, Lewis acid-base adduct model complexes of the form $Ph_3E{\rightarrow}BPh_3$ (E = Sb, Bi), which resulted in divergence of the E-B distances to well outside the sum of the van der Waals radii of the elements. These results indicate that the E→B interactions present in **55** and **56** are enforced by the bridging 1,8-naphthalenediyl linker and should be regarded as weak, second order,

donor-acceptor interactions. Indeed, the only crystallographically characterized Lewis acid-base adducts involving stibanes/bismuthanes and boranes are of the formula $(Me_3Si)_3Sb{\rightarrow}BX_3$ (X = Cl, Br, I) and contain Sb-B bond lengths in the range 2.257-2.268 Å,[238] which is considerably shorter than that found in **55**.

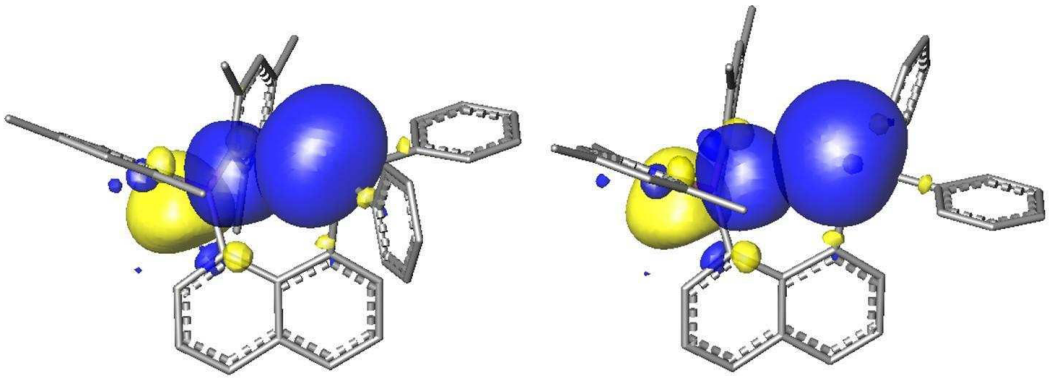

Figure 83. Plots of the NBO donor-acceptor interactions calculated for **55** (left) and **56** (right). Density isovalues are set to 0.03, and hydrogen atoms have been omitted for clarity.

4.4 Conclusions

The results presented in this chapter demonstrate that a vast enhancement in the anion affinity of cationic bidentate boranes is achieved by the introduction of a tetraorganostibonium moiety as a secondary binding site. The Lewis acidity of the stibonium center allows it to engage fluoride and azide in strong donor-acceptor interactions, making $[\mathbf{54}]^+$ a potent bidentate Lewis acid for chelation of these anions. Although $[\mathbf{54}]^+$ effectively binds cyanide anions via complexation to the boron atom, chelation effects are minimal and limited to a weak $\pi_{(CN)} \rightarrow \sigma^*_{(Sb\text{-}C)}$ interaction. Attempts

to prepare an stibonium analog of [**28**]$^+$/[**29**]$^+$ were unsuccessful, most likely due to steric crowding brought about by the narrow bite angle of the 1,8-napthalenediyl backbone. However, the neutral stibine analog **55,** as well as the bismuthine derivative **56,** were synthesized, and this same structural feature was shown to give rise to the formation of weak E→B (E = Sb, Bi) interactions.

4.5 Experimental

General Considerations. *o*-(Ph_2Sb)BrC_6H_4 was prepared according to procedures reported in the literature.[233] Dimesitylboronfluoride (Mes_2BF), tetrabutylammonium cyanide (TBACN), and tetrabutylammonium azide were purchased from Aldrich and used as received. *n*-$Bu_4NF{\cdot}3H_2O$ (TBAF) and 1,2-dibromobenzene were purchased from Alfa Aesar and used as received. Tetrakis(thf)lithium dimesityl-1,8-naphthalenediylborate [117], diphenylchlorostibine [239], and diphenylchlorobismuthane [240] were prepared according to the literature. Solvents were dried by passing through an alumina column (*n*-hexane, CH_2Cl_2) or refluxing under N_2 over Na/K (Et_2O and THF). $CHCl_3$ and $CDCl_3$ were dried by refluxing and distilling over P_2O_5 under an atmosphere of N_2. Methanol was distilled from NaOMe and stored over Linde type 4A molecular sieves. All other solvents were ACS reagent grade and used as received. Air-sensitive compounds were handled under a N_2 atmosphere using standard Schlenk and glovebox techniques. UV-vis spectra were recorded on an Ocean Optics USB4000 spectrometer with an Ocean Optics ISS light source. Elemental analyses were performed at Atlantic Microlab (Norcross, GA). NMR spectra were recorded on a Varian Unity Inova 400 FT NMR (399.59 MHz for ^{1}H, 375.99 MHz for ^{19}F, 128.19 MHz for ^{11}B, 100.45 MHz for

^{13}C) spectrometer at ambient temperature unless otherwise stated. Chemical shifts δ are given in ppm and are referenced against external Me_4Si (^{1}H, ^{13}C) and $BF_3 \cdot Et_2O$ (^{11}B, ^{19}F).

Crystallography. Single crystals of **54**-F, **54**-CN, and **54**-N_3 were obtained by addition of 1 equiv. of TBAF, TBACN, or $TBAN_3$, respectively, to solutions of [**54**]OTf in $CHCl_3$ and subsequent layering with methanol. The details of the data collection and structure refinement for **54**-F, **54**-CN, and **54**-N_3 are included in Table 11. Single crystals of **55** were obtained by slow evaporation of a solution of the compound in 4:1 CH_2Cl_2/MeOH. Single crystals of **56** were obtained by cooling a solution of the compound in 2:1 benzene/pentane. The details of the data collection and structure refinement for **55** and **56** are included in Table 12.

The crystallographic measurements were performed using a Bruker-AXS APEX-II CCD area detector diffractometer, with a graphite-monochromated Mo-Kα radiation (λ = 0.71069 Å). A specimen of suitable size and quality was selected and mounted onto a nylon loop. The semiempirical method SADABS[207] was applied for absorption correction. The structures were solved by direct methods using SHELXTL/PC package (version 6.1)[208] which successfully located most of the non-hydrogen atoms. Subsequent refinement on F^2 allowed location of the remaining non-hydrogen atoms. All H atoms were geometrically placed and refined in a riding model approximation. During the structure refinement of compounds **55** and **56**, we found disorder in one of the phenyl groups. To correct this disorder, we restrained the structure parameters of these rings to the ideal geometries (C-C bond length 1.390(1)Å and C-C-C bond angles 120.0(1)º).

Table 11. Crystal data, data collections, and structure refinements for **54**-F, **54**-CN, and **54**-N_3.

Crystal data	**54**-F	**54**-CN	**54**-N3
Formula	$C_{37}H_{39}BFSb\cdot 0.5CH_2Cl_2$	$C_{38}H_{39}BNSb$	$C_{37}H_{39}BN_3Sb$
Mr	677.71	642.26	658.27
Crystal size/mm	0.20 x 0.10 x 0.05	0.14 x 0.10 x 0.07	0.20 x 0.10 x 0.05
Crystal system	Monoclinic	Monoclinic	Monoclinic
Space group	P2(1)/c	P2(1)/c	P2(1)/c
a/Å	9.0227(2)	16.247(7)	17.154(8)
b/Å	16.3360(4)	9.307(4)	11.271(5)
c/Å	22.9463(5)	25.233(8)	19.904(7)
α /°	90	90	90
β/°	101.6910(10)	124.732(19)	124.47(3)
γ /°	90	90	90
V/Å^3	3312.00(13)	3136(2)	3173(2)
Z	4	4	4
ρ_{calc}/g cm^{-3}	1.359	1.360	1.378
μ/mm^{-1}	0.944	0.907	0.900
F(000)	1388	1320	1352
T/K	110(2)	110(2)	110(2)
Scan mode	ω, φ	ω, φ	ω, φ
hkl Range	-12 → +11	-20 → +20	-20 → +20
	-21 → +21	-11 → +11	-13 → +13
	-30 → +29	-31 → +31	-23 → +23
Measd reflns	38889	31589	26214
Unique reflns [R_{int}]	8141 [0.0432]	6160 [0.0754]	5566 [0.0517]
Reflns used for refinement	8141	6160	5566
Refined parameters	392	364	367
GooF	1.015	1.023	1.029
*R*1,[a] *wR*2[b] (all data)	0.0614, 0.1377	0.0676, 0.1514	0.0536, 0.1261
ρ_{fin} (max., min.)/eÅ^{-3}	2.106, -0.803	1.259, -1.094	1.950, -1.799

[a] $R1 = \Sigma||F_o| - |F_c||/\Sigma|F_o|$. [b] $wR2$ $([\Sigma w(F_o^2 - F_c^2)^2]/[\Sigma\, w(F_o^2)^2])^{1/2}$; $w = 1/[\sigma^2(F_o^2) + (ap)^2 + bp]$; $p = (F_o^2 + 2F_c^2)/3$ with a = 0.0743 for **54**-F, 0.0951 for **54**-CN, and 0.0773 for **54**-N_3; and b = 8.8571 for **54**-F, 0 for **54**-CN, and 3.4228 for **54**-N_3.

Table 12. Crystal data, data collections, and structure refinements for **55** and **56**.

Crystal data	**55**	**56**
Formula	$C_{40}H_{38}BSb \cdot 0.5CH_3OH$	$C_{40}H_{38}BBi \cdot 0.5C_6H_6$
Mr	667.28	777.55
Crystal size/mm	0.19 x 0.07 x 0.06	0.18 x 0.11 x 0.08
Crystal system	Triclinic	Triclinic
Space group	P-1	P-1
a/Å	9.0107(6)	9.027(6)
b/Å	12.5580(9)	12.452(8)
c/Å	16.1242(10)	16.467(10)
α /°	72.755(4)	73.787(10)
β/°	76.087(4)	74.456(10)
γ /°	78.953(4)	78.023(11)
V/Å^3	1677.10(19)	1694.6(19)
Z	2	2
ρ_{calc}/g cm^{-3}	1.321	1.524
μ/mm^{-1}	0.851	5.231
F(000)	686	774
T/K	110(2)	110(2)
Scan mode	ω, φ	ω, φ
hkl Range	-10 → +10	-9 → +11
	-14 → +14	-15 → +15
	-19 → +19	-20 → +20
Measd reflns	24958	12660
Unique reflns [Rint]	5876 [0.0405]	6567 [0.0435]
Reflns used for refinement	5876	6567
Refined parameters	386	413
GooF	1.018	1.047
R1,[a] *w*R2[b] (all data)	0.0761, 0.1793	0.0554, 0.1022
ρ_{fin} (max., min.)/eÅ^{-3}	2.008, -1.862	1.490, -1.704

[a] $R1 = \Sigma||F_o| - |F_c||/\Sigma|F_o|$. [b] $wR2$ $([\Sigma w(F_o^2 - F_c^2)^2]/[\Sigma w(F_o^2)^2])^{1/2}$; $w = 1/[\sigma^2(F_o^2) + (ap)^2 + bp]$; $p = (F_o^2 + 2F_c^2)/3$ with $a = 0.0985$ for **55** and 0.0504 for **56**; and $b = 9.2927$ for **55**, and 0 for **56**.

Theoretical Calculations. Density functional theory (DFT) calculations (full geometry optimization) were carried out on [**54**]$^+$, **54**-F, **54**-CN, and **54**-N_3 starting from the crystal structure geometries with *Gaussian09*[241] and utilizing the gradient-corrected Becke exchange functional (B3LYP) and the Lee-Yang-Parr correlation functional.[242,243] A 6-31+g(d') basis set was used for B, N, and F[244] and 6-31g basis set for C, H.[245] An aug-cc-pvTz-pp basis set[246] was used for Sb. A list of selected bond lengths from the X-ray and DFT optimized structures of these complexes is included in Table 13. The DFT calculations carried out on **55** and **56** were performed using the Gaussian03 program with the B3LYP functional and the mixed basis set: 6-31g for C and H, 6-31+g(d′) for B, and Stuttgart RSC 1997 ECP for Sb and Bi.[247] Frequency calculations were also carried out on the optimized geometry and showed no imaginary frequencies. The electron density of the DFT optimized structures of **54**-F, **54**-CN, and **54**-N_3 were subjected to Atoms-In Molecules analysis[248] using AIM2000.[249] The Natural Bond Orbital (NBO) analysis of **54**-F, **54**-CN, **54**-N_3 , **55** and **56** was carried out using the NBO v3.1 program implemented in Gaussian.[250] The relative enthalpies of [**54**]$^+$, [**25**]$^+$, **54**-F, and **25**-F were calculated using energies obtained from single point calculations carried out at the optimized geometries. Energies were corrected to enthalpy by the "thermal correction to enthalpy" term obtained from the frequency calculations. Single point calculations were performed using the aug-cc-pvTz-pp basis set for Sb and a 6-311+g(d,p) basis set[251,252] for C, H, B, and F.

Table 13. Selected bond lengths in Å from the X-ray and DFT optimized structures of **54**-F, **54**-CN, and **54**-N_3.

	54-F	
	X-Ray	DFT
B(1)-F(1)	1.521(4)	1.587
Sb(1)-F(1)	2.450(4)	2.402

	54-CN	
	X-Ray	DFT
B(1)-C(38)	1.601(8)	1.617
Sb(1)-C(38)	2.943(7)	3.093
Sb(1)-N(1)	3.093(5)	2.938

	54-N_3	
	X-Ray	DFT
B(1)-N(1)	1.623(6)	1.686
Sb(1)-N(1)	2.477(4)	2.522

Synthesis of *o*-(Ph_2Sb)(Mes_2B)C_6H_4. *tert*-Butyllithium (2.7 mL, 4.6 mmol) in pentane was added to a solution of *o*-(Ph_2Sb)BrC_6H_4 (1.0 g, 2.3 mmol) in Et_2O (15 mL) at -78 ˚C. The reaction mixture was allowed to stir for 1.5 hrs at this temperature before adding a solution of Mes_2BF (0.62 g, 2.3 mmol) in Et_2O (10 mL). The reaction mixture was then slowly warmed to room temperature and stirred for an additional 4 hrs. After removing the solvent *in vacuo*, the residue was extracted with CH_2Cl_2/hexanes (20 mL/20 mL) and filtered over Celite. The filtrate was concentrated *in vacuo*, and the resulting residue was recrystallized from a Et_2O/MeOH (10 mL/10 mL) solution at -40 ˚C overnight to yield colorless crystals of *o*-(Ph_2Sb)(Mes_2B)C_6H_4 (1.0 g, 68 % yield, purity >90% based on ^{1}H NMR, see Figure 84). This compound was characterized by

multinuclear NMR and used without further purification. ^{1}H NMR (399.9 MHz, $CDCl_3$): δ 1.48 (brs, 3H, *o*-Mes-C*H*$_3$), 2.03 (brs, 6H, *p*-Mes-C*H*$_3$), 2.12 (brs, 3H, *o*-Mes-C*H*$_3$), 2.17 (brs, 3H, *o*-Mes-C*H*$_3$), 2.29 (brs, 3H, *o*-Mes-C*H*$_3$), 6.14 (brs, 1H, Mes-C*H*), 6.79 (brs, 3H, Mes-C*H*), 7.18-7.30 (m, 10H SbPh + 2H *o*-C_6H_4), 7.36 (m, 1H, *o*-C_6H_4), 7.42 (m, 1H, *o*-C_6H_4). ^{13}C NMR (100.5 MHz, $CDCl_3$): δ 21.25 (*p*-Mes-*C*H_3), 22.47 (*o*-Mes-*C*H_3), 23.08 (*o*-Mes-*C*H_3), 23.83 (*o*-Mes-*C*H_3), 24.28 (*o*-Mes-*C*H_3), 128.11, 128.35, 129.02, 130.50, 135.12, 135.97, 137.61, 138.63, 138.86, 140.21, 141.37, 141.66, 142.63, 143.14, 145.96, 157.43. ^{11}B NMR (128.2 MHz, $CDCl_3$): δ +76.75.

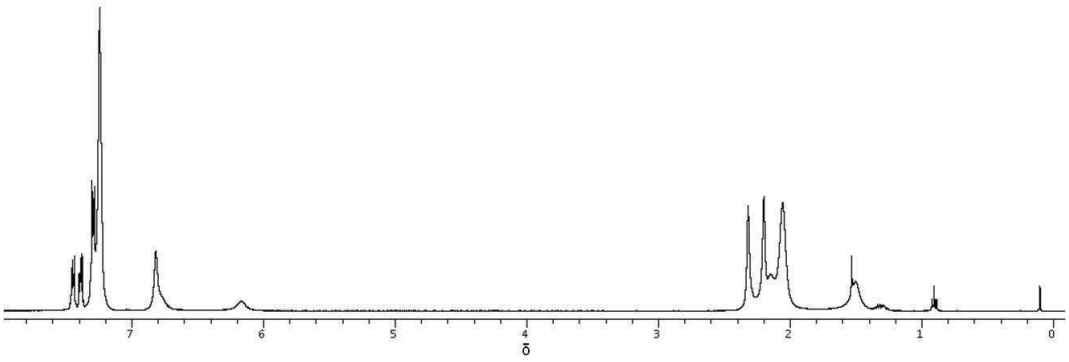

Figure 84. ^{1}H NMR spectrum of *o*-(Ph_2Sb)($BMes_2$)C_6H_4 in $CDCl_3$. The peaks appearing below 1.4 ppm are assigned to pentane solvent and grease impurites.

Synthesis of [54]OTf. MeOTf (0.38 mL, 3.33 mmol) was added to a suspension of *o*-(Ph_2Sb)(Mes_2B)C_6H_4 (1.0 g, 1.66 mmol) in Et_2O (5 mL). The mixture was allowed to stir in a sealed flask at room temperature for 24 hrs, after which the solid was filtered and washed with Et_2O (3 × 5 mL) to afford [**54**]OTf as a moisture sensitive white solid (0.70 g, 55%). ^{1}H NMR (399.9 MHz, $CDCl_3$): δ 1.34 (s, 3H, *o*-Mes-C*H*$_3$), 1.70 (s, 6H,

p-Mes-C*H*$_3$), 1.91 (s, 3H, Sb-C*H*$_3$), 1.96 (brs, 3H, *o*-Mes-C*H*$_3$), 2.24 (s, 6H, *o*-Mes-C*H*$_3$), 6.59 (s, 1H, Mes-C*H*), 6.71 (s, 1H, Mes-C*H*), 6.75 (s, 1H, Mes-C*H*), 6.78 (s, 1H, Mes-C*H*), 7.35 (m, 2H, *o*-C_6H_4), 7.50-7.63 (m, 10H, SbPh + *o*-C_6H_4), 7.67 (m, 2H, *o*-C_6H_4). ^{13}C NMR (100.5 MHz, $CDCl_3$): δ 2.34 (Sb-*C*H$_3$), 21.16 (*p*-Mes-*C*H$_3$), 21.33 (*p*-Mes-*C*H$_3$), 22.32 (*o*-Mes-*C*H$_3$), 23.08 (*o*-Mes-*C*H$_3$), 24.16 (*o*-Mes-*C*H$_3$), 25.21 (*o*-Mes-*C*H$_3$), 124.99, 125.41, 128.62, 128.80, 129.47, 130.31, 130.54, 132.59, 132.72, 132.95, 133.10, 134.50, 134.77, 138.61, 139.14, 139.62, 140.13, 140.88, 141.23, 141.34, 142.80, 143.90, 144.62, 153.82. ^{11}B NMR (128.2 MHz, $CDCl_3$): δ +80.19. Anal. calcd for $C_{38}H_{39}BO_3F_3SSb$: C, 59.63; H, 5.14. Found: C, 59.99; H, 5.21.

Generation of 54-F, 54-CN, 54-N$_3$. Addition of 1 equiv. of TASF, TBACN, or $TBAN_3$ to solutions of [**54**]OTf in $CDCl_3$ resulted in quantitative conversion to the adducts **54**-F, **54**-CN, and **54**-N_3, respectively, as determined by multinuclear NMR experiments. The solid products could be precipitated as colorless, microcrystalline solids by addition of MeOH to these samples. Data for **54**-F: ^{1}H NMR (399.9 MHz, $CDCl_3$): δ 1.34 (d, 3H, Sb-C*H*$_3$, $J_{H\text{-}F}$ = 2.38 Hz), 1.76 (brs, 12H, *p*-Mes-C*H*$_3$), 2.16 (s, 6H, *o*-Mes-C*H*$_3$), 6.56 (s, 4H, Mes-C*H*), 7.11 (t, 1H, *o*-C_6H_4, $^3J_{H\text{-}H}$ = 7.32 Hz), 7.17 (d, 1H, *o*-C_6H_4, $^3J_{H\text{-}H}$ = 7.51 Hz), 7.27 (t, 1H, *o*-C_6H_4, $^3J_{H\text{-}H}$ = 7.32 Hz), 7.43-7.52 (m, 10H SbPh + 1H *o*-C_6H_4). ^{13}C NMR (100.5 MHz, $CDCl_3$): δ 4.83 (d, Sb-*C*H$_3$, $J_{C\text{-}F}$ = 16.02 Hz), 20.80 (*p*-Mes-*C*H$_3$), 24.49 (*o*-Mes-*C*H$_3$), 125.70, 126.31 (d, $J_{C\text{-}F}$ = 12.21 Hz), 128.63, 129.15, 129.32, 129.64, 131.26 (d, $J_{C\text{-}F}$ = 5.34 Hz), 133.32, 133.76, 134.09, 136.79 (d, $J_{C\text{-}F}$ = 6.11 Hz), 140.71 (br), 149.76 (br), 169.56 (br). ^{19}F NMR (375.97 MHz, $CDCl_3$): δ -161.41. ^{11}B NMR (128.2 MHz, $CDCl_3$): δ +7.51. Anal. calcd for

$C_{37}H_{39}BFSb$: C, 69.95; H, 6.19. Found: C, 69.90; H, 6.09. Data for **54**-CN: ^{1}H NMR (399.9 MHz, $CDCl_3$): δ 1.52 (brs, 3H, *o*-Mes-C*H*$_3$), 1.56 (s, 3H, Sb-C*H*$_3$), 1.72 (brs, 3H, *o*-Mes-C*H*$_3$), 2.22 (brs, 6H, *p*-Mes-C*H*$_3$), 2.27 (brs, 6H, *o*-Mes-C*H*$_3$), 6.61 (brs, 1H, Mes-C*H*), 6.66 (brs, 1H, Mes-C*H*), 6.76 (brs, 1H, Mes-C*H*), 6.79 (brs, 1H, Mes-C*H*), 7.09 (t, 1H, *o*-C_6H_4, $^{3}J_{H\text{-}H}$ = 7.32 Hz), 7.21 (m, 2H, *o*-C_6H_4), 7.36 (brm, 2H, SbPh), 7.40 (d, 1H, *o*-C_6H_4, $^{3}J_{H\text{-}H}$ = 7.69 Hz), 7.44-7.53 (m, 8H, SbPh). ^{13}C NMR (100.5 MHz, $CDCl_3$): δ 9.57 (Sb-*C*H_3), 20.79 (*p*-Mes-*C*H_3), 24.57 (*o*-Mes-*C*H_3), 24.76 (*o*-Mes-*C*H_3), 25.65(*o*-Mes-*C*H_3), 25.98 (*o*-Mes-*C*H_3), 125.63, 127.53, 129.01, 129.23, 129.45, 130.00, 130.26, 130.55, 131.13, 131.68, 131.89, 133.11, 133.80, 134.34, 134.75, 139.07, 140.92, 142.86, 143.54, 145.37, 150.25(br), 166.00 (br). ^{11}B NMR (128.2 MHz, $CDCl_3$): δ -11.67. Anal. calcd for $C_{38}H_{39}BNSb$: C, 71.06; H, 6.12. Found: C, 70.54; H, 6.12. Data for **54**-N_3: ^{1}H NMR (399.9 MHz, $CDCl_3$): δ 1.32 (s, 3H, Sb-C*H*$_3$), 1.83 (brs, 12H, *p*-Mes-C*H*$_3$), 2.20 (s, 6H, *o*-Mes-C*H*$_3$), 6.67 (s, 4H, Mes-C*H*), 7.02 (dd, 1H, *o*-C_6H_4, $^{3}J_{H\text{-}H}$ = 7.69 Hz, $^{4}J_{H\text{-}H}$ = 0.92 Hz), 7.08 (ddd, 1H, *o*-C_6H_4, $^{3}J_{H\text{-}H}$ = 7.69 Hz, $^{4}J_{H\text{-}H}$ = 1.65 Hz), 7.25 (ddd, 1H, *o*-C_6H_4, $^{3}J_{H\text{-}H}$ = 7.24 Hz, $^{4}J_{H\text{-}H}$ = 1.28 Hz), 7.32 (d, 4H, SbPh, $^{3}J_{H\text{-}H}$ = 6.80 Hz), 7.43-7.53 (m, 1H *o*-C_6H_4 + 6H SbPh). ^{13}C NMR (100.5 MHz, $CDCl_3$): 6.28 (Sb-*C*H_3), 20.76 (*p*-Mes-*C*H_3), 24.67 (*o*-Mes-*C*H_3), 125.95, 128.53, 129.34, 129.75, 131.03, 131.25, 133.82, 133.91, 134.16, 138.65, 142.42, 147.52, 167.96, (1 *ipso*-C not observed). ^{11}B NMR (128.2 MHz, $CDCl_3$): δ +0.99. Anal. calcd for $C_{37}H_{39}BN_3Sb$: C, 67.51; H, 5.97. Found: C, 67.30; H, 6.03.

Synthesis of 55. A solution of diphenylchloroantimony (0.232 g, 0.745 mmol) in Et_2O (5 mL) was added dropwise to a suspension of tetrakis(thf)lithium dimesityl-1,8-

naphthalenediylborate (0.500 g, 0.745 mmol) in Et_2O (5 mL) at -78 ˚C. The reaction mixture was allowed to warm to room temperature and stirred overnight. The solvent was removed *in vacuo*, and the residue was extracted with 20 mL of CH_2Cl_2 and filtered over Celite. The filtrate was concentrated to *ca.* 5 mL, and the product was precipitated by slow addition of MeOH (5 mL). The solid was filtered and washed with MeOH (3 × 5 mL) to yield 343 mg (71 %) of the pure product as an off-white solid. Single crystals suitable for X-ray diffraction were obtained by slow evaporation of a solution of the compound in 4:1 CH_2Cl_2:MeOH. Anal. Calcd. for $C_{40}H_{38}BSb$: C, 73.76; H, 5.88. Found: C, 73.65 H, 5.72. ^{1}H NMR (399.9 MHz, $CDCl_3$): δ 0.81 (s, 3H, Mes-*CH*$_3$), 1.74 (s, 3H, Mes- *CH*$_3$), 1.90 (s, 3H, Mes-*CH*$_3$), 2.20 (s, 3H, Mes-*CH*$_3$), 2.34 (s, 3H, Mes-*CH*$_3$), 2.61 (s, 3H, Mes-*CH*$_3$), 6.25 (s, 1H, Mes-*CH*), 6.36 (s, 1H, Mes-*CH*), 6.78 (s, 1H, Mes-*CH*), 6.93 (s, 1H, Mes-*CH*), 6.95 (br, 2H, Ph-*CH*), 7.07-7.19 (m, 8H, Ph-*CH*), 7.35-7.40 (m, 2H, Naph-*CH*), 7.51 (dd, 1H, Naph-*CH*, $^3J_{H-H}$ = 6.96 Hz, $^4J_{H-H}$ = 1.10 Hz), 7.59 (dd, 1H, Naph-*CH*, $^3J_{H-H}$ = 6.96 Hz, $^4J_{H-H}$ = 1.10 Hz), 7.87 (dd, 1H, Naph-*CH*, $^3J_{H-H}$ = 8.06 Hz, $^4J_{H-H}$ = 1.28 Hz), 7.91 (dd, 1H, Naph-*CH*, $^3J_{H-H}$ = 8.06 Hz, $^4J_{H-H}$ = 1.28 Hz). ^{13}C NMR (100.5 MHz, $CDCl_3$): δ 21.02, 21.26, 22.80, 23.26, 25.51, 25.61 (6 Mes-*C*H$_3$); 125.87, 126.22, 127.76, 127.92, 128.03, 128.50, 128.90, 129.41, 130.18, 130.34, 133.00, 133.82, 134.99, 135.15, 135.40, 138.86, (Naph/Phenyl/Mes-*C*H); 137.18, 138.37, 139.36, 140.04, 140.63, 141.17, 141.52, 143.56, 144.49, 144.55, 145.16, 152.21 (Mes-*C*-CH3, *ipso*-/*peri*-*C*) . ^{11}B NMR (128.2 MHz, $CDCl_3$): δ 66 (br).

Synthesis of 56. A solution of diphenylchlorobismuth (0.400 g, 1.00 mmol) in THF (20 ml) was added dropwise to a suspension of tetrakis(thf)lithium dimesityl-1,8-

naphthalenediylborate (0.667 g, 1.00 mmol) in Et_2O (10 mL) at -78 ˚C. The reaction mixture was allowed to warm to room temperature and stirred overnight. The solvent was removed *in vacuo*, and the residue was extracted with 20 mL of benzene and filtered over Celite. The yellow filtrate was concentrated to *ca*. 5 mL, and pentane (10 mL) was added. The solution was left at -40 ˚C for 2 days to produce small, yellow crystals of compound **56** (0.260 g, 33% yield). Single crystals suitable for X-ray diffraction were obtained by slow diffusion of pentane into a benzene solution of the compound. Anal. Calcd. for $C_{40}H_{38}BBi$: C, 65.05; H, 5.19, found: C, 65.18 ; H, 5.17. ^{1}H NMR (399.9 MHz, $CDCl_3$): δ 0.91 (s, 3H, Mes-*CH*$_3$), 1.83 (s, 3H, Mes-*CH*$_3$), 2.02 (s, 3H, Mes-*CH*$_3$), 2.24 (s, 3H, Mes-*CH*$_3$), 2.37 (s, 3H, Mes-*CH*$_3$), 2.56 (s, 3H, Mes-*CH*$_3$), 6.39 (s, 1H, Mes-*CH*), 6.57 (s, 1H, Mes-*CH*), 6.84 (s, 1H, Mes-*CH*), 6.97 (s, 1H, Mes-*CH*), 7.21-7.44 (m, 15H, Naph/Ph-*CH*), 7.56-7.59 (d, 1H, Naph-*CH*), 7.63-7.66 (d, 1H, Naph-*CH*), 7.89-7.92 (d, 1H, Naph-*CH*), 7.98-8.0 (d, 1H, Naph-*CH*), 8.25-8.27 (d, 1H, Naph-*CH*). ^{13}C NMR (100.5 MHz, $CDCl_3$): δ 21.06, 21.28, 22.76, 22.99, 25.52, 25.87 (Mes-*CH*$_3$); 125.5, 127.1, 128.5, 128.8, 129, 129.5, 130.0, 130.1, 130.3, 130.8, 135.0, 135.9 (12C, Naph/Ph-*CH*), 127.9, 128.2, 140.0, 140.4 (8C, Ph *o*-/*m*-*C*H); 134.5, 138.0, 141.6, 141.7, 142.1, 143.9 (*C*-CH_3); 141.5, 144.2, 148.3, 149.5 (br, *ipso*-/*peri*-*C*). ^{11}B NMR (128.2 MHz, $CDCl_3$): δ 68 (br).

CHAPTER V

SYNTHESIS AND FLUORIDE BINDING STUDIES OF STIBONIUM/ONIUM DICATIONS

5.1 Introduction

As part of our continuing interest in fluoride and cyanide complexation and sensing in water, we have been drawn to the latent Lewis acidity of main group onium ions. In particular, heteronuclear bidentate Lewis acids containing sulfonium, telluronium, or phosphonium ions proximal to a triarylborane have shown increased anion affinities versus monofunctional triarylborane Lewis acids.[124-126,128] This behavior has been attributed to a combination of Coulombic and chelate effects. In the case of the latter, F→E (E = S, Te, or P) donor-acceptor interactions have been identified in the chelate complexes, confirming the ability of the onium groups to directly assist in anion binding. In addition, a recent study comparing the fluoride receptor strength of bidentate sulfonium- and telluronium-boranes points to significant benefits from incorporation of the heavier main group onium ion.[128]

The previous chapter outlined our investigation of bidentate stibonium/borane Lewis acids and showed that the antimony atom of **54**-F engages in a strong donor acceptor interaction with the bridging fluoride anion. Some early reports indicate that the tetraphenylstibonium cation may be used for the organic solvent/water biphasic extraction of fluoride ions.[163-165] This reactivity relies on the formation of a Sb-F covalent bond or tightly bound ion pair, but it has not been fully exploited within the

context of anion sensing. For this reason, we considered the potential for tetraorganostibonium ions to acts as competent fluoride sensors directly in water. This notion is supported by an inherent Coulombic attraction as well as by the formation of short Sb-F covalent bonds observed in the solid state structures of Ph_4SbF and Ph_3MeSbF.[158,234] In addition, a comparison of these Sb-F bonds to the Sb-X (X = Cl^-, Br^-, and I^-) bonds in Ph_4SbX complexes suggests that the stibonium ion forms a stronger polar covalent bond with fluoride than with other anions.[156,158] This chapter describes our initial efforts to develop tetraorganostibonium ions as water compatible fluoride sensors.

5.2 Fluoride binding study with $[Ph_3MeSb]^+$

As a preliminary test for the viability of tetraorganostibonium cations as fluoride receptors, $[Ph_3MeSb]^+$ ($[\mathbf{57}]^+$) was prepared as the triflate salt by treatment of Ph_3Sb with MeOTf in Et_2O (Figure 85). The ^1H NMR ($CDCl_3$) of $[\mathbf{57}]^+$ displays a singlet at 2.54 ppm, which corresponds to the $SbCH_3$ group. Addition of 1 equiv. of TBAF to $[\mathbf{57}]^+$ in $CDCl_3$ results in the formation of fluorostiborane **57**-F and an upfield shift of the $SbCH_3$ resonance to 1.96 ppm. This change is accompanied by the appearance of a new signal at -77 ppm in the ^{19}F NMR spectrum. To evaluate the fluoride affinity of $[\mathbf{57}]^+$, a UV-Vis titration was carried out. Upon incremental addition of KF (0.006 M, MeOH) to a solution of [**57**]OTf (1.4×10^{-4} M) in THF, a decrease in the absorption band at 264 nm, assigned to the aryl substituent π-π^* transitions, was observed (Figure 86). These changes were fitted to a 1:1 binding isotherm to afford a fluoride binding constant (K_F)

of 8.5(±2.0) × 10^4 M^{-1}. Similar titrations carried out in MeOH or mixed aqueous/organic solvent systems resulted in no changes attributable to fluoride complexation by [**57**]$^+$.

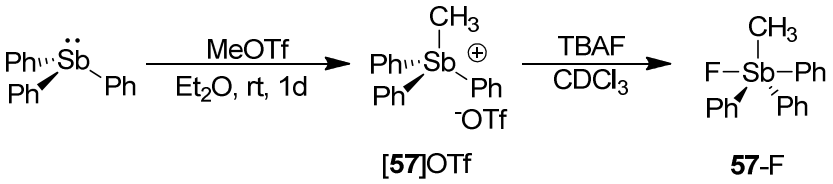

Figure 85. Synthesis of [**57**]OTf and **57**-F.

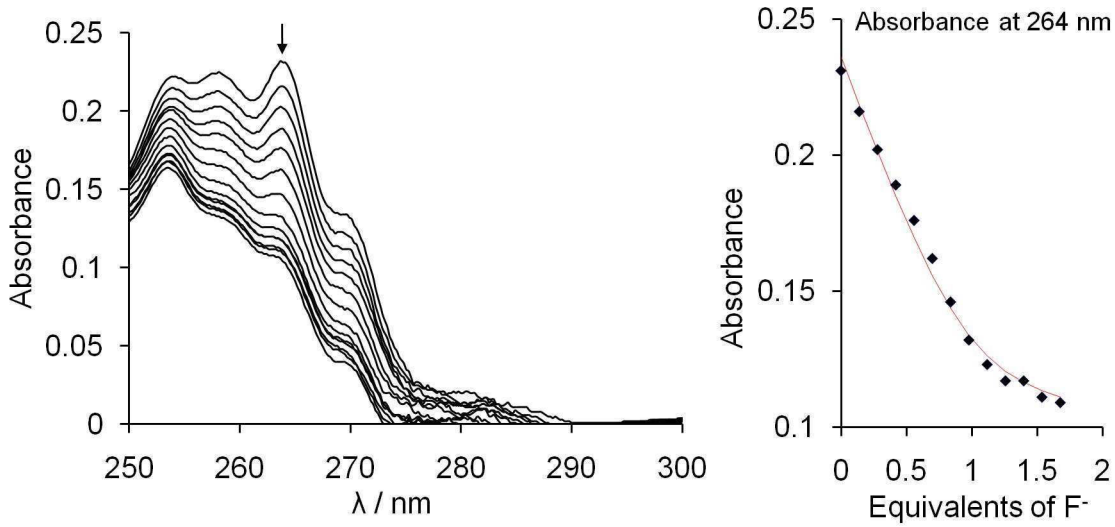

Figure 86. Spectral changes in the UV-Vis absorption spectra of [**57**]OTf (1.4 × 10^{-4} M) in THF upon incremental addition of a KF solution (0.006 M, MeOH). The isotherms are plotted based on the absorbance at 264 nm, and the line indicates the fit to the calculated 1:1 binding isotherm.

5.3 Synthesis and characterization of stibonium/onium dications

The inability of [**57**]$^+$ to bind fluoride in the presence of protic solvents suggested insufficient Lewis acidity at the antimony center. By analogy with the approach employed to enhance the fluoride affinity of triarylboranes, we decided to append a secondary onium group to the stibonium ion in order to boost the anion affinity via Coulombic/cooperative effects. Thus, we set out to prepare and investigate the onium/stibonium dications [**58**]$^{2+}$, [**59**]$^{2+}$, and [**60**]$^{2+}$ bearing pendant ammonium and phosphonium substituents both peripheral and proximal to the stibonium binding site.

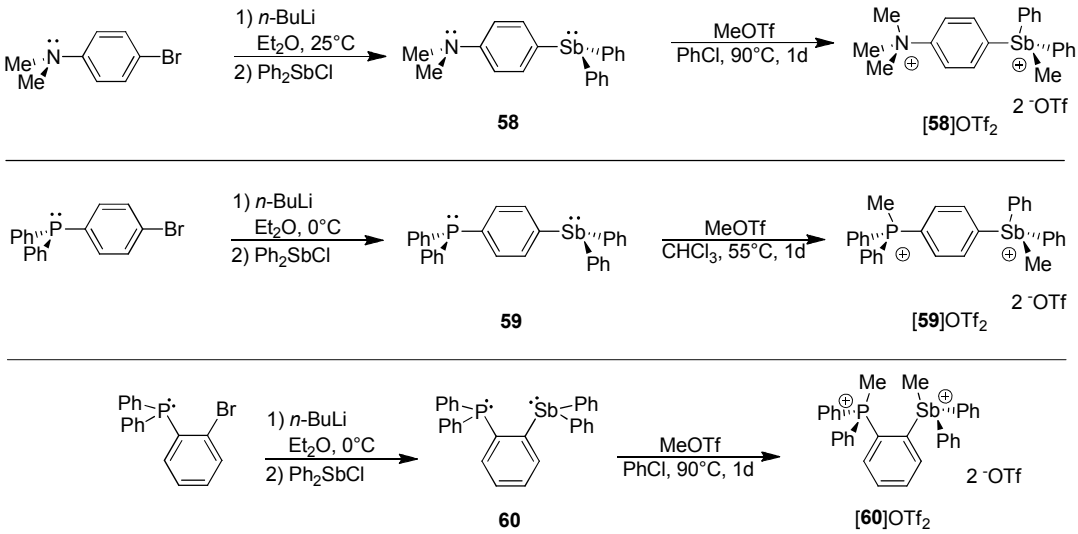

Figure 87. Synthesis of stibonium/onium dications [**58**]OTf_2, [**59**]OTf_2, and [**60**]OTf_2.

The stibines **58**, **59**, and **60** were prepared by treatment of the corresponding aryllithium reagents with Ph_2SbCl according to Figure 87. Subsequent reaction of **58**, **59**, and **60** with MeOTf in $CHCl_3$ or chlorobenzene at elevated temperatures afforded the

onium/stibonium dications $[\mathbf{58}]^{2+}$, $[\mathbf{59}]^{2+}$, and $[\mathbf{60}]^{2+}$, respectively, as the triflate salts. These salts are soluble in water and polar organic solvents such as MeOH, $CHCl_3$, and acetone, but insoluble in less polar solvents such as toluene and Et_2O. The ^1H NMR spectra (CD_3OD) of each of these complexes displayed all expected signals, including those assigned to the $SbCH_3$ and $N(CH_3)_3$ or PCH_3 groups. For **58**$(OTf)_2$, the $SbCH_3$ and $N(CH_3)_3$ resonances both appear as singlets at 2.56 and 3.71 ppm, respectively. The ^1H NMR spectrum of **59**$(OTf)_2$ displays a singlet at 2.58 ppm, assigned to the $SbCH_3$ group, and a doublet at 3.04 ppm ($^2J_{H\text{-}P}$ = 14.10 Hz) assigned to the PCH_3 group. Similarly, the ^1H NMR spectrum of **60**$(OTf)_2$ displays signals at 2.28 ppm and 2.91 ppm (d, $^2J_{H\text{-}P}$ = 13.55 Hz), corresponding to the $SbCH_3$ and PCH_3 groups, respectively. The $^{31}P\{^1H\}$ NMR spectra of **59**$(OTf)_2$ and **60**$(OTf)_2$ exhibit single resonances at 23.93 ppm and 27.51 ppm, respectively, in the expected range for triarylmethylphosphonium cations. The X-ray crystal structures of **58**$(OTf)_2$, **59**$(OTf)_2$, and **60**$(OTf)_2$ have also been determined, confirming quaternization of pnictogen atoms and the dicationic charge of the molecules (Figure 88, Figure 89, and Figure 90).

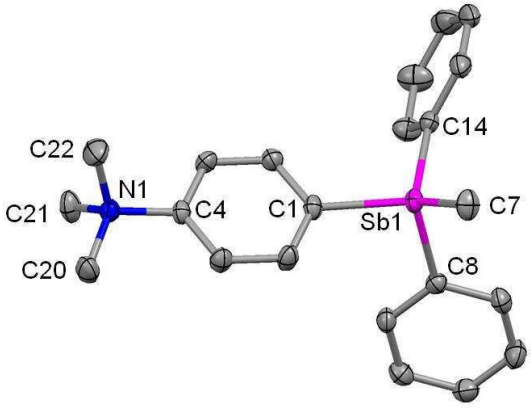

Figure 88. Crystal structure of [**58**]$^{2+}$. Displacement ellipsoids are scaled to the 50% probability level. Hydrogen atoms and triflate anions have been omitted for clarity. Selected bond lengths (Å) and angles (˚): Sb(1)-C(7) 2.091(3), Sb(1)-C(14) 2.093(3), Sb(1)-C(8) 2.096(3), Sb(1)-C(1) 2.103(3), N(1)-C(20) 1.491(4), N(1)-C(4) 1.498(3), N(1)-C(22) 1.499(4), N(1)-C(21) 1.500(4), C(7)-Sb(1)-C(14) 118.88(12), C(7)-Sb(1)-C(8) 108.70(11), C(14)-Sb(1)-C(8) 104.29(11), C(7)-Sb(1)-C(1) 112.45(11), C(14)-Sb(1)-C(1) 106.94(11), C(8)-Sb(1)-C(1) 104.35(11).

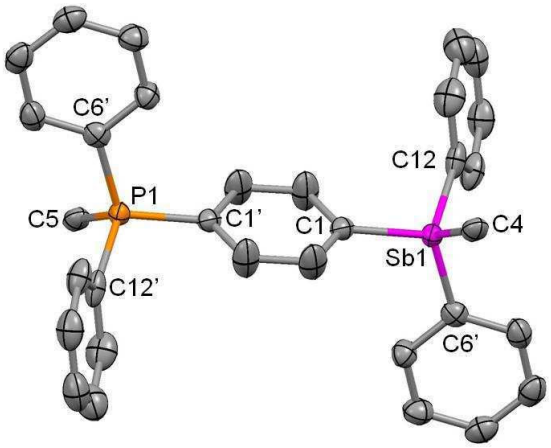

Figure 89. Crystal structure of [**59**]$^{2+}$. Displacement ellipsoids are scaled to the 50% probability level. Hydrogen atoms and triflate anions have been omitted for clarity. Selected bond lengths (Å) and angles (˚): Sb(1)-C(12) 1.923(5), Sb(1)-C(6) 2.005(5), Sb(1)-C(1) 2.018(4), Sb(1)-C(4) 2.072(15), P(1)-C(5) 1.795(19), P(1)-C(1') 1.881(12), P(1)-C(6) 1.890(13), P(1)-C(12) 1.965(14), C(12)-Sb(1)-C(6) 107.8(2), C(12)-Sb(1)-C(1) 102.91(19), C(6)-Sb(1)-C(1) 102.26(16), C(12)-Sb(1)-C(4) 123.9(6), C(6)-Sb(1)-C(4) 108.9(6), C(1)-Sb(1)-C(4) 108.9(7).

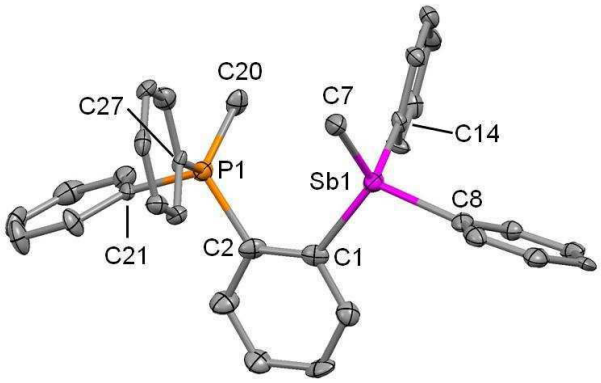

Figure 90. Crystal structure of $[\mathbf{60}]^{2+}$. Displacement ellipsoids are scaled to the 50% probability level. Hydrogen atoms and triflate anions have been omitted for clarity. Selected bond lengths (Å) and angles (˚): Sb(1)-C(7) 2.078(10), Sb(1)-C(8) 2.079(10), Sb(1)-C(14) 2.088(8), Sb(1)-C(1) 2.130(10), P(1)-C(20) 1.691(10), P(1)-C(21) 1.835(10), P(1)-C(27) 1.860(9), P(1)-C(2) 1.887(10), C(7)-Sb(1)-C(8) 110.2(4), C(7)-Sb(1)-C(14) 109.1(4), C(8)-Sb(1)-C(14) 102.9(4), C(7)-Sb(1)-C(1) 120.6(4), C(8)-Sb(1)-C(1) 109.5(4), C(14)-Sb(1)-C(1) 102.9(3).

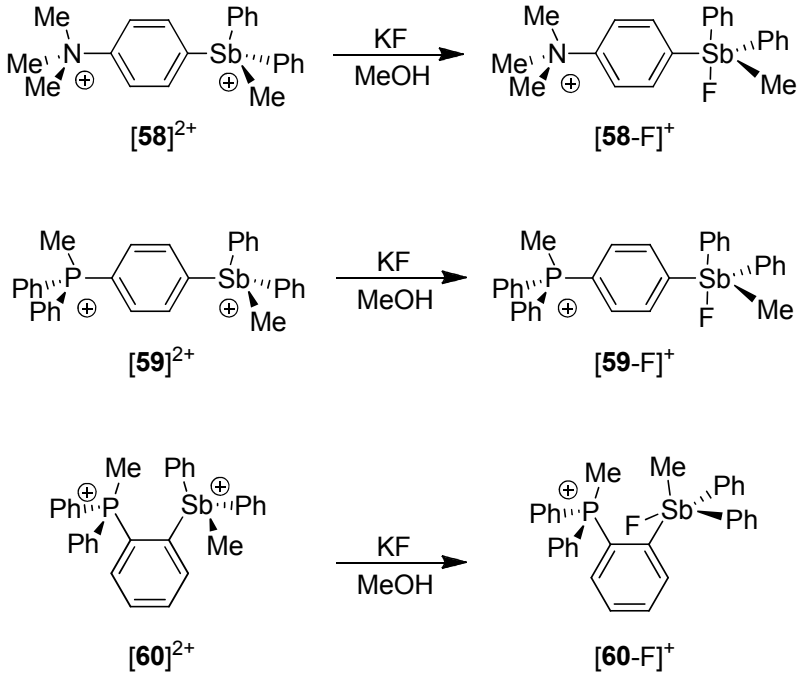

Figure 91. Reaction of onium/stibonium dications $[\mathbf{58}]^{2+}$, $[\mathbf{59}]^{2+}$, and $[\mathbf{60}]^{2+}$ with fluoride.

5.4 Fluoride binding studies with stibonium/onium dications

The reaction of [**58**]$^{2+}$, [**59**]$^{2+}$, and [**60**]$^{2+}$ with an excess of KF in CD_3OD resulted in changes in the ^1H and $^{31}P\{^1H\}$ NMR spectra of these compounds, which implied the formation of the fluorostiborane complexes [**58**-F]$^+$, [**59**-F]$^+$, and [**60**-F]$^+$ (Figure 91). The ^1H NMR spectrum of [**58**-F]$^+$ shows that the $SbCH_3$ resonance is shifted slightly upfield to 2.14 ppm (*vs* 2.56 ppm for [**58**]$^{2+}$), whereas the $N(CH_3)_3$ resonance appears at 3.67 ppm, largely unchanged from that of [**58**]$^{2+}$. Similarly, in [**59**-F]$^+$ the $SbCH_3$ signal is shifted upfield to 2.15 ppm (*vs* 2.58 ppm for [**59**]$^{2+}$) while the PCH_3 signal experiences only a small shift, appearing as a doublet at 2.99 ppm ($^2J_{H\text{-}P}$ = 14.10 Hz). The resonance observed at 23.39 ppm in the $^{31}P\{^1H\}$ NMR spectrum of [**59**-F]$^+$ is close to that measured for [**59**]$^{2+}$. More substantial changes were observed in the ^1H NMR spectrum of [**60**-F]$^+$. The $SbCH_3$ resonance appearing at 1.53 ppm is shifted considerably upfield versus that of [**60**]$^{2+}$ (2.28 ppm), and the PCH_3 resonance is shifted downfield to 3.18 ppm (d, $^2J_{H\text{-}P}$ = 14.28 Hz) versus 2.91 ppm for [**60**]$^{2+}$. Despite the significant changes in its ^1H NMR spectrum, the $^{31}P\{^1H\}$ NMR signal observed at 28.29 ppm for [**60**-F]$^+$ is close to that measured for [**60**]$^{2+}$. In the ^{19}F NMR spectra of [**58**-F]$^+$, [**59**-F]$^+$, and [**60**-F]$^+$, only signals corresponding to the triflate anions and free F^- could be clearly assigned.

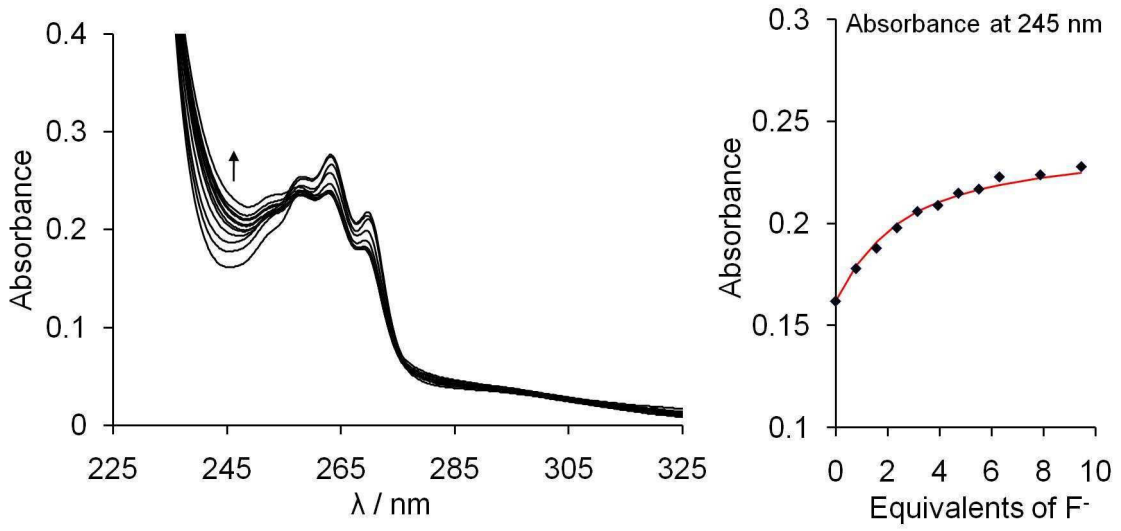

Figure 92. Spectral changes in the UV-Vis absorption spectra of [**58**]OTf_2 (1.3×10^{-4} M) in MeOH upon incremental addition of a KF solution (0.06 M, MeOH). The isotherms are plotted based on the absorbance at 245 nm, and the line indicates the fit to the calculated 1:1 binding isotherm.

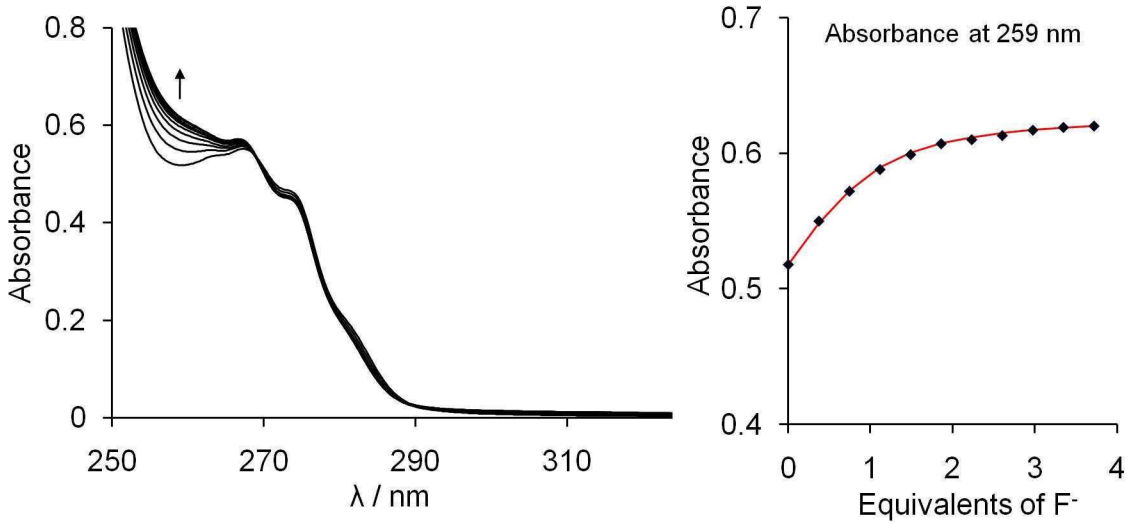

Figure 93. Spectral changes in the UV-Vis absorption spectra of [**59**]OTf_2 (1.4×10^{-4} M) in MeOH upon incremental addition of a KF solution (0.04 M, MeOH). The isotherms are plotted based on the absorbance at 259 nm, and the line indicates the fit to the calculated 1:1 binding isotherm.

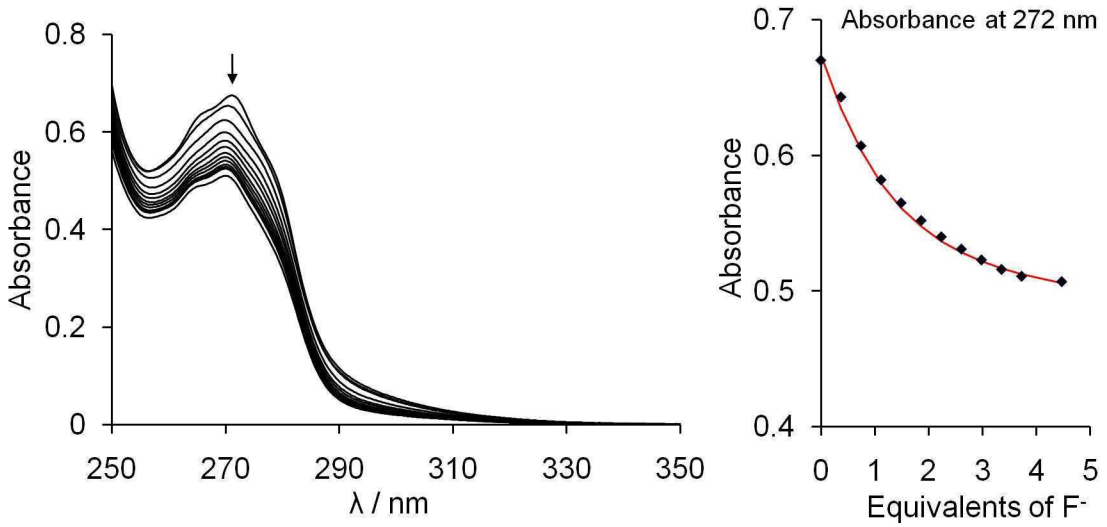

Figure 94. Spectral changes in the UV-Vis absorption spectra of [**60**]OTf_2 (1.4×10^{-4} M) in MeOH upon incremental addition of a KF solution (0.04 M, MeOH). The isotherms are plotted based on the absorbance at 272 nm, and the line indicates the fit to the calculated 1:1 binding isotherm.

Based on the NMR evidence for the formation of fluorostiborane complexes from the reaction of $[\mathbf{58}]^{2+}$, $[\mathbf{59}]^{2+}$, and $[\mathbf{60}]^{2+}$ with KF, we sought to determine the fluoride affinities of these compounds and confirm 1:1 receptor/fluoride binding using UV-Vis spectrophotometric titrations. The UV-Vis spectra of **58**$(OTf)_2$, **59**$(OTf)_2$, and **60**$(OTf)_2$ in MeOH were monitored upon incremental addition of KF (0.06 M in MeOH), as shown in Figure 92, Figure 93, and Figure 94, respectively. In all three cases, the addition of F^- resulted in small changes in the absorption bands in the 240-300 nm range, attributed to π-π* excitation of the phenyl substituents. These changes were appropriately fitted to 1:1 binding isotherms to give fluoride binding constants of $4.0(\pm0.5) \times 10^3$ M^{-1} for $[\mathbf{58}]^{2+}$, $2.6(\pm0.6) \times 10^4$ M^{-1} for $[\mathbf{59}]^{2+}$, and $9.5(\pm2.0) \times 10^3$ M^{-1} for

[**60**]$^{2+}$. No evidence for fluoride binding was observed when these titrations were carried out in H_2O/MeOH mixtures.

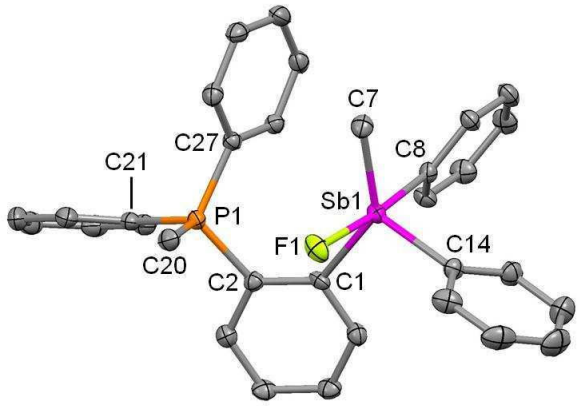

Figure 95. Crystal structure of [**60**-F]$^{+}$. Displacement ellipsoids are scaled to the 50% probability level. Hydrogen atoms and triflate anions have been omitted for clarity. Selected bond lengths (Å) and angles (˚): Sb(1)-F(1) 2.0551(18), Sb(1)-C(7) 2.113(3), Sb(1)-C(14) 2.121(3), Sb(1)-C(1) 2.156(3), Sb(1)-C(8) 2.161(3), F(1)-Sb(1)-C(8) 172.94(10), C(7)-Sb(1)-C(1) 138.09(12), C(14)-Sb(1)-C(1) 104.90(12), C(7)-Sb(1)-C(14) 112.36(12).

Cationic triarylboranes substituted with an onium group at an *ortho*-phenylene position have been shown to exhibit higher fluoride affinities than their *para*-phenylene analogs because of an increase in Coulombic and cooperative effects. Notably, these effects are clearly observed for the phosphonium boranes [*ortho*-$(Ph_2MeP)(Mes_2B)C_6H_4]^+$ ([**25**]$^+$) and [*para*-$(Ph_2MeP)C_6H_4(BMes_2)]^+$ ([**12**]$^+$), which exhibit fluoride binding constants of $>10^6$ M^{-1} and 400 M^{-1}, respectively, in MeOH. In the case of [**60**]$^{2+}$, we had predicted that such a chelate effect should result in an increased fluoride affinity for this receptor versus [**59**]$^{2+}$. Thus, the significantly lower value of K_F for [**60**]$^{2+}$ compared to [**59**]$^{2+}$ was surprising, and we sought structural clues

to explain its weaker fluoride affinity. Although single crystals of [**58**-F]$^+$ and [**59**-F]$^+$ could not be obtained, slow diffusion of Et_2O into a solution of [**60**]$^{2+}$ and KF in MeCN produced crystals that were suitable for X-ray diffraction. The structure of [**60**-F]OTf was determined, confirming the formation of a fluorostiborane and the presence of a remaining triflate anion (Figure 95). The fluoride anion coordinates to the antimony atom via a Sb-F bond distance of 2.055(18) Å. This results in a trigonal bipyramidal geometry around antimony with the fluoride anion and a phenyl substituent as axial ligands. The fluorine atom remains > 3.5 Å from the phosphorus atom ($\Sigma(r_{vdW})$ = 3.45 Å), precluding the presence of even a weak interaction, at least in the solid state. This feature suggests that the phosphonium center might not assist fluoride binding in solution via a F→P donor-acceptor interaction, as has observed for the phosphonium borane species **25**-F. However, a F(1)-C(20) separation of 3.17 Å suggests that intramolecular hydrogen bonding interactions between the fluorine atom and phosphonium methyl group may serve to stabilize the fluorostiborane.[101]

5.5 Conclusions

In conclusion, we have demonstrated that tetraorganostibonium ions hold potential as competent fluoride sensors. The simple stibonium ion [**57**]$^+$ does not possess the ability to complex fluoride directly in protic solvents, as determined by UV-Vis titration. However, decoration of this cation with a secondary onium group, as in the dications [**58**]$^{2+}$, [**59**]$^{2+}$, and [**60**]$^{2+}$, enhances the Lewis acidity of the stibonium center such that it is capable of complexing fluoride in MeOH. Opposite to the trend observed for

triarylboranes, the presence of a phosphonium group *ortho* to the stibonium binding site in $[\mathbf{60}]^{2+}$ results in a lower fluoride affinity versus the *para* isomer $[\mathbf{59}]^{2+}$.

The inability of the stibonium ions discussed here to bind fluoride in water does not dismiss the potential of this class of receptors to act as competent fluoride sensors in water. Substituent effects have not been fully evaluated and could play a role in tuning factors such as hydrophobicity, which has been shown to affect the fluoride affinity of cationic triarylboranes. In addition, incorporation of more responsive chromophores into these systems will allow for a better evaluation of fluoride affinities.

5.6 Experimental

General Considerations. *o*-$(Ph_2P)BrC_6H_4$[253] and *p*-$(Ph_2P)BrC_6H_4$[254] were prepared according to procedures reported in the literature. *n*-$Bu_4NF{\cdot}3H_2O$ (TBAF), KF, MeOTf, and 4-$(Me_2N)C_6H_4Br$ were purchased from Alfa Aesar and used as received. Diphenylchlorostibine was prepared according to the literature[239]. Solvents were dried by passing through an alumina column (*n*-hexane, CH_2Cl_2) or refluxing under N_2 over Na/K (Et_2O and THF). All other solvents were at least ACS reagent grade and used as received. Air-sensitive compounds were handled under a N_2 atmosphere using standard Schlenk and glovebox techniques. UV-vis spectra were recorded on an Ocean Optics USB4000 spectrometer with an Ocean Optics ISS light source. Elemental analyses were performed at Atlantic Microlab (Norcross, GA). NMR spectra were recorded on Varian Unity Inova 400 FT NMR (399.59 MHz for ^{1}H, 375.99 MHz for ^{19}F, 161.75 MHz for ^{31}P, 100.45 MHz for ^{13}C) spectrometer at ambient temperature unless otherwise stated.

Chemical shifts (δ) are given in ppm, and are referenced against external Me_4Si (^1H, ^{13}C), $BF_3{\cdot}Et_2O$ (^{19}F), and H_3PO_4 (^{31}P).

Table 14. Crystal data, data collections, and structure refinements for [**58**]OTf_2, [**59**]OTf_2, and [**60**]OTf_2.

Crystal data	[**58**]$OTf_2{\cdot}2CH_3CN$	[**59**]OTf_2	[**60**]$OTf_2{\cdot}CH_2Cl_2$
Formula	$C_{28}H_{32}N_3O_6F_6S_2Sb$	$C_{34}H_{30}O_6F_6PS_2Sb$	$C_{35}H_{32}O_6F_6PS_2Cl_2Sb$
Mr	806.44	865.42	950.35
Crystal size/mm	0.10 x 0.10 x 0.08	0.17 x 0.07 x 0.05	0.11 x 0.09 x 0.07
Crystal system	Monoclinic	Triclinic	Monoclinic
Space group	P2(1)/c	P-1	Pc
a/Å	15.152(6)	7.8824(15)	10.5965(5)
b/Å	11.111(4)	10.550(2)	8.6602(4)
c/Å	22.015(6)	11.231(2)	21.2033(11)
α /°	90	100.000(2)	90
β/°	114.837(19)	95.635(2)	97.973(3)
γ /°	90	103.754(2)	90
V/Å^3	3363(2)	883.9(3)	1926.9(2)
Z	4	1	2
ρ_{calc}/g cm^{-3}	1.593	1626	1.638
μ/mm^{-1}	1.021	1.019	1.077
F(000)	1624	434	952
T/K	110(2)	110(2)	110(2)
Scan mode	ω, φ	ω, φ	ω, φ
hkl Range	-19 → +19	-9 → +9	-13 → +11
	-13 → +13	-12 → +12	-10 → +10
	-27 → +27	-13 → +13	-23 → +26
Measd reflns	35148	9154	14919
Unique reflns [R_{int}]	6956 [0.0439]	3455 [0.0309]	6270 [0.0380]
Reflns used for refinement	6956	3455	6270
Refined parameters	421	246	460
GooF	1.010	1.026	1.018
*R*1,[a] *wR*2[b] (all data)	0.0386, 0.0907	0.0427, 0.1284	0.0718, 0.1708
ρ_{fin} (max., min.)/eÅ^{-3}	0.517, -0.449	0.460, -0.401	5.064, -1.286

[a] $R1 = \Sigma||F_o| - |F_c||/\Sigma|F_o|$. [b] $wR2$ $([\Sigma w(F_o^2 - F_c^2)^2]/[\Sigma\, w(F_o^2)^2])^{1/2}$; $w = 1/[\sigma^2(F_o^2) + (ap)^2 + bp]$; $p = (F_o^2 + 2F_c^2)/3$ with $a = 0.0533$ for [**58**]OTf_2, 0.0810 for [**59**]OTf_2, and 0.0991 for [**60**]OTf_2; and $b = 1.8806$ for [**58**]OTf_2, 1.054 for [**59**]OTf_2, and 14.5567 for [**60**]OTf_2.

Table 15. Crystal data, data collections, and structure refinements for (**60**-F)OTf·THF.

Crystal data	(**60**-F)OTf·THF
Formula	$C_{37}H_{38}O_4F_4PSSb$
Mr	807.45
Crystal size/mm	0.15 x 0.11 x 0.09
Crystal system	Monoclinic
Space group	P21/c
a/Å	9.3397(3)
b/Å	14.3721(4)
c/Å	27.5839(7)
α /°	90
β/°	106.462(2)
γ /°	90
V/Å^3	3550.8(2)
Z	4
ρ_{calc}/g cm^{-3}	1.510
μ/mm^{-1}	0.940
F(000)	1640
T/K	110(2)
Scan mode	ω, φ
hkl Range	-13 → +12
	-20 → +17
	-28 → +39
Measd reflns	36495
Unique reflns [R_{int}]	10808 [0.0480]
Reflns used for refinement	10808
Refined parameters	433
GooF	1.006
*R*1,[a] *wR*2[b] (all data)	0.0737, 0.1359
ρ_{fin} (max., min.)/eÅ^{-3}	1.134, -0.713

[a] $R1 = \Sigma||F_o| - |F_c||/\Sigma|F_o|$. [b] $wR2$ ($[\_w(F_o^2 - F_c^2)^2]/[\Sigma\, w(F_o^2)^2])^{1/2}$; $w = 1/[\sigma^2(F_o^2) + (ap)^2 + bp]$; $p = (F_o^2 + 2F_c^2)/3$ with $a = 0.0767$ and $b = 0$ for **60**-F.

Crystallography. Single crystals of [**58**]OTf_2 were obtained by slow diffusion of Et_2O into a solution of the compound in MeCN. Single crystals of [**59**]OTf_2 and [**60**]OTf_2 were obtained by slow diffusion of Et_2O into solutions of the compounds in CH_2Cl_2. Details of the data collection and structure refinement for [**58**]OTf_2, [**59**]OTf_2, and [**60**]OTf_2 are included in Table 14. Single crystals of [**60**-F]OTf were obtained by slow

evaporation of a solution of the compound in THF. Details of the data collection and structure refinement for [**60**-F]OTf are included in Table 15.

The crystallographic measurements were performed using a Bruker-AXS APEX-II CCD area detector diffractometer, with a graphite-monochromated Mo-Kα radiation (λ = 0.71069 Å). A specimen of suitable size and quality was selected and mounted onto a nylon loop. The semiempirical method SADABS[207] was applied for absorption correction. The structures were solved by direct methods using SHELXTL/PC package (version 6.1)[208] which successfully located most of the non-hydrogen atoms. Subsequent refinement on F^2 allowed location of the remaining non-hydrogen atoms. All H atoms were geometrically placed and refined in a riding model approximation.

Synthesis of [57]OTf and Reaction with Fluoride. [**57**]OTf was prepared according to the literature.[255] ^{1}H NMR (399.9 MHz, $CDCl_3$): δ 2.54 (s, 3H, Sb-CH_3), 7.53-7.65 (m, 5H, SbPh). ^{19}F NMR (375.97 MHz, $CDCl_3$): δ -82.48 (OTf). **57**-F could be prepared *in situ* by addition of 1 equiv. of TBAF to a solution of [**57**]OTf in $CDCl_3$. Additionally, addition of excess KF to a solution of [**57**]OTf in MeOH resulted in precipitation of **57**-F as a colorless, microcrystalline solid. **57**-F: ^{1}H NMR (399.9 MHz, $CDCl_3$): δ 1.96 (s, 3H, Sb-CH_3), 7.35-7.43 (m, 3H, *meta* + *para* SbPh), 7.61 (d, 2H, *ortho*-SbPh, $^3J_{H\text{-}H}$ = 6.59 MHz). ^{19}F NMR (375.97 MHz, $CDCl_3$): δ -77.06 (SbF).

Synthesis of [58]OTf$_2$. A solution of *n*-butyllithium (2.9 M, 0.59 mL) in hexanes was added dropwise to a solution of 4-$(Me_2N)C_6H_4Br$ (0.31 g, 1.55 mmol) in Et_2O (10 mL) at 0 ˚C. After stirring at this temperature for 30 min., a solution of Ph_2SbCl (0.58 g, 1.86 mmol) in Et_2O (15 mL) was added via cannula. The reaction mixture was allowed

to warm to room temperature and stirred overnight. The solvent was removed *in vacuo*, and the residue was extracted with hexanes (20 mL) and filtered over Celite. The solvent was again removed *in vacuo*, the residue was extracted with Et_2O (15 mL), and the resulting mixture was filtered over a plug of silica. Concentration of the filtrate to *ca.* 5 mL in vacuo and addition of MeOH (20 mL) resulted in the precipitation a colorless solid. The solid was filtered and washed with MeOH (3 × 5 mL) to yield 188 mg (31%) of crude *para*-$(Me_2N)C_6H_4(SbPh_2)$, which was dried overnight *in vacuo* and used without further purification.

MeOTf (0.13 mL, 1.14 mmol) was added to a solution of crude *para*-$(Me_2N)C_6H_4(SbPh_2)$ (0.15 g, 0.38 mmol) in chlorobenzene (2 mL). The mixture was sealed under a N_2 atmosphere in a 50 mL Schlenk tube and heated to 90 ˚C for 18 hrs, after which a colorless precipitate had formed. The solid was filtered, washed with Et_2O (3 × 5 mL), and dried *in vacuo* to afford 109 mg (40 %) of [**58**]OTf_2. ^{1}H NMR (399.9 MHz, CD_3OD): δ 2.56 (s, 3H, Sb-C*H*$_3$), 3.71 (s, 9H, N-C*H*$_3$), 7.65-7.72 (m, 6H, *meta* and *para* Sb*Ph*), 7.79 (d, 4H, *ortho*-Sb*Ph*, $^3J_{H\text{-}H}$ = 8.42 Hz), 7.99 (d, 2H, N-*C*$_6$*H*$_4$-Sb, $^3J_{H\text{-}H}$ = 9.15 Hz), 8.15 (d, 2H, N-*C*$_6$*H*$_4$-Sb, $^3J_{H\text{-}H}$ = 9.15 Hz). ^{13}C NMR (100.5 MHz, CD_3OD): δ 4.02 (Sb-*C*H_3), 57.66 (N-*C*H_3), 122.94, 126.89, 131.58, 133.96, 136.04, 138.27, (Sb-C and N-C ipso carbon signals were not observed). Anal. calcd for $C_{24}H_{26}NO_6F_6S_2Sb$ + 2CH_3CN: C, 41.70; H, 4.00. Found: C, 41.52; H, 3.87.

Synthesis of [59]OTf_2. A solution of *n*-butyllithium (2.8 M, 1.0 mL) in hexanes was added dropwise to a solution of 4-$(Ph_2P)C_6H_4Br$ (0.90 g, 2.60 mmol) in Et_2O (10 mL) at 0 ˚C. After stirring at reduced temperature for 2 hrs, a solution of Ph_2SbCl (0.90 g, 2.89

mmol) in Et_2O (15 mL) was added via cannula. The reaction mixture was allowed to warm to room temperature and stirred overnight. The solvent was removed *in vacuo*, and the residue was extracted with CH_2Cl_2 (20 mL) and filtered over Celite. Concentration of the filtrate to *ca.* 5 mL in vacuo and addition of MeOH (20 mL) resulted in the precipitation a colorless solid. The solid was filtered and washed with MeOH (3 × 10 mL) to yield 600 mg (43%) of crude *para*-$(Ph_2P)C_6H_4(SbPh_2)$, which was dried overnight *in vacuo* and used without further purification.

MeOTf (0.25 mL, 2.23 mmol) was added to a solution of crude *para*-$(Ph_2P)C_6H_4(SbPh_2)$ (0.40 g, 0.74 mmol) in $CHCl_3$ (2 mL). The mixture was sealed under a N_2 atmosphere in a 50 mL Schlenk tube and heated to 55 ˚C for 18 hrs, after which a colorless precipitate had formed. The solid was filtered, washed with Et_2O (3 × 5 mL), and dried *in vacuo* to yield 330 mg (51 %) of [**59**]OTf_2. ^{1}H NMR (399.9 MHz, CD_3OD): δ 2.58 (s, 3H, Sb-C*H*$_3$), 3.04 (d, 3H, P-C*H*$_3$, $^2J_{P\text{-}H}$ = 14.10 Hz), 7.64-7.83 (m, 18H, Sb*Ph* + P*Ph* + P-*C*$_6$*H*$_4$-Sb), 7.87-7.96 (m, 4H, P*Ph*), 8.05 (dd, 2H, P-*C*$_6$*H*$_4$-Sb, $^3J_{H\text{-}P}$ = 8.55 Hz, $^3J_{H\text{-}H}$ = 3.12 Hz). $^{31}P\{^1H\}$ NMR (161.75 MHz, CD_3OD): δ 23.93. Anal. calcd for $C_{34}H_{30}O_6F_6PS_2Sb$: C, 47.19; H, 3.49. Found: C, 46.90; H, 3.40.

Synthesis of [60]OTf$_2$. A solution of *n*-butyllithium (2.8 M, 0.56 mL) in hexanes was added dropwise to a solution of 2-$(Ph_2P)C_6H_4Br$ (0.50 g, 1.46 mmol) in Et_2O (10 mL) at 0 ˚C. After stirring at room temperature for 5 min, 2-$(Ph_2P)C_6H_4Li$ precipitated as a colorless solid. The supernatant was carefully decanted, and the solid was washed with Et_2O (2 × 5 mL). Et_2O (5 mL) was then added, followed by a solution of Ph_2SbCl (0.46 g, 1.48 mmol) in Et_2O (15 mL), and the reaction mixture was stirred overnight. The

solvent was removed *in vacuo*, and the residue was extracted with CH_2Cl_2 (15 mL) and filtered over Celite. Concentration of the filtrate to *ca.* 3 mL in vacuo and addition of MeOH (10 mL) resulted in the precipitation a colorless solid. The solid was filtered and washed with MeOH (3 × 5 mL) to yield 300 mg (38%) of crude *ortho*-$(Ph_2P)C_6H_4(SbPh_2)$, which was dried overnight *in vacuo* and used without further purification.

MeOTf (0.10 mL, 0.93 mmol) was added to a solution of crude *ortho*-$(Ph_2P)C_6H_4(SbPh_2)$ (0.125 g, 0.23 mmol) in chlorobenzene (1 mL). The mixture was sealed under a N_2 atmosphere in a 50 mL Schlenk tube and heated to 90 ˚C for 24 hrs, after which a colorless precipitate had formed. The solid was filtered, washed with Et_2O (3 × 5 mL), and dried *in vacuo* to yield 180 mg (89 %) of [**60**]OTf_2. ^{1}H NMR (399.9 MHz, acetone-d_6): δ 2.58 (s, 3H, Sb-CH_3), 3.10 (d, 3H, P-CH_3, $^2J_{P\text{-}H}$ = 13.73 Hz), 7.60-7.68 (m, 12H, Sb*Ph* + P*Ph*), 7.75 (m, 2H, P*Ph*), 7.86-7.94 (m, 7H, Sb*Ph* + P*Ph* + P-C_6H_4-Sb), 8.03 (ddd, 1H, P-C_6H_4-Sb, *J* = 7.68 , 2.14, 1.35 Hz), 8.11 (ddd, 1H, P-C_6H_4-Sb, *J* = 7.65 , 2.24, 1.48 Hz). 8.24 (ddd, 1H, P-C_6H_4-Sb, *J* = 7.72 , 4.04, 1.09 Hz). ^{13}C NMR (100.5 MHz, acetone-d_6): δ 7.93 (Sb-CH$_3$), 10.34 (d, P-CH$_3$, $^2J_{P\text{-}C}$ = 56.46 Hz), 119.01, 119.89, 122.06 (q, OTf, $^1J_{F\text{-}C}$ = 321.6 Hz), 125.84, 126.76, 131.59, 131.74, 134.30, 134.31 (d, $J_{P\text{-}C}$ = 12.21 Hz), 134.84 (d, $J_{P\text{-}C}$ = 10.68 Hz), 136.38, 136.65 (d, $J_{P\text{-}C}$ = 3.05 Hz), 136.85 (d, $J_{P\text{-}C}$ = 3.06 Hz), 140.99 (d, $J_{P\text{-}C}$ = 12.21 Hz), 141.54 (d, $J_{P\text{-}C}$ = 12.97 Hz). ^{31}P{^{1}H} NMR (161.75 MHz, acetone-d_6): δ 27.12. NMR data in CD_3OD: ^{1}H NMR (399.9 MHz, CD_3OD): δ 2.28 (s, 3H, Sb-CH_3), 2.91 (d, 3H, P-CH_3, $^2J_{P\text{-}H}$ = 13.55 Hz), 7.52 (d, 4H, Sb-Ph, $^3J_{H\text{-}H}$ = 8.35 Hz), 7.57-7.63 (m, 8H, PPh + SbPh), 7.70-7.76 (m,

6H, PPh + SbPh), 7.81-7.89 (m, 3H, P*Ph* + P-C_6H_4-Sb), 7.98 (ddd, 1H, P-C_6H_4-Sb, J = 7.90 , 2.07, 1.45 Hz), 8.06 (ddd, 1H, P-C_6H_4-Sb, J = 7.53 , 2.38, 1.49 Hz), 8.11 (ddd, 1H, P-C_6H_4-Sb, J = 7.71 , 4.01, 1.39 Hz). $^{31}P\{^1H\}$ NMR (161.75 MHz, CD_3OD): δ 27.51 ppm. Anal. calcd for $C_{34}H_{30}O_6F_6PS_2Sb$ + CH_2Cl_2: C, 44.23; H, 3.39. Found: C, 44.85; H, 3.30.

Generation and NMR Characterization of [58-F]OTf, [59-F]OTf, and [60-F]OTf. The cationic fluorostiboranes [**58**-F]OTf, [**59**-F]OTf, and [**60**-F]OTf were prepared and characterized by multinuclear NMR *in situ* by addition of a slight excess of KF to solutions of **58**$(OTf)_2$, **59**$(OTf)_2$, and **60**$(OTf)_2$ in CD_3OD. A small number of single crystals of [**60**-F]OTf were obtained by removing solvent from the NMR sample, extracting the residue with THF, and slow evaporation of this solution. Data for [**58**-F]OTf: ^1H NMR (399.9 MHz, CD_3OD): δ 2.14 (s, 3H, Sb-CH_3), 3.67 (s, 9H, N-CH_3), 7.47-7.56 (m, 6H, *meta* and *para* Sb*Ph*), 7.68 (dd, 4H, *ortho*-Sb*Ph*, $^3J_{H-H}$ = 8.10 Hz, $^4J_{H-H}$ = 1.53 Hz), 7.78 (d, 2H, N-C_6H_4-Sb, $^3J_{H-H}$ = 9.07 Hz), 7.95 (d, 2H, N-C_6H_4-Sb, $^3J_{H-H}$ = 9.07 Hz). ^{13}C NMR (100.5 MHz, $CDCl_3$): δ 8.43 (Sb-CH_3), 57.60 (N-CH_3), 121.39, 130.42, 132.15, 136.17, 136.20, 138.14, 145.40, 149.80. Data for [**59**-F]OTf: ^1H NMR (399.9 MHz, CD_3OD): δ 2.15 (s, 3H, Sb-CH_3), 2.99 (d, 3H, P-CH_3, $^2J_{P-H}$ = 14.10 Hz), 7.47-7.56 (m, 6H, Sb*Ph* + P*Ph*), 7.69-7.79 (m, 14H, Sb*Ph* + P*Ph*), 7.84-7.90 (m, 4H, P-C_6H_4-Sb). $^{31}P\{^1H\}$ NMR (161.75 MHz, CD_3OD): δ 23.39. Data for [**60**-F]OTf: ^1H NMR (399.9 MHz, CD_3OD): δ 1.53 (s, 3H, Sb-CH_3), 3.18 (d, 3H, P-CH_3, $^2J_{P-H}$ = 14.28 Hz), 7.37-7.42 (m, 7H, PPh + SbPh + P-C_6H_4-Sb), 7.46-7.52 (m, 6H, PPh + SbPh), 7.58 (dd, 2H, PPh, J = 15.20, 7.89 Hz), 7.66-7.72 (m, 3H, PPh + P-C_6H_4-Sb), 7.77-7.84 (m,

5H, SbPh + P-C_6H_4-Sb), 7.89 (ddd, 1H, P-C_6H_4-Sb, J = 7.59, 3.85, 1.36 Hz). $^{31}P\{^1H\}$ NMR (161.75 MHz, CD_3OD): δ 28.29. Anal. calcd for $C_{33}H_{30}O_3F_4PSSb$ + $0.5C_4H_8O$ (approx. 0.5 eq. of THF lost in drying): C, 54.49; H, 4.44. Found: C, 54.11; H, 4.65.

UV-Vis Fluoride Titrations. Solutions of [**57**]OTf (1.4×10^{-4} M) in THF were titrated by incremental additions of a KF solution (0.006 M, MeOH). Solutions of **58**$(OTf)_2$ (1.3×10^{-4} M) in MeOH were titrated by incremental addition of a KF solution (0.06 M, MeOH). Solutions of **59**$(OTf)_2$ (1.4×10^{-4} M) and **60**$(OTf)_2$ (1.4×10^{-4} M) in MeOH were titrated by incremental addition of a KF solution (0.04 M, MeOH).

CHAPTER VI

GROUP 10 METAL-STIBORANE COMPLEXES

6.1 Introduction

Previous chapters described our efforts to develop tetraorganostibonium cations as novel Lewis acid receptors for fluoride recognition. Keeping with our continued interest in developing such novel fluoride receptors, we drew an analogy between a tetraorganostibonium cation and triarylstibine coordinated to a cationic transition metal center. Namely, we hypothesized that the antimony atom of such a complex might be sufficiently Lewis acidic to undergo nucleophilic attack by fluoride, resulting in the formation of a transition metal fluorostiborane complex (Figure 96).

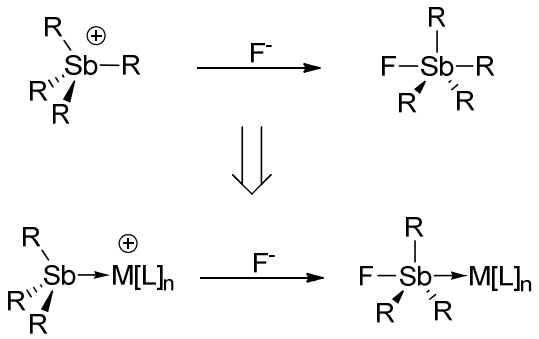

Figure 96. Depiction of the analogy between R_4Sb^+ and $[R_3SbM[L]_n]^+$ species.

While trialkylstibine and triarylstibine ligands have been extensively used in transition metal coordination chemistry,[256,257] complexes containing pentacoordinate stiboranyl ligands are much less common. Only a handful of transition metal complexes containing

stiboranyl ligands of type **I**[258,259] and **II**[260-263] have been reported (Figure 97). However, these reports support the notion that a cationic transition metal stibine complex might act as a fluoride receptor, resulting in the formation of a metal fluorostiborane complex as shown in Figure 96.

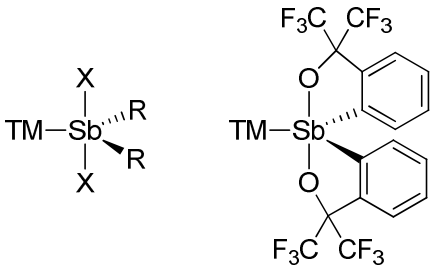

I **II**

Figure 97. Representations of the reported stiboranyl ligand types **I** and **II** (TM = transition metal moiety).

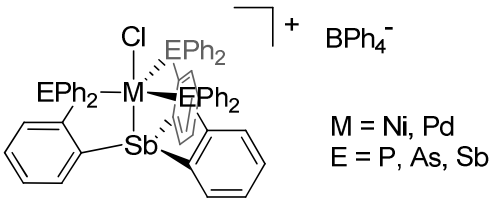

Figure 98. Proposed structure of Ni^{2+} and Pd^{2+} complexes with $(o\text{-}(Ph_2E)C_6H_4)_3Sb$ ligands.

Early reports indicated that tetradentate stibine ligands of the type $(o\text{-}(Ph_2E)C_6H_4)_3Sb$ (E = P, As) adopt a κ-E,E,E,Sb coordination mode to form cationic, trigonal bipyramidal metal complexes with Ni^{2+} and Pd^{2+}, although the structures were not confirmed by X-ray crystallography (Figure 98).[264-266] Given the presence of a cationic charge and

accessibility of a Sb coordination site trans to the metal center in these proposed species, we sought to determine if such complexes would be sufficiently Lewis acidic to afford the type of reactivity depicted in Figure 96. This chapter delineates the synthesis, structures, and fluoride binding properties of the complexes formed with the triphosphanylstibine ligand (o-$(Ph_2P)C_6H_4)_3Sb$ and Group 10 metals Ni, Pd, and Pt.

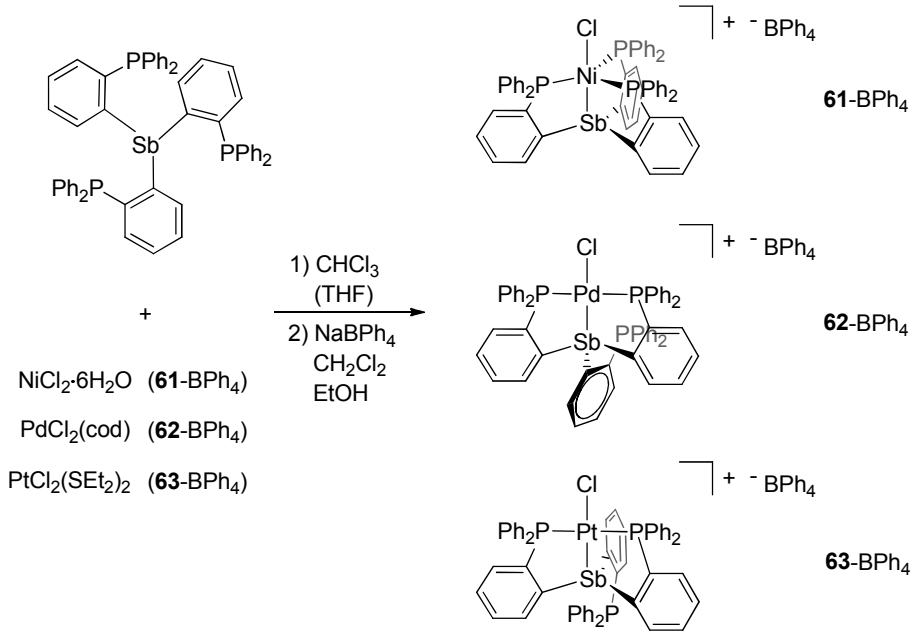

Figure 99. Synthesis of **61**-BPh_4, **62**-BPh_4, and **63**-BPh_4.

6.2 Synthesis and structural characterization of Group 10 metal-stiborane complexes

The reaction of o-$(Ph_2P)C_6H_4)_3Sb$ with $NiCl_2{\cdot}6H_2O$, $PdCl_2(cod)$ (cod = 1,5-cyclooctadiene), and $PtCl_2(Et_2S)_2$ in THF or $CHCl_3$ followed by workup and treatment with 1 equiv. of $NaBPh_4$ in CH_2Cl_2/EtOH afforded the cationic complexes **61**-BPh_4, **62**-BPh_4, and **63**-BPh_4 as deep blue, yellow, and colorless powders, respectively (Figure

99). Only one signal was observed in each of the $^{31}P\{^{1}H\}$ NMR spectra ($CDCl_3$) of these complexes, which appeared at 36.48 ppm for **61**-BPh_4, 39.72 ppm for **62**-BPh_4, and 38.23 ppm ($^{1}J_{195Pt\text{-}P}$ = 1737.35 Hz) for **63**-BPh_4. Variable temperature NMR experiments indicated that these signals show no tendency toward decoalescence upon cooling to -80 ˚C (*vide infra*). Similarly, the ^{1}H NMR spectra display only a single set of resonances corresponding to equivalent PPh_2 and *o*-C_6H_4 groups.

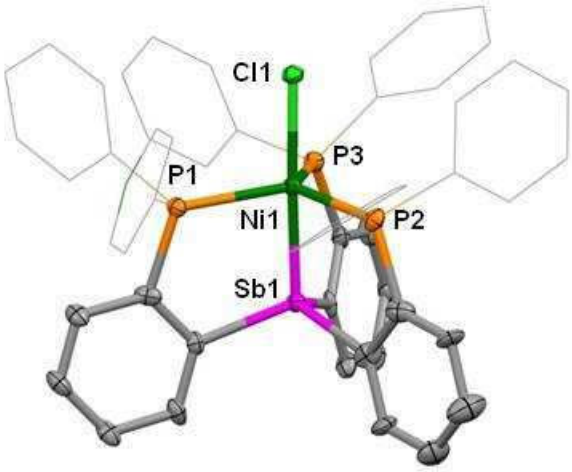

Figure 100. Crystal structure of **61**-BPh_4. Displacement ellipsoids are scaled to the 50% probability level. Hydrogens and have been omitted for clarity, and phenyl groups are depicted in wireframe. Selected bond lengths (Å) and angles (˚): Sb(1)-Ni(1) 2.3548(9), Ni(1)-Cl(1) 2.2423(16), Ni(1)-P(3) 2.3017(17), Ni(1)-P(2) 2.3023(16), Ni(1)-P(1) 2.3160(16), Cl(1)-Ni(1)-Sb(1) 177.32(5), P(1)-Ni(1)-P(2) 113.02(6), P(2)-Ni(1)-P(3) 124.69(6), P(1)-Ni(1)-P(3) 119.73(6), C(19)-Sb(1)-C(37) 109.1(2), C(19)-Sb(1)-C(1) 112.8(2), C(37)-Sb(1)-C(1) 111.7(2).

Single crystals of **61**-BPh_4, **62**-BPh_4, and **63**-BPh_4 were obtained by slow diffusion of Et_2O into $CHCl_3$ or CH_2Cl_2 solutions of the compounds. Surprisingly, the X-ray crystal structure determinations of **61**-BPh_4, **62**-BPh_4, and **63**-BPh_4 revealed significant

structural differences between these complexes. The structure of **61**-BPh_4 shows that the (*o*-$(Ph_2P)C_6H_4)_3Sb$ ligand adopts a κ-P,P,P,Sb coordination mode, resulting in a trigonal bipyramidal coordination geometry around the Ni center (Figure 100). The geometry around the Sb atom is close to tetrahedral (Σ(C-Sb-C) = 333.6˚) with a Sb-Ni distance of 2.3548(9) Å, which is shorter than those measured for *trans*-$(Ph_3Sb)_2Ni(C_6F_3Cl_2)_2$ (2.4480(6) Å)[267] or $(Ph_3Sb)Ni(C_4H_7)Br$ (2.4558(9) Å).[268]

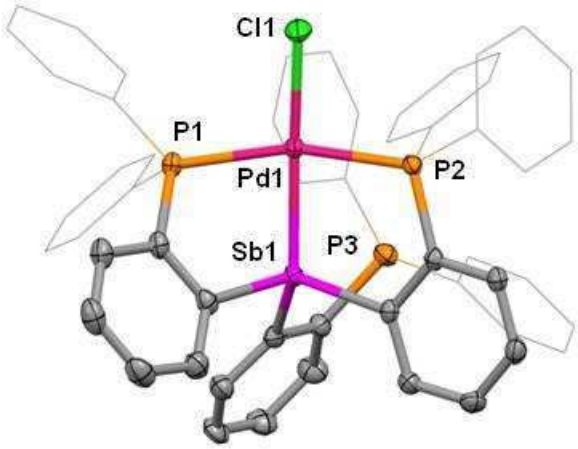

Figure 101. Crystal structure of **62**-BPh_4. Displacement ellipsoids are scaled to the 50% probability level. Hydrogens and have been omitted for clarity, and phenyl groups are depicted in wireframe. Selected bond lengths (Å) and angles (˚): Sb(1)-Pd(1) 2.4689(5), Pd(1)-Cl(1) 2.3314(12), Pd(1)-P(1) 2.3333(11), Pd(1)-P(2) 2.3285(11), Cl(1)-Pd(1)-Sb(1) 174.17(4), P(2)-Pd(1)-P(1) 159.44(4), C(19)-Sb(1)-C(37) 107.20(16), C(19)-Sb(1)-C(1) 110.16(16), C(37)-Sb(1)-C(1) 103.96(17).

The structures of **62**-BPh_4 and **63**-BPh_4 show that the (*o*-$(Ph_2P)C_6H_4)_3Sb$ ligand coordinates to the Pd and Pt centers in a tridentate κ-P,P,Sb fashion, resulting in distorted square planar geometries around these atoms in the solid state (Figure 101 and Figure 102). In the case of **62**-BPh_4, the uncoordinated phosphine remains slightly above

the Pd square plane, but with a Pd-P separation greater than 4 Å. For **63**-BPh_4, the free phosphine arm is rotated anti-parallel to the Pt-Sb axis. The Sb atoms in both complexes retain distorted tetrahedral coordination geometries. Although the Pt-Sb bond distance in **63**-BPh_4 (2.4733(3) Å) is comparable to those measured for *cis*-[$PtBr_2(SbPh_3)(PPh_3)$] (2.463(2) Å)[269] and *cis*-[$PtCl_2(SbPh_3)_2$] (2.50 Å (av.),[270] the Pd-Sb distance in **62**-BPh_4 (2.4689(5) Å) is shorter than those measured in *trans*-(o-$Tol_3Sb)_2PdCl_2$ (Pd-Sb = 2.5658(3) Å)[271] or *trans*-$(Ph_3Sb)_2Pd(Ph)Cl$ (Pd-Sb = 2.5568(5) Å).[272]

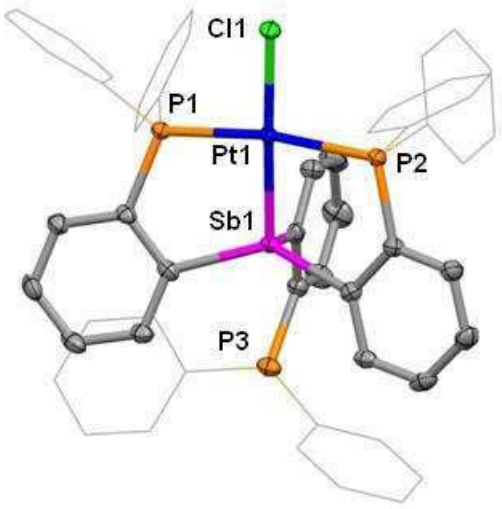

Figure 102. Crystal structure of **63**-BPh_4. Displacement ellipsoids are scaled to the 50% probability level. Hydrogens and have been omitted for clarity, and phenyl groups are depicted in wireframe. Selected bond lengths (Å) and angles (˚):Pt(1)-Sb(1) 2.4733(3), Pt(1)-Cl(1) 2.3536(8), Pt(1)-P(1) 2.3015(9), Pt(1)-P(2) 2.2918(9), Cl(1)-Pt(1)-Sb(1) 178.45(2), P(1)-Pt(1)-P(2) 168.35(3), C(1)-Sb(1)-C(37) 109.29(12), C(37)-Sb(1)-C(19) 107.15(12), C(1)-Sb(1)-C(19) 127.04(12).

The UV-Vis spectra of **62**-BPh_4 and **63**-BPh_4 in CH_2Cl_2 support the retention of the square planar Pd and Pt geometries in solution. The lowest energy absorption bands at 368 nm and 345 nm, respectively, are attributed to mixed MLCT and ligand-centered transitions and more closely resemble the absorption bands observed for square planar Pd and Pt complexes [273,274] than for trigonal bipyramidal complexes.[254,256,264-267] However, only a single $^{31}P\{^1H\}$ NMR signal (acetone-d_6) was observed for these complexes in the +25 ˚C to -80 ˚C temperature range, suggesting that the three phosphine arms should be rapidly exchanging in solution.

Despite the differences between the experimentally determined and anticipated structures of **61**-BPh_4, **62**-BPh_4, and **63**-BPh_4, we set out to investigate their reactivity with fluoride. Solutions of these complexes in $CDCl_3$ were treated with 1 eq. of TBAF. To our delight, the solutions underwent visible color changes from deep blue to purple for **61**-BPh_4, yellow to orange-red for **62**-BPh_4, and pale yellow to deep yellow for **63**-BPh_4 upon addition of F^-. The ^{19}F NMR spectra of these solutions each showed the emergence of a new signal at around -129 ppm, providing initial evidence for the formation of fluorostiborane complexes **61**-F, **62**-F, and **63**-F (Figure 103). In support of this notion, the ^{19}F NMR signals for **62**-F and **63**-F appear as quartets with $^3J_{P\text{-}F}$ coupling constants of 20.66 Hz and 9.86 Hz, respectively. The $^{31}P\{^1H\}$ NMR spectra further support the formation of **61**-F, **62**-F, and **63**-F via the appearance of doublet resonances in the 40-42 ppm range, each exhibiting $^3J_{P\text{-}F}$ coupling constants consistent with those measured in the ^{19}F NMR spectra (Table 16).

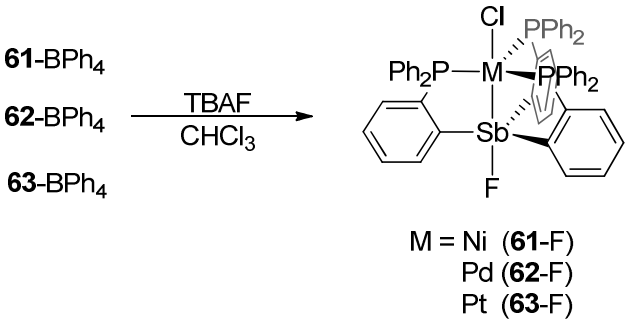

Figure 103. Synthesis of **61**-F, **62**-F, and **63**-F.

Table 16. Comparison of multinuclear ($^{31}P\{^{1}H\}$ and ^{19}F) NMR data in $CDCl_3$, and selected bond lengths for **61**-BPh_4, **62**-BPh_4, **63**-BPh_4, **61**-F, **62**-F, **63**-F, **61**-Cl, **62**-Cl, and **63**-Cl.

	^{31}P NMR (δ)		M-Sb (Å)	
61-BPh_4	+36.48		2.3548(9)	
62-BPh_4	+39.72		2.4689(5)	
63-BPh_4	+38.23 ($^{1}J_{195Pt-P}$ = 1737.35 Hz)		2.4733(3)	
				Sb-Cl (Å)
61-Cl	+35.42		2.4853(5)	2.6834(9)
62-Cl	+38.31		2.5752(9)	2.665(2)
63-Cl	+34.01 ($^{1}J_{195Pt-P}$ = 2305.7 Hz)		2.5762(8)	2.680(2)
		^{19}F NMR (δ)		**Sb-F (Å)**
61-F	+40.91 (d, $^{3}J_{F-P}$ = 6.17 Hz)	-129.55 (br)	2.5321(9)	2.028(2)
62-F	+41.90 (d, $^{3}J_{F-P}$ = 20.66 Hz)	-129.72 (q, $^{3}J_{F-P}$ = 20.66 Hz)	2.5721(7)	2.0320(19)
63-F	+40.07 (d, $^{3}J_{F-P}$ = 9.86 Hz) ($^{1}J_{195Pt-P}$ = 3204.6 Hz)	-129.72 (q, $^{3}J_{F-P}$ = 9.86 Hz)	2.5783(7)	2.036(2)

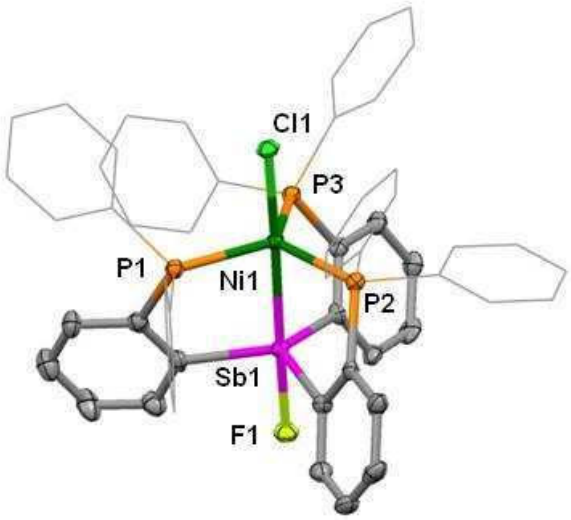

Figure 104. Crystal structure of **61**-F. Displacement ellipsoids are scaled to the 50% probability level. Hydrogens and have been omitted for clarity, and phenyl groups are depicted in wireframe. Selected bond lengths (Å) and angles (˚): Sb(1)-Ni(1) 2.5321(9), Ni(1)-Cl(1) 2.2684(12), Ni(1)-P(1) 2.2263(12), Ni(1)-P(2) 2.2327(13), Ni(1)-P(3) 2.2210(12), Sb(1)-F(1) 2.028(2), Cl(1)-Ni(1)-Sb(1) 175.93(3), F(1)-Sb(1)-Ni(1) 177.63(6), C(1)-Sb(1)-C(37) 115.32(14), C(1)-Sb(1)-C(19) 119.31(14), C(37)-Sb(1)-C(19) 121.10(14).

Single crystal X-ray diffraction studies confirmed the formation of **61**-F (Figure 104), **62**-F (Figure 105), and **63**-F (Figure 106). As opposed to its binding mode in the BPh_4^- salts, the $(o\text{-}(Ph_2P)C_6H_4)_3Sb$ ligand adopts a κ-P,P,P,Sb coordination mode in all three fluorostiborane complexes. The ligand coordination mode and formation of Sb-F bonds results in distorted trigonal bipyramidal geometries around both the transition metal and Sb atoms in these complexes. The measured Sb-F bond distances fall in the 2.028 - 2.036 Å range, shorter than those observed in the polymeric structure of Ph_2SbF (2.19 Å *av.*)[275] or the fluorostiborane Ph_4SbF (2.0530(8) Å).[158] The M-Sb distances in **61**-F, **62**-F, and **63**-F are all slightly longer than those measured for **61**-BPh_4, **62**-BPh_4, and **63**-BPh_4 (Table 16).

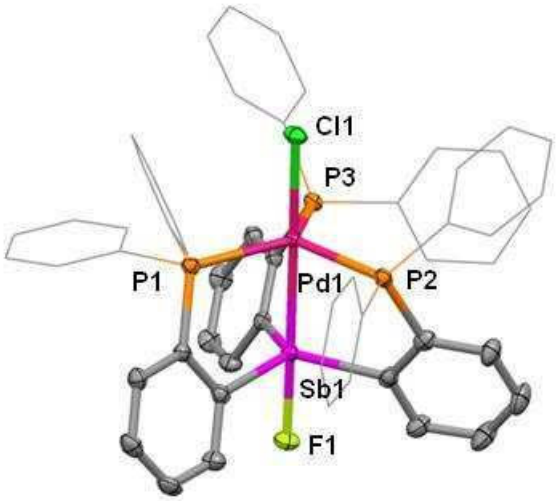

Figure 105. Crystal structure of **62**-F. Displacement ellipsoids are scaled to the 50% probability level. Hydrogens and have been omitted for clarity, and phenyl groups are depicted in wireframe. Selected bond lengths (Å) and angles (˚): Pd(1)-Cl(1) 2.4365(10), Sb(1)-Pd(1) 2.5721(7), Pd(1)-P(1) 2.3316(10), Pd(1)-P(3) 2.3480(10), Pd(1)-P(2) 2.3647(11), Sb(1)-F(1) 2.0320(19), Cl(1)-Pd(1)-Sb(1) 176.13(2), F(1)-Sb(1)-Pd(1) 177.59(5), C(37)-Sb(1)-C(1) 116.76(12) , C(37)-Sb(1)-C(19) 118.56(12), C(1)-Sb(1)-C(19) 120.70(12).

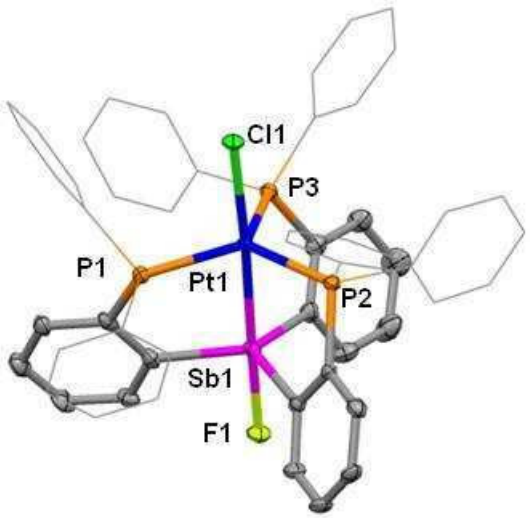

Figure 106. Crystal structure of **63**-F. Displacement ellipsoids are scaled to the 50% probability level. Hydrogens and have been omitted for clarity, and phenyl groups are depicted in wireframe. Selected bond lengths (Å) and angles (˚): Pt(1)-Sb(1) 2.5783(7), Pt(1)-Cl(1) 2.4493(12), Pt(1)-P(3) 2.2999(13), Pt(1)-P(1) 2.3179(13), Pt(1)-P(2) 2.3209(13), Sb(1)-F(1) 2.036(2), Cl(1)-Pt(1)-Sb(1) 176.07(3), F(1)-Sb(1)-Pt(1) 177.79(8), C(1)-Sb(1)-C(37) 116.36(17), C(1)-Sb(1)-C(19) 118.89(17), C(37)-Sb(1)-C(19) 121.02(17).

To determine the viability of **61**-BPh_4, **62**-BPh_4, and **63**-BPh_4 as fluoride sensors, the UV-Vis spectra of these complexes in CH_2Cl_2 were monitored upon incremental addition of a solution of TBAF (CH_2Cl_2). The UV-Vis spectrum of **61**-BPh_4 displays a broad absorption band centered at 587 nm assigned to d-d electronic transitions.[254,256,264-267] The addition of TBAF results in a slight quenching of this band, which is accompanied by a small hypsochromic shift of the center of the band to 557 nm (Figure 107). Fitting of these spectral changes to a 1:1 binding isotherm indicated that the fluoride binding constant (K_F) is $>10^6$ M^{-1}.

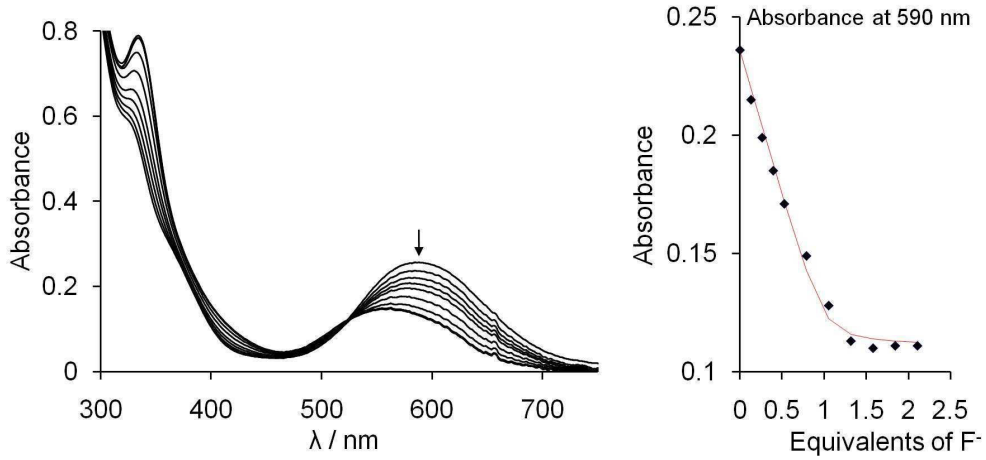

Figure 107. Spectral changes in the UV-Vis absorption spectra of **61**-BPh_4 (4.9×10^{-5} M) in CH_2Cl_2 upon incremental addition of a TBAF solution (3.9×10^{-3} M, CH_2Cl_2). The isotherms are plotted based on the absorbance at 590 nm, and the line indicates the fit to the calculated 1:1 binding isotherm.

The low energy edge of the UV-Vis spectrum of **62**-BPh_4 exhibits an absorption band centered at 368 nm. This band is quenched upon addition of TBAF, concomitant with the appearance of a new, broad absorption spanning from 400-560 nm (Figure 108). The

appearance of this band is responsible for the observed solution color change from yellow for **62**-BPh_4 to orange-red upon formation of **62**-F. The shape of the binding isotherm indicates that **62**-BPh_4 complexes fluoride almost quantitatively with a calculated K_F of $>10^8$ M^{-1}. The only low energy feature appearing in the UV-Vis spectrum of **63**-BPh_4 is a shoulder at around 345 nm. Incremental addition of TBAF results in the appearance of a broad absorption spanning from 380-500 nm, which is responsible for the appearance of the yellow color upon formation of **63**-F (Figure 109). Similar to **62**-BPh_4, the shape of the binding isotherm for **63**-BPh_4 suggests nearly quantitative fluoride binding in CH_2Cl_2 and a K_F greater than 10^8 M^{-1}.

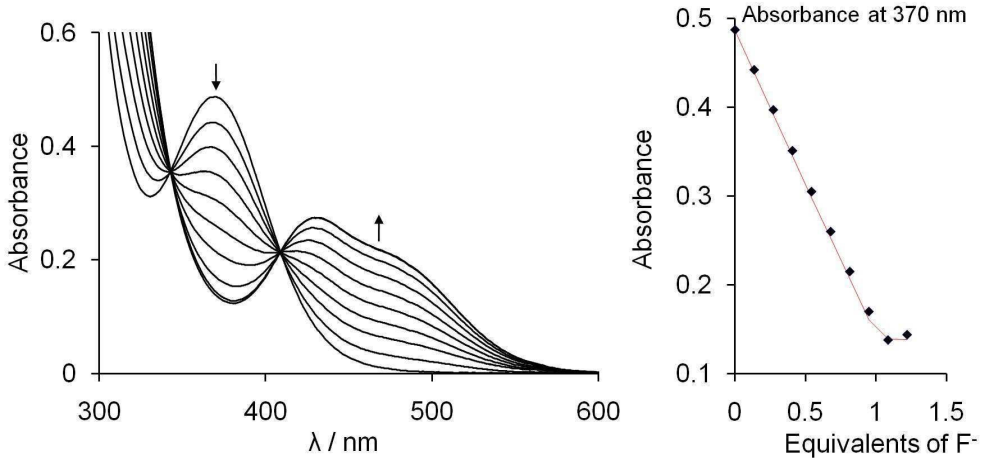

Figure 108. Spectral changes in the UV-Vis absorption spectra of **62**-BPh_4 (5.1×10^{-5} M) in CH_2Cl_2 upon incremental addition of a TBAF solution (4.1×10^{-3} M, CH_2Cl_2). The isotherms are plotted based on the absorbance at 370 nm, and the line indicates the fit to the calculated 1:1 binding isotherm.

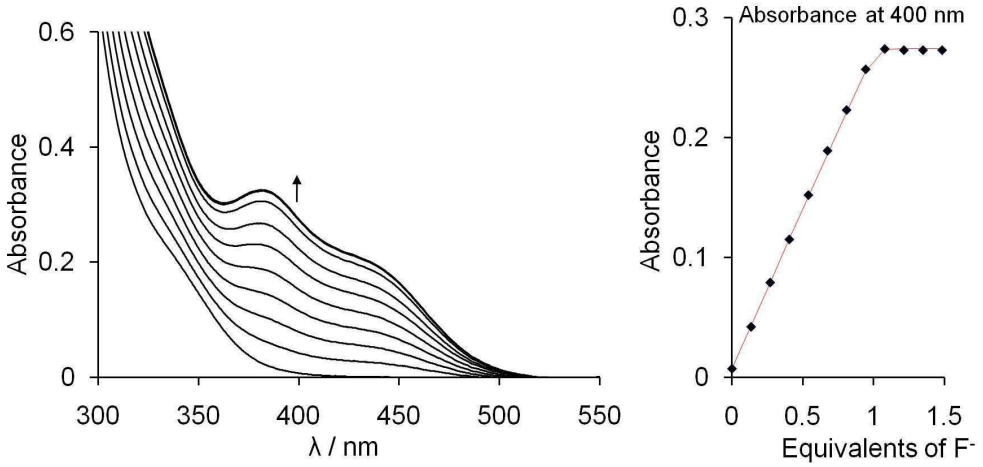

Figure 109. Spectral changes in the UV-Vis absorption spectra of **63**-BPh_4 (5.2×10^{-5} M) in CH_2Cl_2 upon incremental addition of a TBAF solution (4.2×10^{-3} M, CH_2Cl_2). The isotherms are plotted based on the absorbance at 400 nm, and the line indicates the fit to the calculated 1:1 binding isotherm.

The shift of the ligand field absorption band from λ_{max} = 587 nm for **61**-BPh_4 to λ_{max} = 557 nm for **61**-F reflects an increase in energy of the d-d transitions (xy, x^2-$y^2 \rightarrow z^2$) and (xz, yz $\rightarrow z^2$).[276] This increase may be attributed to a rise in energy of the unoccupied dz^2 orbital in **61**-F due to its stronger interaction with the with the equatorial phosphine ligands (Ni-P: 2.23 Å av. for **61**-F and 2.31 Å av. for **61**-BPh_4). Fluoride coordination to the Sb atom might also be expected lead to an increase of the donor strength of this axial ligand, pushing the dz^2 orbital up in energy. However, this effect is likely counteracted by the lengthening of the Ni-Sb bond distance going from **61**-BPh_4 (2.3548(9) Å) to **61**-F (2.5321(9) Å). In contrast, the changes in the UV-Vis absorption spectra of **62**-BPh_4 and **63**-BPh_4 upon reaction with fluoride reflect the change in the metal coordination geometry. The transformation of the Pd and Pt geometries from square planar to trigonal bipyramidal is concomitant with the appearance of bands assigned to the ligand field

transitions (xy, x^2-$y^2 \rightarrow z^2$) and (xz, yz $\rightarrow z^2$), which appear in the range 400-560 nm for **62**-F and 380-500 nm for **63**-F. This interpretation is in agreement with similar bands observed in the electronic spectra of other trigonal bipyramidal Pd and Pt complexes bearing pnictogen ligands.[264,266,276-279] In addition, the synthesis of the Pd pincer complex **64**-BPh_4 has been carried out in our lab. Preliminary studies show that, similar to **62**-BPh_4, **64**-BPh_4 binds fluoride to afford the fluorostiborane **64**-F (Figure 110). In addition, the Pd atom adopts a square planar geometry in both **64**-BPh_4 and **64**-F. The lowest energy absorption band in the electronic spectrum of **64**-BPh_4 appears at 353 nm, and, upon fluoride binding, the band shifts to higher energy, appearing at 318 nm for **64**-F. This observation supports our proposal that the appearance of the low energy bands in **62**-F and **63**-F is caused by a change in metal coordination geometry.

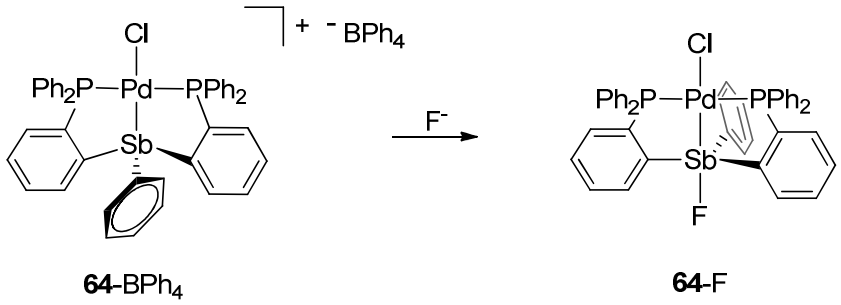

Figure 110. Reaction of the Pd pincer complex **64**-BPh_4 with F^-.

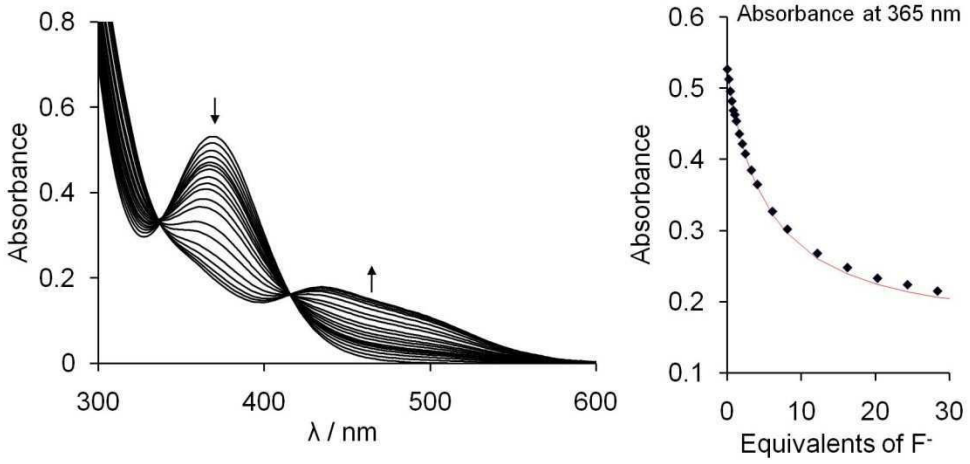

Figure 111. Spectral changes in the UV-Vis absorption spectra of **62**-BPh_4 (5.0×10^{-5} M) in MeOH/CH_2Cl_2 (9/1 vol.) upon incremental addition of a KF solution (6.0×10^{-3} M or 6.0×10^{-2} M, MeOH). The isotherms are plotted based on the absorbance at 455 nm and the line indicates the fit to the calculated 1:1 binding isotherm.

Considering the large fluoride binding constants measured for **61**-BPh_4, **62**-BPh_4, and **63**-BPh_4 in CH_2Cl_2, we sought to determine if these complexes would bind fluoride in protic solvents such as MeOH or MeOH/water. Unfortunately, **61**-BPh_4 quickly decomposed in MeOH/CH_2Cl_2 (9/1 vol.), as determined by the disappearance of the low energy absorption band at 587 nm over time. Under similar conditions, the titration of **63**-BPh_4 with a solution of KF in MeOH suffered from precipitation, which precluded completion of the titration and calculation of a binding constant. However, when a solution of **62**-BPh_4 in MeOH/CH_2Cl_2 (9/1 vol.) was titrated with a solution of KF in MeOH, changes similar to those for the titration in CH_2Cl_2 were observed resulting in a K_F of $4.5(\pm 1.0) \times 10^3$ M^{-1} (Figure 111).

The application of **61**-BPh_4, **62**-BPh_4, or **63**-BPh_4 as fluoride sensors is hampered by their incompatibility with protic solvents where sensing would be most practical.

Although a fluoride binding constant was obtained for **62**-BPh_4 in a MeOH/CH_2Cl_2 mixed solvent system, attempts to observe fluoride binding in the mixed organic solvent/H_2O solvent systems was complicated by precipitation of the complex. Additionally, changes in the UV-Vis spectra of **61**-BPh_4, **62**-BPh_4, and **63**-BPh_4 in CH_2Cl_2 upon addition of Cl^-, Br^-, and I^- pointed to possible interferences from these anions in fluoride sensing applications. In particular, we noticed that addition of Cl^- resulted in changes in the UV-Vis absorption spectra that were similar to those observed upon formation of **61**-F, **62**-F, and **63**-F. These changes suggested the likely formation of chlorostiborane species in CH_2Cl_2 solution.

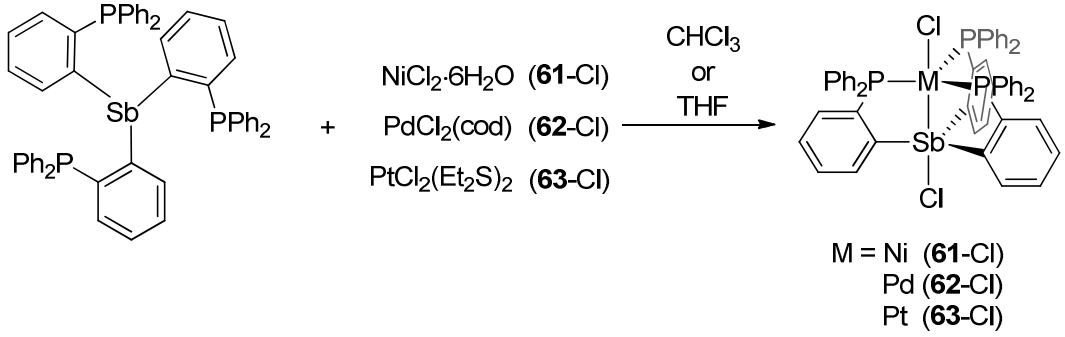

Figure 112. Synthesis of **61**-Cl, **62**-Cl, and **63**-Cl.

To verify this possibility, **61**-Cl, **62**-Cl, and **63**-Cl were isolated from the reaction of (*o*-$(Ph_2P)C_6H_4)_3Sb$ with $NiCl_2 \cdot 6H_2O$, $PdCl_2(cod)$, and $PtCl_2(Et_2S)_2$, respectively (Figure 112). Compound **61**-Cl -Cl was isolated as a dark purple powder, while compounds **62**-Cl and **63**-Cl are red and yellow, respectively, in the solid state. The color of these compounds in the solid state closely matches those of **61**-F, **62**-F, and **63**-F, providing an

initial indication of the formation of chlorostiborane species. The $^{31}P\{^{1}H\}$ NMR spectra ($CDCl_3$) of **61**-Cl, **62**-Cl, and **63**-Cl display single resonances at 35.4, 38.3, and 34.0 ppm, respectively (Table 16).

The X-ray crystal structures of **61**-Cl (Figure 113), **62**-Cl (Figure 114), and **63**-Cl (Figure 115) were determined, confirming the formation of Sb-Cl bonds in the solid state. The structures of these complexes are very similar to those observed for **61**-F, **62**-F, and **63**-F with the transition metal and Sb atoms each adopting trigonal bipyramidal geometries. In addition, the M-Sb distances remain largely unchanged from those measured for the respective fluorostiborane complexes (Table 16). The Sb-Cl bond distances for **61**-Cl, **62**-Cl, and **63**-Cl fall in the range 2.66-2.68 Å, longer than those measured for Ph_3SbCl_2 (2.49 Å *av*.)[280] or $[Ph_2SbCl_2]^-$ (2.61 Å *av*.).[281]

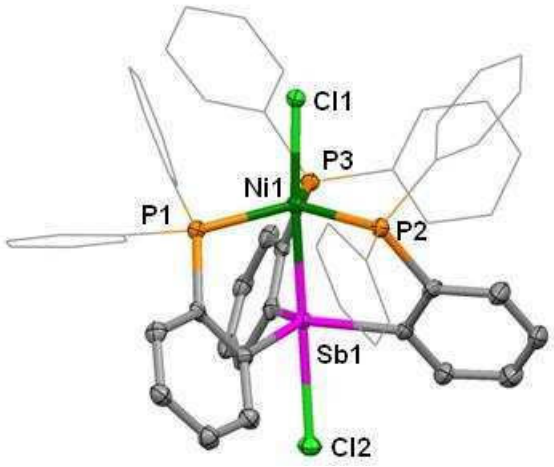

Figure 113. Crystal structure of **61**-Cl. Displacement ellipsoids are scaled to the 50% probability level. Hydrogens and have been omitted for clarity, and phenyl groups are depicted in wireframe. Selected bond lengths (Å) and angles (˚): Sb(1)-Ni(1) 2.4853(5), Ni(1)-Cl(1) 2.2813(9), Ni(1)-P(1) 2.2192(10), Ni(1)-P(2) 2.2277(10), Ni(1)-P(3) 2.2468(10), Sb(1)-Cl(2) 2.6834(9), Cl(1)-Ni(1)-Sb(1) 175.97(3), P(1)-Ni(1)-P(2) 119.47(4), P(1)-Ni(1)-P(3) 121.09(4), P(2)-Ni(1)-P(3) 117.41(4), Ni(1)-Sb(1)-Cl(2) 179.19(2), C(19)-Sb(1)-C(1) 114.11(12), C(19)-Sb(1)-C(37) 116.12(12), C(1)-Sb(1)-C(37) 125.58(12).

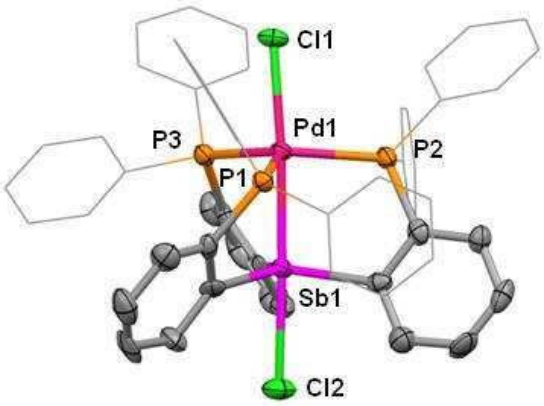

Figure 114. Crystal structure of **62**-Cl. Displacement ellipsoids are scaled to the 50% probability level. Hydrogens and have been omitted for clarity, and phenyl groups are depicted in wireframe. Selected bond lengths (Å) and angles (˚): Sb(1)-Pd(1) 2.5752(9), Pd(1)-Cl(1) 2.4687(18), Pd(1)-P(2) 2.3465(19), Pd(1)-P(1) 2.3838(19), Pd(1)-P(3) 2.4020(19), Sb(1)-Cl(2) 2.665(2), Cl(1)-Pd(1)-Sb(1) 174.31(5), P(2)-Pd(1)-P(1) 119.33(7), P(2)-Pd(1)-P(3) 122.28(6), P(1)-Pd(1)-P(3) 113.69(7), Pd(1)-Sb(1)-Cl(2) 177.62(5), C(19)-Sb(1)-C(37) 121.4(2), C(19)-Sb(1)-C(1) 114.8(2), C(37)-Sb(1)-C(1) 120.5(3).

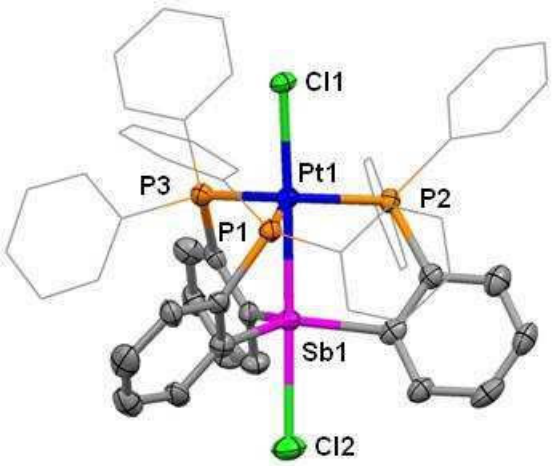

Figure 115. Crystal structure of **63**-Cl. Displacement ellipsoids are scaled to the 50% probability level. Hydrogens and have been omitted for clarity, and phenyl groups are depicted in wireframe. Selected bond lengths (Å) and angles (˚): Pt(1)-Sb(1) 2.5762(8), Pt(1)-Cl(1) 2.472(2), Pt(1)-P(1) 2.309(2), Pt(1)-P(2) 2.330(2), Pt(1)-P(3) 2.331(2), Sb(1)-Cl(2) 2.680(2), Cl(1)-Pt(1)-Sb(1) 174.68(5), P(1)-Pt(1)-P(2) 122.47(7), P(1)-Pt(1)-P(3) 119.94(8), P(2)-Pt(1)-P(3) 114.15(8), Pt(1)-Sb(1)-Cl(2) 177.36(6), C(1)-Sb(1)-C(37) 115.5(3), C(1)-Sb(1)-C(19) 122.3(3), C(37)-Sb(1)-C(19) 119.2(3).

The reported 1:1 electrolyte behavior of **61**-Cl and [Sb(*o*-$C_6H_4(AsPh_2)$)$_3$]$PdCl_2$, the arsine analog of **62**-Cl, in $MeNO_2$ suggests that the Sb-Cl bond dissociates and the Cl^- anion exhibits outer sphere behavior in polar solvents.[264-266] Indeed, the UV-Vis spectra of **61**-Cl, **62**-Cl, and **63**-Cl in MeOH closely match those of **61**-BPh_4, **62**-BPh_4, or **63**-BPh_4, indicating that the Cl^- anion should be dissociated in this solvent. Taking this into consideration, solutions of **61**-Cl, **62**-Cl, and **63**-Cl in $CDCl_3$ were treated with 1 equiv. of TBAF, and multinuclear NMR experiments confirmed quantitative formation to the fluorostiboranes **61**-F, **62**-F, and **63**-F. Similarly, layering the solutions of **61**-Cl, **62**-Cl, and **63**-Cl in $CDCl_3$ with 5 equiv. of KF in D_2O resulted in full conversion to the fluorostiborane species.

Based on the greater hydrophilicity of Cl^- versus BPh_4^-, we speculated that **61**-Cl, **62**-Cl, and **63**-Cl might exhibit greater solubility in MeOH or H_2O containing solvent mixtures. Therefore, we set out to perform UV-Vis fluoride titrations of these complexes in the presence of protic solvents, hoping to overcome the solubility and stability issues encountered with **61**-BPh_4, **62**-BPh_4, and **63**-BPh_4. Similar to **61**-BPh_4, UV-Vis samples of **61**-Cl were found to quickly decompose in the presence of MeOH. A UV-Vis fluoride titration was carried out on **62**-Cl in 9/1 MeOH/CH_2Cl_2 (Figure 116) to afford a calculated fluoride binding constant of 2.7(±0.2) × 10^3 M^{-1}, which is almost an order of magnitude lower than that found for **62**-BPh_4 (1.1(±0.2) × 10^4 M^{-1}) in the same solvent mixture. The decreased fluoride affinity of **62**-Cl versus **62**-BPh_4 seems to indicate that the Cl^- anion effectively competes with F^- for coordination to the Sb center.

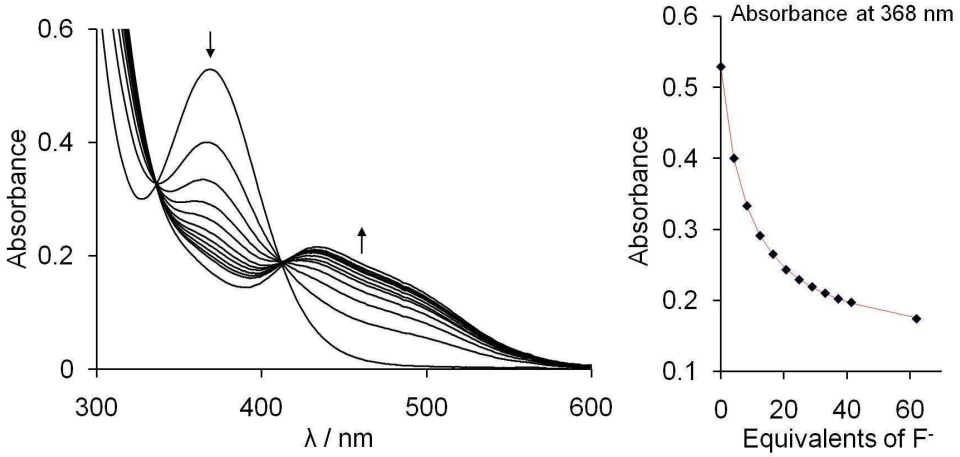

Figure 116. Spectral changes in the UV-Vis absorption spectra of **62**-Cl (5.1×10^{-5} M) in MeOH/CH_2Cl_2 (9/1 vol.) upon incremental addition of a KF solution (6.3×10^{-2} M, MeOH). The isotherms are plotted based on the absorbance at 368 nm, and the line indicates the fit to the calculated 1:1 binding isotherm.

Although attempted fluoride titrations of **63**-Cl in MeOH/CH_2Cl_2 mixtures again suffered from precipitation of the fluorostiborane, the titration of this complex was successfully carried out in a 2:1 MeOH/DMSO solvent mixture to afford a K_F of 8.5(±1.0) × 10^4 M^{-1} (Figure 117). The fluoride titration of **62**-Cl was carried out in the same solvent mixture with a calculated K_F of 4.5(±0.5) × 10^4 M^{-1} (Figure 118). The results of these titrations point to a higher fluoride affinity for the Pt complex **63**-Cl over the Pd complex **62**-Cl. Neither complex was sufficiently soluble to in varying H_2O/DMSO mixtures to obtain a full titration and fluoride binding constants.

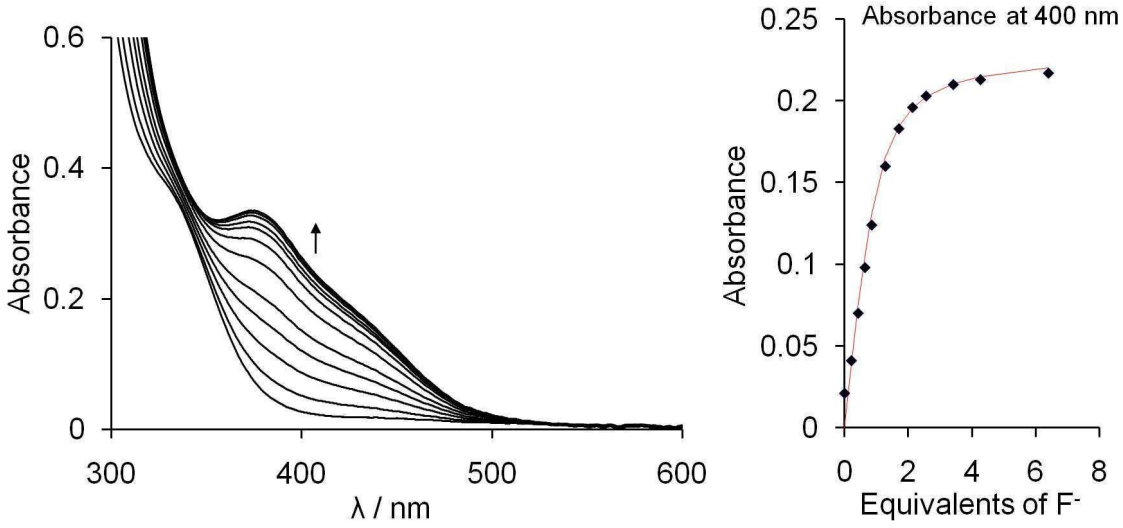

Figure 117. Spectral changes in the UV-Vis absorption spectra of **63**-Cl (5.0×10^{-5} M) in MeOH/DMSO (2/1 vol.) upon incremental addition of a KF solution (6.3×10^{-3} M, MeOH). The isotherms are plotted based on the absorbance at 400 nm, and the line indicates the fit to the calculated 1:1 binding isotherm.

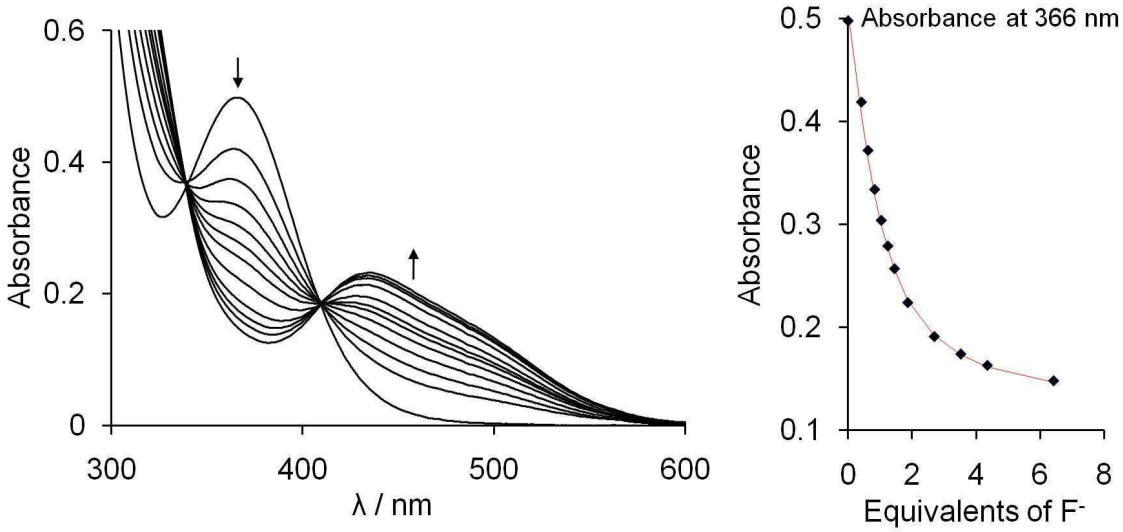

Figure 118. Spectral changes in the UV-Vis absorption spectra of **62**-Cl (5.1×10^{-5} M) in MeOH/DMSO (2/1 vol.) upon incremental addition of a KF solution (6.3×10^{-2} M, MeOH). The isotherms are plotted based on the absorbance at 266 nm, and the line indicates the fit to the calculated 1:1 binding isotherm.

6.3 Conclusions

In conclusion, we have structurally characterized a series of Group 10 transition metal complexes bearing the phosphanylstibine ligand (o-$(Ph_2P)C_6H_4)_3Sb$ and investigated their fluoride binding affinities. The cationic derivatives **61**-BPh_4, **62**-BPh_4, and **63**-BPh_4, containing the weakly coordinating BPh_4^- anion, are structurally dissimilar in the solid state, with the phosphanylstibine ligand adopting a κ-P,P,P,Sb coordination mode in the Ni^{2+} complex **61**-BPh_4 and a κ- P,P,Sb mode for the Pd^{2+} and Pt^{2+} complexes **62**-BPh_4 and **63**-BPh_4. In agreement with the crystal structures, the UV-Vis spectra of **62**-BPh_4 and **63**-BPh_4 support square planar geometries for the Pd and Pt atoms in solution. However, the presence of only a single $^{31}P\{^1H\}$ NMR resonance for these complexes in $CDCl_3$ suggests that the phosphines are in fast exchange on the NMR timescale.

Complexes **61**-BPh_4, **62**-BPh_4, and **63**-BPh_4 all exhibit a high affinity for fluoride in CH_2Cl_2 solution, resulting in formation of these fluorostiborane species **61**-F, **62**-F, and **63**-F. The crystal structures of the fluorostiboranes shows that fluoride coordination to the Sb center triggers κ-P,P,P,Sb coordination of the phosphanylstibine ligand and trigonal bipyramidal geometries around the Pd^{2+} and Pt^{2+} atoms in **62**-BPh_4 and **63**-BPh_4.

The solid state structures of the chloride derivatives **61**-Cl, **62**-Cl, and **63**-Cl were also determined, confirming formation of chlorostiborane species in the solid state. The similarity of the UV-Vis spectra of these complexes to **61**-BPh_4, **62**-BPh_4, and **63**-BPh_4 in polar organic solvents such as MeOH and DMSO suggest that the Cl^- anion at least partially dissociates in these solvents. This finding is in agreement with reported

conductivity studies which showed that **61**-Cl and an arsine derivative of **62-**Cl behave as 1:1 electrolytes in $MeNO_2$ solution.[264-266] In line with this interpretation, **61**-Cl, **62-**Cl, and **63-**Cl quantitatively bind fluoride under $CHCl_3/H_2O$ biphasic conditions to generate the corresponding fluorostiboranes. UV-Vis fluoride titrations of **62-**Cl and **63-**Cl with KF in a MeOH/DMSO (2/1 vol.) mixed solvent system afford fluoride binding constants of $4.5(\pm0.5) \times 10^4$ M^{-1} and $8.5(\pm1.0) \times 10^4$, respectively.

This work provides a proof of concept for our analogy between a tetraorganostibonium ion and transition metal-coordinated triarylstibine, with both showing a high affinity for F^- to produce fluorostiborane species. However, further investigations are needed for this concept to evolve into the development of useful fluoride sensors. Ligand modification or substitution to provide anion selectivity and water compatibility are major challenges to be addressed in the future. In addition, further studies into the electronic structure of these complexes will aid in the understanding of their inherent Lewis acidity.

6.4 Experimental

General Considerations. Antimony compounds are toxic and should be handled cautiously. KF and TBAF were purchased from Alfa Aesar. The ligand (*o*-$(Ph_2P)C_6H_4)_3Sb$[266], $PdCl_2(cod)$,[282] and $PtCl_2(SEt_2)_2$[283] were prepared according to the reported procedures. All preparations were carried out without any special precautions to exclude oxygen. Solvents were dried by passing through an alumina column (pentane and CH_2Cl_2) or refluxing under N_2 over Na/K (Et_2O, n-hexane, and THF). All other solvents were used as received. Ambient temperature NMR spectra were recorded on a Varian Unity Inova 400 FT NMR (399.59 MHz for ^1H, 375.99 MHz for ^{19}F, 161.74

MHz for ^{31}P, 100.45 MHz for ^{13}C) spectrometer. Low temperature ^{31}P NMR spectra were recorded on a Varian Inova 300 FT NMR spectrometer (121.42 MHz for ^{31}P). Chemical shifts (δ) are given in ppm and are referenced against residual solvent signals (^{1}H, ^{13}C) or external $BF_3 \cdot Et_2O$ (^{19}F) and H_3PO_4 (^{31}P).

Synthesis of 61-BPh_4. $NiCl_2 \cdot 6H_2O$ (31 mg, 0.13 mmol) was added as a solid to a solution of $(o\text{-}C_6H_4P(PPh_2))_3Sb$ (122 mg, 0.13 mmol) in THF (10 mL). The resulting purple solution was allowed to stir for 12 hrs at room temperature before removing the solvent *in vacuo*. The resulting dark purple residue was dissolved in CH_2Cl_2 (2 mL) and a solution of $NaBPh_4$ (44 mg, 0.13 mmol) in EtOH (8 mL) was added dropwise with stirring. A bright blue precipitate began to form immediately and the reaction mixture was stirred at room temperature for 2 hrs. The solid was collected by filtration, and washed with EtOH (3 × 2 mL) and Et_2O (3 × 2 mL) to afford 123 mg (77 % yield). Single crystals of **61**-BPh_4 suitable for X-ray diffraction were obtained by vapor diffusion of Et_2O into a solution of the compound in CH_2Cl_2. ^{1}H NMR (399.59 MHz; $CDCl_3$): δ 6.86-6.91 (m, 4H BPh + 12H PPh), 6.98-7.04 (m, 8H BPh + 12H PPh), 7.15 (t, 6H, *para*-PPh, $^{3}J_{H\text{-}H}$ = 7.41 Hz), 7.25 (m, 3H, *o*-P(Sb)C_6H_4), 7.52 (m, 3H *o*-P(Sb)C_6H_4 + 8H BPh), 7.61 (t, 3H, *o*-P(Sb)C_6H_4, $^{3}J_{H\text{-}H}$ = 7.51 Hz), 7.92 (d, 3H, *o*-P(Sb)C_6H_4, $^{3}J_{H\text{-}H}$ = 7.32 Hz). $^{13}C\{^{1}H\}$ NMR (100.45 MHz; $CDCl_3$): δ 121.61 (s), 125.56 (m), 128.43 (m), 129.88 (m), 131.88 (m), 132.64 (s), 134.24 (m), 134.44 (s), 136.43 (s), 136.98 (s), 142.09 (bm), 164.38 (q, J = 49.71 Hz), (2 *ipso*-C signals not observed). $^{31}P\{^{1}H\}$ NMR (161.74 MHz; $CDCl_3$): δ 36.48 (s). Elemental analysis calculated (%) for

$C_{78}H_{62}BClNiP_3Sb$ + 0.7 CH_2Cl_2: C, 68.57 H, 4.64; found C, 68.62; H 4.59 (approx. 0.8 eq. of CH_2Cl_2 was lost in drying).

Synthesis of 62-BPh_4. A solution of $PdCl_2$(cod) (cod = 1,5-cyclooctadiene) (38 mg, 0.13 mmol) in $CHCl_3$ (2 mL) was added to a solution of (*o*-$C_6H_4P(PPh_2)$)$_3$Sb (122 mg, 0.13 mmol) in $CHCl_3$ (10 mL) and the resulting red solution was allowed to stir for 12 hrs at room temperature before removing the solvent *in vacuo*. The resulting red/orange residue was dissolved in CH_2Cl_2 (2 mL) and a solution of $NaBPh_4$ (44 mg, 0.13 mmol) in EtOH (8 mL) was added dropwise with stirring. A pale yellow precipitate began to form immediately and the reaction mixture was stirred at room temperature for 2 hrs. The solid was collected by filtration and washed with EtOH (3 × 2 mL) and Et_2O (3 × 2 mL) to afford 143 mg (90 % yield). Single crystals of **62-**BPh_4 suitable for X-ray diffraction were obtained by vapor diffusion of Et_2O into a solution of the compound in $CHCl_3$. ^{1}H NMR (399.59 MHz; $CDCl_3$): δ 6.79 (t, 4H, BPh, $^3J_{H\text{-}H}$ = 7.14 Hz), 6.94 (t, 8H, BPh, $^3J_{H\text{-}H}$ = 7.33 Hz), 7.12 (m, 12H, *meta*-PPh), 7.20 (t, 12H, *ortho*-PPh, $^3J_{H\text{-}H}$ = 7.59 Hz), 7.26-7.36 (m, 6H *o*-P(Sb)C_6H_4 + 6H *para*-PPh), 7.40 (m, 8H, BPh), 7.45 (t, 3H, *o*-P(Sb)C_6H_4, $^3J_{H\text{-}H}$ = 7.51 Hz), 7.51 (d, 3H, *o*-P(Sb)C_6H_4, $^3J_{H\text{-}H}$ = 7.51 Hz). ^{13}C{^{1}H} NMR (100.45 MHz; $CDCl_3$): δ 121.54 (s), 125.42 (m), 129.03 (s), 129.27 (m), 131.30 (s), 133.25 (m), 135.52 (bs), 136.33 (s), 139.6 (bm), 164.25 (q, *J* = 49.59 Hz), (4 *ipso*-C signals not observed). ^{31}P{^{1}H} NMR (161.74 MHz; $CDCl_3$): δ 39.72 (s). ^{11}B NMR (128.2 MHz; $CDCl_3$): δ -6.75 (s). Elemental analysis calculated (%) for $C_{78}H_{62}BClPdP_3Sb$ + 2 $CHCl_3$: C, 59.85 H, 4.02; found C, 59.96; H 3.95.

Synthesis of 63-BPh_4. A solution of $PtCl_2(Et_2S)_2$ (56 mg, 0.12 mmol) in $CHCl_3$ (2 mL) was added to a solution of $(o\text{-}C_6H_4P(PPh_2))_3Sb$ (112 mg, 0.12 mmol) in $CHCl_3$ (10 mL). The resulting yellow solution was allowed to stir for 12 hrs at room temperature before removing the solvent *in vacuo*. The resulting yellow residue was dissolved in CH_2Cl_2 (2 mL), and a solution of $NaBPh_4$ (40 mg, 0.12 mmol) in EtOH (8 mL) was added dropwise with stirring. A white precipitate began to form immediately and the reaction mixture stirred at room temperature for 2 hrs. The solid was collected by filtration, and washed with EtOH (3 × 2 mL) and Et_2O (3 × 2 mL) to afford 145 mg (93 % yield). Single crystals of **63**-BPh_4 suitable for X-ray diffraction were obtained by vapor diffusion of Et_2O into a solution of the compound in $CHCl_3$. ^{1}H NMR (399.59 MHz; $CDCl_3$): δ 6.79 (t, 4H, BPh, $^3J_{H\text{-}H}$ = 7.14 Hz), 6.94 (t, 8H, BPh, $^3J_{H\text{-}H}$ = 7.33 Hz), 7.16-7.40 (m, 47H, *o*-P(Sb)C_6H_4 + BPh + PPh), 7.65 (d, 3H, *o*-P(Sb)C_6H_4, $^3J_{H\text{-}H}$ = 7.08 Hz). $^{13}C\{^1H\}$ NMR (100.45 MHz; $CDCl_3$): δ 121.51 (s), 125.41 (m), 129.01 (m), 129.22 (m), 131.36 (s), 132.87 (s), 133.04 (s), 133.25 (m), 135.59 (q, *J* = 6.86 Hz), 136.14 (s), 136.30 (s), 138.06 (m), 140.24 (m), 164.25 (q, *J* = 49.59 Hz). $^{31}P\{^1H\}$ NMR (161.74 MHz; $CDCl_3$): δ 38.23 (s, $^1J_{P\text{-}195Pt}$ = 1737.35 Hz). ^{11}B NMR (128.2 MHz; $CDCl_3$): δ -6.77 (s).

Synthesis of 61-F, 62-F, and 63-F. The fluorostiborane complexes could be prepared *in situ* by the addition of 1 equiv. of TBAF to solutions of **61**-BPh_4, **62**-BPh_4, and **63**-BPh_4 in $CDCl_3$. Alternatively, solutions of **61**-Cl, **62**-Cl, and **63**-Cl in $CHCl_3$ were layered and shaken with aqueous solutions of KF (5 equiv.). Multinuclear NMR experiments confirmed quantitative conversion to the fluorostiborane species in both

cases. For the biphasic reaction, the layers were carefully separated, and vapor diffusion of Et_2O into the $CHCl_3$ solution generated single crystals of **61**-F, **62**-F, and **63**-F suitable for X-ray diffraction. Data for **61**-F: ^{1}H NMR (399.59 MHz; $CDCl_3$): δ 6.90-7.01 (m, 12H PPh + 3H *o*-P(Sb)C_6H_4), 7.08-7.21 (m, 18H PPh + 3H *o*-P(Sb)C_6H_4), 7.33 (t, 3H, *o*-P(Sb)C_6H_4, $^3J_{H\text{-}H}$ = 7.51 Hz), 8.39 (d, 3H, *o*-P(Sb)C_6H_4, $^3J_{H\text{-}H}$ = 7.69 Hz). ^{13}C{^{1}H} NMR (100.45 MHz; $CDCl_3$): δ 127.52 (m), 128.67 (s), 129.61 (s), 130.23 (s), 132.85 (s), 133.49 (m), 135.19 (bs), (3 *ipso*-C signals not observed). ^{31}P{^{1}H} NMR (161.74 MHz; $CDCl_3$): δ 40.91 (d, $^3J_{F\text{-}P}$ = 6.17 Hz). ^{19}F NMR (375.97 MHz; $CDCl_3$): δ -129.55 (bs). Data for **62**-F: ^{1}H NMR (399.59 MHz; $CDCl_3$): δ 6.88 (d, 3H, *o*-P(Sb)C_6H_4, $^3J_{H\text{-}H}$ = 7.32 Hz), 7.03 (t, 12H, PPh, $^3J_{H\text{-}H}$ = 7.51 Hz), 7.09-7.15 (m, 6H PPh + 3H *o*-P(Sb)C_6H_4), 7.21-7.29 (m, 12H PPh + 3H *o*-P(Sb)C_6H_4), 8.29 (d, 3H, *o*-P(Sb)C_6H_4, $^3J_{H\text{-}H}$ = 7.87 Hz). ^{13}C{^{1}H} NMR (100.45 MHz; $CDCl_3$): δ 127.83 (m), 129.11 (s), 129.75 (s), 130.28 (s), 132.55 (s), 133.49 (m), 133.65 (m), 136.03 (m), 138.88 (q, *J* = 10.69 Hz), 148.41 (m). ^{31}P{^{1}H} NMR (161.74 MHz; $CDCl_3$): δ 41.90 (d, $^3J_{F\text{-}P}$ = 20.66 Hz). ^{19}F NMR (375.97 MHz; $CDCl_3$): δ -129.72 (q, $^3J_{F\text{-}P}$ = 20.66 Hz). Data for **63**-F: ^{1}H NMR (399.59 MHz; $CDCl_3$): δ 6.95 (t, 12H, PPh, $^3J_{H\text{-}H}$ = 7.51 Hz), 7.05-7.12 (m, 18H PPh), 7.14-7.22 (m, 6H, *o*-P(Sb)C_6H_4), 7.41 (t, 3H, *o*-P(Sb)C_6H_4, $^3J_{H\text{-}H}$ = 6.86 Hz), 8.83 (d, 3H, *o*-P(Sb)C_6H_4, $^3J_{H\text{-}H}$ = 7.69 Hz). ^{13}C{^{1}H} NMR (100.45 MHz; $CDCl_3$): δ 127.61 (m), 128.81 (s), 130.12 (s), 130.28 (s), 132.93 (m, 2C), 135.32 (m), 136.81 (bs), 138.07 (m), 148.93 (m). ^{31}P{^{1}H} NMR (161.74 MHz; $CDCl_3$): δ 40.07 (d, $^3J_{F\text{-}P}$ = 9.86 Hz, , $^1J_{P\text{-}195Pt}$ = 3204.6 Hz). ^{19}F NMR (375.97 MHz; $CDCl_3$): δ -129.72 (q, $^3J_{F\text{-}P}$ = 9.86 Hz).

Synthesis of 61-Cl. $NiCl_2 \cdot 6H_2O$ (62 mg, 0.26 mmol) was added as a solid to a solution of $(o\text{-}C_6H_4P(PPh_2))_3Sb$ (236 mg, 0.26 mmol) in THF (10 mL). The resulting purple solution was allowed to stir for 12 hrs at room temperature before removing the solvent *in vacuo*. The dark purple residue was extracted with 20 mL of $CHCl_3$, filtered over Celite, and concentrated to *ca.* 5 mL *in vacuo*. The product was precipitated by addition of Et_2O (10 mL), filtered, and washed with Et_2O (3 × 5 mL) to afford 220 mg (81 % yield) as a dark purple solid. Single crystals of **61**-Cl suitable for X-ray diffraction were obtained by vapor diffusion of Et_2O into a solution of the compound in $CHCl_3$. ^{1}H NMR (399.59 MHz; $CDCl_3$): δ 6.89 (t, 12H, *ortho* Ph-C*H,* $^3J_{H\text{-}H}$ = 7.70 Hz), 7.05 (m, 12H, *meta* Ph-C*H*), 7.11-7.18 (m, 9H, *o*-P(Sb)C_6H_4 + *para* Ph-C*H*), 7.45 (t, 3H, *o*-P(Sb)C_6H_4, $^3J_{H\text{-}H}$ = 7.69 Hz), 7.84 (t, 3H, *o*-P(Sb)C_6H_4, $^3J_{H\text{-}H}$ = 7.69 Hz), 9.99 (d, 3H, *o*-P(Sb)C_6H_4, $^3J_{H\text{-}H}$ = 7.69 Hz). $^{13}C\{^1H\}$ NMR (100.45 MHz; $CDCl_3$): δ 128.14 (s), 129.47 (s), 131.74 (s), 132.26 (s), 133.58 (s), 135.53 (s), 137.80 (m), 139.75 (dd, *J* = 38.14 Hz, *J* = 20.60 Hz), 141.33 (dd, *J* = 27.46 Hz, *J* = 14.50 Hz), (one *ipso*-C signal not observed). $^{31}P\{^1H\}$ NMR (161.74 MHz; $CDCl_3$): δ 35.42 (s).

Synthesis of 62-Cl. A solution of $PdCl_2$(cod) (cod = 1,5-cyclooctadiene) (47 mg, 0.16 mmol) in $CHCl_3$ (2 mL) was added to a solution of $(o\text{-}C_6H_4P(PPh_2))_3Sb$ (150 mg, 0.16 mmol) in $CHCl_3$ (10 mL). The resulting red solution was allowed to stir for 12 hrs at room temperature. The reaction mixture was concentrated to *ca.* 5 mL *in vacuo* and the product was precipitated by addition of Et_2O (10 mL). The product was filtered and washed with Et_2O (3 × 5 mL) to afford 124 mg (70 % yield) as a red solid. Single crystals of **62**-Cl suitable for X-ray diffraction were obtained by vapor diffusion of Et_2O

into a solution of the compound in $CHCl_3$. ^1H NMR (399.59 MHz; $CDCl_3$): δ 7.12-7.20 (m, 27H, *o*-P(Sb)C_6H_4 + *para* Ph-C*H*), 7.28 (m, 6H, *para* Ph-C*H*), 7.47 (t, 3H, *o*-P(Sb)C_6H_4, $^3J_{H\text{-}H}$ = 7.42 Hz), 7.59 (t, 3H, *o*-P(Sb)C_6H_4, $^3J_{H\text{-}H}$ = 7.51 Hz), 8.43 (d, 3H, *o*-P(Sb)C_6H_4, $^3J_{H\text{-}H}$ = 7.69 Hz). $^{13}C\{^1H\}$ NMR (100.45 MHz; $CDCl_3$): δ 128.73 (q, *J* = 3.05 Hz), 130.37 (dd, *J* = 23.65 Hz, *J* = 10.68 Hz), 130.71 (s), 132.35 (s), 132.83 (s), 133.23 (q, *J* = 5.34 Hz), 135.51 (s), 136.73 (q, *J* = 6.86 Hz), 139.46 (m), 141.42 (m). $^{31}P\{^1H\}$ NMR (161.74 MHz; $CDCl_3$): δ 38.31 (s). Elemental analysis calculated (%) for $C_{54}H_{42}Cl_2PdP_3Sb$ + $CHCl_3$: C, 54.94 H, 3.60; found C, 55.08; H 3.57.

Synthesis of 63-Cl. A solution of $PtCl_2(Et_2S)_2$ (74 mg, 0.16 mmol) in $CHCl_3$ (2 mL) was added to a solution of (*o*-$C_6H_4P(PPh_2)$)$_3$Sb (150 mg, 0.16 mmol) in $CHCl_3$ (10 mL). The resulting yellow solution was allowed to stir for 12 hrs at room temperature. The reaction mixture was concentrated to *ca.* 5 mL *in vacuo*, and the product was precipitated by addition of Et_2O (10 mL). The product was filtered and washed with Et_2O (3 × 5 mL) to afford 127 mg (65 % yield) as a yellow solid. Single crystals of **63**-Cl suitable for X-ray diffraction were obtained by vapor diffusion of Et_2O into a solution of the compound in $CHCl_3$. ^1H NMR (399.59 MHz; $CDCl_3$): δ 7.08-7.17 (m, 27H, *o*-P(Sb)C_6H_4 + *para* Ph-C*H*), 7.23 (m, 6H, *para* Ph-C*H*), 7.37 (t, 3H, *o*-P(Sb)C_6H_4, $^3J_{H\text{-}H}$ = 7.41 Hz), 7.55 (t, 3H, *o*-P(Sb)C_6H_4, $^3J_{H\text{-}H}$ = 7.51 Hz), 9.08 (d, 3H, *o*-P(Sb)C_6H_4, $^3J_{H\text{-}H}$ = 7.50 Hz). $^{13}C\{^1H\}$ NMR (100.45 MHz; $CDCl_3$): δ 128.46 (s), 130.33 (s), 131.62 (dd, *J* = 27.41 Hz, *J* = 16.38 Hz), 131.94 (s), 132.48 (s), 132.96 (q, *J* = 4.66 Hz), 134.99 (bs), 137.29 (q, *J* = 5.35 Hz), 139.42-140.55 (bm, 2C). $^{31}P\{^1H\}$ NMR (161.74 MHz;

$CDCl_3$): δ 34.01 (s, $^1J_{P\text{-}195Pt}$ = 2305.7 Hz). Elemental analysis calculated (%) for $C_{54}H_{42}Cl_2PtP_3Sb + CHCl_3$: C, 51.17 H, 3.36; found C, 51.20; H 3.30.

Crystallography. Single crystals of **61**-BPh_4 suitable for X-ray diffraction were obtained by vapor diffusion of Et_2O into a solution of the compound in CH_2Cl_2. Single crystals of **62-**BPh_4, **63-**BPh_4, **61**-Cl, **62-**Cl, **63-**Cl, **61**-F, **62-**F, and **63-**F suitable for X-ray diffraction were obtained by vapor diffusion of Et_2O into a solution of the compound in $CHCl_3$. Crystal data, details of data collection, and structure refinement parameters for compounds **61**-BPh_4, **62-**BPh_4, and **63-**BPh_4 are included in Table 17. Data for **61**-F, **62-**F, and **63-**F are included in Table 18. Data for **61**-Cl, **62-**Cl, and **63-**Cl are listed in Table 19. The crystallographic measurements were performed using a Bruker-AXS APEX-II CCD area detector diffractometer, with a graphite-monochromated Mo-Kα radiation (λ = 0.71069 Å). A specimen of suitable size and quality was selected and mounted onto a nylon loop. The semiempirical method SADABS[207] was applied for absorption correction. The structures were solved by direct methods using SHELXTL/PC package (version 6.1)[208] which successfully located most of the non-hydrogen atoms. Subsequent refinement on F^2 allowed location of the remaining non-hydrogen atoms. All H atoms were geometrically placed and refined in a riding model approximation.

Table 17. Crystal data, data collections, and structure refinements for **61**-BPh_4, **62-**BPh_4, and **63-**BPh_4.

Crystal data	**61**-BPh_4·1.5CH_2Cl_2	**62-**BPh_4·2$CHCl_3$	**63-**BPh_4·$CHCl_3$
Formula	$C_{79.5}H_{65}BCl_4NiP_3Sb$	$C_{80}H_{64}BCl_7PdP_3Sb$	$C_{79}H_{63}BCl_4PtP_3Sb$
Mr	1446.40	1605.33	1574.65
Crystal size/mm	0.16 x 0.12 x 0.09	0.30 x 0.14 x 0.10	0.21 x 0.12 x 0.09
Crystal system	Monoclinic	Monoclinic	Monoclinic
Space group	C2/c	C2/c	P2(1)/c
a/Å	49.945(4)	35.659(3)	10.2383(10)
b/Å	9.6700(9)	13.8104(13)	30.025(3)
c/Å	34.967(3)	29.789(3)	21.705(2)
α /°	90	90	90
β/°	129.231(4)	104.9710(10)	93.4090(10)
γ /°	90	90	90
V/Å^3	13081(2)	14172(2)	6660.4(11)
Z	4	8	4
ρ_{calc}/g cm^{-3}	1.469	1.505	1.570
μ/mm^{-1}	0.984	1.012	2.782
F(000)	5912	6480	3136
T/K	173(2)	110(2)	110(2)
Scan mode	ω, φ	ω, φ	ω, φ
hkl Range	-60 → +60	-43 → +43	-12 → +12
	-11 → +11	-17 → +17	-37 → +37
	-42 → +42	-36 → +36	-26 → +26
Measd reflns	62666	73196	69770
Unique reflns [Rint]	12176 [0.0744]	13935 [0.0501]	13088 [0.0484]
Reflns used for refinement	12176	13935	13088
Refined parameters	808	838	802
GooF	1.065	1.016	1.022
R1,[a] *w*R2[b] (all data)	0.0848, 0.1702	0.0631, 0.1314	0.0359, 0.0651
ρ_{fin} (max., min.)/eÅ^{-3}	1.506, -1.905	4.241, -3.494	1.424, -1.343

[a] $R1 = \Sigma||F_o| - |F_c||/\Sigma|F_o|$. [b] $wR2$ $([\Sigma w(F_o^2 - F_c^2)^2]/[\Sigma\, w(F_o^2)^2])^{1/2}$; $w = 1/[\sigma^2(F_o^2) + (ap)^2 + bp]$; $p = (F_o^2 + 2F_c^2)/3$ with $a = 0.0635$ for **61**-BPh_4, 0.0534 for **62-**BPh_4, and 0.0227 for **63-**BPh_4; and $b = 201.6285$ for **61**-BPh_4, 155.6418 for **62-**BPh_4, and 11.6973 for **63-**BPh_4.

Table 18. Crystal data, data collections, and structure refinements for **61**-F, **62-**F, and **63-**F.

Crystal data	**61**-F	**62-**F	**63-**F
Formula	$C_{54}H_{42}ClFNiP_3Sb$	$C_{54}H_{42}ClFPdP_3Sb$	$C_{54}H_{42}ClFPtP_3Sb$
Mr	1018.70	1066.39	1155.08
Crystal size/mm	0.14 x 0.07 x 0.06	0.13 x 0.11 x 0.06	0.14 x 0.09 x 0.05
Crystal system	Monoclinic	Monoclinic	Monoclinic
Space group	P2(1)/c	P2(1)/c	P2(1)/c
a/Å	12.768(5)	12.920(4)	12.865(4)
b/Å	17.378(7)	17.451(6)	17.498(5)
c/Å	19.853(8)	19.915(6)	19.948(6)
α /°	90	90	90
β/°	99.777(5)	98.913(4)	99.066(4)
γ /°	90	90	90
V/Å^3	4341(3)	4436(2)	4434(2)
Z	4	4	4
ρ_{calc}/g cm^{-3}	1.559	1.597	1.730
μ/mm^{-1}	1.271	1.225	3.971
F(000)	2064	2136	2264
T/K	110(2)	110(2)	110(2)
Scan mode	ω, φ	ω, φ	ω, φ
hkl Range	-15 → +15	-15 → +15	-15 → +15
	-21 → +21	-21 → +21	-21 → +21
	-24 → +24	-24 → +24	-24 → +24
Measd reflns	44167	43805	37957
Unique reflns [Rint]	8516 [0.0697]	8712 [0.0585]	8713 [0.0570]
Reflns used for refinement	8516	8712	8713
Refined parameters	550	550	550
GooF	1.018	1.036	1.025
R1,[a] *w*R2[b] (all data)	0.0557, 0.1039	0.0448, 0.0733	0.0447, 0.0718
ρ_{fin} (max., min.)/eÅ^{-3}	0.750, -0.668	0.623, -0.594	0.765, -0.763

[a] $R1 = \Sigma||F_o| - |F_c||/\Sigma|F_o|$. [b] $wR2$ $([\Sigma w(F_o^2 - F_c^2)^2]/[\Sigma w(F_o^2)^2])^{1/2}$; $w = 1/[\sigma^2(F_o^2) + (ap)^2 + bp]$; $p = (F_o^2 + 2F_c^2)/3$ with a = 0.0520 for **61**-F, 0.0268 for **62-**F, and 0.0313 for **63-**F; and b = 3.3536 for **61**-F, 4.1355 for **62-**F, and 1.9695 for **63-**F.

Table 19. Crystal data, data collections, and structure refinements for **61**-Cl, **62-**Cl, and **63-**Cl.

Crystal data	**61**-Cl	**62-**Cl·$CHCl_3$	**63-**Cl·$CHCl_3$
Formula	$C_{54}H_{42}Cl_2NiP_3Sb$	$C_{55}H_{43}Cl_5PdP_3Sb$	$C_{55}H_{43}Cl_5PtP_3Sb$
Mr	1035.15	1202.2	1290.89
Crystal size/mm	0.10 x 0.08 x 0.06	0.21 x 0.16 x 0.11	0.05 x 0.04 x 0.03
Crystal system	Orthorhombic	Monoclinic	Monoclinic
Space group	Pbca	P2(1)/c	P2(1)/c
a/Å	20.9921(11)	21.575(7)	21.367(6)
b/Å	19.6914(10)	13.656(5)	13.698(4)
c/Å	21.4716(11)	17.907(6)	17.659(5)
α /°	90	90	90
β/°	90	108.984(6)	109.346(4)
γ /°	90	90	90
V/Å^3	8875.6(8)	4989(3)	4136.5(6)
Z	8	4	4
ρ_{calc}/g cm^{-3}	1.549	1.601	1.758
μ/mm^{-1}	1.300	1.304	3.830
F(000)	4192	2400	2528
T/K	110(2)	110(2)	110(2)
Scan mode	ω, φ	ω, φ	ω, φ
hkl Range	-25 → +25	-22 → +26	-25 → +25
	-23 → +23	-15 → +16	-16 → +16
	-25 → +26	-21 → +19	-21 → +21
Measd reflns	102989	27466	34894
Unique reflns [Rint]	8256 [0.1033]	9239 [0.0720]	8745 [0.1073]
Reflns used for refinement	8256	9239	8745
Refined parameters	550	586	605
GooF	1.024	1.028	1.021
R1,[a] *w*R2[b] (all data)	0.0566, 0.0838	0.0992, 0.1522	0.0842, 0.1310
ρ_{fin} (max., min.)/eÅ^{-3}	0.476, -0.814	1.010, -0.974	2.138, -1.522

[a] $R1 = \Sigma||F_o| - |F_c||/\Sigma|F_o|$. [b] $wR2$ $([\Sigma\, w(F_o^2 - F_c^2)^2]/[\Sigma\, w(F_o^2)^2])^{1/2}$; $w = 1/[\sigma^2(F_o^2) + (ap)^2 + bp]$; $p = (F_o^2 + 2F_c^2)/3$ with a = 0.0414 for **61**-Cl, 0.0732 for **62-**Cl, and 0.0502 for **63-**Cl; and b = 4.8577 for **61**-Cl, 0 for **62-**Cl, and 0 for **63-**Cl.

CHAPTER VII

BIS-GOLD(I) AND GOLD(I)/BORON COMPLEXES WITH *PERI*-NAPHTHALENEDIYL BACKBONES*

7.1 Introduction

Interest in bridged dinuclear gold(I) complexes containing short, intramolecular Au-Au distances arises from their often rich optical properties[284,285] as well as their unique structures which allow for study of the metal-metal interactions.[286] A number of bridging ligands, such as diphosphines,[287-291] phosphine ylides,[292-297] or cyclometalating phosphines or arsines,[298,299] have been used to scaffold both homo- and heterobridged molecules. Dinuclear gold(I) complexes bearing dianionic μ-C-C bridging ligands are more scarce, particularly those which allow short Au-Au contacts. Two examples of such structures include 1,1'-*bis*(triphenylphosphinegold)-biphenyl and 1,1'-*bis*(triphenylphosphinegold)-diphenylmethane for which, despite the flexibility of the bridging diaryl ligand, Au-Au distances of 3.169 Å and 3.012 Å, respectively, were reported.[300,301] In addition, Yam, *et al*. have described the preparation of a 1,8-diaurionaphthalene complex (**65**) and examined its luminescence properties and reactivity with respect to oxidative addition (Figure 119).[302]

---

* Reprinted in part from: "Synthesis, structure and luminescence of 1,8-diaurionaphthalenes" Wade, C. R.; Yakovenko, A. A.; Gabbaï F. P. *New J. Chem.* **2010***, 34*, 1646-1651. -Reproduced by permission of The Royal Society of Chemistry (RSC) on behalf of the Centre National de la Reecherche Scientifique (CNRS) and the RSC.

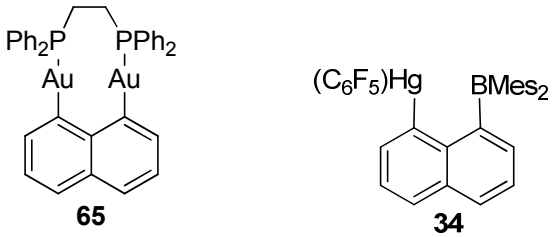

Figure 119. Diaurionaphthalene complex **65** and mercury/borane **34**.

In the interest of developing synthetic routes to access gold(I)/boron complexes, we began investigating the synthesis of 1,8-diaurionaphthalene complexes using 1,8-dilithionaphthalene as a precursor. As a result, the synthesis, structural characterization, and photophysical properties of two new 1,8-diaurionaphthalene complexes $[Au_2(\mu\text{-}C_{10}H_6)(Et_3P)_2]$ (**66**) and $[Au_2(\mu\text{-}C_{10}H_6)(\mu\text{-dppm})]$ (dppm = $Ph_2P(CH_2)PPh_2$) (**67**), are described in this chapter. In the course of this work, we prepared a novel $[Au_4Ag_2]^{2+}$ metallocycle (**68**), which is also described.

Based on our previous work with *peri*-substituted naphthalene derivatives such as **34**,[122] we considered the use of the 1,8-naphthalenediyl backbone as a bridging scaffold to support gold(I)/boron complexes (Figure 119). Our interest in such complexes arises from their analogy to the Hg/B compound **34**, which forms a B-F-Hg chelate complex with fluoride and acts as a phosphorescent sensor for this anion. Additionally, the 1,8-naphthalenediyl backbone could be expected to enforce a short Au-B separation, potentially leading to a strong Au→B Z-type bonding interaction. The use of triarylboranes as σ-acceptor ligands toward transition metals has garnered a great deal of attention.[303] Although most studies describing complexes containing metal→triarylborane interactions have focused on fundamental bonding aspects, a recent

report detailing the reactivity of a complex containing a Fe→B interaction suggests that these ligands may be useful for supporting multiple redox states.[304] As a result of these interests, this chapter includes the synthesis and structural characterization of two new gold(I)/boron complexes **69** and **70**.

7.2 Synthesis and structural characterization of 1,8-diaurionaphthalenes

The synthesis described by Yam, *et al.* for **65** involves the reaction of 1,8-*bis*(trimethylstannyl)naphthalene with $[Au_2Cl_2(\mu\text{-dppe})]$ (dppe = 1,2-*bis*(diphenylphosphino)ethane).[302] To avoid the use of toxic organotin reagents and additional synthetic steps, we employed 1,8-dilithionaphthalene as a starting material for our investigation of aurated napthalene derivatives. Reaction of this dilithium reagent with *in situ* prepared $[AuCl(Et_3P)]$ and $[Au_2Cl_2(\mu\text{-dppm})]$ afforded **66** and **67**, respectively (Figure 120). Although **67** was obtained in up to 71 % yield, only small amounts of **66** (≤10 % yield) were isolated from the reaction mixtures. Both **66** and **67** have been fully characterized by multinuclear NMR and X-ray diffraction. The compounds are moderately soluble in CH_2Cl_2, C_6H_6, and THF but are insoluble in MeOH, Et_2O, and hydrocarbon solvents. The $^{31}P\{^1H\}$ NMR spectra of **66** and **67** display single resonances at 38 ppm (CD_2Cl_2) and 29 ppm ($CDCl_3$), respectively, indicating the symmetrical nature of the structures in solution. Accordingly, the ^1H NMR spectrum of each complex displays all the expected resonances, including three sets of signals corresponding to the symmetrically substituted 1,8-naphthalene backbones.

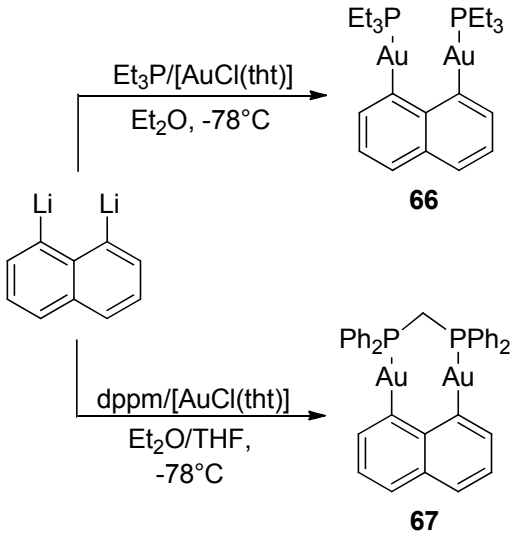

Figure 120. Synthesis of **66** and **67**.

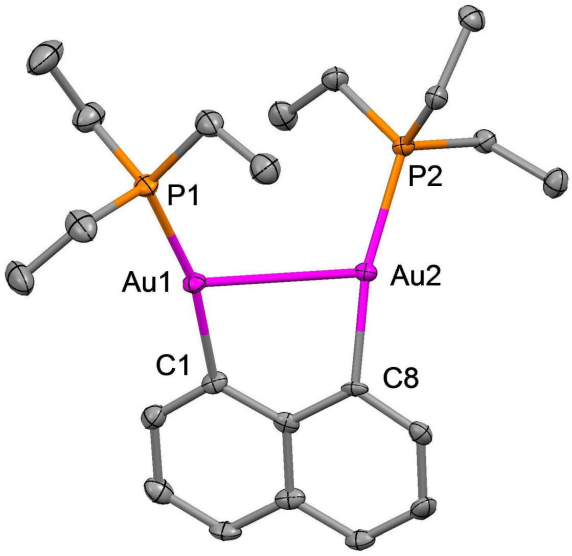

Figure 121. Crystal structure of complex **66**. Ellipsoids are scaled to the 50% probability level, and hydrogen atoms have been omitted for clarity. Selected bond lengths (Å) and angles (˚): Au(1)-Au(2) 2.9982(5), Au(1)-P(1) 2.2855(11), Au(2)-P(2) 2.2893(11), Au(1)-C(1) 2.057(4), Au(2)-C(8) 2.055(4); C(1)-Au(1)-P(1) 166.89(12), C(8)-Au(2)-P(2) 163.89(11).

The X-ray crystal structure of **66** was determined using single crystals obtained by cooling a CH_2Cl_2/Et_2O solution of the compound (Figure 121). The complex crystallizes in the space group $P2_1/n$ and exhibits linearly coordinated gold atoms (C(1)-Au(1)-P(1), 166.89(12)˚; C(8)-Au(2)-P(2), 163.89(11)˚) with an intramolecular Au-Au contact (Au(1)-Au(2), 2.9982(5) Å). Single crystals of **67** suitable for X-ray diffraction were obtained by cooling a solution of the compound in CH_2Cl_2/MeOH (4:1). This compound crystallizes in the orthorhombic space group $P2_12_12_1$, with the unit cell containing three independent molecules. One of these molecules (molecule **A**), which does not form any unusual intermolecular contacts, displays a relatively short intramolecular Au(1)-Au(2) distance of 2.8137(8) Å (Figure 122). The other two independent molecules (molecules **B** and **C**) present in the asymmetric unit are associated end to end by an unsupported aurophilic Au(1B)-Au(1C) interaction of 3.0983(8) Å (Figure 123). Formation of this intermolecular aurophilic interaction induces a noticeable lengthening of the intramolecular Au-Au interactions in molecules **B** and **C** (Au(1B)-Au(2B) = 2.8693(8) Å and Au(1C)-Au(2C) 2.8658(8) Å) when compared to that observed in molecule **A** (2.8137(8) Å). The coordination environment of the gold(I) atoms in **67** is also more linear than observed for **66** with C-Au-P angles in the range 173.0(4)-178.5(4)˚ for the combined independent molecules.

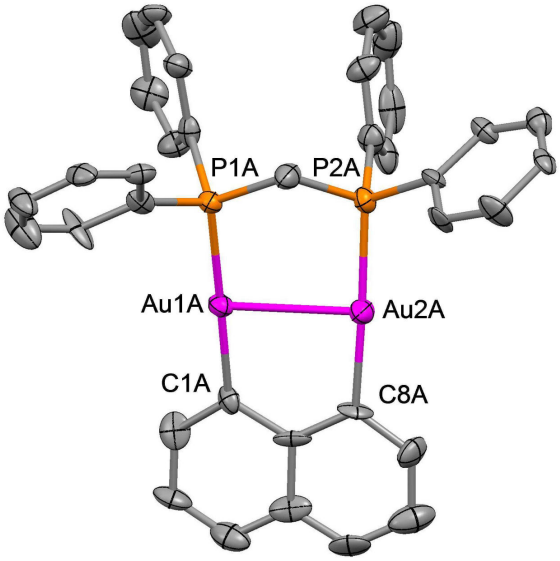

Figure 122. Crystal structure of independent molecule **A** present in the asymmetric unit of **67**. Ellipsoids are scaled to the 50% probability level. Hydrogen atoms have been omitted for clarity. Selected bond lengths (Å) and angles (˚): Au(1A)-Au(2A) 2.8137(8), Au(1A)-P(1A) 2.283(3), Au(1A)-C(1A) 2.044(13), Au(2A)-P(2A) 2.299(4), Au(2A)-C(8A) 2.052(12); C(1A)-Au(1A)-P(1A) 177.5(4), C(8A)-Au(2A)-P(2A) 177.8(4).

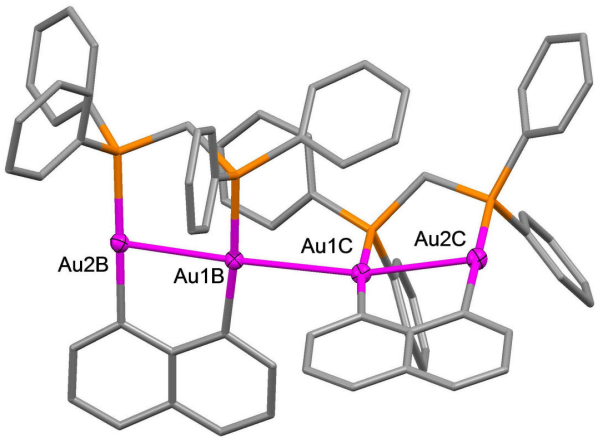

Figure 123. Crystal structure of independent molecules **B** and **C** present in the asymmetric unit of **67**. Ellipsoids are scaled to the 50% probability level. The ligands are represented using a stick model. Hydrogen atoms have been omitted for clarity. Selected bond lengths (Å) and angles (˚): Au(1B)-Au(1C) 3.0983(8), Au(1B)-Au(2B) 2.8693(8), Au(1C)-Au(2C) 2.8658(8); Au(2B)-Au(1B)-Au(1C) 172.27(2), (2C)-Au(1C)-Au(1B) 166.10(2).

Comparison of the structures of **66** and **67** with the reported structure of **65** shows a trend in the intramolecular Au-Au distances with respect to the rigidity and bridging ability of the phosphine ligands. The longest of these distances is observed for **66** (2.9982(5) Å), indicating that the bulk of the monodentate Et_3P ligands impedes a close approach of the two Au atoms. A comparison of the intramolecular Au-Au distances in **67** (av. 2.85 Å) and **65** (av. 2.90 Å) suggests that the narrower dppm ligand promotes the formation of a shorter Au-Au contact. The short intramolecular Au-Au distances observed in **67** are also comparable, or shorter than, those measured for the 8-membered cyclometalated gold(I) dimers $[Au_2(\mu\text{-}2\text{-}C_6H_4PPh_2)_2]$ (2.8594(3) Å) and $[Au_2(\mu\text{-}C_6H_3\text{-}2\text{-}PPh_2\text{-}6\text{-}Me)2]$ (2.861(2) Å).[305,306]

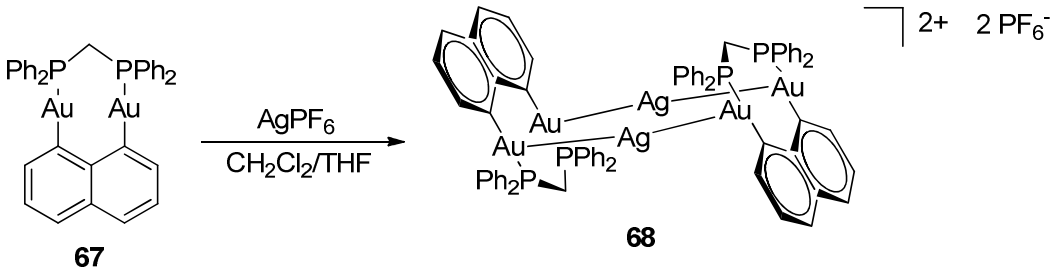

67 **68**

Figure 124. Synthesis of **68**.

The metallophilicity of gold(I) complexes extends beyond inter- and intramolecular Au-Au interactions, and the presence of other heavy metal ions such as Cu(I), Ag(I), and Tl(I) may result in formation of intermetallic aggregates or polymeric materials supported by heterometallic, closed shell interactions.[284,307] In the present case, we have found that upon layering a solution of **67** in CH_2Cl_2 with 1 eq. of $AgPF_6$ in THF, pale

yellow crystals formed, which were identified by X-ray diffraction as the hexafluorophosphate salt of a dicationic complex featuring a Au_2AgAu_2Ag six-membered ring (**68**) (Figure 124). This salt crystallizes in the space group *P*-1 with two independent molecules, referred to as molecules **A** and **B**, two PF_6^- counteranions, and disordered THF/CH_2Cl_2 solvent molecules in the asymmetric unit (Figure 125). The independent molecules each consist of a single Ag atom and one $[Au_2(\mu\text{-}C_{10}H_6)(\mu\text{-}dppm)]$ unit with the remainder of the hexanuclear "sandwich" structures and counteranions being generated by an inversion center located at the center of the 6-membered metalloring. Restraints placed on the naphthalenediyl and phenyl rings to correct distortions, probably due to crystal twinning, limit detailed discussion of some aspects of the bonding in this complex. However, the distinguishing features of **68**, including the metal-metal and some metal-carbon bond distances, may be addressed. The presence of nearby Ag atoms does not induce any major distortions in the core structure of the $[Au_2(\mu\text{-}C_{10}H_6)(\mu\text{-}dppm)]$ moiety. The observed intramolecular Au(1)-Au(2) distances of 2.8278(12) Å for molecule **A** and 2.8501(12) Å for molecule **B** are close to those observed in complex **67**. Similarly, the C-Au-P bond angles ranging from 176.5(2)˚ to 177.0(2)˚ in molecules **A** and **B** show little deviation from linearity. The Au(1')-Ag(1) (2.740(2) Å for molecule **A** and 2.7646(19) Å for molecule **B**) and Au(2)-Ag(1) (2.783(2) Å for molecule **A** and 2.802(2) Å for molecule **B**) distances are close to one another and commensurate with the presence of metallophilic contacts such as those observed in the aryl-bridged heterometallic complexes $[\{Au(\mu\text{-}Mes)(Ph_3As)\}_2Ag]ClO_4$ (Au-Ag = 2.7758(8) Å)[308] and $[\{Au(\mu\text{-}Mes)(Ph_3P)Ag(tht)\}_2]^{2+}$ (Au-Ag = 2.8245(6)

Å).[309] Cohesion of the hexanuclear cluster also benefits from π-interactions involving the naphthalene ligands and the silver cation (Ag(1)-C(8) = 2.434(7) Å for molecule **A** and 2.344(7) Å for molecule **B**, Ag(1)-C(7) = 2.482(9) Å for molecule **A** and 2.521(9) Å for molecule **B**, Ag(1)-C(1') = 2.347(4) Å for molecule **A** and 2.321(5) Å for molecule **B**). Finally, we note that formation of this cluster results in a slight lengthening of the Au-C bonds (av. 2.13 Å *vs.* 2.06 Å in **67**).

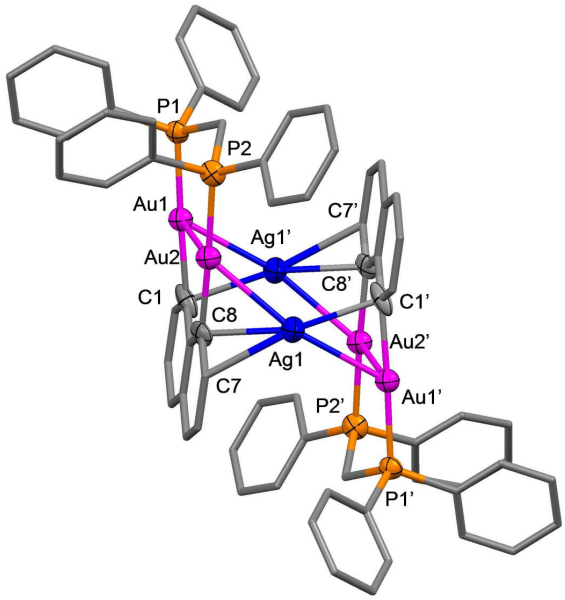

Figure 125. Structure of independent molecule **A** of complex **68**. The symmetry equivalent half of the molecule is generated by inversion ((atom)(number)' = -x, -y, -z+1). Ellipsoids are scaled to the 50% probability level. Hydrogen atoms, PF_6^- counteranions, and solvent molecules have been omitted for clarity. Selected bond lengths (Å) and angles (°) for molecule **A**, with those for the independent molecule **B** given in brackets: Au(1)-Au(2) 2.8278(12) [2.8501(12)], Au(1)-P(1) 2.300(5) [2.286(6)], Au(1)-C(1) 2.125(6) [2.143(6)], Au(2)-P(2) 2.290(5) [2.304(5)], Au(2)-C(8) 2.099(7) [2.143(6)], Au(1')-Ag(1) 2.740(2) [2.7647(19)], Au(2)-Ag(1) 2.783(2) [2.802(2)], Ag(1)-C(1') 2.347(4) [2.321(5)], Ag(1)-C(8) 2.434(7) [2.344(7)], Ag(1)-C(7) 2.482(9) [2.521(9)]; C(1)-Au(1)-P(1) 176.8(2) [176.5(2)], C(8)-Au(2)-P(2) 177.0(2) [176.3(2)], Au(1')-Ag(1)-Au(2) 164.09(9) [163.54(11)].

The electronic spectra of complexes **67** and **68** in CH_2Cl_2 both display broad absorption bands around 310 nm, which arise from a mixture of metal perturbed naphthalene and phenyl π-π* excitations and metal centered transitions (Figure 126).[302,310,311] In deaerated CH_2Cl_2 solution, both complexes display emission bands in the 475-650 nm range (Figure 127). The vibronic progression observed in these emission spectra are characteristic of the triplet state of naphthalene, thus indicating the occurrence of an internal heavy atom effect.[302,312,313] Related heavy atom induced triplet emissions have been observed for other aurated polycyclic aromatics including naphthalene, anthracene, and pyrene.[314-318] Upon exposure to air, nearly complete loss of emission intensity was observed for both complexes, thus confirming the triplet nature of the emissive state. In addition, the emission band of **68** is redshifted by *ca.* 20 nm versus that of **67**, indicating that the Au-Ag metallophilic interactions observed in the solid state might be retained in solution.

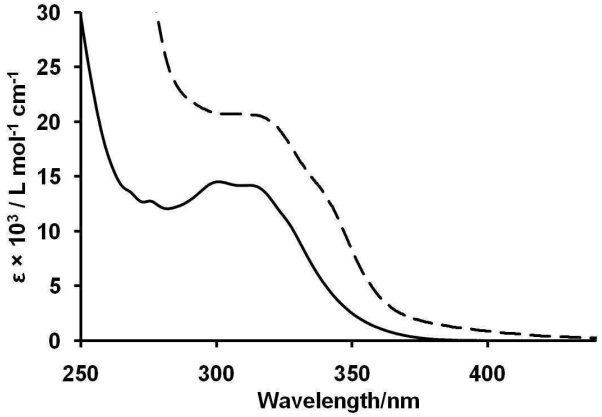

Figure 126. UV-Vis absorption spectra of complexes **67** (—) and **68** (- - -) in CH_2Cl_2 solution under ambient conditions.

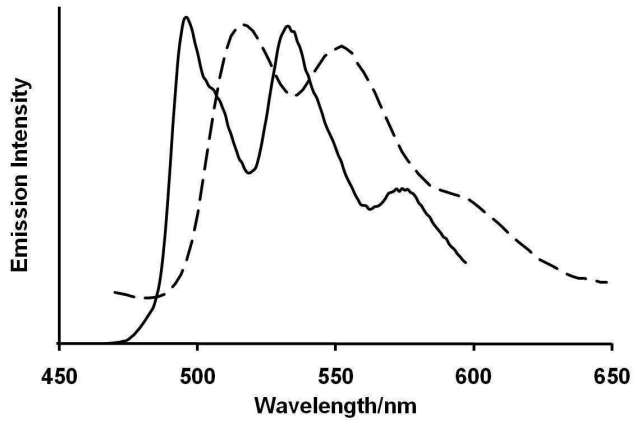

Figure 127. Luminescence spectra of complexes **67** (—, λ_{exc} = 310 nm) and **68** (**- - -**, λ_{exc} = 350 nm) in deoxygenated CH_2Cl_2 solution (1 mM) at room temperature. The spectra have been corrected for the I *vs.* λ bias introduced by the PMT detector.

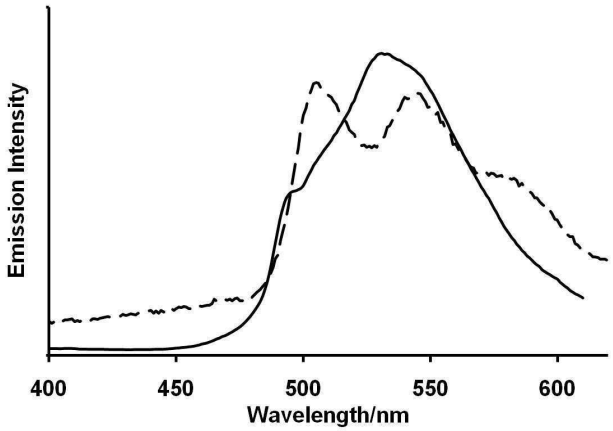

Figure 128. Luminescence spectra of complexes **67** (—) and **68** (- - -) (λ_{exc} = 315 nm) in the solid state at room temperature. The spectra have been corrected for the I *vs.* λ bias introduced by the PMT detector.

The solid state spectra of **67** and **68** also display relatively broad emission bands around 475-650 nm (Figure 128). However, the emission band of **67** is distinctly broadened and more red-shifted. Since it has been previously shown that aggregation and aurophilic interactions play an important role in the luminescence of gold(I) complexes,[319] we assign the differences observed in the solution and solid state spectra of **67** to the presence of an aurophilic dimer in its solid state structure.

7.3 Synthesis and structural characterization of gold-borane complexes **69** and **70**

Next, we set out to synthesize gold(I)/boron complexes supported by the 1,8-naphthalendiyl backbone. Attempts to prepare this type of compound by an electrophilic ring opening reaction of the dimesityl-1,8-naphthalenediylborate anion with gold chloride salts proved unsuccessful, despite the success of this synthetic strategy for accessing analogous Hg/B complexes such as **34**.[122] As a result, we considered the use of a less sterically demanding diarylboron halide, namely 9-thia-10-bromoboranthracene. The reaction of 9-thia-10-bromoboranthracene with 1,8-dilithionaphthalene in Et_2O generated a colorless precipitate that was subsequently allowed to react with thtAuCl/Et_3P or Ph_3PAuCl in Et_2O. Concentration of the reaction mixture, followed by extraction with benzene and layering with hexanes afforded a small amount of yellow single crystals of the gold-borane complexes **69** and **70** (Figure 129). Single resonances observed at 41 ppm for **69** and 44 ppm for **70** in the $^{31}P\{^1H\}$ NMR spectra (C_6D_6) are consistent with a triorganophosphine coordinated to a gold(I) fragment. The ^1H NMR spectra of both compounds displayed signals consistent with an unsymmetrical 1,8-naphthalenediyl group as well as the presence of the thiaboranthracene group.

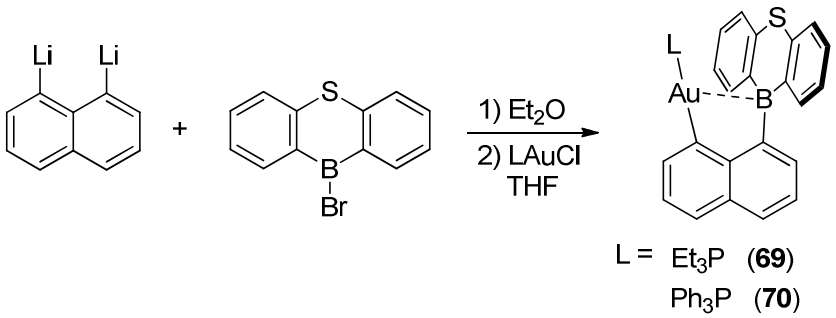

Figure 129. Synthesis of **69** and **70**.

The X-ray crystal structures of **69** and **70** have been determined. Compound **69** crystallizes in the space group $Pca2_1$ with two similar independent molecules in the asymmetric unit. The structure of one of the independent molecules is shown in Figure 130. Both molecules display a short intramolecular Au-B distance (2.70 Å *av.*) and nearly linear P-Au-C bond angle of 170.1˚. The thiaboranthracene group is oriented perpendicular to the plane of the naphthalene backbone with the boron atom remaining in a trigonal planar coordination environment (Σ∢(C–B–C) = 358.2˚).

Compound **70** crystallizes in the $P2_1$ space group with two independent molecules and a benzene solvent molecule in the asymmetric unit. The structure of one of the independent molecules is shown in Figure 131 and appears very similar to that determined for **69**. However, the Au-B distances measured for **70** (2.84 Å *av.*) are longer than those in **69**. The P-Au-C bond angles (169.0˚ *av.*) are still very linear and the boron atom retains a trigonal planar geometry (Σ∢(C–B–C) = 358.5˚).

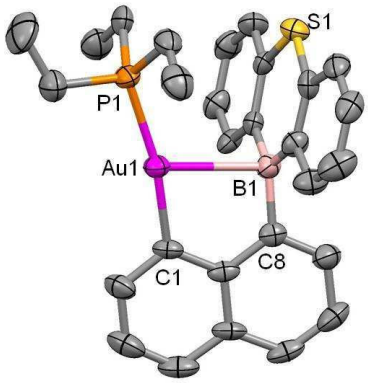

Figure 130. Structure of one of the independent molecules present in the asymmetric unit of **69**. Ellipsoids are scaled to the 50% probability level. Hydrogen atoms have been omitted for clarity. Selected bond lengths (Å) and angles (˚) [with the corresponding bond lengths and angles for the other independent molecule listed in brackets]: Au(1)-C(1) 2.042(6) [2.058(7)], Au(1)-P(1) 2.307(2) [2.307(2)], Au(1)-B(1) 2.680(9) [2.719(9)], C(1)-Au(1)-P(1) 170.2(2) [170.1(2)], C(22)-B(1)-C(16) 120.1(7) [118.7(7)], C(22)-B(1)-C(8) 120.4(8) [119.0(8)], C(16)-B(1)-C(8) 117.7(8) [120.5(7)].

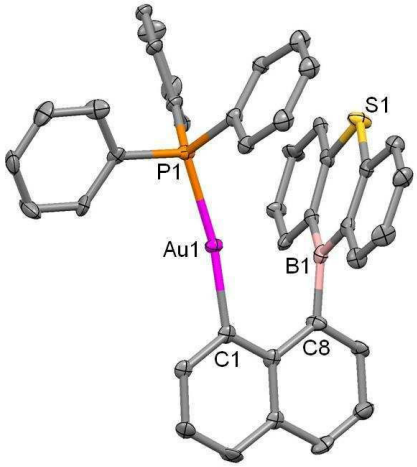

Figure 131. Structure of one of the independent molecules present in the asymmetric unit of **70**. Ellipsoids are scaled to the 50% probability level. Hydrogen atoms have been omitted for clarity. Selected bond lengths (Å) and angles (˚) [with the corresponding bond lengths and angles for the other independent molecule listed in brackets]: Au(1)-C(1) 2.072(10) [2.076(10)], Au(1)-P(1) 2.301(3) [2.293(3)], Au(1)-B(1) 2.831(16) [2.853(15)], C(1)-Au(1)-P(1) 169.7(3) [168.4(3)], C(22)-B(1)-C(16) 119.5(11) [119.3(10)], C(22)-B(1)-C(8) 118.5(11) [119.5(10)], C(16)-B(1)-C(8) 120.5(11) [119.7(10)].

Attempts to optimize the reaction conditions to afford higher yields of compounds **69** and **70** were unsuccessful. Consequently, we could not undertake anion binding studies. However, the short Au-B bond distance in **69** led us to consider the possible presence of a Z-type interaction. In fact, the Au-B distance measured for **69** is only marginally longer than that reported for the phosphoranylborane gold complex **71** (Au-B: 2.663(8) Å) reported by Bourissou (Figure 132).[320] Other di- and tri-phosphoranylborane gold complexes have also been reported and shown contain shorter Au-B bond distances in the 2.309 to 2.448 Å range,[321,322] but none contain a Au-C bond.

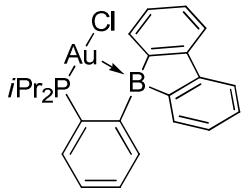

71

Figure 132. Phosphoranylborane gold complex **71**.

In order to investigate the nature of the potential Au→B interactions in these complexes, we carried out DFT calculations on **69** using the ADF program. All calculations were carried out at the BP86/TZP level of theory using the zero-order regular approximation (ZORA). Geometry optimization starting from the solid state structure of one of the independent molecules of **69** afforded a structure that is in close agreement with that observed experimentally. Compound **69** was subjected to a Boys localization analysis because of extensive delocalization of the occupied Kohn-Sham orbitals. This analysis identified an occupied orbital of σ-symmetry along the Au-B axis

(Figure 133). Although this orbital is strongly polarized toward the Au atom, there is a small contribution from the boron atom, signaling the presence of a Z-type interaction. An NBO analysis (Gaussian: BP86 with 6-31g for H, C; 6-311+g(d) for B, P, Cl; and CRENBS ECP for Au) identified lp(Au) → p(B) and σ(Au-C) → p(B) interactions as the primary components of the Z-type bonding (Figure 134). An NBO deletion calculation to zero the Kohn-Sham matrix elements corresponding to the lp(Au) → p(B) interaction resulted in an increase in the energy (E_{del}) of **69** by 9.2 kcal/mol, which is comparable to that found for deletion of the lp(Au) → p(B) interaction in **71** (E_{del} = 12.8 kcal/mol).[320] Deletion of both the lp(Au) → p(B) and σ(Au-C) → p(B) interactions in **69** provided a significantly increased E_{del} of 35.5 kcal/mol.

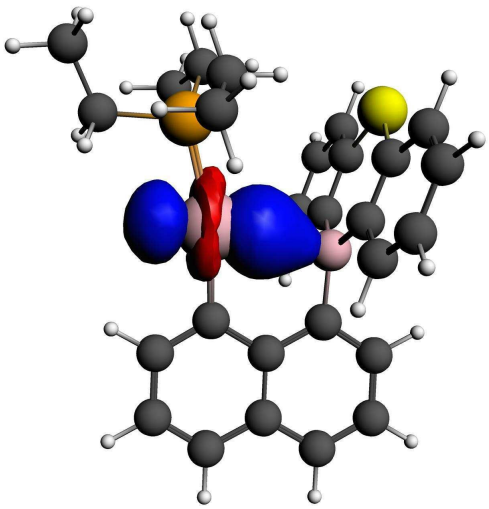

Figure 133. Gold-centered Boys orbital for **69** (drawn with a 0.03 isodensity value).

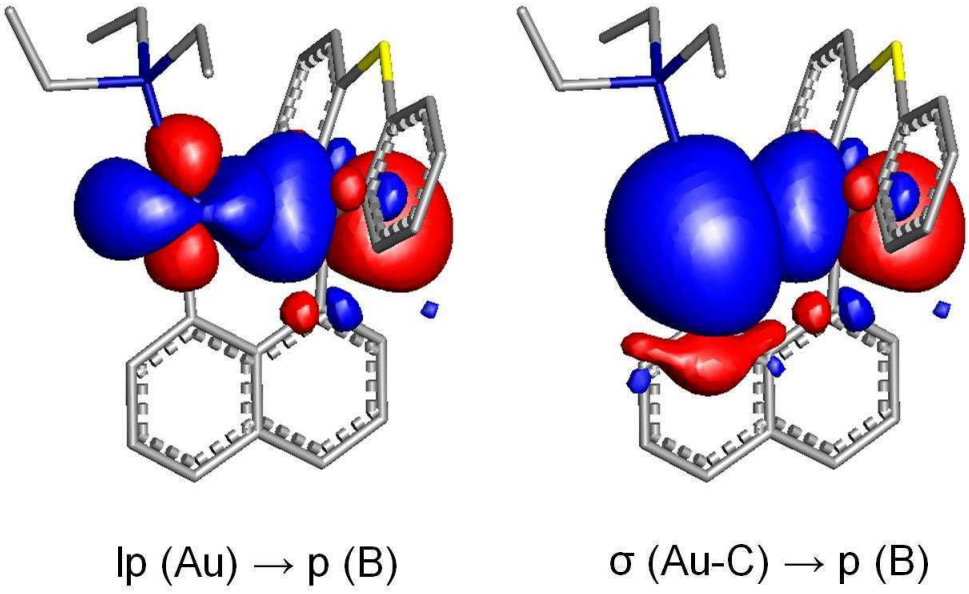

Figure 134. Plots of NBO donor-acceptor interactions in **69** (drawn with a 0.03 isodensity value). Hydrogens have been omitted for clarity.

7.4 Conclusions

In conclusion, we have found that 1,8-diaurionaphthalene complexes such as **67** can be readily prepared from 1,8-dilithionaphthalene and may be used as a building block for the construction of a larger complexes such as **68**, which contains a $[Au_4Ag_2]^{2+}$ metallocycle. The luminescence properties of **67** and **68** in CH_2Cl_2 solution arise from triplet state phosphorescence of the naphthalene backbone, thus indicating the occurrence of an internal heavy atom effect. A redshift (*ca.* 20 nm) in the emission spectrum of **68** versus that of **67** suggests that the Au-Ag metallophilic interactions remain in solution. Similarly, broadening of the solid state emission spectrum of **67** is attributed to the presence of an intramolecular aurophilic contact observed in the solid state structure of the complex.

A similar synthetic approach using 1,8-dilithionaphthalene to prepare gold/boron compounds **69** and **70** was also successful. However, the low yields of these reactions precluded the study of fluoride or cyanide complexation by these compounds. The short Au-B bond distance found in **69** prompted a DFT study of this bonding interaction, and NBO analysis identified a Au→B Z-type interaction similar to that described for the phosphoranylborane gold complex **71**.

7.5 Experimental

General Considerations. 1,8-dilithionaphthalene,[323] 9-thia-10-bromoboranthracene,[99] and [AuCl(tht)][324] were prepared according to the literature. *Bis*(diphenylphosphino)methane and triethylphosphine were purchased from Alfa Aesar and used as received. $AgPF_6$ was purchased from Sigma Aldrich and used as received. Solvents were dried by passing through an alumina column (*n*-hexane, CH_2Cl_2) or refluxing under N_2 over Na/K (Et_2O and THF). Air-sensitive compounds were handled under a N_2 atmosphere using standard Schlenk and glovebox techniques. Elemental analyses were performed at Atlantic Microlab (Norcross, GA). NMR spectra were recorded on a Varian Unity Inova 400 FT NMR (399.59 MHz for ^{1}H, 161.75 MHz for ^{31}P, 128.19 MHz for ^{11}B, 100.45 MHz for ^{13}C) spectrometer at ambient temperature. Chemical shifts δ are given in ppm and are referenced against external Me_4Si (^{1}H, ^{13}C), H_3PO_4 (^{31}P), and $BF_3 \cdot Et_2O$ (^{11}B, ^{19}F).

Table 20. Crystal data, data collections, and structure refinements for **66**, **67**, and **68**.

Crystal data	**66**	**67**	**68**
Formula	$C_{22}H_{36}Au_2P_2$	$C_{35}H_{28}Au_2P_2 \cdot 0.66(CH_2Cl_2)$	$C_{74}H_{64}Ag_2Au_4F_{12}OP_6$
Mr	756.38	961.08	2386.68
Crystal size/mm	0.12 x 0.08 x 0.004	0.10 x 0.10 x 0.03	0.33 x 0.05 x 0.03
Crystal system	Monoclinic	Orthorhombic	Triclinic
Space group	*P*2(1)/n	*P*2(1)2(1)2(1)	*P*-1
a/Å	14.589(2)	15.312(3)	13.721(3)
b/Å	11.7417(17)	20.213(3)	15.084(4)
c/Å	15.155(2)	30.189(5)	19.253(5)
α /°	90	90	84.974(2)
β/°	113.913(2)	90	69.611(2)
γ /°	90	90	84.399(3)
V/Å^3	2373.3(6)	9343(3)	3711.0(16)
Z	4	12	2
ρ_{calc}/g cm^{-3}	2.117	2.050	2.136
μ/mm^{-1}	12.488	9.652	8.597
F(000)	1424	5448	2248 (2461)[a]
T/K	110(2)	110(2)	110(2)
Scan mode	ω	ω	ω
hkl Range	-17 → +17	-17 → +17	-16 → +16
	-13 → +13	-23 → +23	-16 → +18
	-17 → +17	-35 → +35	-23 → +23
Measd reflns	21290	85668	37102
Unique reflns [Rint]	3948 [0.0298]	15533 [0.0817]	14427 [0.0910]
Reflns used for refinement	3948	15533	14427
Refined parameters	235	1066	646
GooF	1.002	1.049	1.025
R1,[b] *w*R2[c] (all data)	0.0214, 0.0429	0.0472, 0.0795	0.1328, 0.1836
ρ_{fin} (max., min.)/eÅ^{-3}	1.246, -0.491	1.576, -1.045	2.923, -1.898
Absolute structure parameter	N/A	-0.009(6)	N/A

[a] The F(000) value in parentheses includes the amount of electrons in the structure removed using the SQUEEZE program.
[b] $R1 = \Sigma||F_o| - |F_c||/\Sigma|F_o|$. [c] $wR2$ $([\Sigma w(F_o^2 - F_c^2)^2]/[\Sigma w(F_o^2)^2])^{1/2}$; $w = 1/[\sigma^2(F_o^2) + (ap)^2 + bp]$; $p = (F_o^2 + 2F_c^2)/3$ with $a = 0.0258$ for **66**, 0.0250 for **67**, and 0.0300 for **68**; and $b = 3.1624$ for **66**, 10 for **67**, and 130 for **68**.

Table 21. Crystal data, data collections, and structure refinements for **69** and **70**.

Crystal data	**69**	**70**
Formula	$C_{28}H_{29}AuBPS$	$C_{86}H_{64}Au_2B_2P_2S_2$
Mr	636.32	1638.98
Crystal size/mm	0.14 x 0.10 x 0.08	0.30 x 0.30 x 0.25
Crystal system	Orthorhombic	Monoclinic
Space group	Pca21	P21
a/Å	18.5032(13)	9.3608(18)
b/Å	9.0744(6)	37.954(7)
c/Å	29.821(2)	9.5399(18)
β/°	-	101.429(2)
V/Å^3	5007.1(6)	3322.1(11)
Z	8	2
ρ_{calc}/g cm^{-3}	1.688	1.638
μ/mm^{-1}	6.038	4.571
F(000)	2496	1620
T/K	110(2)	110(2)
Scan mode	ω, φ	ω, φ
hkl Range	-22 → +22	-11 → +11
	-11 → +11	-46 → +46
	-36 → +36	-11 → +11
Measd reflns	49372	34189
Unique reflns [R_{int}]	9843[0.0488]	13059 [0.0704]
Reflns used for refinement	9843	13059
Refined parameters	578	704
GooF	1.006	1.009
$R1$,[a] $wR2$[b] (all data)	0.0462, 0.0908	0.0608, 0.1044
ρ_{fin} (max., min.)/eÅ^{-3}	0.543, -0.891	1.743, -1.557

[a] $R1 = \Sigma||F_o| - |F_c||/\Sigma|F_o|$. [b] $wR2 = ([\Sigma w(F_o^2 - F_c^2)^2]/[\Sigma\, w(F_o^2)^2])^{1/2}$; $w = 1/[\sigma^2(F_o^2) + (ap)^2 + bp]$; $p = (F_o^2 + 2F_c^2)/3$ with $a = 0.0528$ for **69**, 0.0420 for **70**; and $b = 0$ for **69**, 0 for **70**.

Crystallography. Crystal data, details of data collection, and structure refinement parameters for compounds **66**, **67**, and **68** are presented in Table 20. The data for compounds **69** and **70** are presented in Table 21. The crystallographic measurements were performed using a Bruker-AXS APEX-II CCD area detector diffractometer, with a graphite-monochromated Mo-Kα radiation (λ = 0.71069 Å). A specimen of suitable size and quality was selected and mounted onto a nylon loop. The semiempirical method

SADABS[207] was applied for absorption correction. The structures were solved by direct methods using SHELXTL/PC package (version 6.1)[208] which successfully located most of the non-hydrogen atoms. Subsequent refinement on F^2 allowed location of the remaining non-hydrogen atoms. All H atoms were geometrically placed and refined in a riding model approximation. During the structure refinement of complex **68**, we found large planarity, bond length and bond angle distortions in the phenyl and naphthyl rings in both molecules of complex. This effect is probably due to twinning of the crystal which could, however, not be resolved using the CELL NOW,[325] ROTAX,[326] or APEX2[327] software. To correct this distortion, we restrained the structure parameters of these rings to the ideal geometries (C-C bond length 1.390(1)Å and C-C-C bond angles 120.0(1)º). In addition, the PF_6^- counter-anions were found to be highly disordered. Attempts to solve this disorder were not successful. Since, these anions do not bring any new structural information to our research, after restraining their geometry to the ideal (P-F bond length 1.581(1) Å and F-P-F bond angle 90.0(1) º), they were left as is.

There are large, channel-like volumes permeating the crystal that are occupied by heavily disordered solvent molecules. Modeling attempts indicate a mixture of CH_2Cl_2 and THF. No satisfactory disorder model could be achieved, and therefore the Squeeze program implemented in PLATON was used to model this electron density.[328] The program calculated a solvent-accessible volume of 272.1 $Å^3$ (7.33 % of the total unit cell volume), which was then removed from subsequent structure factor calculations.

Synthesis of 66. A mixture of AuCl(tht) (0.200 g, 0.62 mmol) and Et_3P (0.074 g, 0.62 mmol) in Et_2O (10 mL) was added to a solution of 1,8-dilithionaphthalene·1.5TMEDA

(0.099 g, 0.31 mmol) in Et_2O (5 mL) at -78˚C. The yellow suspension was stirred for 15 min at this temperature and then for 3 hrs at room temperature. The solvent was removed *in vacuo*, and the residue was extracted with 15mL of CH_2Cl_2 and filtered over Celite. The extract was then concentrated, and a yellow precipitate was obtained by addition of hexanes. Recrystallization of the crude material from CH_2Cl_2/Et_2O (3mL/5mL) gave the pure product as bright yellow blocks (0.020 g, 10 % yield). Attempts to obtain more product from the recrystallization supernatant resulted only in the isolation of decomposition products. ^{1}H NMR (399.9 MHz, $CDCl_3$): δ 1.29 (dt, 18H, P-CH_2-*CH_3*, $^3J_{H\text{-}H}$ = 7.60 Hz, $^3J_{H\text{-}P}$ = 16.8 Hz), 1.84 ((dq, 12H, P-*CH_2*-*C*H_3, $^3J_{H\text{-}H}$ = 7.60 Hz, $^2J_{H\text{-}P}$ = 8.80 Hz), 7.32 (t, 2H, Naph-*CH*, $^3J_{H\text{-}H}$ = 7.20 Hz), 7.60 (d, 2H, Naph-*CH*, $^3J_{H\text{-}H}$ = 8.00 Hz), 7.67 (t, 2H, Naph-*CH*, $^3J_{H\text{-}H}$ = 7.20 Hz). ^{13}C NMR (100.5 MHz, $CDCl_3$): δ 9.12 (s, P-CH_2-*CH_3*), 18.67 (d, P-*CH_2*-CH_3, $^1J_{C\text{-}P}$ = 26.7 Hz), 123.94, 125.54, 135.39, (ipso C1, C8, C9, and C10 not observed).^{31}P{^{1}H} NMR (161.75 MHz, $CDCl_3$): δ 38.04. Anal. Calcd for $C_{22}H_{36}Au_2P_2$: C, 34.93; H, 4.80. Found: C, 34.69; H, 4.77.

Synthesis of 67. A mixture of AuCl(tht) (0.834 g, 2.60 mmol) and dppm (0.500 g, 1.30 mmol) in THF/Et_2O (5mL/5mL) was added dropwise to a solution of 1,8-dilithionaphthalene·1.5 TMEDA (0.413g, 1.30mmol) in Et_2O (10 mL) at -78˚C. The yellow suspension was stirred for 15 min at reduced temperature then overnight at room temperature. The solvent was removed *in vacuo*, and the residue was extracted with 15mL of CH_2Cl_2 and filtered over Celite. The extract was then concentrated, and a yellow precipitate was obtained by addition of Et_2O. The solid was filtered and washed copiously with Et_2O. The resulting crude product was recrystallized from CH_2Cl_2:MeOH

(4:1) to give the pure product as bright yellow blocks (840 mg, 71% yield). ^{1}H NMR (399.9 MHz, C_6D_6): δ 2.83 (t, 2H, P-C*H*$_2$, $^{2}J_{H\text{-}P}$ = 10.8 Hz), 6.75-6.86 (m, 12H, *m*-, *p*-Ph-*CH*), 7.33 (dd, 8H, *o*-Ph-*CH*, $^{3}J_{H\text{-}P}$ = 12.1 Hz), 7.65 (t, 2H, Naph-*CH*, $^{3}J_{H\text{-}H}$ = 7.14 Hz),), 7.97 (t, 2H, Naph-*CH*, $^{3}J_{H\text{-}H}$ = 7.87 Hz), 8.49 (br, 2H, Naph-*CH*). ^{13}C NMR (100.5 MHz, $CDCl_3$): δ 30.19 (t, P-*CH*$_2$-P, $^{1}J_{C\text{-}P}$ = 22.1 Hz), 124.22, 126.42, 128.92, 130.53, 131.29, 133.44, 135.87, 135.99, 154.73, 174.25. ^{31}P{^{1}H} NMR (161.75 MHz, CD_2Cl_2): δ 29.09 (s). Anal. Calcd for $C_{35}H_{28}Au_2P_2$·0.66 CH_2Cl_2: C, 44.57; H, 3.08. Found: C, 44.61; H, 2.99.

Synthesis of 68. Colorless crystals of **68** suitable for X-ray diffraction were obtained by layering a solution of **67** (0.060 g, 0.066 mmol) in 3 mL CH_2Cl_2 with a solution of $AgPF_6$ (0.017 g, 0.067 mmol) in 3 mL THF. ^{1}H NMR (399.9 MHz, CD_2Cl_2): δ 2.53 (br, 1H, dppm-C*H*$_2$), 4.06(br, 1H, dppm-C*H*$_2$), 7.03 (br, 4H), 7.16-7.36 (t, br, 12H), 7.53-7.75 (d, br, 8H), 8.05 (br, 2H). ^{31}P{^{1}H} NMR (161.75 MHz, CD_2Cl_2): δ -144.38 (sept., *P*F_6, $^{1}J_{F\text{-}P}$ = 711 Hz), 31.03 (s,dppm-*P*). Anal. Calcd. for $C_{70}H_{56}F_{12}Au_4Ag_2P_6$: C, 36.32; H, 2.44. Found: C, 36.09; H, 2.41.

Synthesis of 69. A solution of 9-thia-10-bromoboranthracene (0.200 g, 0.73 mmol) in Et_2O (5 mL) was added dropwise to a suspension of 1,8-dilithionaphthalene·1.5 TMEDA (0.186 g, 0.73 mmol) in Et_2O (10 mL) at -78˚C. The mixture was allowed to warm to room temperature and stirred for 45 min, resulting in precipitation of an off-white solid. The solid was filtered and washed with Et_2O (3 × 3 mL). A solution of AuCl(tht) (0.234 g, 0.73 mmol) and Et_3P (0.086 g, 0.73 mmol) in THF (10 mL) was then added dropwise to a suspension of the solid in Et_2O (10 mL) at -78˚C. The reaction was

stirred for 30 min. at -78˚C and allowed to stand 12 hrs. at -20˚C. The mixture was then filtered over Celite, and the volatiles were removed *in vacuo*. The resulting residue was extracted with benzene (5 mL), filtered over Celite, and layered with hexanes (10 mL). After 2 days, a small amount of yellow single crystals (< 10 % yield) had formed and were identified by X-ray diffraction as compound **69**. ^{1}H NMR (399.9 MHz, C_6D_6): δ 0.32 (dt, 9H, PCH_2-C*H*$_3$, $^{3}J_{H\text{-}H}$ = 7.59, $^{3}J_{H\text{-}P}$ = 17.18 Hz), 0.86 (dq, 6H, PCH_2-C*H*$_3$, $^{3}J_{H\text{-}H}$ = 7.59, $^{3}J_{H\text{-}P}$ = 16.78 Hz), 6.81 (td, 2H, $C_{12}H_8BS$-C*H*, $^{3}J_{H\text{-}H}$ = 7.19, $^{4}J_{H\text{-}H}$ = 1.20 Hz), 7.06 (td, 2H, $C_{12}H_8BS$-C*H*, $^{3}J_{H\text{-}H}$ = 6.79, $^{4}J_{H\text{-}H}$ = 1.60 Hz), 7.15 (m, 1H, Naph-C*H*), 7.37 (dd, 2H, $C_{12}H_8BS$-C*H*, $^{3}J_{H\text{-}H}$ = 7.59, $^{4}J_{H\text{-}H}$ = 1.20 Hz), 7.44 (dd, 1H, Naph-C*H*, $^{3}J_{H\text{-}H}$ = 7.99, 6.80), 7.65 (t, 1H, Naph-C*H*, $^{3}J_{H\text{-}H}$ = 7.19), 7.88 (d, 1H, Naph-C*H*, $^{3}J_{H\text{-}H}$ = 7.99), 7.95 (d, 1H, Naph-C*H*, $^{3}J_{H\text{-}H}$ = 7.99), 8.08 (t, 1H, Naph-C*H*, $^{3}J_{H\text{-}H}$ = 6.80), 8.12 (dd, 2H, $C_{12}H_8BS$-C*H*, $^{3}J_{H\text{-}H}$ = 7.99, $^{4}J_{H\text{-}H}$ = 1.20 Hz). $^{31}P\{^{1}H\}$ NMR (161.75 MHz, C_6D_6): δ 40.34 (s).

Synthesis of 70. This compound was prepared analogous to **69** with $AuCl(PPh_3)$ in place of the $AuCl(tht)/Et_3P$ mixture. As in the previous synthesis, this reaction afforded a small amount (< 10 % yield) of yellow single crystals identified by X-ray diffraction as compound **70**. $^{31}P\{^{1}H\}$ NMR (161.75 MHz, C_6D_6): δ 44.74 (s).

Computational Details. DFT structural optimizations for **69** and **70** were carried out using the ADF program (2008.01).[329-331] All calculations were carried out using the BP86 functional[332,333] with the all electron TZP basis sets for all atoms.[334] These calculations were performed using ZORA.[335-339] The Boys[340-342] localizations were carried out in the ADF program and visualized using Jimp2.[343,344] The Natural Bond

Order (NBO) analysis was performed on the optimized structure using the NBO v3.1[345] software available in the Gaussian09[241] program. This analysis was carried out using the BP86 functional and the mixed basis set: 6-31g for H, C; 6-311+g(d) for B, P, Cl; and CRENBS ECP for Au. The resulting donor acceptor interactions were visualized using Jimp2.[343,344]

UV-Vis Absorption and Luminescence Measurements. Electronic absorption spectra were recorded using an Ocean Optics USB4000 spectrometer with an Ocean Optics ISS light source. Steady state emission spectra were collected at room temperature using a PTI QuantaMaster 4 fluorescence spectrophotometer equipped with a Model 810 PMT detector. Solution based samples were prepared at *ca.* 1 mM concentrations under an atmosphere of N_2 using dry, degassed CH_2Cl_2. Solid samples were loaded as powders in 0.7 mm glass capillaries and suspended in the sample cavity so as to sit at the intersection of the excitation and emission optical paths.

CHAPTER VIII

A 14-ELECTRON, T-SHAPED STIBORANYL-GOLD COMPLEX*

8.1 Introduction

T-shaped, 14-electron transition metal complexes constitute an interesting class of compounds because of their inherent unsaturation.[346-348] Such complexes can be stabilized through the use of non-coordinating anions and/or bulky ligands, which sterically hinder the coordination of a fourth ligand to the unsaturated transition metal center.[349-352] Another useful strategy relies on the use of silyl[353-356] or boryl ligands,[357,358] whose strong σ-donating properties can be used to increase the lability of the trans-ligand. The properties of these ligands can be illustrated by a series of cationic T-shaped bis(phosphine)platinum boryl derivatives, which can be formed when a non-coordinating anion is employed.[359,360]

In the course of our earlier investigations into transition metal chlorostiborane and fluorostiborane complexes, we considered that stiboranyl ligands might possess strong σ-donating properties, similar to boryl and silyl ligands, and be well-adapted for the formation of T-shaped, 14-electron transition metal complexes. This notion is supported by the electropositive character of antimony and the fact that antimony species such as Ph_4SbX (X = halogen) become increasingly ionic as the size of the halogen

---

* Reprinted with permission from, "Synthesis, structure and properties of a T-shaped 14-electron stiboranyl-gold complex"; Wade, C. R.; Lin, T.-P.; Nelson, R. C.; Marder, E. A.; Miller, J. T.; Gabbaï, F. P. *J. Am. Chem. Soc.* **2011**, *133*, 8948-8955. Copyright 2007 by the American Chemical Society.

increases.[156,158,159] As noted in an earlier chapter, triaryl and trialkyl stibines have a wide precedent in coordination chemistry, although only two classes of stiboranyl-transition metal complexes, namely of type **I**[258,259] and **II**,[260-263] have been reported (Figure 135). However, the electron withdrawing character of the halogen and alkoxy groups may limit the σ-donating properties of the stiboranyl ligand in these species. Consequently, we considered the use of a tetraorganostiboranyl (R_4Sb) ligand. Having recently succeeded in the isolation of the cyclic mercury-stibonium compound **72**,[361] we decided to target the synthesis of a gold analog of this compound with the goal of obtaining a novel, T-shaped, 14-electron complex and investigating the bonding nature of R_4Sb-type ligands.

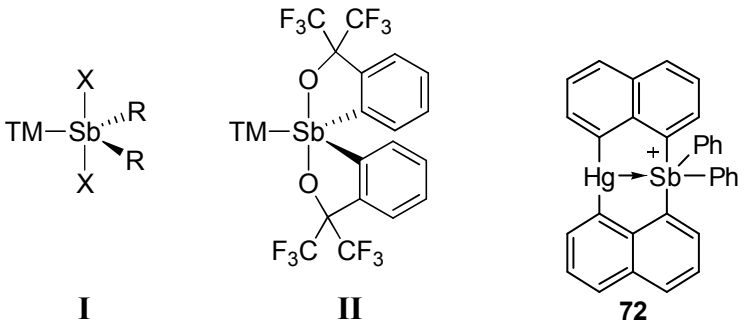

I **II** **72**

Figure 135. Representations of the reported stiboranyl ligand types **I** and **II** (TM = transition metal moiety) and the mercury-stibonium compound **72**.

8.2 Synthesis and structural characterization of a cyclic, stiboranyl-gold complex

The synthesis of the stiboranyl-gold complex **73** was carried out in a similar fashion to that for the Hg analog **72**. The reaction of Ph_3SbBr_2 with 1,8-dilithionaphthalene

followed by AuCl(tht) and Ph_3P in THF afforded a yellow solution that was layered with Et_2O and hexanes. Upon diffusion of the layers, a mixture of yellow and colorless crystals was obtained. X-ray diffraction experiments (*vide infra*) identified the colorless crystals as $AuBr(PPh_3)_2$ and the yellow crystals as complex **73**. Repeated recrystallization of the mixture from CH_2Cl_2 afforded an analytically pure sample of **73** in 37 % yield (Figure 136). This compound is air stable and has been characterized by conventional means, including ^1H NMR spectroscopy, which confirms the unsymmetrical substitution of the naphthalenediyl backbones.

Compound **73** crystallizes in the space group *P*-1 with two independent molecules in the asymmetric unit (Figure 137). The two independent molecules possess almost identical structures and feature a short Au-Sb bond distance of 2.76 Å (av.). This bond distance is essentially equal to the sum of the covalent radii of the two elements (2.75 Å),[236] and is only marginally longer than the Au-Sb bonds found in stibine-gold complexes such as $[Au(SbMes_3)_2][ClO_4]$ (2.58 Å)[362] and $[Au(SbPh_3)_4][ClO_4]$ (2.656 − 2.658 Å).[363]

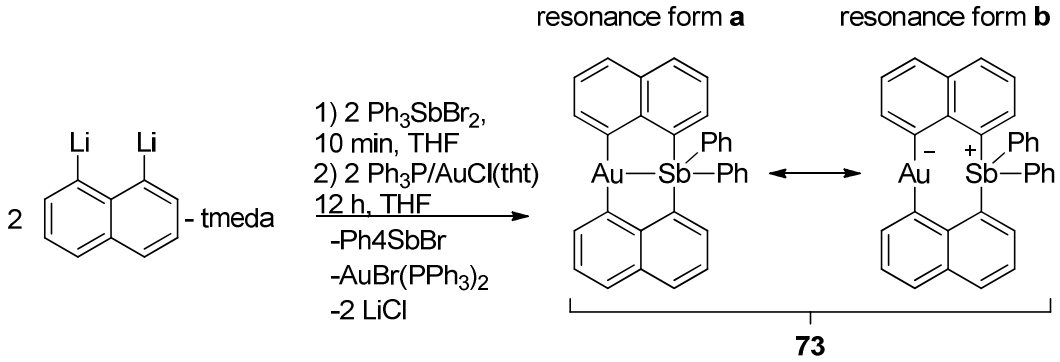

Figure 136. Synthesis of the gold-antimony complex **73**.

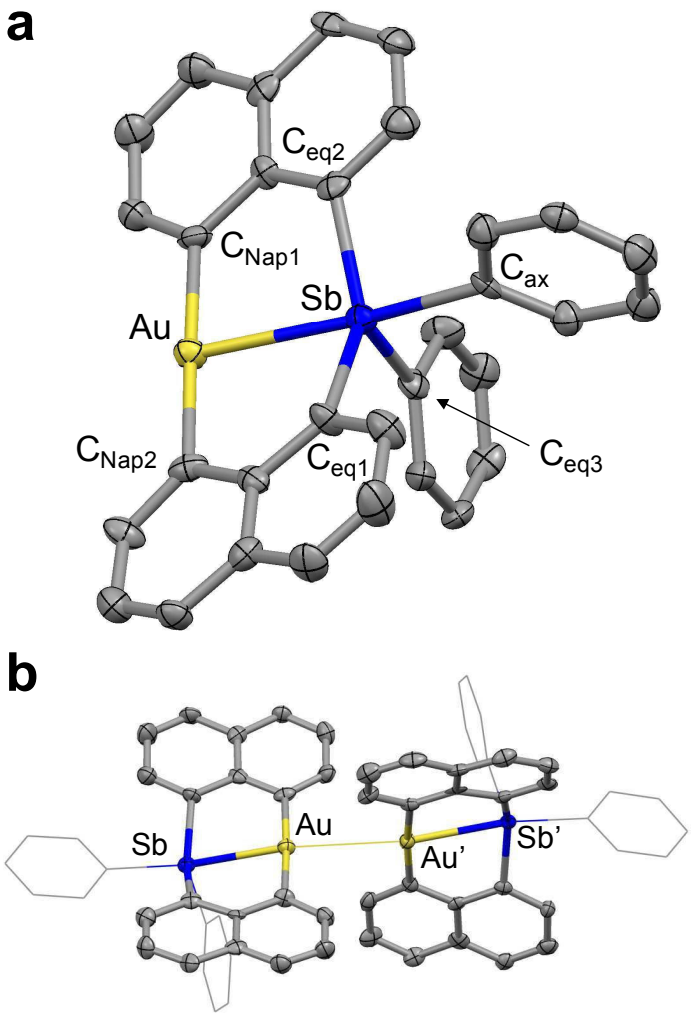

Figure 137. Crystal structure of (**a**) one of the independent molecules of **73** and (**b**) both independent molecules showing the presence of the aurophilic contact. Thermal ellipsoids are drawn at the 50% probability level. Hydrogen atoms are omitted for clarity. Selected bond lengths (Å) and angles (deg) (the metrical parameters of the second independent molecule are given in brackets): Au-Sb 2.7486(7) [2.7746(8)], Au-Au' 3.2551(7); C_{Nap1}-Au-C_{Nap2} 177.0(3) [172.4(3)], C_{Nap1}-Au-Sb 88.8(3) [88.6(2)], C_{Nap2}-Au-Sb 89.2(3) [88.5(3)], Au-Sb-C_{ax} 172.0(2) [171.4(3)].

Considering these comparisons, the short Au-Sb distance in **73** suggests a strong bonding interaction between the two atoms. This view is further reinforced by a comparison of **73** with its isoelectronic mercury analogue.[361] Indeed, despite the

similarity of the covalent radii of mercury (1.32 Å) and gold (1.36 Å),[236] the average Au-Sb bond distance in **73** (2.76 Å, respectively) is markedly shorter than the Hg→Sb bond observed in **72** (3.0601(7) Å). Owing to the presence of this Au-Sb bond, the gold atom adopts a T-shaped geometry, as confirmed by the average C_{Nap}-Au-Sb and C_{Nap1}-Au-C_{Nap2} angles of 88.8° and 174.7°, respectively. Accordingly, the antimony atom displays a distorted trigonal bipyramidal geometry with the gold atom in an axial position. The Au-Sb-C_{ax} angle of 171.8° (av.), as well as the sum of the C_{eq}-Sb-C_{eq} angles of 356.3° (av.), supports this view (Figure 137). Additionally, the Sb-C_{ax} bond (2.48 Å av.), trans to the gold atom, is only slightly longer than the equatorial Sb-C_{eq3} bond (2.11 Å av.). A last point of interest in this structure relates to the presence of an aurophilic interaction of 3.2551(7) Å that connects the two independent molecules (Figure 137). The formation of such a contact, as well as the perpendicular orientation of the two monomers, is reminiscent of monovalent gold compounds such as Me_3PAuI[364] or (2,6-$Me_2C_6H_3NC$)AuCl,[365] which also form perpendicular aurophilic dimers with Au-Au distances of 3.168(1) Å and 3.3555(5) Å, respectively.[286] Aurophilic contacts involving trivalent species are limited to two examples each of which displays stacked square planar units and Au-Au distances longer than 3.5 Å.[366-368] This structural analysis indicates that the gold atom of **73** may be as electron rich as that of gold monohalide complexes.

Based on these observations and analysis, we considered two possible resonance forms, **a** and **b**, to represent Au-Sb bonding in **73** (Figure 136). While the short Au-Sb bond distance supports resonance form **a** with a larger degree of covalent bonding

between the two atoms, the presence of aurophilic interactions in the solid state are characteristic of simple monovalent complexes and point to the relevance of the ionic resonance form **b**. To help assign the relative abundance of these resonance forms and gain further insight into the electronic structure of **73**, we decided to perform Au L_3- and Sb K-edge X-ray Absorption Near Edge Structure (XANES) spectroscopy measurements, an experimental technique that has been shown to provide information related to the oxidation states of these elements.

8.3 X-ray absorption spectroscopy studies

The room temperature, solid state Au L_3-edge XANES spectra of **73** and two reference compounds, $AuCl(PPh_3)$ and $CsAuCl_4$, were measured (Figure 138). In the case of gold(III) compounds, the L_3-edge XANES spectra are dominated by $2p \rightarrow 5d$ transitions. As a result, trivalent gold compounds display an intense white-line feature at the edge and lower L_3-edge energies than their monovalent counterparts, which have a filled d-shell.[369-373] In agreement with this established trend, we observed that the edge position of the trivalent gold reference $CsAuCl_4$ (11918.9 eV) is at lower energy than that measured for the monovalent gold reference compound $AuCl(PPh_3)$ (11921.2 eV). Notably, the Au L_3 XANES spectrum of **73** shows an edge position of 11921.4 eV, a value very close to that measured for the monovalent gold reference $AuCl(PPh_3)$.

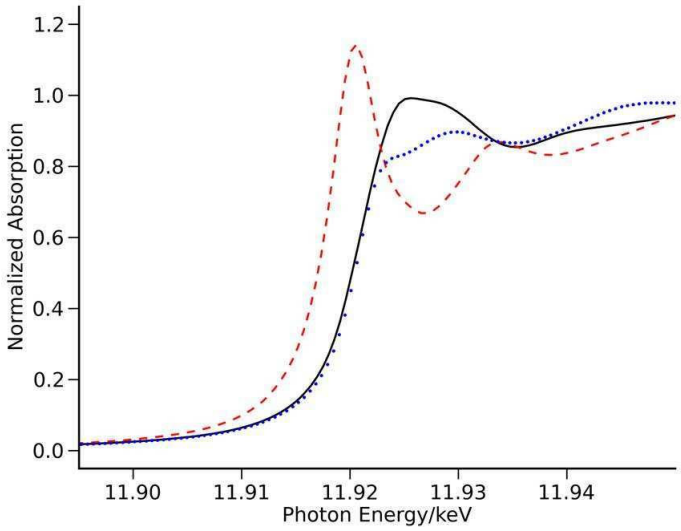

Figure 138. Solid-state Au L3–edge XANES spectra of **73** (—) and reference complexes $CsAuCl_4$ (- - -) and $AuCl(PPh_3)$ (•••).

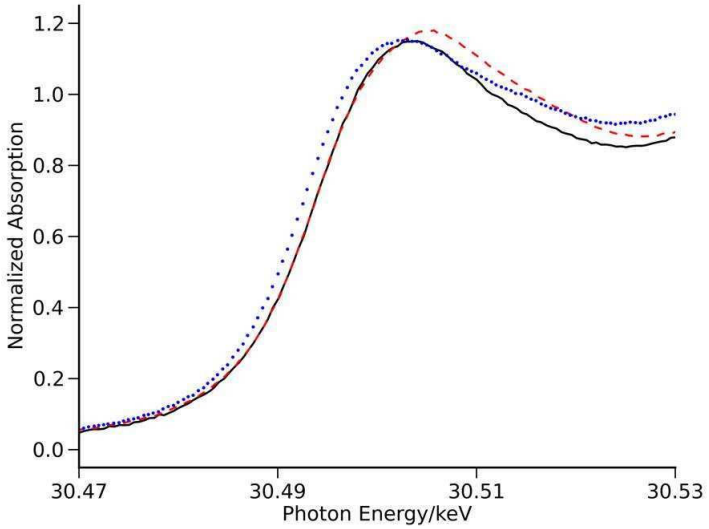

Figure 139. Solid-state Sb K-edge XANES spectra of **73** (—) and reference complexes $[SbPh_4]OTf$ (- - -) and $SbPh_3$ (•••).

Next, we decided to study compound **73** by Sb K-edge-XANES spectroscopy. The Sb K-edge of XANES spectra is typically dominated by 1s→p transitions, whose energy increases with the valence of the antimony atom. Our measurements, shown in Figure 139, indicate that the Sb K-edge of **73** (30493.3 eV) is identical to that measured for the stibonium salt $[SbPh_4][OTf]$ (30493.3 eV) and appears at higher energy than that of the trivalent reference compound $SbPh_3$ (30492.0 eV). Although only a small energy difference (1.3 eV) was observed between the Sb K-edge of $SbPh_3$ and those of **73** and $[SbPh_4][OTf]$, multiple recordings of each spectrum showed very little variance (less than 0.1 eV), confirming that the difference is not the result of random measurement error. Collectively, these results indicate that the aurate-stibonium resonance structure **b** (Figure 136) for **73** must be considered, possibly as the most important contributor. It follows that **73** is closely related to a series of complexes such as **71**[374] and **74**,[320] which have been described according to a donor-acceptor formalism with the late transition metal center acting as a σ-donor and the main group element serving as a σ-acceptor ligand (Figure 140).[303,375-378,321,379-393]

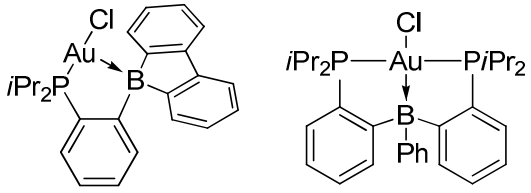

71 **74**

Figure 140. Phosphoranylborane gold complexes **71** and **74**.

8.4 Computational studies

To increase our understanding of the electronic structure of **73**, we carried out DFT calculations using the ADF program. All calculations were carried out at the BP86/TZP level of theory using the zero-order regular approximation (ZORA). Geometry optimization, starting from the solid state structure of one of the independent molecules of **73**, afforded a structure that is in excellent agreement with that observed experimentally.

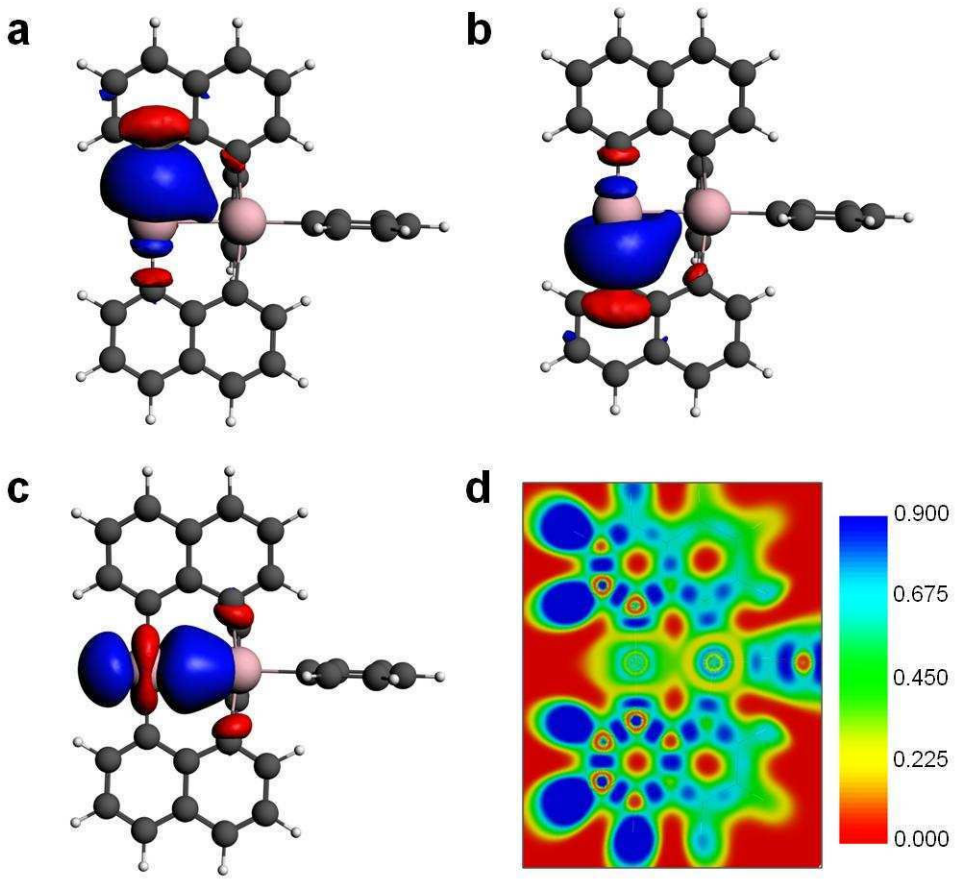

Figure 141. (**a-c**) Gold-centered Boys orbitals for **73** (drawn with a 0.02 isodensity value). (**d**) Plot of the Electron Localization Function for **73**.

A first assessment of the nature of the Au-Sb bond was derived from the Electron Localization Function (ELF), which can be used to map the electron pair localization in a molecule.[394] The ELF map of **73** is characterized by a continuum of relatively elevated ELF values along the Au-Sb vector, indicating some degree of electron sharing between the two heavy atoms (Figure 141). Additional insight into the nature of the Au-Sb bond was provided by a molecular orbital analysis. Compound **73** was subjected to a Boys localization analysis because of extensive delocalization of the occupied Kohn-Sham orbitals. This analysis identified two C-Au σ-bonding orbitals connecting the Au atom to the two naphthalene ligands. These σ-orbitals show little polarization, in agreement with the low electronegativity difference between carbon ($\chi = 2.54$) and gold ($\chi = 2.55$). By contrast, the only orbital of σ-symmetry oriented along the Au-Sb axis is very strongly polarized toward the gold atom with very little contribution from the antimony atom. This observation supports the notion that the stiboranyl ligand acts as a strong σ-donor. It also lends further support to the relevance of the aurate-stibonium contribution in the description of **73**. In addition, the electrostatic potential map of **73** shows a clear accumulation of negative charge on the gold atom (Figure 142).

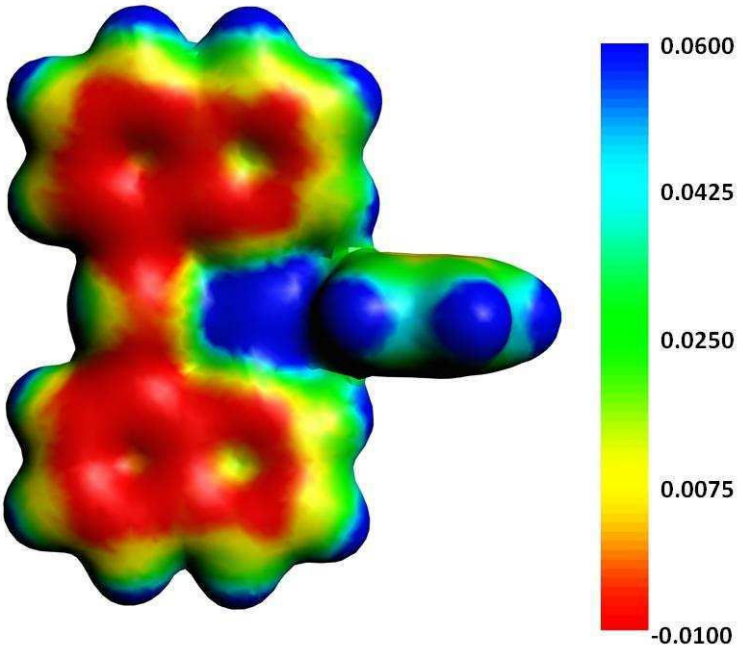

Figure 142. Electrostatic potential surface map of **73** plotted at a 0.01 isodensity value.

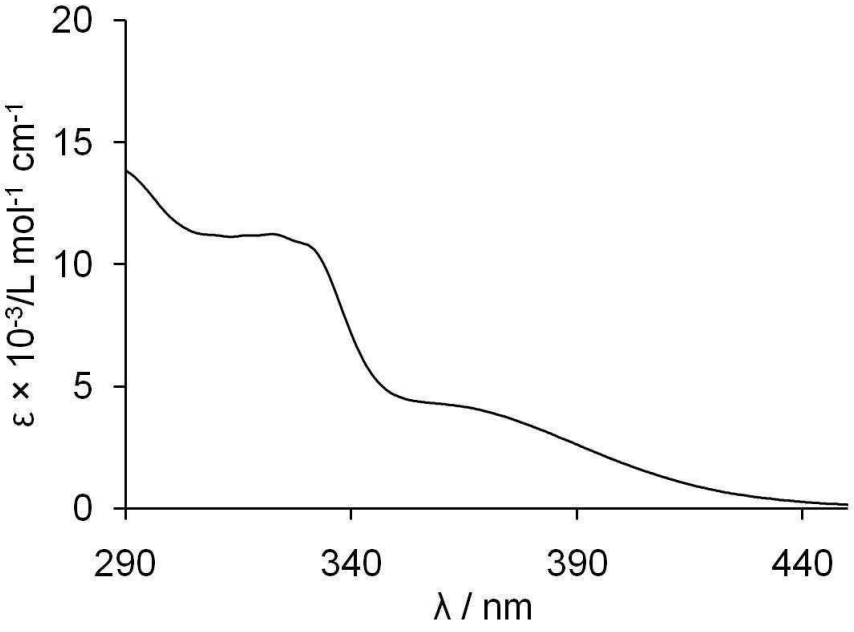

Figure 143. UV-Vis absorption spectra of **73** in CH_2Cl_2.

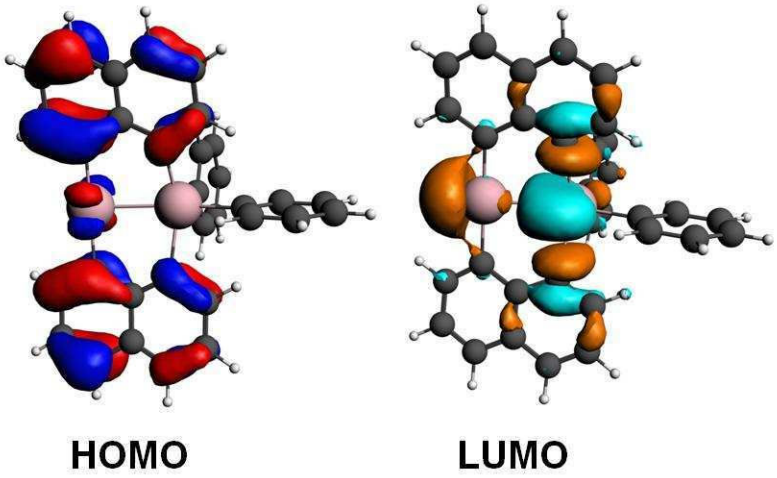

Figure 144. Frontier molecular orbitals of **73** (drawn with a 0.02 isodensity value).

8.5 Photophysical properties

The electronic absorption spectrum of **73** in CH_2Cl_2 displays a broad band that spanns the 350 - 440 nm range (Figure 143). This low energy feature is attributed to a transition from the naphthalene-based HOMO to the LUMO, which bears a significant contribution from the gold 6p and Sb-C_{Ph} σ* orbitals (Figure 144). The solid state emission spectrum of **73**, measured at 77 K, shows a broad emission centered at around 660 nm (Figure 145). This band is not observed at room temperature, suggesting that it corresponds to a triplet excited state arising from a gold heavy atom effect. This view is confirmed by the excited state lifetime of 6.8 μs, which is comparable to that observed for other aurated aromatic derivatives.[302,317,318] Oxygen-free solutions of **73** in CH_2Cl_2 are not visibly luminescent at room temperature. Upon freezing, however, these solutions give rise to a bright orange emission centered at 560 nm (Figure 145). In turn, the emission of **73** in frozen solution is distinctly blue shifted when compared to that of

the solid state, a phenomenon that we assign to the absence of aurophilic interactions under these conditions.

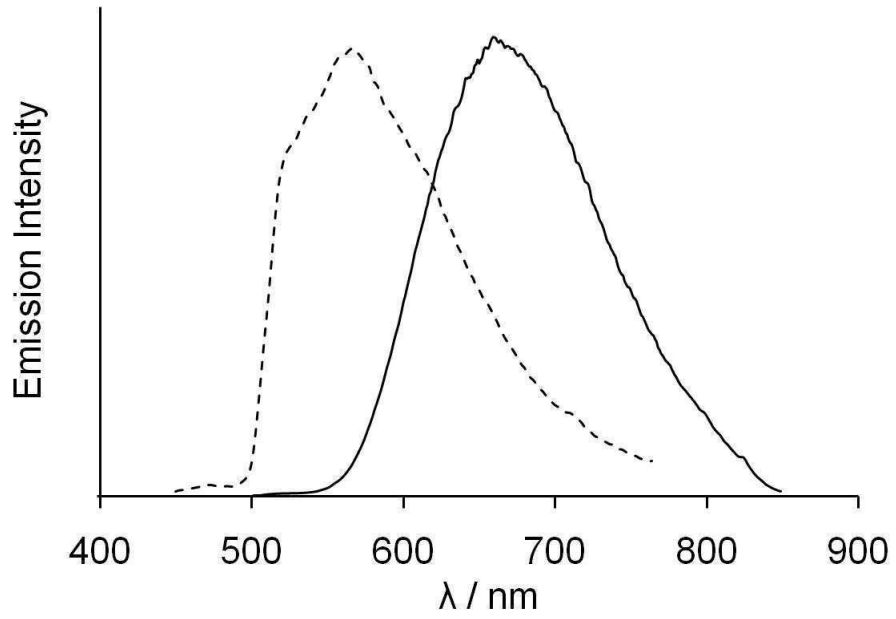

Figure 145. Low temperature (77 K) emission spectra of **73** in the solid state (—) and frozen CH_2Cl_2 solution (····).

8.6 Reactions with halide ions

In line with an accumulation of electron density on the gold atom, and hence the strong σ-donating properties of the stiboranyl ligand, ^{1}H NMR and crystallization experiments indicate that the gold atom of **73** shows no affinity for chloride, bromide or iodide anions in $CDCl_3$. The NMR experiments also showed no detectable interaction between these halide anions and the antimony center of **73**. However, **73** quickly reacts

with tetra-*n*-butylammonium fluoride (TBAF) to form an aurated fluoroantimonate anion [**75**]$^-$, which has been isolated as the tetra-*n*-butylammonium salt (Figure 146).

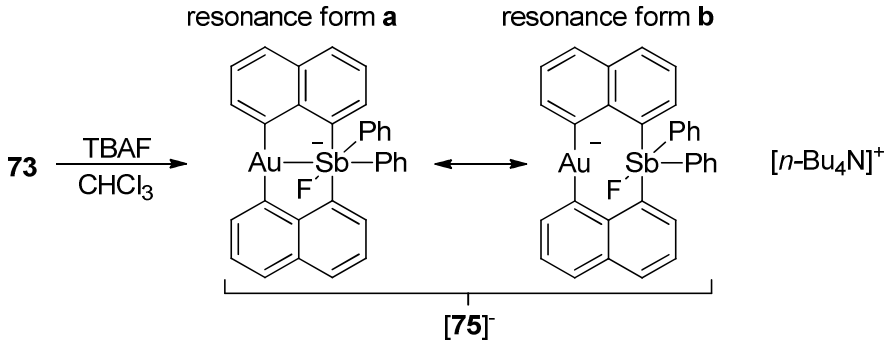

Figure 146. Synthesis of [*n*-Bu_4N][**75**] (TBAF = tetra-*n*-butylammonium fluoride).

Evidence for the formation of a Sb-F bond, rather than a Au-F bond, was provided by the detection of a ^{19}F NMR signal (in acetone-d_6) at -41 ppm, a chemical shift close to that observed for Me_4SbF.[395] The selectivity of the antimony center for fluoride over the larger halides is a well-documented phenomenon that can be assigned to the increased contribution of the stibonium halide form as the size of the halogen increases.[158] The formation of [**75**]$^-$ was monitored by UV-vis spectroscopy upon incremental addition of TBAF to a solution of **73** in CH_2Cl_2 . The resulting spectra show that fluoride binding to the antimony quenches the low energy band present in the spectrum of **73** (Figure 147). Additionally, fitting of this data to a 1:1 binding isotherm indicates that the fluoride binding constant of **73** is $>10^7$ M^{-1}. The changes in the UV-Vis spectra can be rationalized by an increase in the energy of the LUMO of [**75**]$^-$ caused by anion coordination. Although DFT calculations (BP86/TZP level of theory with ZORA)

indicate that the make-up of this orbital remains similar to that of **73** (Figure 148), fluoride coordination to the antimony center increases the energy of the HOMO-LUMO energy gap. In line with this argument, the spectrum of [*n*-Bu_4N][**75**] shows the emergence of a new absorption band centered at around 310 nm.

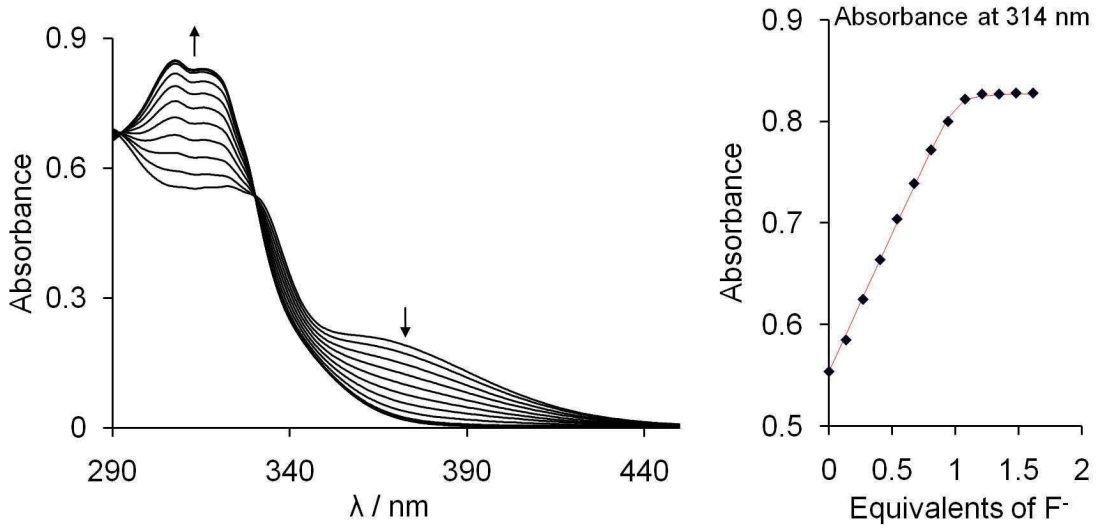

Figure 147. Spectral changes in the UV-Vis absorption spectrum of **73** (5.0×10^{-5} M in CH_2Cl_2) upon incremental addition of a TBAF solution (4.0×10^{-3} M, CH_2Cl_2). The isotherms are plotted based on the absorbance at 314 nm, and the line indicates the fit to the calculated 1:1 binding isotherm.

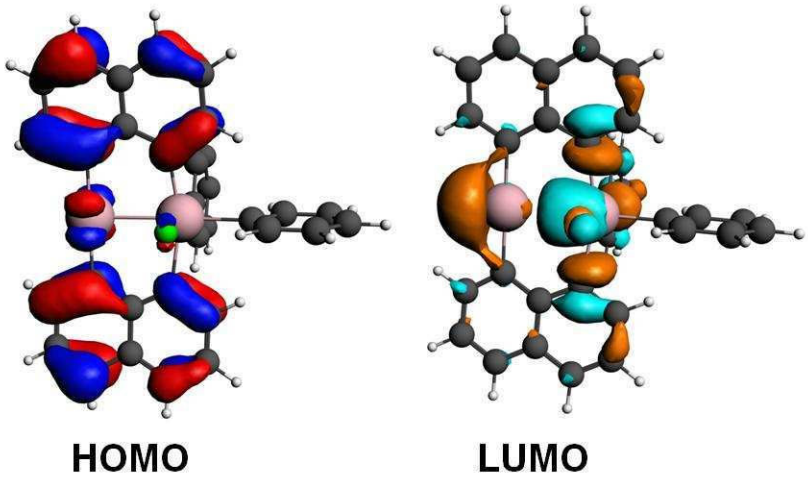

Figure 148. Frontier molecular orbitals of [**75**]$^-$ (drawn with a 0.02 isodensity value).

Recrystallization of [*n*-Bu_4N][**75**] from THF/toluene (1:1) afforded colorless, plate-like crystals that are not luminescent. The salt crystallizes in the space group *P*-1 with two independent molecules in the asymmetric unit. The structure of [**75**]$^-$ shows fluoride coordination to the antimony center with an average Sb-F bond distance of 2.08(2) Å (Figure 149). This Sb-F distance is similar to that observed in Ph_4SbF (2.0530(8) Å)[158] or Ph_3MeSbF (2.069(3) Å).[234] Fluoride coordination results in a nearly octahedral geometry around antimony with average angles of 174.7˚ for C_{Ph1}-Sb-F, 172.6˚ for C_{Ph2}-Sb-Au, and 163.4˚ for C_{Nap1}-Sb-C_{Nap2}. The coordination environment of the Au atom remains T-shaped with average C_{Naph}-Au-Sb and C_{Nap1}-Au-C_{Nap2} angles of 90.3˚ and 178.2˚, respectively. The Au-Sb distance of 2.77 Å (*av.*) is virtually unchanged compared to that in **73**. Inspection of the ELF map and Boys orbitals calculated for [**75**]$^-$ shows that they are strikingly similar to those of **73**, thus indicating that the nature of the Au-Sb bond is not significantly altered by coordination of a fluoride anion to the

antimony center (Figure 150). In turn, compound [**75**]$^-$ can also be described by two resonance structures: the first one corresponding to an aurated antimonate anion (resonance form **a**), and the second one to an aurate fluorostiborane derivative (resonance form **b**) (Figure 146).

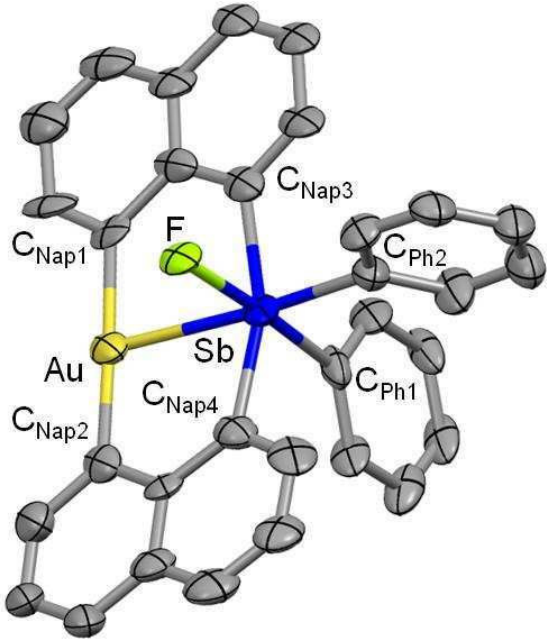

Figure 149. Crystal structure of [**75**]$^-$. Only one of the independent molecules is shown. Thermal ellipsoids are drawn at the 50% probability. Hydrogen atoms and *n*-Bu_4N^+ counterion are omitted for clarity. Selected bond lengths (Å) and angles (deg) (the metrical parameters of the second independent molecule are given in brackets): Au-Sb 2.7694(8) [2.7728(9)], Sb-F 2.091(5) [2.060(5)]; C_{Nap1}-Au-C_{Nap2} 179.2(4) [177.3(3)], C_{Nap1}-Au-Sb 89.9(3) [91.4(3)], C_{Nap2}-Au-Sb 90.4(2) [89.4(3)], Au-Sb-C_{Ph2} 170.4(3) [174.9(3)], F-Sb-C_{Ph1} 174.5(3) [174.9(3)], C_{Nap3}-Sb-C_{Nap4} 164.0(4) [162.9(4)].

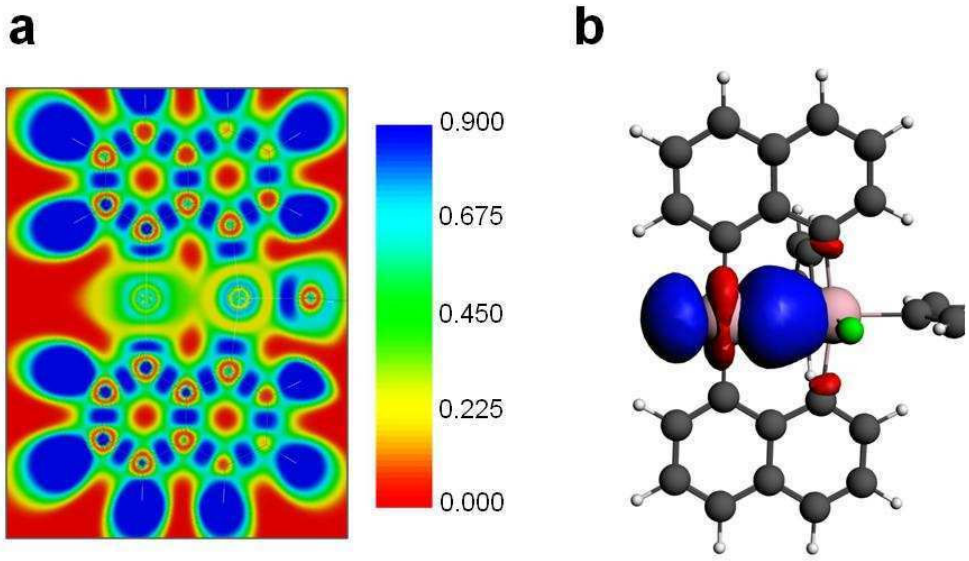

Figure 150. (**a**) Plot of the Electron Localization Function for [**75**]¯. (**b**) Gold-centered Boys orbitals for [**75**]¯ (drawn with a 0.02 isodensity value).

8.7 Conclusions

We have prepared and structurally characterized the first example of a tetraorganostiboranyl-gold complex **73**. The structural and computational results obtained for this compound support the hypothesis that tetraorganostiboranyl ligands have strong σ-donating properties. This strong σ-donation leads to an accumulation of electron density on the gold center of **73**, giving rise to the emergence of aurophilicity, a phenomenon typically only observed for monovalent gold species.[286] Another manifestation of these strong σ-donating properties is the stabilization of the gold atom in a T-shaped geometry. These observations, complemented by the results of the XANES measurements and DFT calculations, underscore the importance of a diarylaurate-stibonium resonance structure in the description of complex **73**. Adopting

the donor-acceptor formalism that has been recently popularized for late transition metals coordinated to Lewis acidic ligands, complex **73** can be described as a diarylaurate anion stabilized by partial electron donation to a Lewis acidic stibonium ligand. The same reasoning can be applied to [**75**]$^{-}$, which can be described as a diarylaurate anion intramolecularly stabilized by a Lewis acidic fluorostiborane.[321,374,376,377,379-384,386-388]

8.8 Experimental

General Considerations. Antimony compounds are highly toxic and should be handled cautiously. Triphenylphosphine was purchased from Aldrich. Tetra-*n*-butylammonium fluoride was purchased from Alfa Aesar. 1,8-dilithionaphthalene·TMEDA,[323] triphenyl-dibromoantimony,[396] and AuCl(tht)[324] (tht = tetrahydrothiophene) were prepared according to the reported procedures. All preparations were carried out under an atmosphere of dry N_2 employing either a glove box or standard Schlenk techniques. Solvents were dried by passing through an alumina column (CH_2Cl_2) or refluxing under N_2 over Na/K (Et_2O, n-hexane, and THF). NMR spectra were recorded on a Varian Unity Inova 400 FT NMR (399.59 MHz for ^{1}H, 375.99 MHz for ^{19}F, 100.45 MHz for ^{13}C) spectrometer at ambient temperature. Chemical shifts are given in ppm and are referenced to residual ^{1}H and ^{13}C solvent signals and external $BF_3 \cdot Et_2O$ for ^{19}F. Elemental analyses were performed by Atlantic Microlab (Norcross, GA).

Table 22. Crystal Data, Data Collection, and Structure Refinement for **73** and *n*-Bu_4N[**75**].

	73	*n*-Bu_4N[**75**]
Formula	$C_{64}H_{44}Au_2Sb_2$	$C_{96}H_{116}N_2F_2Au_2Sb_2$
Mr	1450.42	1973.34
Crystal system	Triclinic	Triclinic
Space group	*P-1*	*P-1*
a (Å)	12.386(3)	12.6431(16)
b (Å)	14.009(3)	15.846(2)
c (Å)	14.412(3)	23.458(3)
α (°)	86.286(3)	85.612(2)
β (°)	82.757(3)	83.940(2)
γ (°)	69.417(3)	83.805(2)
V (Å^3)	2321.9(10)	4636.0(10)
Z	2	2
ρ calc (g cm^{-3})	2.075	1.414
μ (mm^{-1})	7.494	3.777
F (000)	1376	1968
Crystal size (mm^3)	0.25 x 0.15 x 0.07	0.40 x 0.10 x 0.04
T/K	110(2)	110(2)
Scan mode	ω, φ	ω, φ
hkl range	-14 → +14	-15 → +15
	-16 → +16	-18 → +18
	-17 → +17	-27 → +27
Measd reflns	22264	44374
Unique reflns (Rint)	8148 (0.0457)	16255 (0.0842)
Reflns used for refinement	8148	16255
Refined parameters	613	925
GooF on F^2	1.043	1.036
R_1,[a] wR_2[b] all data	0.0506, 0.1085	0.1082, 0.1179
ρ_{fin} (max., min.)/eÅ^{-3}	2.845, -1.669	1.595, -1.757

[a] $R1 = \Sigma||F_o| - |F_c||/\Sigma|F_o|$. [b] $wR2 = ([\Sigma\, w(F_o^2 - F_c^2)^2]/[\Sigma\, w(F_o^2)^2])^{1/2}$; $w = 1/[\sigma^2(F_o^2) + (ap)^2 + bp]$; $p = (F_o^2 + 2F_c^2)/3$ with a = 0.0540 for **73** and 0.0250 for *n*-Bu_4N[**75**]; and b = 6.9500 for **73** and 1.700 for *n*-Bu_4N[**75**].

Crystallography. Single crystals of **73** suitable for X-ray diffraction were obtained by layering the reaction mixture with Et_2O and hexanes. Single crystals of *n*-Bu_4N[**75**] were obtained by slow evaporation of a solution of the compound in THF/toluene (1/1 vol.). Details of the structure, data collection, and structure refinement for **73** and *n*-Bu_4N[**75**] are included in Table 22. The crystallographic measurements were performed using a

Bruker-AXS APEX-II CCD area detector diffractometer, with a graphite-monochromated Mo-Kα radiation (λ = 0.71069 Å). A specimen of suitable size and quality was selected and mounted onto a nylon loop. The semiempirical method SADABS[207] was applied for absorption correction. The structures were solved by direct methods using SHELXTL/PC package (version 6.1)[208] which successfully located most of the non-hydrogen atoms. Subsequent refinement on F^2 allowed location of the remaining non-hydrogen atoms. All H atoms were geometrically placed and refined in a riding model approximation.

After numerous modeling attempts, heavily disordered solvent molecules in the structure of [*n*-Bu_4N][**75**] were handled using the Squeeze program implemented in PLATON.[328] The program calculated a solvent-accessible volume of 726.9 $Å^3$ (15.68 % of the total unit cell volume), which was then removed from subsequent structure factor calculations.

Synthesis of 73. A solution of Ph_3SbBr_2 (500 mg, 0.976 mmol) in THF (3 mL) was added dropwise to a solution of 1,8-dilithionaphthalene (250 mg, 0.976 mmol) in THF (2 mL) at ambient temperature. The mixture was allowed to stir for 10 min before adding a solution of AuCl(tht) (313 mg, 0.976 mmol) and Ph_3P (256 mg, 0.976 mmol) in THF (5 mL). The resulting clear yellow solution was layered with Et_2O (5 mL) and hexane (5 mL) and allowed to stand at room temperature. After 2 days, a mixture of yellow and colorless crystals was obtained. Both types of crystals were suitable for X-ray diffraction, which identified the colorless crystals as $AuBr(Ph_3P)_2$ and the yellow crystals as complex **73**. Multiple recrystallizations of the crude mixture from hot CH_2Cl_2

(10 mL) provided a pure sample of **73** (130 mg, 37% yield). ^{1}H NMR (399.59 MHz; $CDCl_3$): δ 8.02 (d, 2H, Naph-CH, $^{3}J_{H-H}$ = 7.81 Hz), 7.89 (dd, 2H, Naph-CH, $^{3}J_{H-H}$ = 6.6 Hz, $^{4}J_{H-H}$ = 1.2 Hz), 7.77 (dd, 2H, Naph-CH, $^{3}J_{H-H}$ = 8.1 Hz, $^{4}J_{H-H}$ = 1.2 Hz), 7.64-7.58 (m, 4H, Naph-CH), 7.44 (t, 2H, p-Ph-CH, $^{3}J_{H-H}$ = 7.3 Hz), 7.34 (t, 4H, m-Ph-CH, $^{3}J_{H-H}$ = 7.3 Hz), 7.27-7.20 (m, 6H, o-Ph-CH and Naph-CH); $^{13}C\{^{1}H\}$ NMR (100.45 MHz; $CDCl_3$): δ 183.71, 145.82, 139.66, 136.68, 135.69, 134.80, 134.62, 134.20, 133.13, 130.49, 129.66, 126.78, 124.33, 124.18; elemental analysis calculated (%) for $C_{32}H_{22}AuSb$: C 52.99, H 3.06, found C 52.38, H 3.12.

Synthesis of [n-Bu$_4$N][75]. Solid TBAF·3H$_2$O (4.4 mg, 0.013 mmol) was added to a solution of **73** (10 mg, 0.013 mmol) in $CHCl_3$ (1mL). Upon standing, [n-Bu$_4$N][**75**] precipitated as a colorless microcrystalline solid, which was washed with Et_2O (2mL) and dried in vacuum to yield 9.1 mg (70 %). Crystals of [n-Bu$_4$N][**75**] suitable for X-ray diffraction were obtained by slow evaporation of a solution of the compound in THF/toluene (1/1 vol.). ^{1}H NMR (399.59 MHz; acetone-d_6): δ 7.95 (br, 2H, Ph-CH), 7.75 (d, 2H, Naph-CH, $^{3}J_{H-H}$ = 7.88 Hz), 7.63 (d, 2H, Naph-CH, $^{3}J_{H-H}$ = 6.59 Hz), 7.58 (d, 2H, Naph-CH, $^{3}J_{H-H}$ = 8.06 Hz), 7.42-7.52 (m, 3H, Ph-CH), 7.37 (dd, 2H, Naph-CH, $^{3}J_{H-H}$ = 8.06, 6.59 Hz), 7.33 (d, 2H, Ph-CH, $^{3}J_{H-H}$ = 6.96 Hz), 7.07 (t, 2H, Naph-CH, $^{3}J_{H-H}$ = 6.96 Hz), 6.97 (t, 1H, Ph-CH, $^{3}J_{H-H}$ = 6.96 Hz), 6.78-6.88 (m, 4H, Naph-CH, Ph-CH), 3.24 (m, 8H, n-Bu$_4$N$^+$), 1.63 (m, 8H, n-Bu$_4$N$^+$), 1.26 (tq, 8H, n-Bu$_4$N$^+$, $^{3}J_{H-H}$ = 7.51 Hz) 0.88 (t, 8H, n-Bu$_4$N$^+$, $^{3}J_{H-H}$ = 7.33 Hz). $^{13}C\{^{1}H\}$ NMR (100.45 MHz; acetone-d_6): δ 187.97, 145.86, 137.87, 136.86, 136.37, 135.74, 135.64, 135.08, 134.70, 131.45, 131.32, 130.06, 129.47, 129.03, 127.96, 125.71, 124.07, 123.95, 59.10, 24.33, 20.25, 13.86. ^{19}F

NMR (375.99 MHz; acetone-d_6): δ -43.26. HRMS: m/z calculated for $C_{32}H_{22}FAuSb^-$: 743.0409, found: 743.0425.

Computational Details. DFT structural optimizations for **73** and [**75**]$^-$ were carried out using the ADF program (2008.01).[329-331] All calculations were carried out using the BP86 functional[332,333] with the all electron TZP basis sets for all atoms.[334] These calculations were performed using ZORA.[335-339] Electron localization function (ELF)[394] and Boys[340-342] localization were carried out in the ADF program. ELF plots as well as Boys localized orbitals were visualized in the ADFview program.

X-ray Absorption Spectroscopy. X-ray absorption measurements were acquired on Materials Research Collaborative Access Team (MR-CAT) beam lines at the Advanced Photon Source, Argonne National Laboratory. The Au L_3 edge (11,919 eV) spectra were acquired on an insertion-device beam line, and measurements of the Sb K edge (30,491 eV) were made on a bending magnet beam line. In both cases, spectra of elemental foils (Au and Sb, respectively) were collected simultaneously with the sample measurements for energy calibration, and multiple scans were taken to ensure spectrum reproducibility.

Insertion-device experiments utilized a cryogenically cooled double-crystal Si (111) monochromator in conjunction with an uncoated glass mirror to minimize the presence of harmonics. The monochromator was scanned continuously during the measurements with data points integrated over 0.6 eV for 0.07 s per data point. Measurements were made in transmission mode with the ionization chambers optimized for the maximum current with linear response (~1010 photons detected/s) using a mixture of nitrogen and

helium in the incident X-ray detector and a mixture of ca. 20% argon in nitrogen in the transmission X-ray detector.

Photon energies at the bending magnet were selected using a water-cooled, double-crystal Si(111) monochromator, which was detuned by approximately 50% to reduce harmonic reflections. Measurements were made in transmission mode with argon filled ionization chambers. Data points were acquired in four separate regions (energies relative to the elemental Sb K edge): a pre-edge region -250 to -30 eV (step size = 10 eV, dwell time = 0.3 s), the XANES region from -30 to +40 eV (step size = 0.5 eV, dwell time = 0.2 s), an initial EXAFS region from +40 eV to 6 k (step size = 0.07 k, dwell time = 0.5 s), and a final EXAFS region from 6 to 14 k (step size = 0.07 k, dwell time = 0.5 s). Samples were prepared by pressing ~20 mg finely ground powders of the compounds mixed with silica gel into 4 mm diameter cylindrical sample holder. Mixtures were made to be approximately 7.5 wt % Au for Au L_3-edge and 10 wt % Sb for Sb K-edge, and enough sample was used to obtain step height of about 1.5. Grinding and sample preparation was done in air, and the sample spectra were acquired in air at room temperature. In order to determine accurate and reproducible edge energies, the slightly asymmetric, initial positive feature in the first derivative XANES spectrum was fit using a linear combination of two independent Gaussian functions (generally over an energy range of +/- 10 eV around the peak). The fitted position of the Gaussian peak that best overlaps with the initial first derivative maximum was then chosen to represent the edge energy.

UV-Vis Absorption and Luminescence Measurements. Electronic absorption spectra were recorded using an Ocean Optics USB4000 spectrometer with an Ocean Optics ISS light source. Steady state emission spectra were collected at room temperature using a PTI QuantaMaster 4 fluorescence spectrophotometer equipped with a Model 810 PMT detector. Solution based samples were prepared at *ca.* 1 mM concentrations under an atmosphere of N_2 using dry, degassed CH_2Cl_2. Solid samples were loaded as powders in standard quartz NMR tubes and suspended in the sample cavity to sit at the intersection of the excitation and emission optical paths. Time-resolved phosphorescence lifetime data were collected using a PTI QuantaMaster spectrophotometer equipped with a pulsed Xenon light source and gated PMT detector.

CHAPTER IX

SYNTHESIS, STRUCTURE, AND REACTIVITY OF A TRIPHOSPHANYLSTIBINE GOLD COMPLEX*

9.1 Introduction

Two-electron redox processes occurring at the core of dinuclear metal complexes are important because of their implication in a number of chemical transformations ranging from the photocatalytic production of dihydrogen[397-399] to the oxidative functionalization of C-H bonds.[400-404] These processes are also well documented for binuclear gold complexes,[405,406] as well as for gold/rhodium,[407] gold/iridium[408] and gold/platinum[409] heterobimetallic complexes. One of the common features displayed by all of these complexes relates to their ability to undergo these changes without decomposition of the bimetallic core. As part of our recent interest in transition metal stiborane complexes, we questioned whether two-electron redox processes could be observed at the dinuclear core of transition metal/antimony complexes.

Triarylstibines are well known to undergo facile two-electron oxidation when exposed to oxidizing agents such as halogens.[410] In addition, there is precedent for Group 6 transition metal dialkylstibido complexes to undergo oxidative addition of bromine at the antimony center to afford metal-dibromostiborane species, as shown in Figure 151.[258,259]

---

* Reprinted in part with permission from, "Two-electron redox chemistry and reversible umpolung of a gold-antimony bond"; Wade, C. R.; Gabbaï F. P. *Angew. Chem. Int. Ed.* **2011**, *50*, 7369-7372. Copyright 2011 by John Wiley & Sons, Inc.

Our previous studies with d^8-transition metal complexes bearing the $(o\text{-}(Ph_2P)C_6H_4)_3Sb$ ligand showed that the metal-coordinated triarylstibine was sufficiently Lewis acidic to bind F^- and Cl^- anions, resulting in the formation of fluoro- and chlorostiborane complexes. Thus, for two-electron oxidation to occur at a binuclear metal/antimony core with this type of ligand, we predicted that a more electron rich transition metal would be required. Therefore we set out to prepare a d^{10} Au(I) complex with the $(o\text{-}(Ph_2P)C_6H_4)_3Sb$ ligand and explore its potential to undergo two-electron redox processes at the gold-antimony core. This chapter delineates our efforts in this area.

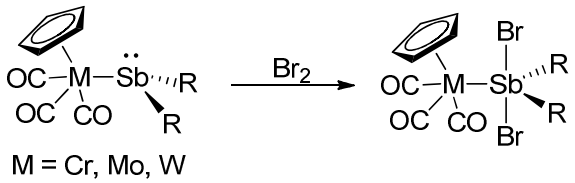

Figure 151. Reaction of transition metal stibido complexes with Br_2 to form metal dibromostiboranes.

9.2 Synthesis and reversible two-electron redox chemistry of a triphosphanylstibine gold complex

The triphosphanylstibine ligand $(o\text{-}(Ph_2P)C_6H_4)_3Sb$ (referred to as L)[266] was allowed to react with AuCl(tht) in CH_2Cl_2/acetone to generate **76**-Cl as a pale yellow precipitate (Figure 152). At -55 ˚C in $CDCl_3$, the $^{31}P\{^1H\}$ NMR spectrum of **76**-Cl displays two signals, at +39.5 and -7.37 ppm, in a 2:1 intensity ratio, thus suggesting that only two of the three phosphine arms of the ligand are coordinated to the gold atom. Upon elevation

of the temperature, these two peaks coalesce into one signal at 24.4 ppm, indicating the onset of a rapid exchange. Line shape analysis of the $^{31}P\{^{1}H\}$ NMR spectra of **76**-Cl over the -55 ˚C to +22 ˚C temperature range, followed by an Eyring analysis, afforded $\Delta H^{\ddagger}$ = +16.7(±0.9) kcal mol^{-1} and $\Delta S^{\ddagger}$ = +16.6(±3.8) cal mol^{-1} K^{-1}, suggesting a dissociative exchange of the phosphine arms. The ESI mass spectrum of this complex shows a peak at m/z = 1101.1180 amu, corresponding to the $[LAu]^{+}$ ion. The crystal structure determination of this compound confirmed the coordination of two of the phosphorus atoms to the gold chloride fragment (Figure 153). Inspection of the P-Au-P and P-Au-Cl angles (Σ =359.46 º) shows that these primary ligands are arranged around the gold atom in a trigonal planar fashion. Further inspection of the structure reveals a Au(1)-Sb(1) separation of 2.8374(4) Å. This separation is longer than the Au-Sb bond distances found in complexes such as $[Au(SbPh_3)_4][ClO_4]$ (2.656 − 2.658 Å).[363] Another noteworthy metrical feature is the value of the Au(1)-Sb(1)-C(37) angle (164.80(11)˚), which indicates that the stibine ligand approaches the gold atom to achieve a seesaw, rather than a tetrahedral, geometry.

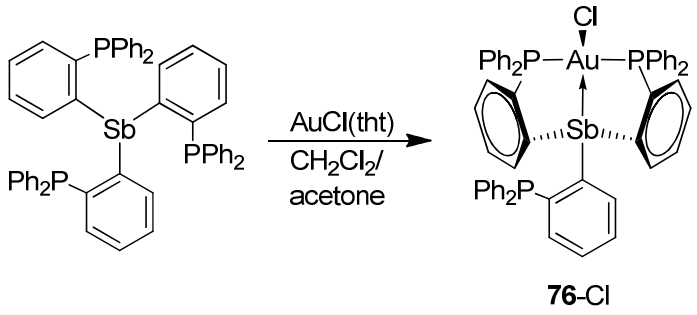

76-Cl

Figure 152. Synthesis of complex **76**-Cl.

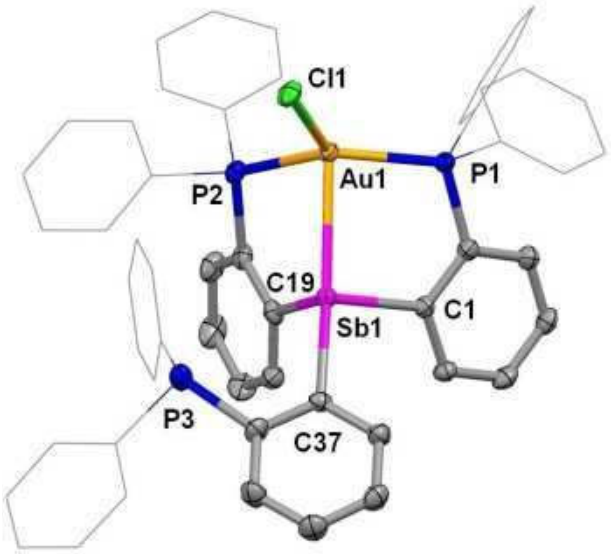

Figure 153. Crystal structure of **76**-Cl. Thermal ellipsoids are drawn at the 50% probability. Phenyl groups are drawn in wireframe, and hydrogen atoms are omitted for clarity. Selected bond lengths (Å) and angles (deg): Au(1)-P(1) 2.3084(11), Au(1)-P(2) 2.3305(11), Au(1)-Cl(1) 2.4990(11), Au(1)-Sb(1) 2.8374(4), Sb(1)-C(37) 2.175(4), Sb(1)-C(1) 2.178(4), Sb(1)-C(19) 2.178(4), P(1)-Au(1)-P(2) 133.46(4), P(1)-Au(1)-Cl(1) 116.99(4), P(2)-Au(1)-Cl(1) 109.01(4), P(1)-Au(1)-Sb(1) 86.99(3), P(2)-Au(1)-Sb(1) 83.94(3), Cl(1)-Au(1)-Sb(1) 109.91(3), C(1)-Sb(1)-C(37) 98.06(15), C(19)-Sb(1)-C(37) 100.34(16), C(1)-Sb(1)-C(19) 90.97(15), C(37)-Sb(1)-Au(1) 164.80(11).

With compound **76**-Cl in hand, we sought to determine if the gold-antimony core could sustain oxidation. Consequently, **76**-Cl was allowed to react with $PhICl_2$ in CH_2Cl_2 resulting in the formation of complex **77**-Cl as a yellow, air stable derivative (Figure 154). The ESI mass spectrum of **77**-Cl, which displays a peak corresponding to the $[LCl_2Au]^+$ ion (m/z = 1171.0551 amu), provided initial evidence for the oxidative addition of chlorine. The $^{31}P\{^1H\}$ NMR spectrum of **77**-Cl in $CDCl_3$ shows a single resonance at 41.9 ppm, which, in light of the crystal structure (*vide infra*), suggests rapid exhange of the phosphines on the NMR timescale. This signal showed no tendency

toward decoalescence upon cooling to -50 ºC. This finding is in agreement with the ^{1}H NMR ($CDCl_3$), which exhibits a single downfield doublet at 8.2 ppm corresponding to the phenylene proton ortho to antimony. The crystal structure of **77**-Cl shows coordination of two of the phosphine arms to gold and confirms addition of Cl_2 to the antimony center (Figure 155). While it is tempting to argue that oxidation is limited to the antimony center, the dinuclear core of the structure shows a clear response to oxidation. In particular, the Au-Sb distance in **77**-Cl (2.7086(9) Å) is shorter than that measured for **76**-Cl. Changes are also observed in the coordination sphere of the metals, which adopt a distorted octahedral and square planar geometry for antimony and gold, respectively. In particular, the square planar geometry of the gold atom suggests that it is affected by oxidation and transitions from a monovalent form in **76**-Cl to trivalent form in **77**-Cl.

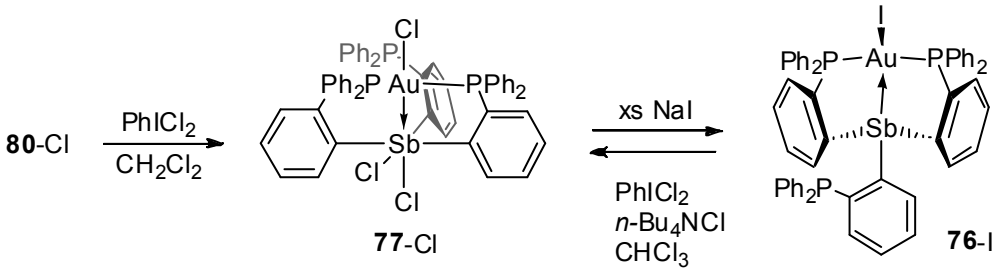

Figure 154. Synthesis of complex **77**-Cl and its reversible conversion into **76**-I.

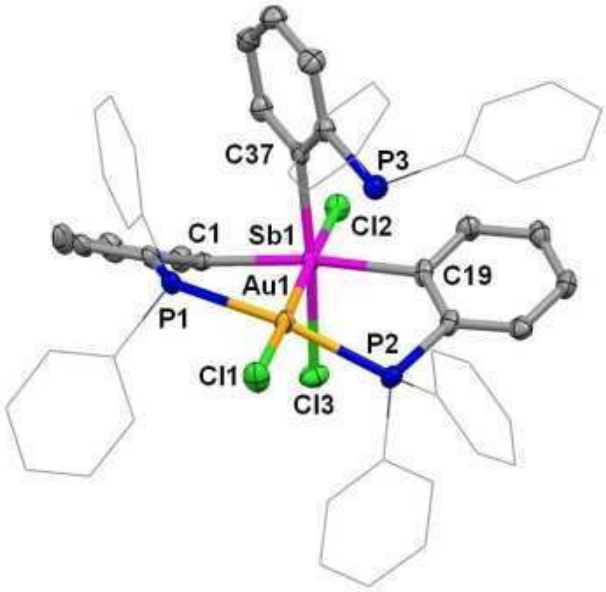

Figure 155. Crystal structure of **77**-Cl. Thermal ellipsoids are drawn at the 50% probability. Phenyl groups are drawn in wireframe, and hydrogen atoms are omitted for clarity. Selected bond lengths (Å) and angles (deg): Au(1)-P(1) 2.3246(15), Au(1)-P(2) 2.3328(14), Au(1)-Cl(1) 2.4601(14), Au(1)-Sb(1) 2.7086(9), Sb(1)-C(1) 2.193(5), Sb(1)-C(19) 2.197(5), Sb(1)-C(37) 2.215(5), Sb(1)-Cl(2) 2.4960(14), Sb(1)-Cl(3) 2.5627(15), P(1)-Au(1)-P(2) 166.20(5), Cl(1)-Au(1)-Sb(1) 178.18(3), C(1)-Sb(1)-C(19) 169.56(17), C(37)-Sb(1)-Cl(3) 171.29(12), Cl(2)-Sb(1)-Au(1) 177.37(3), Cl(2)-Sb(1)-Cl(3) 85.47(5).

Since the reversibility of redox processes is often key to catalytic chemical transformations with bimetallic systems, we set out to address the reversibility of the redox process supported by the gold-antimony platform. Although we found that **77**-Cl did not react cleanly with strong reducing agents such as Na or Na/Hg, we observed a clean reaction in the presence of NaI. Indeed, upon mixing **77**-Cl with 4 eq. of NaI in acetone, the solution quickly developed a brown color, which we assigned to the formation of I_3^- (Figure 154). The reaction could be conveniently followed by $^{31}P\{^1H\}$ NMR spectroscopy, which clearly indicates formation of a new species featuring a broad

resonance at 22.7 ppm. Reduction of **77**-Cl is supported by the ESI mass spectrum of the reaction mixture, which exhibits a peak corresponding to the $[LAu]^+$ ion (m/z = 1101.1188). Single crystal X-ray diffraction confirmed the identity of the reduction product as **76**-I, the iodide analog of **76**-Cl (Figure 156). This product was isolated in 63% yield and was fully characterized. Lastly, we found that **76**-I can be reoxidized into **77**-Cl by reaction with $PhICl_2$ in the presence of excess nBu$_4$NCl in $CHCl_3$, as indicated by ^{31}P NMR and ESI MS monitoring of the reaction.

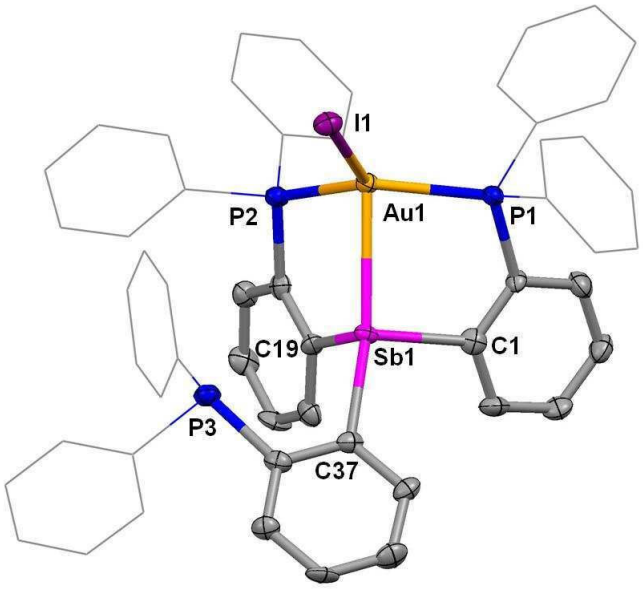

Figure 156. Crystal structure of **76**-I. Thermal ellipsoids are drawn at the 50% probability. Phenyl groups are drawn in wireframe, and hydrogen atoms are omitted for clarity. Selected bond lengths (Å) and angles (deg): Au(1)-Sb(1) 2.7958(11), Au(1)-I(1) 2.7818(11), Au(1)-P(1) 2.348(4), Au(1)-P(2) 2.336(4), P(1)-Au(1)-P(2) 131.58(13), P(1)-Au(1)-I(1) 110.10(9), P(2)-Au(1)-I(1) 117.71(9), P(1)-Au(1)-Sb(1) 84.79(9), P(2)-Au(1)-Sb(1) 85.15(9), I(1)-Au(1)-Sb(1) 111.10(3), C(1)-Sb(1)-C(37) 102.3(5), C(19)-Sb(1)-C(37) 98.5(5), C(1)-Sb(1)-C(19) 91.9(5), C(37)-Sb(1)-Au(1) 160.7(4).

9.3 Computational studies on **76**-Cl and **77**-Cl

To characterize the changes induced by oxidation, the structures of **76**-Cl and **77**-Cl were optimized using the ADF program and subjected to a Boys localization analysis and an NBO analysis. For **76**-Cl, the NBO analysis identified a relatively weak lp(Sb)→p(Au) donor-acceptor interaction (E_{del} = 35.28 kcal/mol) as the primary interaction (Figure 157). Accordingly, the Boys orbital corresponding to this interaction is localized on antimony and shows only a slight polarization toward the gold atom, supporting the presence of a rather weak dative bond (Figure 157). For **77**-Cl, Au-Sb bonding is dominated by Au→Sb donation. The primary interactions identified by NBO include a lp(Au)→σ*(Sb-Cl) and two lp(Au)→σ*(Sb-C) interactions, whose concomitant deletion gave rise to an increase of the energy of the complex by E_{del} = 63.59 kcal/mol (Figure 158). These computational results support a strengthening of the Au-Sb bond on going from **76**-Cl to **77**-Cl. They also indicate an umpolung of the Au-Sb dative bond, which switches from Sb→Au in **76**-Cl to Au→Sb in **77**-Cl. This umpolung is consistent with a transition of the gold atom from monovalent in **76**-Cl to trivalent in **77**-Cl. This view was validated by the results of the Boys localization analysis for **77**-Cl, which identified a Au-Sb σ-bond that clearly engages both metal atoms (Figure 158). Complex **77**-Cl is related to a series of complexes with Au→Lewis acid interactions[303,375-378,411] pioneered by Bourissou.[320-322,384,386,393,412] Such complexes have typically been assembled by coordination of phosphine/Lewis acid ambiphilic ligands to gold(I) synthons. In this respect, the synthesis of **77**-Cl stands out because it is achieved via oxidation of a pre-assembled complex.[304,413-417]

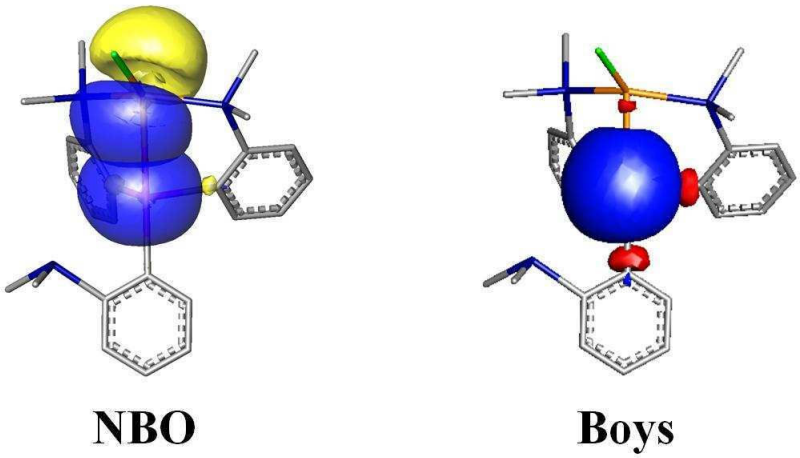

Figure 157. Plots of the primary NBO donor-acceptor interactions in **76**-Cl and the Au-Sb Boys orbital (0.03 isodensity value). Hydrogens and phenyl rings have been omitted for clarity.

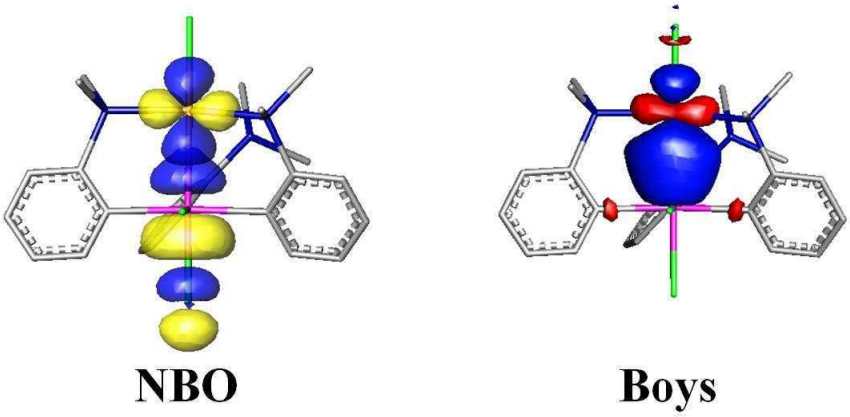

Figure 158. Plots of the primary NBO donor-acceptor interactions in **77**-Cl and the Au-Sb Boys orbital (0.03 isodensity value). Hydrogens and phenyl rings have been omitted for clarity.

9.4 Halide exchange

The addition of 6 equiv. of KF to a solution of **77**-Cl in MeOH results in the formation of the fluorinated derivative **77**-F as a yellow precipitate (Figure 159). The $^{31}P\{^{1}H\}$

NMR spectrum of **77**-F in $CDCl_3$ displays two signals, at +60.4 and +22.4 ppm, appearing with primary doublet and triplet splitting patterns, respectively, in a 2:1 intensity ratio. The downfield chemical shifts and $^2J_{P\text{-}P}$ coupling of the signals suggests unsymmetrical coordination of the three phosphine arms to the Au atom. The appearance of two signals, at -9.4 and -153.0 ppm, in the ^{19}F NMR spectrum further support the formation of a difluorostiborane complex.

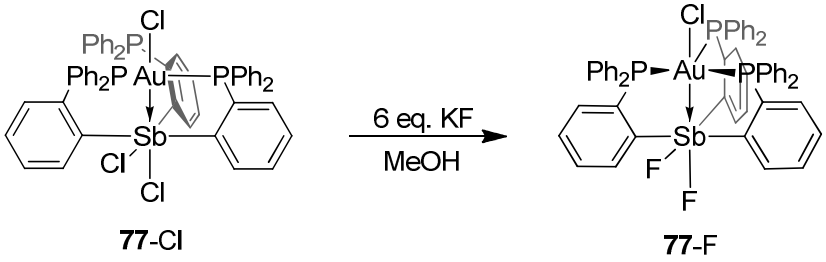

77-Cl **77**-F

Figure 159. Synthesis of **77**-F.

The X-ray crystal structure of **77**-F corroborates these spectroscopic results showing the addition of two fluorine atoms to the antimony center (Figure 160). Like **77**-Cl, the antimony atom of **77**-F adopts an octahedral coordination environment. Notably, a distorted trigonal bipyramidal geometry is observed around the gold center, with the three phosphine ligands occupying the trigonal plane ($\Sigma_{P\text{-}Au\text{-}P}$ = 358.27˚) and the chloride and antimony ligands in the axial positions (Cl(1)-Au(1)-Sb(1) 178.42(3)˚). Only a few examples of five coordinate, trigonal bipyramidal gold complexes have been reported in the literature, and these are limited to complexes containing ambiphilic Z-type ligands with B or Ga acceptor ligands and a formally trivalent complex $AuI_3(PMe_3)_3$.[321,418,419]

The rarity of this gold coordination geometry, and its propensity to form in the trivalent state or with Z-type ligand coordination, further substantiates the Au→Sb bonding description in **77**-F and **77**-Cl.

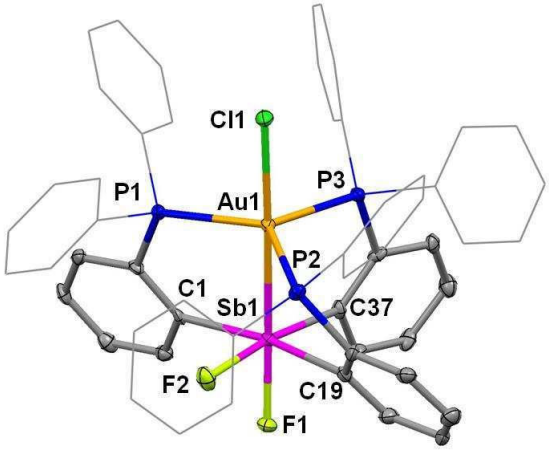

Figure 160. Crystal structure of **77**-F. Thermal ellipsoids are drawn at the 50% probability. Phenyl groups are drawn in wireframe, and hydrogen atoms are omitted for clarity. Selected bond lengths (Å) and angles (deg): Au(1)-P(1) 2.3747(14), Au(1)-P(3) 2.4202(15), Au(1)-P(2) 2.4434(15), Au(1)-Cl(1) 2.5299(12), Au(1)-Sb(1) 2.7355(4), Sb(1)-F(1) 1.950(3), Sb(1)-F(2) 2.024(3), P(1)-Au(1)-P(3) 121.60(5), P(1)-Au(1)-P(2) 121.88(5), P(3)-Au(1)-P(2) 114.79(5), Cl(1)-Au(1)-Sb(1) 178.42(3).

9.5 Oxidation of **76**-Cl with *o*-chloranil

In addition to their reaction with halogens, triarylstibines have been shown to react with *o*-quinones, undergoing oxidative addition to form Sb(V) catecholate complexes.[420,421] Therefore, to begin expanding the scope of oxidative addition reactions to the gold-stibine complex **76**-Cl, we tested its reactivity with *o*-chloranil (*o*-$O_2C_6Cl_4$). Gold-stibine complex **76**-Cl was allowed to react with 1 equiv. of *o*-chloranil in CH_2Cl_2,

resulting in the precipitation of compound **78** as an orange-yellow powder (Figure 161). The $^{31}P\{^{1}H\}$ NMR spectrum of **78** in $CDCl_3$ shows triplet and doublet resonances, in a 2:1 ratio, appearing at +66.48 and +22.63 ppm, respectively, with $^{2}J_{P\text{-}P}$ coupling constants of 162.88 Hz. Similar to **77**-F, the downfield shift of these signals and presence of $^{2}J_{P\text{-}P}$ coupling indicates unsymmetrical coordination of the phosphine arms to the Au atom.

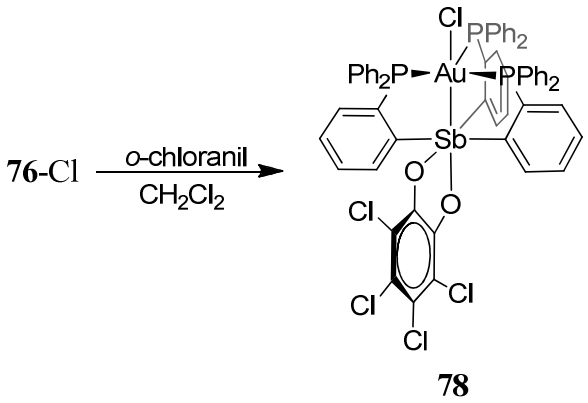

Figure 161. Synthesis of **78.**

The X-ray crystal structure of **78** confirms the oxidative addition of *o*-chloranil to the Sb atom, resulting in κ^2-*O*,*O* coordination of the tetrachlorocatecholate ligand and a distorted octahedral geometry around this atom (Figure 162). The Sb-O distances (Sb(1)-O(1) 2.078(5) Å, Sb(1)-O(2) 2.144(5) Å) are comparable to those measured in $Ph_3Sb(O_2C_6Cl_4)$ (2.019(3)-2.107(3) Å).[420] The structure also confirms the coordination of the three phosphine arms to the Au center, which adopts a distorted trigonal bipyramidal geometry ($\Sigma_{P\text{-}Au\text{-}P}$ = 359.06˚, Cl(1)-Au(1)-Sb(1) 173.16(5)˚) similar to **77**-F.

The trigonal bipyramidal geometry around the gold atom and the contraction of the Au-Sb bond distance (2.6767(11) Å) in **78** versus **76**-Cl again points to oxidation of the dinuclear core and an umpolung of the Au-Sb bonding.

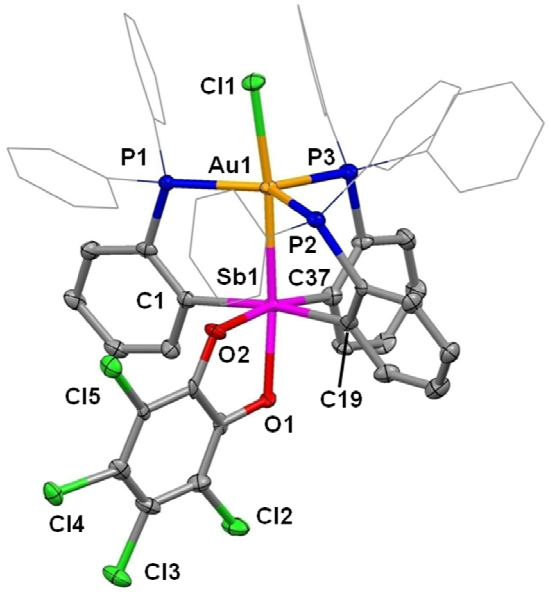

Figure 162. Crystal structure of **78**. Thermal ellipsoids are drawn at the 50% probability. Phenyl groups are drawn in wireframe, and hydrogen atoms are omitted for clarity. Selected bond lengths (Å) and angles (deg): Au(1)-P(1) 2.367(2), Au(1)-P(2) 2.401(2), Au(1)-Cl(1) 2.482(2), Au(1)-P(3) 2.533(2), Au(1)-Sb(1) 2.6767(11), Sb(1)-O(1) 2.078(5), Sb(1)-O(2) 2.144(5), Sb(1)-C(37) 2.170(7), Sb(1)-C(19) 2.179(8), Sb(1)-C(1) 2.203(7), Cl(1)-Au(1)-Sb(1) 173.16(5), P(1)-Au(1)-P(2) 135.99(7), P(1)-Au(1)-P(3) 112.28(7), P(2)-Au(1)-P(3) 110.79(7), O(1)-Sb(1)-O(2) 78.59(18), O(1)-Sb(1)-Au(1) 169.28(13), O(2)-Sb(1)-C(37) 169.7(2), C(19)-Sb(1)-C(1) 170.0(3).

9.6 Conclusions

In summary, this chapter describes a rare example of a reversible two-electron redox process at a dinuclear main group/transition metal core. Although a number of redox

processes have been shown to occur at the transition metal component of main group/transition metal complexes, few involve addition or elimination reactions at the main group element and, in any case, often lead to loss of the transition metal-main group bonding interaction. As such, the present examples are exceptional since an Au-Sb bonding interaction is not only sustained in both the reduced and oxidized forms but experiences an umpolung of the bond polarization between forms.

9.7 Experimental

General Considerations. $SbCl_3$ was purchased from Alfa Aesar, NaI was purchased from Aldrich, and both were used as received. The ligand (*o*-$(Ph_2P)C_6H_4)_3Sb$,[266] $PhICl_2$,[422] and (tht)AuCl[324] (tht = tetrahydrothiophene) were prepared according to the reported procedures. All air and moisture sensitive manipulations were carried out under an atmosphere of dry N_2 employing either a glove box or standard Schlenk techniques. Pentane and CH_2Cl_2 were dried by passing through an alumina column. All other solvents were used as received. Ambient temperature NMR spectra were recorded on a Varian Unity Inova 400 FT NMR (399.59 MHz for ^1H, 161.74 MHz for ^{31}P, 100.45 MHz for ^{13}C) spectrometer. Low temperature $^{31}P\{^1H\}$ NMR spectra were recorded on a Varian Inova 300 FT NMR spectrometer (121.42 MHz for ^{31}P). Chemical shifts are given in ppm, and are referenced to residual ^1H and ^{13}C solvent signals and external H_3PO_4 for ^{31}P. Elemental analyses were performed at Atlantic Microlab (Norcross, GA). Electrospray mass spectra were obtained with a SciexQstarr Pulsar and a Protana Nanospray ion source.

Synthesis of 76-Cl. A solution of AuCl(tht) (35 mg, 0.110 mmol) in acetone (2 mL) was added dropwise to a solution of $(o\text{-}C_6H_4P(PPh_2))_3Sb$ (100 mg, 0.1 mmol) in acetone/CH_2Cl_2 (5/1 mL) at ambient temperature. The resulting yellow solution was allowed to stir for 15 min after which time a pale yellow precipitate began to form. Pentane (10 mL) was added to complete precipitation of the product. The precipitate was filtered and washed with pentane (3 × 3 mL) and dried *in vacuo* to afford 105 mg (83 %) of **76**-Cl as a pale yellow powder. Single crystals of **76**-Cl·(acetone) suitable for X-ray diffraction were obtained by vapor diffusion of pentane into a solution of the compound in acetone. ^{1}H NMR (399.59 MHz; $CDCl_3$): δ 7.10-7.17 (m, 9H, PPh-C*H*), 7.27-7.32 (m, 18H, PPh-C*H*), 7.39-7.46 (m, 12H, PPh-C*H*), 7.67 (d, 3H, *o*-P(Sb)C_6H_4, $^3J_{H\text{-}H}$ = 6.96 Hz). ^{13}C NMR (100.45 MHz; $CDCl_3$): δ 128.35 (bs, CH_{Ph}), 128.54 (bs, CH_{Ph}), 129.88 (bs, CH_{Ph}), 130.33 (bs, CH_{Ph}), 133.33 (pseudo-quart, *o*-P(Sb)C_6H_4, $J_{C\text{-}P}$ = 10.17 Hz), 133.72 (bs, CH_{Ph}), 133.97 (pseudo-quart, *o*-P-CH_{Ph}, $J_{C\text{-}P}$ = 5.34 Hz), 137.21 (pseudo-quart, P-$C_{Ph\ ipso}$, $J_{C\text{-}P}$ = 5.33 Hz), 140.33 (pseudo-quart, Sb-C_{ipso}, $J_{C\text{-}P}$ = 11.70 Hz), 150.95 (pseudo-quart, P-C_{ipso}, $J_{C\text{-}P}$ = 22.38 Hz). $^{31}P\{^1H\}$ NMR (161.74 MHz; $CDCl_3$): δ 24.4. HRMS: m/z calculated for $C_{54}H_{42}AuP_3Sb^+$: 1101.1203, found: 1101.1180. Elemental analysis calculated (%) for $C_{54}H_{42}AuClP_3Sb + C_3H_6O$: C, 57.24 H, 4.04; found C, 56.50 H 4.24 (approx. 1 eq. of acetone was lost in drying).

Synthesis of 77-Cl. A solution of $PhICl_2$ (60 mg, 0.22 mmol) in CH_2Cl_2 (1 mL) was added dropwise to a solution of **76**-Cl (250 mg, 0.22 mmol) in CH_2Cl_2 (5 mL) at ambient temperature. The reaction was stirred for 20 min. before removing the solvent *in vacuo*. The resulting yellow solid was washed with acetone (2 × 2 mL) and pentane (2 × 3 mL)

and dried *in vacuo* to afford 195 mg (73 %) of **77**-Cl as a yellow powder. Single crystals of **77**-Cl·2(CH_2Cl_2) suitable for X-ray diffraction were obtained by vapor diffusion of pentane into a solution of the compound in CH_2Cl_2. ^{1}H NMR (399.59 MHz; $CDCl_3$): δ 6.88 (m, 3H, *o*-P(Sb)C_6H_4), 7.19-7.36 (m, 36H, Ph-C*H*), 8.25 (d, 3H, Ph-C*H*, $^3J_{H\text{-}H}$ = 7.87 Hz). ^{13}C NMR (100.45 MHz; $CDCl_3$): δ 128.69 (bm, CH_{Ph}), 128.98 (bs, CH_{Ph}), 130.56 (bm, Sb-C_{ipso}), 131.60 (bs, CH_{Ph}), 131.81 ((bs, CH_{Ph}), 132.36 (bs, CH_{Ph}), 133.77 (bd, $CH_{Phortho}$, $^2J_{C\text{-}P}$ = 4.58 Hz), 134.11 (bs, CH_{Ph}), 136.53 (bd, P-$C_{Ph\ ipso}$, $^1J_{C\text{-}P}$ = 5.38 Hz), 154.64 (bm, P-C_{ipso}). $^{31}P\{^1H\}$ NMR (161.74 MHz; $CDCl_3$): δ 41.91. HRMS: m/z calculated for $C_{54}H_{42}AuCl_2P_3Sb^+$: 1171.0580, found: 1171.0551. Elemental analysis calculated (%) for $C_{54}H_{42}AuCl_3P_3Sb$ + $2CH_2Cl_2$: C, 48.78 H, 3.36; found C, 48.06 H 3.34 (approx. 1 eq. of CH_2Cl_2 was lost in drying).

Synthesis of 76-I. A solution of **77**-Cl (50 mg, 0.041mmol) in CH_2Cl_2 (0.5 mL) was added dropwise to a solution of NaI (24 mg, 0.16mmol) in acetone (1.5 mL) at ambient temperature, resulting in the formation of a yellow precipitate and a dark red supernatant. The solid was filtered and extracted with CH_2Cl_2. This organic mixture was extracted with an aqueous solution of $Na_2S_2O_3$ (2 mL, 1.0 M) followed by brine (2 mL). The resulting yellow organic layer was dried over $MgSO_4$ and filtered over a small plug of silica. Removal of the solvent *in vacuo* afforded AuI[Sb(*o*-$C_6H_4(PPh_2)$)] (32 mg, 63 %) as a yellow solid. Single crystals of AuI[Sb(*o*-$C_6H_4(PPh_2)$)] were obtained by slow evaporation of a solution in CH_2Cl_2/acetone (1/1).^{1}H NMR (399.59 MHz; $CDCl_3$): δ 7.09-7.17 (m, 9H, PPh-C*H*), 7.25-7.32 (m, 18H, PPh-C*H*), 7.36-7.43 (m, 12H, PPh-C*H*), 7.68 (d, 3H, *o*-P(Sb)C_6H_4, $^3J_{H\text{-}H}$ = 6.59 Hz). ^{13}C NMR (100.45 MHz; $CDCl_3$):

δ128.43(bm, CH_{Ph}), 129.76 (s, CH_{Ph}), 130.24 (s, CH_{Ph}), 133.54-134.04 (bm, CH_{Ph} + *o*-P-CH_{Ph}), 137.05 (pseudo-quart, *o*-P-CH_{Ph}, $J_{C\text{-}P}$ = 5.34 Hz), 140.57(m, Sb-C_{ipso}), 150.62 (pseudo-quart, P-C_{ipso}, $J_{C\text{-}P}$ = 22.63 Hz). $^{31}P\{^{1}H\}$ NMR (161.74 MHz; $CDCl_3$): δ +22.7. HRMS: m/z calculated for $C_{54}H_{42}AuP_3Sb^+$: 1101.1203, found: 1101.1188. Elemental analysis calculated (%) for $C_{54}H_{42}AuIP_3Sb$ + 0.5 C_3H_6O + 0.5 CH_2Cl_2: C, 51.70 H, 3.56; found C, 51.53 H 3.67 (approx. 0.5 eq. of acetone and 0.5 eq. of dichloromethane were lost in drying).

Reaction of 76-I with $PhICl_2$. $PhICl_2$ (5.8 mg, 0.021 mmol) was added as a solid to a mixture of **76**-I (20 mg, 0.015 mmol) and [(*n*-Bu)$_4$N]Cl (36 mg, 0.13 mmol) in $CDCl_3$. The reaction mixture immediately turned from pale yellow to dark orange, and the $^{31}P\{^{1}H\}$ NMR spectrum showed the appearance of a signal at 42.7 ppm corresponding to the formation of **77**-Cl (51 % yield by NMR integration). This was confirmed by ESI-MS which displayed a set of peaks with an isotopic distribution pattern matching the $C_{54}H_{42}AuCl_2P_3Sb^+$ ion (m/z = 1171.0554 amu).

Synthesis of 77-F. A solution of KF (0.043 g, 0.74 mmol) in MeOH (1 mL) was added to a solution of **77-**Cl (0.15 g, 0.12 mmol) in MeOH (3 mL) and stirred at ambient temperature for 3 hrs, resulting in the precipitation of a yellow solid. The solvent was removed *in vacuo*, and the residue was extracted with CH_2Cl_2 (5 mL). The resulting mixture was filtered over Celite and concentrated to *ca.* 1 mL. Addition of pentane (5 mL) resulted in precipitation of a yellow powder that was filtered, washed with MeOH (3 × 3 mL), and dried *in vacuo* to afford 121 mg (83%) of **77**-F. Single crystals of **77**-F suitable for X-ray diffraction were obtained by slow evaporation of the compound in

$CHCl_3$/MeOH (1/1). ^{1}H NMR (399.59 MHz; $CDCl_3$): δ 6.93-7.23 (m, 32 H, *o*-P(Sb)C_6H_4 + PPh), 7.30-7.40 (m, 6H, *ortho*-PPh), 7.54 (ddd, 1H, *o*-P(Sb)C_6H_4, $^3J_{H\text{-}H}$ = 7.32 Hz, $^4J_{H\text{-}H}$ = 2.76 Hz, $^3J_{H\text{-}F}$ = 1.24 Hz) 8.42 (d, 2H, *o*-P(Sb)C_6H_4, $^3J_{H\text{-}H}$ = 7.80 Hz), 8.59 (d, 1H, *o*-P(Sb)C_6H_4, $^3J_{H\text{-}H}$ = 7.80 Hz).). ^{31}P{^{1}H} NMR (161.74 MHz; $CDCl_3$): δ 22.40 (td, 1P, $^2J_{P\text{-}P}$ = 148.60 Hz, $^3J_{P\text{-}F}$ = 7.36 Hz), 60.42 (dq, 2P, $^2J_{P\text{-}P}$ = 148.60 Hz, $^3J_{P\text{-}F}$ = 15.32, 7.77 Hz). ^{19}F NMR (375.97 MHz; $CDCl_3$): -9.42 (d, $^2J_{F\text{-}F}$ 41.9 Hz), -153.03 (brm).

Synthesis of 78. A solution of o-chloranil (0.022 g, 0.09 mmol) in CH_2Cl_2 (1 mL) was added dropwise to a solution of **76**-Cl (0.10 g, 0.09 mmol) in CH_2Cl_2 (1 mL) at room temperature. The resulting deep yellow solution was allowed to stir for 15 min before adding pentane (10 mL), upon which a yellow precipitate was formed. The solid was filtered, washed with pentane (3 × 3 mL) and dried *in vacuo* to afford 60 mg (49 %) of **78**. Single crystals of **78** suitable for X-ray difraction were obtained by slow diffusion of pentane into a solution of the compound in $CHCl_3$. ^{1}H NMR (399.59 MHz; $CDCl_3$): δ 6.79 (q, 4H, Ph-C*H*, $^3J_{H\text{-}H}$ = 6.10 Hz), 6.88 (t, 4H, Ph-C*H*, $^3J_{H\text{-}H}$ = 7.70 Hz), 6.99-7.03 (m, 10H, Ph-C*H*), 7.08-7.20 (m, 11H, Ph-C*H*, *o*-P(Sb)C_6H_4), 7.26-7.38 (m, 9H, Ph-C*H*, *o*-P(Sb)C_6H_4), 7.79 (td, 1H, *o*-P(Sb)C_6H_4, $^3J_{H\text{-}H}$ = 7.51 Hz, $^4J_{H\text{-}H}$ = 2.07 Hz), 8.23 (d, 2H, *o*-P(Sb)C_6H_4, $^3J_{H\text{-}H}$ = 7.69 Hz), 9.29 (d, 1H, *o*-P(Sb)C_6H_4, $^3J_{H\text{-}H}$ = 7.87 Hz). ^{13}C NMR (100.45 MHz; $CDCl_3$): δ 116.25 (s, $O_2C_6Cl_4$), 116.67 (s, $O_2C_6Cl_4$), 117.77 (s, $O_2C_6Cl_4$), 119.63 (s, $O_2C_6Cl_4$), 126.38 (t, $J_{C\text{-}P}$ = 27.55 Hz), 127.65 (t, $J_{C\text{-}P}$ = 5.54 Hz), 128.41 (s), 128.51 (s), 128.69 (t, $J_{C\text{-}P}$ = 5.38 Hz), 129.22 (d, $J_{C\text{-}P}$ = 4.70 Hz), 129.76 (s,), 130.06 (d, $J_{C\text{-}P}$ = 6.05 Hz), 131.01 (t, $J_{C\text{-}P}$ = 27.04 Hz), 131.98 (s,), 132.17 (s,), 132.44 (d, $J_{C\text{-}P}$ =

11.09 Hz), 132.94-133.18 (m, 2C), 133.59 (t, $J_{C\text{-}P}$ = 4.20 Hz), 133.86 (dt, $J_{C\text{-}P}$ = 26.04 Hz, 4.03 Hz), 134.34 (t, $J_{C\text{-}P}$ = 6.05 Hz), 137.06 (s, *o*-P(Sb)C_6H_4), 145.47 (s, $O_2C_6Cl_4$), 148.87 (s, $O_2C_6Cl_4$), 162.59 (t, *o*-P(Sb)C_6H_4, $^3J_{C\text{-}P}$ = 48.99 Hz), 170.77 (d, *o*-P(Sb)C_6H_4, $^3J_{C\text{-}P}$ = 37.77 Hz). $^{31}P\{^1H\}$ NMR (161.74 MHz; $CDCl_3$): δ 22.63 (t, 1P, $^2J_{P\text{-}P}$ = 162.88 Hz), 66.48 (d, 2P, $^2J_{P\text{-}P}$ = 162.88 Hz). Elemental analysis calculated (%) for $C_{60}H_{42}AuCl_5P_3Sb$ + 1.5$CHCl_3$: C, 47.26 H, 2.81; found C, 47.17 H 2.94 (approx. 0.5 eq. of $CHCl_3$ was lost in drying).

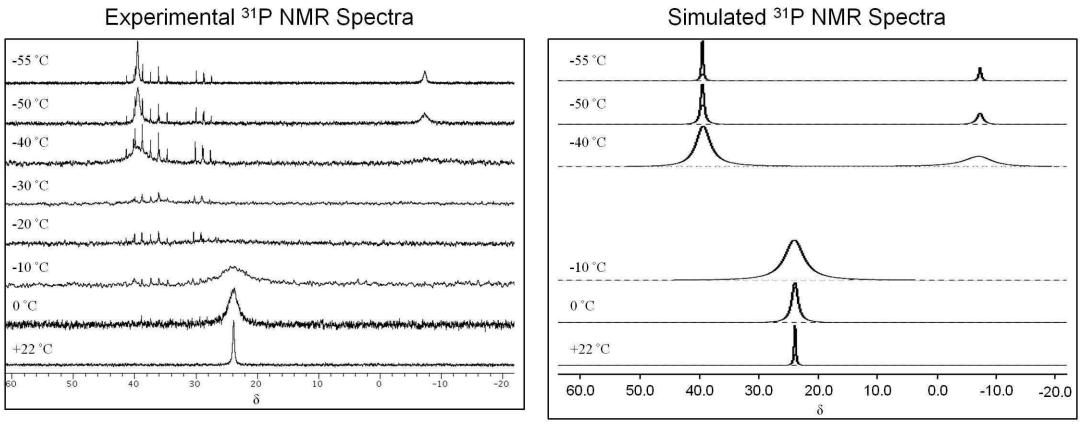

Figure 163. Plots of the experimental and simulated variable temperature $^{31}P\{^1H\}$ NMR spectra of **76**-Cl.

Variable Temperature ^{31}P NMR and Simulation. Variable temperature ^{31}P NMR spectra were recorded on a Varian Inova300 FT NMR spectrometer (121.42 MHz for ^{31}P). Chemical shifts are given in ppm and are referenced to external H_3PO_4. The peak linewidths in the experimental spectra were measured using the Varian VNMRJ v2.2. The ligand exchange rates (k) at each temperature were determined by fitting the chemical shifts and peak line widths of the simulated spectra to those in the

experimentally measured spectra using the gNMR v5.0 program. Plots of the experimental and simulated variable temperature $^{31}P\{^{1}H\}$ NMR spectra of **76**-Cl are included in Figure 163. The experimentally measured and simulated linewidths at each temperature are listed in Table 23. An Eyring plot of the kinetic data is shown in Figure 164, and the data used for the plot are listed in Table 24.

Table 23. Experimentally observed and simulated peak line-widths for the variable temperature $^{31}P\{^{1}H\}$ NMR spectra of **76**-Cl.

Temperature	Measured Line-widths (Hz)		Simulated Line-widths (Hz)	
		+24ppm		+24 ppm
22 ˚C		34.78		34.35
0 ˚C		150		149.18
-10 ˚C		470		469.47
	+39.5 ppm	-7.37 ppm	+39.5 ppm	-7.37 ppm
-40 ˚C	355	639	349.26	685.71
-50 ˚C	76	143	78.46	139.08
-55 ˚C	35.3	53.16	35.49	53.09

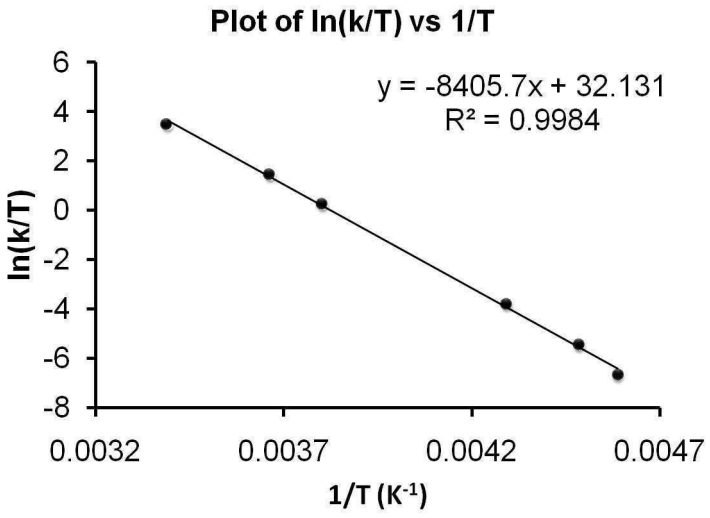

Figure 164. Eyring plot for the phosphine arm exchange in **76**-Cl.

Table 24. Data for the calculated phosphine arm exchange rates from the simulated variable temperature $^{31}P\{^{1}H\}$ NMR spectra of **76-**Cl.

T (˚C)	T (K)	1/T (K^{-1})	k	ln(k/T)
22	295	3.3898E-03	9500	3.472
0	273	3.6630E-03	1150	1.438
-10	263	3.8023E-03	335	0.242
-20	253	3.9526E-03		
-30	243	4.1152E-03		
-40	233	4.2918E-03	5.2	-3.802
-50	223	4.4843E-03	0.95	-5.458
-55	218	4.5872E-03	0.275	-6.675
$\Delta H^{\ddagger}$ = 16.7(±0.9) kcal mol^{-1}				
$\Delta S^{\ddagger}$ = 16.6(±3.8) cal mol^{-1} K^{-1}				

Computational Details. DFT structural optimizations for **76-**Cl and **77-**Cl were carried out using the ADF program (2010.01).[329-331] All calculations were performed with the BP86 functional[332,333] and the all electron TZP basis sets for all atoms[334] using ZORA.[335-339] Table 25 includes a list of pertinent experimentally determined and calculated bond lengths and angles for comparison. The Boys[340-342] localizations were carried out in the ADF program and visualized using Jimp2.[343,344] The Natural Bond Order (NBO) analysis was performed on the optimized structure using the NBO v3.1[345] software available in the Gaussian03[241] program. This analysis was carried out using the BP86 functional and the mixed basis set: 6-31g for H, C; 6-311+g(d) for P, Cl; and CRENBS ECP for Sb, Au. The resulting donor acceptor interactions were visualized using Jimp2.[343,344]

Table 25. Selected bond lengths (Å) and angles (˚) observed in the crystal structures and DFT optimized structures of complexes **76**-Cl and **77**-Cl.

76-Cl			**77**-Cl		
	X-Ray	**DFT**		**X-Ray**	**DFT**
Au-Sb	2.8374(4)	3.027	Au-Sb	2.7086(9)	2.799
Au-Cl(1)	2.4990(11)	2.555	Au-Cl(1)	2.4601(14)	2.537
Au-P(1)	2.3084(11)	2.362	Au-P(1)	2.3246(15)	2.363
Au-P(2)	2.3305(11)	2.369	Au-P(2)	2.3328(14)	2.377
Au-Sb-C(37)	164.80(11)	174.1	Sb-Cl(2)	2.4960(14)	2.552
			Sb-Cl(3)	2.5627(15)	2.607

NBO Analysis. In addition to the primary NBO interactions discussed in the text, a more in depth analysis of the NBO output reveals further interactions that contribute to the Au-Sb bonding in **76**-Cl and **77**-Cl. All identified interactions for **76**-Cl and **77**-Cl are plotted in Figure 165 and Figure 166, respectively. An NBO deletion calculation including only interaction 1 in compound **76**-Cl provides a stabilization energy of E_{del} = 35.28 kcal/mol. The total deletion energy obtained from deleting interactions 1-5 is E_{del} = 53.98 kcal/mol. Deletion of interactions 1-3 in compound **77**-Cl provides a stabilization energy of E_{del} = 63.59 kcal/mol. The total deletion energy obtained when deleting interactions 1-7 is E_{del} = 160.07 kcal/mol.

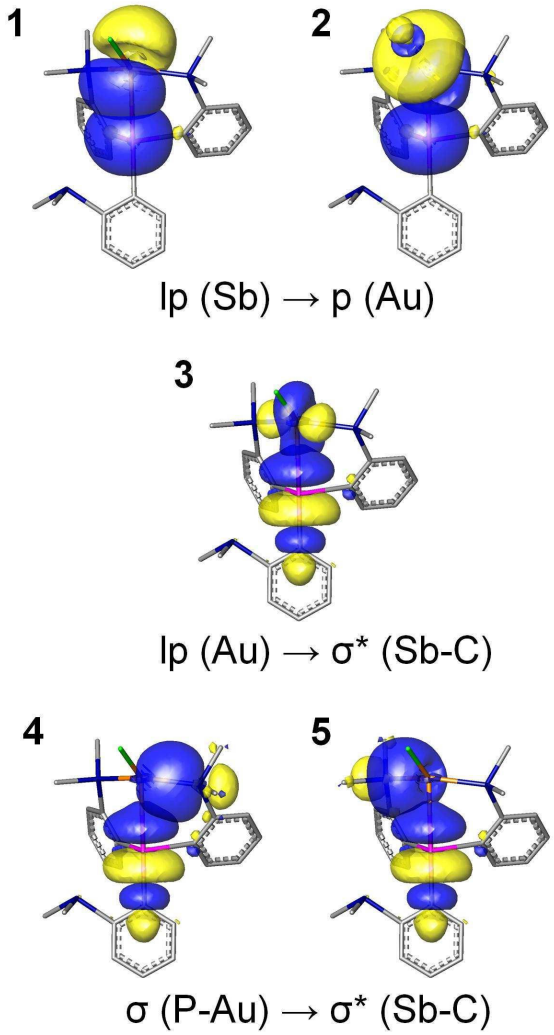

Figure 165. Plot of all NBO Au-Sb donor-acceptor interactions in **76**-Cl.

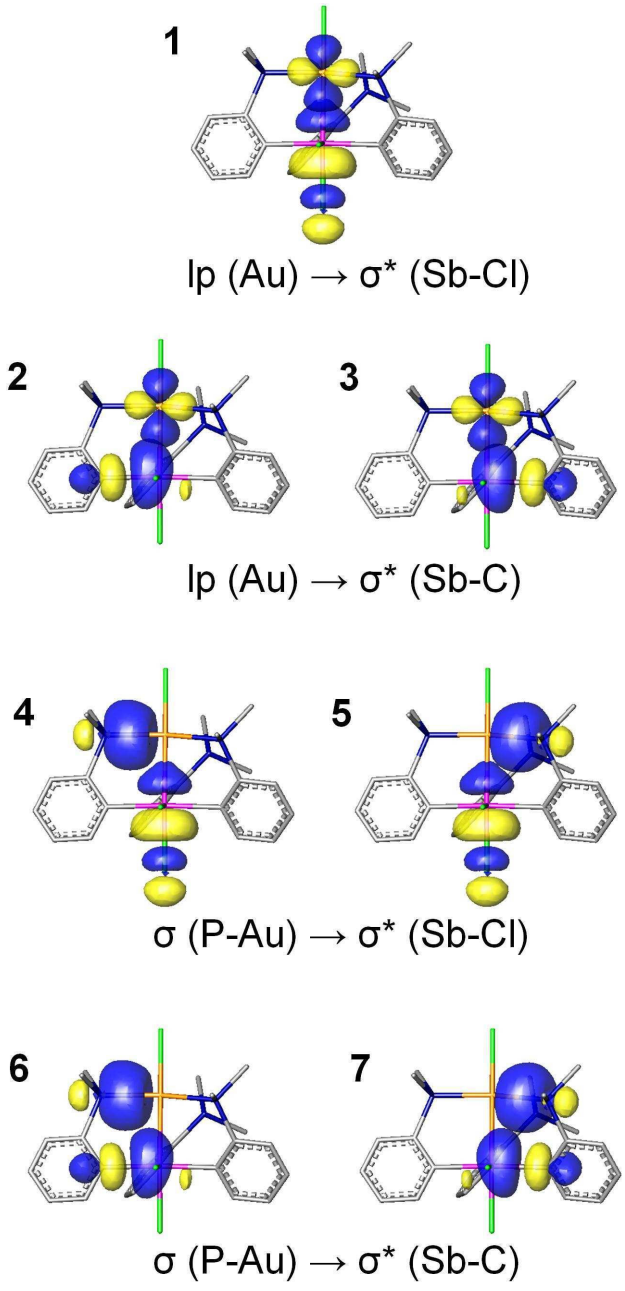

Figure 166. Plot of all NBO Au-Sb donor-acceptor interactions in **77**-Cl.

Crystallography. Single crystals of **76**-Cl were obtained by slow diffusion of pentane into a solution of the compound in acetone. Single crystals of **76-**I were obtained by slow diffusion of pentane into a solution of the compound in CH_2Cl_2/acetone (1/1 vol.). Single crystals of **77-**Cl were obtained by slow diffusion of pentane into a solution of the compound in CH_2Cl_2. Single crystals of **77-**F were obtained by slow evaporation of a solution of the compound in CH_2Cl_2/MeOH (1/1 vol.). Single crystals of **78** were obtained by slow diffusion of pentane into a solution of the compound in $CHCl_3$. Crystal data, details of data collection, and structure refinement parameters for compounds **76-**Cl, **76-**I, and **77-**Cl are included in Table 26. Data for **77-**F and **78** are included in Table 27. The crystallographic measurements were performed using a Bruker-AXS APEX-II CCD area detector diffractometer, with a graphite-monochromated Mo-Kα radiation (λ = 0.71069 Å). A specimen of suitable size and quality was selected and mounted onto a nylon loop. The semiempirical method SADABS[207] was applied for absorption correction. The structures were solved by direct methods using SHELXTL/PC package (version 6.1)[208] which successfully located most of the non-hydrogen atoms. Subsequent refinement on F^2 allowed location of the remaining non-hydrogen atoms. All H atoms were geometrically placed and refined in a riding model approximation.

During the structure refinement of **77-**F, disordered MeOH solvent molecules were identified. No satisfactory disorder model could be achieved, and therefore the Squeeze program implemented in PLATON was used to model this electron density.[328] The program calculated a solvent-accessible volume of 588.7 $Å^3$ (3.11 % of the total unit cell volume), which was then removed from subsequent structure factor calculations.

Table 26. Crystal data, data collections, and structure refinements for **76-**Cl, **76-**I, and **77-**Cl.

Crystal data	**76**-Cl·2C_3H_6O	**76**-I·C_3H_6O,CH_2Cl_2	**77**-Cl·3CH_2Cl_2
Formula	$C_{60}H_{54}O_2P_3ClAuSb$	$C_{58}H_{50}OP_3Cl_2IAuSb$	$C_{57}H_{48}P_3Cl_9AuSb$
Mr	1254.11	1372.41	1463.63
Crystal size/mm	0.35 x 0.28 x 0.25	0.12 x 0.06 x 0.04	0.28 x 0.08 x 0.07
Crystal system	Triclinic	Triclinic	Triclinic
Space group	P-1	P-1	P-1
a/Å	11.2460(8)	11.969(2)	12.869(6)
b/Å	15.3283(11)	15.220(3)	14.409(6)
c/Å	17.8014(13)	15.891(3)	16.375(7)
α /°	66.6870(10)	79.393(2)	104.844(5)
β/°	76.3670(10)	74.386(2)	91.700(5)
γ /°	71.8780(10)	70.364(2)	103.447(5)
V/Å^3	2655.9(3)	2611.9(8)	2842(2)
Z	2	2	2
ρ_{calc}/g cm^{-3}	1.5568	1.745	1.711
μ/mm^{-1}	3.450	4.148	3.599
F(000)	1244	1336	1436
T/K	110(2)	110(2)	110(2)
Scan mode	ω, φ	ω, φ	ω, φ
hkl Range	-14 → +14	-14 → +14	-15 → +15
	-19 → +19	-18 → +18	-17 → +17
	-22 → +22	-19 → +19	-20 → +20
Measd reflns	30239	27330	29661
Unique reflns [R_{int}]	11546 [0.0389]	10238 [0.0514]	11107 [0.0425]
Reflns used for refinement	11546	10238	11107
Refined parameters	587	586	640
GooF	1.015	1.055	1.058
*R*1,[a] *wR*2[b] (all data)	0.0404, 0.0845	0.0653, 0.1428	0.0495, 0.0882
ρ_{fin} (max., min.)/eÅ^{-3}	2.446, -1.818	3.363, -2.406	1.529, -1.552

[a] $R1 = \Sigma||F_o| - |F_c||/\Sigma|F_o|$. [b] $wR2$ $([\Sigma w(F_o^2 - F_c^2)^2]/[\Sigma\, w(F_o^2)^2])^{1/2}$; $w = 1/[\sigma^2(F_o^2) + (ap)^2 + bp]$; $p = (F_o^2 + 2F_c^2)/3$ with a = 0.0384 for **76**-Cl, 0.0780 for **76**-I, and 0.0362 for **77**-Cl; and b = 3.9944 for **76**-Cl, 6.5141 for **76**-I, and 2.4802 for **77**-Cl.

Table 27. Crystal data, data collections, and structure refinements for **77**-F and **78**.

Crystal data	**77**-F·CH_3OH	**78**·$2CHCl_3$
Formula	$C_{55}H_{46}OF_2P_3ClAuSb$	$C_{62}H_{44}O_2P_3Cl_{11}AuSb$
Mr	1207.99	1622.55
Crystal size/mm	0..05 x 0.05 x 0.03	0.07 x 0.06 x 0.04
Crystal system	Orthorhombic	Triclinic
Space group	Fdd2	P-1
a/Å	19.730(2)	11.385(6)
b/Å	75.805(9)	14.991(8)
c/Å	12.665(2)	19.609(10)
α /°	90	71.274(6)
β/°	90	74.998(6)
γ /°	90	81.435(6)
V/Å^3	18942(4)	3054(3)
Z	16	2
ρ_{calc}/g cm^{-3}	1.694	1.765
μ/mm^{-1}	3.871	3.446
F(000)	9504	1588
T/K	110(2)	110(2)
Scan mode	ω, φ	ω, φ
hkl Range	-24 → +24	-14 → +14
	-93 → +93	-18 → +18
	-15 → +15	-24 → +24
Measd reflns	48246	31125
Unique reflns [R_{int}]	9314 [0.0598]	11934 [0.0705]
Reflns used for refinement	9314	11934
Refined parameters	577	721
GooF	1.003	1.014
$R1$,[a] $wR2$[b] (all data)	0.0303, 0.0771	0.0769, 0.1291
ρ_{fin} (max., min.)/eÅ^{-3}	1.442, -1.164	1.520, -1.746

[a] $R1 = \Sigma||F_o| - |F_c||/\Sigma|F_o|$. [b] $wR2$ $([\Sigma w(F_o^2 - F_c^2)^2]/[\Sigma\, w(F_o^2)^2])^{1/2}$; $w = 1/[\sigma^2(F_o^2) + (ap)^2 + bp]$; $p = (F_o^2 + 2F_c^2)/3$ with $a = 0.0405$ for **77**-F and 0.0612 for **78**; and $b = 0$ for **77**-F and 0 for **78**.

CHAPTER X

SUMMARY

10.1 Fluoride and cyanide sensing with pyridinium triarylboranes

We have investigated the synthesis and anion binding properties of several pyridinium triarylboranes with the goal of developing sensors for aqueous fluoride and cyanide. Our strategy in this area was founded on quaternization of a peripheral pyridyl group, via methylation or coordination to a cationic transition metal fragment, to impart beneficial Coulombic effects that would enhance the anion affinity of the borane moiety. The methylation strategy generated cationic boranes $[\mathbf{45}]^+$ and $[\mathbf{46}]^+$, which exhibit a colorimetric turn-on response to fluoride binding attributed to an intramolecular charge transfer process. Despite the desirable turn-on response in organic solvents, these receptors were found to be incapable of complexing fluoride directly in aqueous media.

Our efforts in this area also resulted in the synthesis of the cationic, cyclometalated complexes $[\mathbf{48}]^+$, $[\mathbf{50}]^+$, and $[\mathbf{51}]^+$. The cationic complexes $[\mathbf{48}]^+$ and $[\mathbf{50}]^+$, containing square planar Pd^{2+} and Pt^{2+} metal centers, respectively, bind fluoride in organic solvents such as $CHCl_3$ and THF, but not in the presence of MeOH or H_2O. In addition, these receptors showed a lack of selectivity for fluoride due to ancillary ligand substitution reactions at the metal centers in the presence of common anions such as Cl^-, Br^-, I^-, and CN^-. The octahedral Ru^{2+} complex $[\mathbf{51}]^+$ showed a high affinity for F^- and CN^- in THF/DMF and $CHCl_3$/DMF mixed solvents, with selectivity over other common anions such as Cl^-, Br^-, I^-. In addition, the potential of the $Ru^{II/III}$ redox couple undergoes a

cathodic shift upon anion binding, making this compound attractive for electrochemical sensing applications.

10.2 Synthesis and characterization of zwitterionic aryltrifluoroborates

Our group has previously shown that decoration of triarylboranes with proximal cationic ammonium and phosphonium groups enhances the fluoride and cyanide affinity of the boron center via Coulombic effects and intramolecular onium group-anion interactions. Applying this strategy toward the stabilization of aryltrifluoroborates for application in PET imaging with ^{18}F, we synthesized the zwitterionic ammonium and phosphonium aryltrifluoroborates **52**-BF_3 and **53**-BF_3. These compounds exhibit exceptional stability against hydrolysis in D_2O/CD_3CN (8/2 vol.) at pH 7.5 with first order rate constants for the hydrolysis of $k_{obs} = 6.3 \times 10^{-5}$ min^{-1} for **52**-BF_3 and 3.4×10^{-6} min^{-1} for **53**-BF_3. **52**-BF_3 and **53**-BF_3 were also characterized by X-ray diffraction, and the crystal structures suggested the presence of hydrogen bonding interactions between the trifluoroborate and ammonium/phosphonium substituents, which are expected to contribute to their stability. In addition, the exceptional stability of **53**-BF_3 may be assisted by the presence of a weak F(lone pair)→P-C(σ*) donor-acceptor interaction, which is evidenced by the short F-P separation (3.05 Å *av.*) observed in the structure of **53**-BF_3.

10.3 Synthesis, structure, and anion binding studies of bifunctional boron/antimony Lewis acids

The stibonium borane [**54**]$^+$ was synthesized in an effort to develop new, potent bifunctional Lewis acids. A competition reaction between [**54**]$^+$ and the fluoride adduct of its phosphonium analog **25**-F resulted in quantitative conversion to **54**-F and the cationic borane [**25**]$^+$. The structure of **54**-F was determined and showed that the compound forms a B-F-Sb chelate with a Sb-F distance of 2.450(2) Å, shorter than the P-F distance in the phosphonium analog **25**-F (2.666(2) Å). The F→Sb bonding interaction was investigated using DFT calculations. An AIM calculation found the density at the bond critical point between F and Sb to be 4.26×10^{-2} e bohr^{-3}, over two times greater than that calculated for the critical point between the F and P atoms of **25**-F (2.05×10^{-2} e bohr^{-3}). Similarly, NBO analysis located the $lp_{(F)} \rightarrow \sigma^*_{(Sb\text{-}C)}$ donor–acceptor interaction, which was found to contribute 15.2 kcal mol^{-1} to the stability of **54**-F, a value which greatly exceeds that found for the $lp_{(F)} \rightarrow \sigma^*_{(P\text{-}C)}$ interaction in **25**-F (5.0 kcal mol^{-1}). Finally, DFT calculations indicated that the competition reaction between [**54**]$^+$ and **25**-F, which proceeds experimentally to form **54**-F and [**25**]$^+$ quantitatively, is exothermic by −4.9 kcal/mol, supporting the experimental observation.

The cyanide and azide adducts, **54**-CN and **54**-N_3, were also isolated and structurally characterized. Although the long C_{CN}-Sb (2.943(7) Å) and N_{CN}-Sb (3.093(5) Å) bond distances measured in **54**-CN preclude the formation of a strong CN→Sb bonding interaction, NBO analysis identified a weak a weak $\pi_{(CN)} \rightarrow \sigma^*_{(Sb\text{-}C)}$ interaction (E_{del} = 3.54 kcal mol^{-1}). Structural and DFT analysis of **54**-N_3 revealed a strong B-N-Sb

bridging interaction. This is supported by a Sb-N_{N3} distance of 2.477(4) Å, which is significantly shorter than the corresponding P-N_{N3} bond distance (2.790(2) Å) in **25**-N_3. NBO analysis located a $lp_{(N)} \rightarrow \sigma^*_{(Sb\text{-}C)}$ donor-acceptor interaction in **54**-N_3 whose deletion resulted in an increase in the total energy of the molecule by 15.15 kcal mol^{-1}.

The synthesis of a stibonium borane supported by a 1,8-naphthalenediyl backbone was also attempted. Although the synthesis of the parent stibino borane **55** was easily carried out by the reaction of tetrakis(thf)lithium dimesityl-1,8-naphthalenediylborate with Ph_2SbCl, subsequent attempts to isolate the stibonium derivative via methylation were unsuccessful. Despite the inaccessibility of the stibonium derivative, the X-ray crystal structure of **55** and its Bi analog **56** revealed unusual E→B (E = Sb, Bi) donor-acceptor interactions based on short Sb-B (3.216 Å) and Bi-B (3.330 Å) separations. NBO analysis located the corresponding lp(E)→p(B) interactions, whose subsequent deletion afforded stabilization energies of 8.65 kcal/mol for **55** and 6.32 kcal/mol for **56**.

10.4 Synthesis and fluoride binding studies of stibonium/onium dications

Based on our preceding results on the anion binding properties of a bifunctional stibonium borane, we sought to exploit the inherent Lewis acidity of tetraorganostibonium cations for anion sensing. As a result, the fluoride affinity of the simple stibonium cation $[Ph_3MeSb]^+$ ($[\mathbf{57}]^+$) was examined using UV-Vis spectroscopy. The titration of $[\mathbf{57}]^+$ in THF yielded a fluoride binding constant of 8.5(±2.0) × 10^4 M^{-1} but no binding was observed in MeOH or mixed aqueous/organic solvent systems.

In an effort to obtain stibonium cations with an enhanced fluoride affinity, the onium/stibonium dications $[\mathbf{58}]^{2+}$, $[\mathbf{59}]^{2+}$, and $[\mathbf{60}]^{2+}$, bearing pendant ammonium and

phosphonium substituents, were synthesized. These cations exhibit a high affinity for fluoride in MeOH, giving binding constants of 4.0(±0.5) × 10^3 M^{-1} for [**58**]$^{2+}$, 2.6(±0.6) × 10^4 M^{-1} for [**59**]$^{2+}$, and 9.5(±2.0) × 10^3 M^{-1} for [**60**]$^{2+}$, as determined by UV-Vis spectroscopic titrations. No fluoride binding was observed for any of these compounds in H_2O or H_2O/MeOH mixtures. Surprisingly, the *ortho* phosphonium derivative [**60**]$^{2+}$ displays a lower fluoride affinity than the *para* isomer [**59**]$^{2+}$ in MeOH. This is opposite to the trend observed for the analogous phosphonium boranes and is attributed to steric crowding and metrical constraints that preclude fluoride chelation by the phosphonium and stibonium groups. Supporting this explanation, the X-ray crystal structure of the fluoride adduct [**60**-F]$^{2+}$ shows that, whereas the F atom coordinates to Sb with a bond distance of 2.055(18) Å, the F-P separation is > 3.5 Å, a separation that precludes even a weak bridging interaction.

10.5 Group 10 metal-stiborane complexes

In an extension of our fluoride binding studies with stibonium ions, we proposed an analogy between a tetraorganostibonium cation and triarylstibine coordinated to a cationic transition metal. Thus, we prepared a series of cationic Group 10 (Ni, Pd, and Pt) complexes bearing the trisphosphanylstibine ligand *o*-$(Ph_2P)C_6H_4)_3Sb$ as the BPh_4^- salts. Single crystal X-ray diffraction showed that the *o*-$(Ph_2P)C_6H_4)_3Sb$ ligand adopts a tetradentate κ-P,P,P,Sb coordination mode in the Ni complex (**61**-BPh_4) resulting in a trigonal bipyramidal geometry around the Ni atom and tetrahedral geometry around the central Sb atom. However, a tridentate κ-P,P,Sb coordination mode is adopted by the Pd and Pt complexes **62**-BPh_4 and **63**-BPh_4, resulting in disorted square planar geometries

around the metal atoms. These cationic complexes all react with fluoride in CH_2Cl_2 (K_F $>10^8$ M^{-1}) to afford the metal fluorostiborane complexes **61**-F, **62**-F, and **63**-F. Structural characterization of these complexes showed that the formation of an Sb-F bond in **62**-F and **63**-F triggers changes in the ligand denticity from κ-P,P,Sb in **62**-BPh_4 and **63**-BPh_4 to κ-P,P,P,Sb in the fluorostiboranes. The resulting trigonal bipyramidal geometries around the Pd and Pt centers are responsible for the appearance of bands in the visible region of the electronic spectra of **62**-F and **63**-F, making **62**-BPh_4 and **63**-BPh_4 turn-on colorimetric fluoride sensors.

The analogous chlorostiborane complexes **61**-Cl, **62**-Cl, and **63**-Cl were also isolated and found to be structurally similar to **61**-F, **62**-F, and **63**-F in the solid state via formation of Sb-Cl bonds. However, in polar solvents such as MeOH, **61**-Cl, **62**-Cl, and **63**-Cl are believed to be at least partially ionized. This assumption is upheld by the facile formation of **61**-F, **62**-F, and **63**-F upon treatment of **61**-Cl, **62**-Cl, and **63**-Cl with fluoride in organic solvents. Although the Ni complexes **61**-BPh_4 and **61**-Cl decompose in the presence of MeOH, UV-Vis fluoride titrations of **62**-Cl and **63**-Cl were successfully carried out in 2/1 vol MeOH/DMSO to provide fluoride binding constants of $4.5(\pm0.5) \times 10^4$ M^{-1} and $8.5(\pm1.0) \times 10^4$ M^{-1}, respectively. A comparison of the fluoride binding constants of the Pd complexes **62**-BPh_4 ($K_F = 1.1(\pm0.2) \times 10^4$ M^{-1}) and **62**-Cl ($K_F = 2.7(\pm0.2) \times 10^3$ M^{-1}) in 9/1 vol. MeOH/CH_2Cl_2 suggests that chloride effectively competes with fluoride for coordination to the Sb center in solution. Overall, the ability of these complexes to act as receptors for fluoride supports our initial

hypothesis and paves the way for further development of novel anion receptors based on this concept.

10.6 Bis-gold(I) and gold(I)/boron complexes with peri-napthalendiyl backbones

The 1,8-*bis*-(phosphino)gold(I)-naphthalenediyl complexes **66** and **67** were synthesized as part of an investigation of the synthesis of gold(I)-functionalized naphthalene derivatives. These syntheses showed that 1,8-dilithionaphthalene is a viable precursor for the preparation of such derivatives. The X-ray crystal structures of these compounds display short intramolecular Au-Au contacts of 2.9982(5) Å for **66** and 2.85 Å av. for **67**, with the shorter Au-Au distance observed in the latter compound attributed to the bridging nature of the dppm ligand. The digold compound **67** reacts with Ag^+ in CH_2Cl_2 to afford the Au_4Ag_2 metallocycle **68** in which two Ag^+ ions are sandwiched between two molecules of **67**. Both **67** and **68** are luminescent in the solid state and in oxygen-free CH_2Cl_2 solution. The broad, structured emission displayed by these complexes in solution appears around 475-650 nm and is assigned to a heavy atom induced triplet emission of the naphthalene chromophore. In the solid state, the emission band of **67** is distinctly broadened and red-shifted versus that of **68**, an observation attributed to the presence of the intermolecular aurophilic contacts in **67**.

The heterodinuclear gold(I)/boron complexes **69** and **70**, supported by the 1,8-naphthalenediyl backbone, were also synthesized. Although low yields prevented fluoride binding studies, the crystal structures of these complexes were determined. Both compounds feature short Au-B separations (2.70 Å av. for **69**, 2.84 Å av. for **70**), suggesting the formation of Au→B, Z-type bonding interactions. DFT calculations were

carried out on **69** to study the nature and strength of this interaction. A NBO analysis identified a lp(Au) → p(B) donor-acceptor interaction that provides a stabilization energy of E_{del} = 9.2 kcal/mol, similar to that calculated for a related phosphoranylborane gold complex containing a gold→triarylborane Z-type interaction.

10.7 A 14-electron, T-shaped stiboranyl-gold complex

As part of our developing interest in metal stiborane complexes, we recognized that stiboranyl ligands bear a resemblence to strongly σ-donating boryl and silyl ligands, which have been employed for the isolation of T-shaped, 14-electron transition metal complexes. Accordingly, the cyclic stiboranyl-gold complex **73** was synthesized, and the nature of Au-Sb bonding was studied using XANES spectroscopy and DFT calculations. The short Au-Sb bond distance (2.76 Å av.) in the solid state structure of this complex suggests the formation of a strong polar covalent bond. However, the presence of intermolecular aurophilic contacts, as well as the results of the XANES experiments, point to the importance of a bonding contribution from an aurate-stibonium resonance form. In addition, DFT calculations and a Boys localization analysis identified an occupied orbital oriented along the Au-Sb axis that is polarized toward the gold atom. Collectively, these results argue for the strong σ-donating properties of the stiboranyl ligand. Additionally, **73** reacts with KF in MeOH, resulting in the formation of the gold-fluoroantimonate complex [**75**]$^{-}$. Structural analysis and DFT calculations indicate that formation of the fluorostiborane has little effect on the Au-Sb bonding relative to **73**.

10.8 Synthesis, structure, and reactivity of a triphosphanylstibine gold complex

Based on our interest in exploring two-electron redox processes at the core of heterodinuclear main group/transition metal compounds, the gold(I)-stibine complex **76**-Cl was synthesized from the reacton of *o*-$(Ph_2P)C_6H_4)_3Sb$ with AuCl(tht). The ligand adopts a κ-P,P,Sb coordination mode, resulting in a distorted trigonal pyramidal geometry around the gold atom in this complex. Reaction of **76**-Cl with $PhICl_2$ results in oxidative addition of one equivalent of Cl_2 to the antimony atom to generate **77**-Cl. This redox process was shown to be reversible upon reaction of **77**-Cl with excess NaI in $CHCl_3$/acetone, resulting in the formation of I_3^- concomitant with reduction of the antimony center to afford **76**-I, the iodide analog of **76**-Cl. Furthermore, **76**-I could be reoxidized to **77**-Cl with $PhICl_2$ in the presence of excess chloride ions.

While the gold atom in **76**-Cl adopts a distorted trigonal pyramidal coordination geometry, that of **77**-Cl is close to square planar. Moreover, the Au-Sb separation in **77**-Cl (2.7086(9) Å) is distinctly shorter than that measured for **76**-Cl (2.8374(4) Å). These features suggest a transition from a monovalent gold center in **76**-Cl to trivalent gold in **77**-Cl. DFT studies of **76**-Cl and **77**-Cl also suggest an umpolung of the Au-Sb bond polarization upon oxidation of the antimony center. NBO analysis identified a relatively weak lp(Sb)→p(Au) donor-acceptor interaction (E_{del} = 35.28 kcal/mol) for **76**-Cl, whereas Au-Sb bonding in **77**-Cl is dominated by a lp(Au)→σ*(Sb-Cl) and two lp(Au)→ σ*(Sb-C) interactions (E_{del} = 63.59 kcal/mol). Thus, oxidation of the antimony center results in an umpolung of the Au-Sb dative bond, which increases in strength upon oxidation.

The reaction of **77**-Cl with 6 equiv. of KF in methanol afforded the difluorostiboranyl-gold complex **77**-F. Additionally, the reaction of **76**-Cl with *o*-$O_2C_6Cl_4$ resulted in oxidative addition of the quinone to the antimony center to afford complex **78**. The uncommon trigonal bipyramidal geometries adopted by the gold atoms in **77**-F and **78** further support the trivalent assignment of this atom in these oxidized complexes as well as provide evidence for the Au→Sb bonding description.

REFERENCES

(1) Aaseth, J.; Shimshi, M.; Gabrilove, J. L.; Birketvedt, G. S. *J. Trace Elem. Exp. Med.* **2004**, *17*, 83-92.

(2) Carton, R. J. *Fluoride* **2006**, *39*, 163-172.

(3) *Environmental Health Criteria 36,* IPCS International Programme on Chemical Safety, World Health Organization **1984**.

(4) *Environmental Health Criteria 227,* IPCS International Programme on Chemical Safety, World Health Organization **2002**.

(5) Arancibia, J. A.; Rullo, A.; Olivieri, A. C.; Di Nezio, S.; Pistonesi, M.; Lista, A.; Fernandez Band, B. S. *Anal. Chim. Acta* **2004**, *512*, 157-163.

(6) Cametti, M.; Rissanen, K. *Chem. Commun.* **2009**, 2809-2829.

(7) Gale, P. A.; Garcia-Garrido, S. E.; Garric, J. *Chem. Soc. Rev.* **2008**, *37*, 151-190.

(8) Sessler, J. L.; Gale, P. A.; Cho, W.-S. *Anion Receptor Chemistry*; Royal Society of Chemistry: Cambridge, 2006.

(9) Martinez-Manez, R.; Sancenon, F. *Chem. Rev.* **2003**, *103*, 4419-4476.

(10) Choi, K.; Hamilton, A. D. *Coord. Chem. Rev.* **2003**, *240*, 101-110.

(11) Bondy, C. R.; Loeb, S. J. *Coord. Chem. Rev.* **2003**, *240*, 77-99.

(12) Gale, P. A. *Coord. Chem. Rev.* **2003**, *240*, 191-221.

(13) Sessler, J. L.; Camiolo, S.; Gale, P. A. *Coord. Chem. Rev.* **2003**, *240*, 17-55.

(14) Sessler, J. L.; Davis, J. M. *Acc. Chem. Res.* **2001**, *34*, 989-997.

(15) Beer, P. D.; Gale, P. A. *Angew. Chem., Int. Ed.* **2001**, *40*, 486-516.

(16) Gale, P. A. *Coord. Chem. Rev.* **2001**, *213*, 79-128.

(17) Gale, P. A.; Anzenbacher, P., Jr.; Sessler, J. L. *Coord. Chem. Rev.* **2001**, *222*, 57-102.

(18) Gale, P. A. *Coord. Chem. Rev.* **2000**, *199*, 181-233.

(19) Beer, P. D.; Cadman, J. *Coord. Chem. Rev.* **2000**, *205*, 131-155.

(20) Miyaji, H.; Sato, W.; Sessler, J. L. *Angew. Chem., Int. Ed.* **2000**, *39*, 1777-1780.

(21) Snowden, T. S.; Anslyn, E. V. *Curr. Opin. Chem. Biol.* **1999**, *3*, 740-746.

(22) Beer, P. D. *Acc. Chem. Res.* **1998**, *31*, 71-80.

(23) de Silva, A. P.; Gunaratne, H. Q. N.; Gunnlaugsson, T.; Huxley, A. J. M.; McCoy, C. P.; Rademacher, J. T.; Rice, T. E. *Chem. Rev.* **1997**, *97*, 1515-1566.

(24) Bianchi, A.; Bowman-James, K.; Garcia-Espana, E. *Supramolecular Chemistry of Anions*; Wiley VCH: New York, 1997.

(25) Schmidtchen, F. P.; Berger, M. *Chem. Rev.* **1997**, *97*, 1609-1646.

(26) Arnendola, V.; Bonizzoni, M.; Esteban-Gomez, D.; Fabbrizzi, L.; Licchelli, M.; Sancenon, F.; Taglietti, A. *Coord. Chem. Rev.* **2006**, *250*, 1451-1470.

(27) Lin, Z.-H.; Ou, S.-J.; Duan, C.-Y.; Zhang, B.-G.; Bai, Z.-P. *Chem. Commun.* **2006**, 624-626.

(28) Palacios, M. A.; Nishiyabu, R.; Marquez, M.; Anzenbacher, P. *J. Am. Chem. Soc.* **2007**, *129*, 7538-7544.

(29) Aydogan, A.; Coady, Daniel J.; Kim, Sung K.; Akar, A.; Bielawski, Christopher W.; Marquez, M.; Sessler, Jonathan L. *Angew. Chem. Int. Ed.* **2008**, *47*, 9648-9652.

(30) Boiocchi, M.; Del Boca, L.; Gomez, D. E.; Fabbrizzi, L.; Licchelli, M.; Monzani, E. *J. Am. Chem. Soc.* **2004**, *126*, 16507-16514.

(31) Wang, L.; Meyerhoff, M. E. *Anal. Chim. Acta* **2008**, *611*, 97-102.

(32) Pietrzak, M.; Meyerhoff, M. E.; Malinowska, E. *Anal. Chim. Acta* **2007**, *596*, 201-209.

(33) Kang, Y.; Kampf, J. W.; Meyerhoff, M. E. *Anal. Chim. Acta* **2007**, *598*, 295-303.

(34) Mitchell-Koch, J. T.; Pietrzak, M.; Malinowska, E.; Meyerhoff, M. E. *Electroanalysis* **2006**, *18*, 551-557.

(35) Mitchell-Koch, J. T.; Malinowska, E.; Meyerhoff, M. E. *Electroanalysis* **2005**, *17*, 1347-1353.

(36) Gorski, L.; Saniewska, A.; Parzuchowski, P.; Meyerhoff, M. E.; Malinowska, E. *Anal. Chim. Acta* **2005**, *551*, 37-44.

(37) Badr, I. H. A.; Meyerhoff, M. E. *Anal. Chem.* **2005**, *77*, 6719-6728.

(38) Badr, I. H. A.; Meyerhoff, M. E. *Anal. Chim. Acta* **2005**, *553*, 169-176.

(39) Badr, I. H. A.; Meyerhoff, M. E. *J. Am. Chem. Soc.* **2005**, *127*, 5318-5319.

(40) Bayer, M. J.; Jalisatgi, S. S.; Smart, B.; Herzog, A.; Knobler, C. B.; Hawthorne, M. F. *Angew. Chem., Int. Ed.* **2004**, *43*, 1854-1857.

(41) Chaniotakis, N.; Jurkschat, K.; Mueller, D.; Perdikaki, K.; Reeske, G. *Eur. J. Inorg. Chem.* **2004**, 2283-2288.

(42) Newcomb, M.; Horner, J. H.; Blanda, M. T.; Squattrito, P. J. *J. Am. Chem. Soc.* **1989**, *111*, 6294-6301.

(43) Cametti, M.; Dalla Cort, A.; Mandolini, L.; Nissinen, M.; Rissanen, K. *New J. Chem.* **2008**, *32*, 1113-1116.

(44) Cametti, M.; Dalla Cort, A.; Bartik, K. *ChemPhysChem* **2008**, *9*, 2168-2171.

(45) Holland, M. A.; Kozlowski, L. M. *Clin. Pharmacy* **1986**, *5*, 737-741.

(46) Zelder, F. H.; Mannel-Croise, C. *Chimia* **2009**, *63*, 58-62.

(47) Xu, Z.; Chen, X.; Kim, H. N.; Yoon, J. *Chem. Soc. Rev.* **2010**, *39*, 127-137.

(48) Raja, K. C. M. *Trends Carbohydr. Chem.* **1999**, *5*, 25-35.

(49) Nhassico, D.; Muquingue, H.; Cliff, J.; Cumbana, A.; Bradbury, J. H. *J. Sci. Food Agric.* **2008**, *88*, 2043-2049.

(50) Melamed, A. *Chem. Rev. (Deddington, U. K.)* **1998**, *8*, 2-6.

(51) Koenig, R. *Science* **2000**, *287*, 1737-1738.

(52) Lou, B.; Chen, Z. Q.; Bian, Z. Q.; Huang, C. H. *New J. Chem.* **2010**, *34*, 132-136.

(53) Jo, J.; Lee, D. *J. Am. Chem. Soc.* **2009**, *131*, 16283-16291.

(54) Sessler, J. L.; Cho, D.-G. *Org. Lett.* **2008**, *10*, 73-75.

(55) Niu, H.-T.; Su, D.; Jiang, X.; Yang, W.; Yin, Z.; He, J.; Cheng, J.-P. *Org. Biomol. Chem.* **2008**, *6*, 3038-3040.

(56) Niu, H.-T.; Jiang, X.; He, J.; Cheng, J.-P. *Tetrahedron Lett.* **2008**, *49*, 6521-6524.

(57) Cho, D.-G.; Kim, J. H.; Sessler, J. L. *J. Am. Chem. Soc.* **2008**, *130*, 12163-12167.

(58) Yang, Y.-K.; Tae, J. *Org. Lett.* **2006**, *8*, 5721-5723.

(59) Tomasulo, M.; Sortino, S.; White, A. J. P.; Raymo, F. M. *J. Org. Chem.* **2006**, *71*, 744-753.

(60) Chung, Y.; Lee, H.; Ahn, K. H. *J. Org. Chem.* **2006**, *71*, 9470-9474.

(61) Tomasulo, M.; Raymo, F. M. *Org. Lett.* **2005**, *7*, 4633-4636.

(62) Garcia, F.; Garcia, J. M.; Garcia-Acosta, B.; Martinez-Manez, R.; Sancenon, F.; Soto, J. *Chem. Commun.* **2005**, 2790-2792.

(63) Ros-Lis, J. V.; Garcia, B.; Jimenez, D.; Martinez-Manez, R.; Sancenon, F.; Soto, J.; Gonzalvo, F.; Valldecabres, M. C. *J. Am. Chem. Soc.* **2004**, *126*, 4064-4065.

(64) Ros-Lis, J. V.; Martinez-Manez, R.; Soto, J. *Chem. Commun.* **2002**, 2248-2249.

(65) Lee, K.-S.; Kim, H.-J.; Kim, G.-H.; Shin, I.; Hong, J.-I. *Org. Lett.* **2008**, *10*, 49-51.

(66) Ros-Lis, J. V.; Martinez-Manez, R.; Soto, J. *Chem. Commun.* **2005**, 5260-5262.

(67) Shang, L.; Zhang, L.; Dong, S. *Analyst* **2009**, *134*, 107-113.

(68) Männel-Croisé, C.; Zelder, F. *Inorg. Chem.* **2009**, *48*, 1272-1274.

(69) Männel-Croisé, C.; Probst, B.; Zelder, F. *Anal. Chem.* **2009**, *81*, 9493-9498.

(70) Lou, X. D.; Qiang, L.; Qin, J. G.; Li, Z. *ACS Appl. Mater. Interfaces* **2009**, *1*, 2529-2535.

(71) Touceda-Varela, A.; Stevenson, E. I.; Galve-Gasion, J. A.; Dryden, D. T. F.; Mareque-Rivas, J. C. *Chem. Commun.* **2008**, 1998-2000.

(72) Lou, X.; Zhang, L.; Qin, J.; Li, Z. *Chem. Commun.* **2008**, 5848-5850.

(73) Poland, K.; Topoglidis, E.; Durrant, J. R.; Palomares, E. *Inorg. Chem. Commun.* **2006**, *9*, 1239-1242.

(74) Liu, H.; Shao, X.-B.; Jia, M.-X.; Jiang, X.-K.; Li, Z.-T.; Chen, G.-J. *Tetrahedron* **2005**, *61*, 8095-8100.

(75) Chow, C.-F.; Lam, M. H. W.; Wong, W.-Y. *Inorg. Chem.* **2004**, *43*, 8387-8393.

(76) Kim, Y.-H.; Hong, J.-I. *Chem. Commun.* **2002**, 512-513.

(77) Galbraith, E.; James, T. D. *Chem. Soc. Rev.* **2010**, *39*, 3831-3842.

(78) Hudnall, T. W.; Chiu, C.-W.; Gabbaï, F. P. *Acc. Chem. Res.* **2009**, *42*, 388-397.

(79) Hudson, Z. M.; Wang, S. *Acc. Chem. Res.* **2009**, *42*, 1584-1596.

(80) Cho, D. G.; Sessler, J. L. *Chem. Soc. Rev.* **2009**, *38*, 1647-1662.

(81) Liu, S. J.; Zhao, Q.; Xu, W. J.; Huang, W. *Prog. Chem.* **2008**, *20*, 1708-1715.

(82) Yamaguchi, S.; Wakamiya, A. *Pure Appl. Chem.* **2006**, *78*, 1413-1424.

(83) Yamaguchi, S.; Akiyama, S.; Tamao, K. *J. Organomet. Chem.* **2002**, *652*, 3-9.

(84) Badugu, R.; Lakowicz, J. R.; Geddes, C. D. *Curr. Anal. Chem.* **2005**, *1*, 157-170.

(85) Entwistle, C. D.; Marder, T. B. *Chem. Mater.* **2004**, *16*, 4574-4585.

(86) Entwistle, C. D.; Marder, T. B. *Angew. Chem., Int. Ed.* **2002**, *41*, 2927-2931.

(87) Gabbaï, F. P. *Angew. Chem., Int. Ed.* **2003**, *42*, 2218-2221.

(88) Hoefelmeyer, J. D.; Schulte, M.; Tschinkl, M.; Gabbaï, F. P. *Coord. Chem. Rev.* **2002**, *235*, 93-103.

(89) Melaïmi, M.; Gabbaï, F. P. *Adv. Organomet. Chem.* **2005**, *53*, 61-99.

(90) Bauman, A. *Mikrochim. Acta* **1977**, *1*, 69-72.

(91) Veltheer, J. E.; Burger, P.; Bergman, R. G. *J. Am. Chem. Soc.* **1995**, *117*, 12478-12488.

(92) Timoshkin, A. Y.; Frenking, G. *Organometallics* **2008**, *27*, 371-380.

(93) Krossing, I.; Raabe, I. *Chem. Eur. J.* **2004**, *10*, 5017-5030.

(94) Melaïmi, M.; Sole, S.; Chiu, C.-W.; Wang, H.; Gabbaï, F. P. *Inorg. Chem.* **2006**, *45*, 8136-8143.

(95) Bresner, C.; Haynes, C. J. E.; Addy, D. A.; Broomsgrove, A. E. J.; Fitzpatrick, P.; Vidovic, D.; Thompson, A. L.; Fallis, I. A.; Aldridge, S. *New J. Chem.* **2010**, *34*, 1652-1659.

(96) Kuz'mina, L. G.; Struchkov, Y. T.; Lemenovsky, D. A.; Urazowsky, I. F. *J. Organomet. Chem.* **1984**, *277*, 147-151.

(97) Yamaguchi, S.; Akiyama, S.; Tamao, K. *J. Am. Chem. Soc.* **2001**, *123*, 11372-11375.

(98) Huh, J. O.; Kim, H.; Lee, K. M.; Lee, Y. S.; Do, Y.; Lee, M. H. *Chem. Commun.* **2010**, *46*, 1138-1140.

(99) Solé, S.; Gabbaï, F. P. *Chem. Commun.* **2004**, 1284-1285.

(100) Mayer, U.; Gutmann, V.; Gerger, W. *Monatsh. Chem.* **1975**, *106*, 1235-1257.

(101) Chiu, C.-W.; Gabbaï, F. P. *J. Am. Chem. Soc.* **2006**, *128*, 14248-14249.

(102) Chiu, C.-W.; Gabbaï, F. P. *Dalton Trans.* **2008**, 814-817.

(103) Broomsgrove, A. E. J.; A. Addy, D.; Di Paolo, A.; Morgan, I. R.; Bresner, C.; Chislett, V.; Fallis, I. A.; Thompson, A. L.; Vidovic, D.; Aldridge, S. *Inorg. Chem.* **2010**, *49*, 157-173.

(104) Hudnall, T. W.; Gabbaï, F. P. *J. Am. Chem. Soc.* **2007**, *129*, 11978-11986.

(105) Matsumoto, T.; Wade, C. R.; Gabbaï, F. P. *Organometallics* **2010**, *29*, 5490-5495.

(106) Chiu, C.-W.; Kim, Y.; Gabbaï, F. P. *J. Am. Chem. Soc.* **2009**, *131*, 60-61.

(107) Lee, M. H.; Agou, T.; Kobayashi, J.; Kawashima, T.; Gabbaï, F. P. *Chem. Commun.* **2007**, 1133-1135.

(108) Kim, Y.; Gabbaï, F. P. *J. Am. Chem. Soc.* **2009**, *131*, 3363-3369.

(109) Kim, Y.; Huh, H.-S.; Lee, M. H.; Lenov, I. L.; Zhao, H.; Gabbaï, F. P. *Chem. Eur. J.* **2011**, *17*, 2057-2062.

(110) Agou, T.; Sekine, M.; Kobayashi, J.; Kawashima, T. *Chem. Eur. J.* **2009**, *15*, 5056-5062.

(111) Agou, T.; Kobayashi, J.; Kawashima, T. *Inorg. Chem.* **2006**, *45*, 9137-9144.

(112) Agou, T.; Kobayashi, J.; Kim, Y.; Gabbaï, F. P.; Kawashima, T. *Chem. Lett.* **2007**, *36*, 976-977.

(113) Shriver, D. F.; Biallas, M. J. *J. Am. Chem. Soc.* **1967**, *89*, 1078-1081.

(114) Katz, H. E. *Inclusion Compd.* **1991**, *4*, 391-405.

(115) Katz, H. E. *J. Am. Chem. Soc.* **1985**, *107*, 1420-1421.

(116) Katz, H. E. *J. Org. Chem.* **1985**, *50*, 5027-5032.

(117) Hoefelmeyer, J. D.; Gabbaï, F. P. *Organometallics* **2002**, *21*, 982-985.

(118) Hoefelmeyer, J. D.; Solé, S.; Gabbaï, F. P. *Dalton Trans.* **2004**, 1254-1258.

(119) Dorsey, C. L.; Jewula, P.; Hudnall, T. W.; Hoefelmeyer, J. D.; Taylor, T. J.; Honesty, N. R.; Chiu, C.-W.; Schulte, M.; Gabbaï, F. P. *Dalton Trans.* **2008**, 4442-4450.

(120) Kawachi, A.; Tani, A.; Shimada, J.; Yamamoto, Y. *J. Am. Chem. Soc.* **2008**, *130*, 4222-4223.

(121) Boshra, R.; Venkatasubbaiah, K.; Doshi, A.; Lalancette, R. A.; Kakalis, L.; Jäkle, F. *Inorg. Chem.* **2007**, *46*, 10174-10186.

(122) Melaïmi, M.; Gabbaï, F. P. *J. Am. Chem. Soc.* **2005**, *127*, 9680-9681.

(123) Lee, M. H.; Gabbaï, F. P. *Inorg. Chem.* **2007**, *46*, 8132-8138.

(124) Kim, Y.; Hudnall, T. W.; Bouhadir, G.; Bourissou, D.; Gabbaï, F. P. *Chem. Commun.* **2009**, 3729-3731.

(125) Hudnall, T. W.; Kim, Y.-M.; Bebbington, M. W. P.; Bourissou, D.; Gabbaï, F. P. *J. Am. Chem. Soc.* **2008**, *130*, 10890-10891.

(126) Kim, Y.; Zhao, H.; Gabbaï, F. P. *Angew. Chem., Int. Ed.* **2009**, *48*, 4957-4960.

(127) *Official Journal of the European Communities* **1998**, *L 330*, 32-54.

(128) Zhao, H.; Gabbaï, F. P. *Nat. Chem.* **2010**, *2*, 984-990.

(129) Zhou, Z.; Yang, H.; Shi, M.; Xiao, S.; Li, F.; Yi, T.; Huang, C. *ChemPhysChem* **2007**, *8*, 1289-1292.

(130) Zhou, Z.; Xiao, S.; Xu, J.; Liu, Z.; Shi, M.; Li, F.; Yi, T.; Huang, C. *Org. Lett.* **2006**, *8*, 3911-3914.

(131) Zhao, Q.; Li, F.; Liu, S.; Yu, M.; Liu, Z.; Yi, T.; Huang, C. *Inorg. Chem.* **2008**, *47*, 9256-9264.

(132) Lam, S.-T.; Zhu, N.; Yam, V. W.-W. *Inorg. Chem.* **2009**.

(133) Sun, Y.; Ross, N.; Zhao, S. B.; Huszarik, K.; Jia, W. L.; Wang, R. Y.; Macartney, D.; Wang, S. *J. Am. Chem. Soc.* **2007**, *129*, 7510-7511.

(134) Sun, Y.; Wang, S. *Inorg. Chem.* **2009**, *48*, 3755-3767.

(135) Zhao, S.-B.; McCormick, T.; Wang, S. *Inorg. Chem.* **2007**, *46*, 10965-10967.

(136) Rao, Y.-L.; Wang, S. *Inorg. Chem.* **2009**, *48*, 7698-7713.

(137) Hudson, Z. M.; Zhao, S.-B.; Wang, R.-Y.; Wang, S. *Chem. Eur. J.* **2009**, *15*, 6131-6137.

(138) Sun, Y.; Hudson, Z. M.; Rao, Y.; Wang, S. *Inorg. Chem.* **2011**, *50*, 3373-3378.

(139) Sakuda, E.; Funahashi, A.; Kitamura, N. *Inorg. Chem.* **2006**, *45*, 10670-10677.

(140) Hudson, Z. M.; Sun, C.; Harris, K. J.; Lucier, B. E. G.; Schurko, R. W.; Wang, S. *Inorg. Chem.* **2011**, *50*, 3447-3457.

(141) Broomsgrove, A. E. J.; Addy, D. A.; Bresner, C.; Fallis, I. A.; Thompson, A. L.; Aldridge, S. *Chem. Eur. J.* **2008**, *14*, 7525-7529.

(142) Carpenter, B. E.; Piers, W. E.; Parvez, M.; Yap, G. P. A.; Rettig, S. J. *Can. J. Chem.* **2001**, *79*, 857-867.

(143) Olah, G. A.; Schlosberg, R. H. *J. Am. Chem. Soc.* **1968**, *90*, 2726-2727.

(144) Hyman, H. H.; Quarterman, L. A.; Kilpatrick, M.; Katz, J. J. *J. Phys. Chem.* **1961**, *65*, 123-127.

(145) Kolditz, L.; Daunicht, H. *Z. Anorg. Allg. Chem.* **1959**, *302*, 230-236.

(146) Mootz, D.; Bartmann, K. *Z. Naturforsch., B: Chem. Sci.* **1991**, *46*, 1659-1663.

(147) Mootz, D.; Bartmann, K. *Angew. Chem.* **1988**, *100*, 424-425.

(148) Lim, Y. Y.; Drago, R. S. *Inorg. Chem.* **1972**, *11*, 202-204.

(149) Bamgboye, T. T.; Begley, M. J.; Sowerby, D. B. *J. Organomet. Chem.* **1989**, *362*, 77-85.

(150) Nishii, N.; Hashimoto, K.; Okawara, R. *J. Organomet. Chem.* **1973**, *55*, 133-137.

(151) Nishii, N.; Matsumura, Y.; Okawara, R. *J. Organomet. Chem.* **1971**, *30*, 59-65.

(152) Popov, V. I.; Kondratenko, N. V. *Zh. Obshch. Khim.* **1976**, *46*, 2597-2601.

(153) Singhal, K.; Yadav, R. N. P.; Raj, P.; Agarwal, A. K. *J. Fluorine Chem.* **2003**, *121*, 131-134.

(154) Low, J. N.; Ferguson, G.; Wardell, J. L. *Acta Crystallogr., Sect. C: Cryst. Struct. Commun.* **2000**, *56*, E317-E317.

(155) Bricklebank, N.; Godfrey, S. M.; Lane, H. P.; McAuliffe, C. A.; Pritchard, R. G. *J. Chem. Soc., Dalton Trans.* **1994**, 1759-1763.

(156) Ferguson, G.; Glidewell, C.; Lloyd, D.; Metcalfe, S. *J. Chem. Soc., Perk. Trans. 2* **1988**, 731-735.

(157) Lloyd, M. A.; Brock, C. P. *Acta Crystallogr., Sect. B: Struct. Sci* **1997**, *53*, 773-779.

(158) Sharutin, V. V.; Sharutina, O. K.; Pakusina, A. P.; Smirnova, S. A.; Pushilin, M. A. *Russ. J. Coord. Chem.* **2005**, *31*, 108-114.

(159) Baker, L.-J.; Rickard, C. E. F.; Taylor, M. J. *Dalton Trans.* **1995**, 2895-2899.

(160) Lebedev, V. A.; Bochkova, R. I.; Kuz'min, E. A.; Sharutin, V. V.; Belov, N. V. *Doklady Akademii Nauk SSSR* **1981**, *260*, 1124-1127.

(161) Sharutin, V. V.; Sharutina, O. K.; Pakusina, A. P.; Platonova, T. P.; Zadachina, O. P.; Gerasimenko, A. V. *Russ. J. Coord. Chem.* **2003**, *29*, 89-92.

(162) Khan, A.; Azad, A. K.; Hussain, I.; Uddin, F. *Asian J. Chem.* **2010**, *22*, 3583-3590.

(163) Moffett, K. D.; Simmler, J. R.; Potratz, H. A. *Anal. Chem.* **1956**, *28*, 1356-1356.

(164) Orenberg, J. B.; Morris, M. D. *Anal. Chem.* **1967**, *39*, 1776-1780.

(165) Bowen, L. H.; Rood, R. T. *J. Inorg. Nucl. Chem.* **1966**, *28*, 1985-1990.

(166) Wade, C. R.; Gabbaï, F. P. *Dalton Trans.* **2009**, 9169-9175.

(167) Wade, C. R.; Broomsgrove, A. E. J.; Aldridge, S.; Gabbaï, F. P. *Chem. Rev.* **2010**, *110*, 3958-3984.

(168) Parab, K.; Venkatasubbaiah, K.; Jäkle, F. *J. Am. Chem. Soc.* **2006**, *128*, 12879-12885.

(169) Parab, K.; Venkatasubbaiah, K.; Qin, Y.; Jäkle, F. *Polym. Prepr.* **2007**, *48*, 699-700.

(170) Huh, J. O.; Do, Y.; Lee, M. H. *Organometallics* **2008**, *27*, 1022-1025.

(171) Dusemund, C.; Sandanayake, K. R. A. S.; Shinkai, S. *Chem. Commun.* **1995**, 333-334.

(172) Venkatasubbaiah, K.; Nowik, I.; Herber, R. H.; Jäkle, F. *Chem. Commun.* **2007**, 2154-2156.

(173) Welch, G. C.; Cabrera, L.; Chase, P. A.; Hollink, E.; Masuda, J. D.; Wei, P.; Stephan, D. W. *Dalton Trans.* **2007**, 3407-3414.

(174) Bai, D.-R.; Liu, X.-Y.; Wang, S. *Chem. Eur. J.* **2007**, *13*, 5713-5723.

(175) Liu, X. Y.; Bai, D. R.; Wang, S. *Angew. Chem., Int. Ed.* **2006**, *45*, 5475-5478.

(176) Yuan, M.-S.; Liu, Z.-Q.; Fang, Q. *J. Org. Chem.* **2007**, *72*, 7915-7922.

(177) DiCesare, N.; Lakowicz, J. R. *Anal. Biochem.* **2002**, *301*, 111-116.

(178) Oehlke, A.; Auer, A. A.; Jahre, I.; Walfort, B.; Rueffer, T.; Zoufala, P.; Lang, H.; Spange, S. *J. Org. Chem.* **2007**, *72*, 4328-4339.

(179) Day, J. K.; Bresner, C.; Coombs, N. D.; Fallis, I. A.; Ooi, L.-L.; Aldridge, S. *Inorg. Chem.* **2008**, *47*, 793-804.

(180) You, Y.; Park, S. Y. *Adv. Mater.* **2008**, *20*, 3820-3826.

(181) Zhou, G.; Ho, C.-L.; Wong, W.-Y.; Wang, Q.; Ma, D.; Wang, L.; Lin, Z.; Marder, T. B.; Beeby, A. *Adv. Funct. Mater.* **2008**, *18*, 499-511.

(182) Parab, K.; Jäkle, F. *Macromolecules* **2009**, *42*, 4002-4007.

(183) Aldridge, S.; Bresner, C.; Fallis, I. A.; Coles, S. J.; Hursthouse, M. B. *Chem. Commun.* **2002**, 740-741.

(184) Bresner, C.; Aldridge, S.; Fallis, I. A.; Jones, C.; Ooi, L.-L. *Angew. Chem., Int. Ed.* **2005**, *44*, 3606-3609.

(185) Coombs, N. D.; Aldridge, S.; Wiltshire, G.; Kays, D. L.; Bresner, C.; Ooi, L.-l. *J. Organomet. Chem.* **2005**, *690*, 2725-2731.

(186) Bresner, C.; Day, J. K.; Coombs, N. D.; Fallis, I. A.; Aldridge, S.; Coles, S. J.; Hursthouse, M. B. *Dalton Trans.* **2006**, 3660-3667.

(187) Williams, V. C.; Piers, W. E.; Clegg, W.; Elsegood, M. R. J.; Collins, S.; Marder, T. B. *J. Am. Chem. Soc.* **1999**, *121*, 3244-3245.

(188) Miyasaka, S.; Kobayashi, J.; Kawashima, T. *Tetrahedron Lett.* **2009**, *50*, 3467-3469.

(189) Cossi, M.; Barone, V.; Cammi, R.; Tomasi, J. *Chem. Phys. Lett.* **1996**, *255*, 327-335.

(190) Tomasi, J.; Cammi, R.; Mennucci, B. *Int. J. Quantum Chem.* **1999**, *75*, 783-803.

(191) Dreuw, A.; Weisman, J. L.; Head-Gordon, M. *J. Chem. Phys.* **2003**, *119*, 2943-2946.

(192) Kozhevnikov, D. N.; Kozhevnikov, V. N.; Ustinova, M. M.; Santoro, A.; Bruce, D. W.; Koenig, B.; Czerwieniec, R.; Fischer, T.; Zabel, M.; Yersin, H. *Inorg. Chem.* **2009**, *48*, 4179-4189.

(193) Hudson, Z. M.; Sun, C.; Helander, M. G.; Amarne, H.; Lu, Z.-H.; Wang, S. *Adv. Funct. Mater.* **2010**, *20*, 3426-3439.

(194) Brooks, J.; Babayan, Y.; Lamansky, S.; Djurovich, P. I.; Tsyba, I.; Bau, R.; Thompson, M. E. *Inorg. Chem.* **2002**, *41*, 3055-3066.

(195) Chi, Y.; Chou, P.-T. *Chem. Soc. Rev.* **2010**, *39*, 638-655.

(196) Reveco, P.; Schmehl, R. H.; Cherry, W. R.; Fronczek, F. R.; Selbin, J. *Inorg. Chem.* **1985**, *24*, 4078-4082.

(197) Constable, E. C.; Holmes, J. M. *J. Organomet. Chem.* **1986**, *301*, 203-208.

(198) Reveco, P.; Cherry, W. R.; Medley, J.; Garber, A.; Gale, R. J.; Selbin, J. *Inorg. Chem.* **1986**, *25*, 1842-1845.

(199) Constable, E. C.; Leese, T. A. *J. Organomet. Chem.* **1987**, *335*, 293-299.

(200) Constable, E. C.; Housecroft, C. E. *Polyhedron* **1990**, *9*, 1939-1947.

(201) Sasaki, I.; Vendier, L.; Sournia-Saquet, A.; Lacroix, P. G. *Eur. J. Inorg. Chem.* **2006**, 3294-3302.

(202) Andres, R.; Brissard, M.; Gruselle, M.; Train, C.; Vaissermann, J.; Malezieux, B.; Jamet, J.-P.; Verdaguer, M. *Inorg. Chem.* **2001**, *40*, 4633-4640.

(203) Brissard, M.; Gruselle, M.; Malezieux, B.; Thouvenot, R.; Guyard-Duhayon, C.; Convert, O. *Eur. J. Inorg. Chem.* **2001**, 1745-1751.

(204) Sandee, A. J.; Williams, C. K.; Evans, N. R.; Davies, J. E.; Boothby, C. E.; Koehler, A.; Friend, R. H.; Holmes, A. B. *J. Am. Chem. Soc.* **2004**, *126*, 7041-7048.

(205) Sullivan, B. P.; Salmon, D. J.; Meyer, T. J. *Inorg. Chem.* **1978**, *17*, 3334-3341.

(206) Bagnoli, F.; Belli Dell'Amico, D.; Calderazzo, F.; Englert, U.; Marchetti, F.; Merigo, A.; Ramello, S. *J. Organomet. Chem.* **2001**, *622*, 180-189.

(207) Sheldrick, G. M., .

(208) Sheldrick, G. M. *SHELXTL Version 6.1; Bruker Analytical X-ray Systems, Inc., Madison, Wisconsin, USA*, 2000.

(209) Miller, P. W.; Long, N. J.; Vilar, R.; Gee, A. D. *Angew. Chem. Int. Ed.* **2008**, *47*, 8998-9033.

(210) Cai, L.; Lu, S.; Pike, V. W. *Eur. J. Org. Chem.* **2008**, 2853-2873.

(211) Schirrmacher, R.; Bradmoeller, G.; Schirrmacher, E.; Thews, O.; Tillmanns, J.; Siessmeier, T.; Bucholz, H. G.; Bartenstein, P.; Waengler, B.; Niemeyer, C. M.; Jurkschat, K. *Angew. Chem., Int. Ed.* **2006**, *45*, 6047-6050.

(212) Ting, R.; Harwig, C.; auf dem Keller, U.; McCormick, S.; Austin, P.; Overall, C. M.; Adam, M. J.; Ruth, T. J.; Perrin, D. M. *J. Am. Chem. Soc.* **2008**, *130*, 12045-12055.

(213) Ting, R.; Harwig, C. W.; Lo, J.; Li, Y.; Adam, M. J.; Ruth, T. J.; Perrin, D. M. *J. Org. Chem.* **2008**, *73*, 4662-4670.

(214) Ting, R.; Adam, M. J.; Ruth, T. J.; Perrin, D. M. *J. Am. Chem. Soc.* **2005**, *127*, 13094-13095.

(215) Albrecht, K.; Kaiser, V.; Boese, R.; Adams, J.; Kaufmann, D. E. *J. Chem. Soc., Perkin Trans. 2* **2000**, 2153-2157.

(216) Harwig, C. W.; Ting, R.; Adam, M. J.; Ruth, T. J.; Perrin, D. M. *Tetrahedron Lett.* **2008**, *49*, 3152-3156.

(217) Moebs-Sanchez, S.; Saffon, N.; Bouhadir, G.; Maron, L.; Bourissou, D. *Dalton Trans.* **2010**, *39*, 4417-4420.

(218) Schmidbaur, H.; Mitschke, K. H.; Weidlein, J. *Angew. Chem. Int. Ed.* **1972**, *11*, 144-145.

(219) Hudnall, T. W.; Melaïmi, M.; Gabbaï, F. P. *Org. Lett.* **2006**, *8*, 2747-2749.

(220) Kubo, Y.; Ishida, T.; Minami, T.; James, T. D. *Chem. Lett.* **2006**, *35*, 996-997.

(221) Xu, Z.; Kim, S. K.; Han, S. J.; Lee, C.; Kociok-Kohn, G.; James, T. D.; Yoon, J. *Eur. J. Org. Chem.* **2009**, 3058-3065.

(222) Batsanov, S. S. *Inorg. Mater.* **2001**, *37*, 871-885.

(223) Porcel, S.; Bouhadir, G.; Saffon, N.; Maron, L.; Bourissou, D. *Angew. Chem. Int. Ed.* **2010**, *49*, 6186-6189.

(224) Biallas, M. J.; Shriver, D. F. *J. Am. Chem. Soc.* **1966**, *88*, 375-376.

(225) Wang, H.; Sole, S.; Gabbaï, F. P. *ACS Symp. Ser.* **2006**, *917*, 208-220.

(226) Piers, W. E.; Irvine, G. J.; Williams, V. C. *Eur. J. Inorg. Chem.* **2000**, 2131-2142.

(227) Lewis, S. P.; Taylor, N. J.; Piers, W. E.; Collins, S. *J. Am. Chem. Soc.* **2003**, *125*, 14686-14687.

(228) Zhao, H.; Gabbaï, F. P. *Org. Lett.* **2011**, 1444-1446.

(229) Williams, V. C.; Irvine, G. J.; Piers, W. E.; Li, Z.; Collins, S.; Clegg, W.; Elsegood, M. R. J.; Marder, T. B. *Organometallics* **2000**, *19*, 1619-1621.

(230) Chai, J.; Lewis, S. P.; Collins, S.; Sciarone, T. J. J.; Henderson, L. D.; Chase, P. A.; Irvine, G. J.; Piers, W. E.; Elsegood, M. R. J.; Clegg, W. *Organometallics* **2007**, *26*, 5667-5679.

(231) Wade, C. R.; Zhao, H.; Gabbaï, F. P. *Chem. Commun.* **2010**, *46*, 6380-6381.

(232) Metrangolo, P.; Resnati, G. *Chem. Eur. J.* **2001**, *7*, 2511-2519.

(233) Levason, W.; McAuliffe, C. A.; Murray, S. G. *J. Organomet. Chem.* **1975**, *88*, 171-174.

(234) Bordner, J.; Andrews, B. C.; Long, G. G. *Cryst. Struct. Commun.* **1976**, *5*, 801-804.

(235) Schwarz, W.; Guder, H. J. *Z. Anorg. Allg. Chem.* **1978**, *444*, 105-111.

(236) Cordero, B.; Gomez, V.; Platero-Prats, A. E.; Reves, M.; Echeverria, J.; Cremades, E.; Barragan, F.; Alvarez, S. *Dalton Trans.* **2008**, 2832-2838.

(237) Haiges, R.; Schroer, T.; Yousuffudin, M.; Christe, K. O. *Z. Anorg. Allg. Chem.* **2005**, *631*, 2691-2695.

(238) Lube, M. S.; Wells, R. L.; White, P. S. *J. Chem. Soc., Dalton Trans.* **1997**, 285-286.

(239) Becker, G.; Mundt, O.; Sachs, M.; Breunig, H. J.; Lork, E.; Probst, J.; Silvestru, A. *Z. Anorg. Allg. Chem.* **2001**, *627*, 699-714.

(240) Barton, D. H. R.; Bhatnagar, N. Y.; Finet, J. P.; Motherwell, W. B. *Tetrahedron* **1986**, *42*, 3111-3122.

(241) Frisch, M. J.; Trucks, G. W.; Schlegel, H. B.; G. E. Scuseria; Robb, M. A.; Cheeseman, J. R.; Scalmani, G.; Barone, V.; Mennucci, B.; Petersson, G. A.; Nakatsuji, H.; Caricato, M.; Li, X.; Hratchian, H. P.; Izmaylov, A. F.; Bloino, J.; Zheng, G.; Sonnenberg, J. L.; Hada, M.; Ehara, M.; Toyota, K.; Fukuda, R.; Hasegawa, J.; Ishida, M.; Nakajima, T.; Honda, Y.; Kitao, O.; Nakai, H.; Vreven, T.; J. A. Montgomery, J.; Peralta, J. E.; Ogliaro, F.; Bearpark, M.; Heyd, J. J.; Brothers, E.; Kudin, K. N.; Staroverov, V. N.; R. Kobayashi, J. N.; Raghavachari, K.; Rendell, A.; Burant, J. C.; Iyengar, S. S.; Tomasi, J.; Cossi, M.; Rega, N.; Millam, J. M.; Klene, M.; Knox, J. E.; Cross, J. B.; Bakken, V.; Adamo, C.; Jaramillo, J.; Gomperts, R.; Stratmann, R. E.; Yazyev, O.; Austin, A. J.; Cammi, R.; Pomelli, C.; Ochterski, J. W.; Martin, R. L.; Morokuma, K.; Zakrzewski, V. G.; Voth, G. A.; Salvador, P.; Dannenberg, J. J.; Dapprich, S.; Daniels, A. D.; Farkas, O.; Foresman, J. B.; Ortiz, J. V.; Cioslowski, J.; Fox, D. J. *Gaussian 09,* Revision A. 02; Gaussian, Inc.: Wallingford CT, 2009.

(242) Miehlich, B.; Savin, A.; Stoll, H.; Preuss, H. *Chem. Phys. Lett.* **1989**, *157*, 200-206.

(243) Lee, C. T.; Yang, W. T.; Parr, R. G. *Phys. Rev. B* **1988**, *37*, 785-789.

(244) Hariharan, P. C.; Pople, J. A. *Theor. Chim. Acta* **1973**, *28*, 213-222.

(245) Hehre, W. J.; Ditchfield, R.; Pople, J. A. *J. Chem. Phys.* **1972**, *56*, 2257-2261.

(246) Peterson, K. A. *J. Chem. Phys.* **2003**, *119*, 11099-11112.

(247) Dunning, T. H. J.; Hay, P. J. *Modern Theoretical Chemistry*; Plenum: New York 1976; Vol. 3.

(248) Bader, R. F. W. *Atoms in Molecules: A Quantum Theory*; Oxford University Press: UK, 1994.

(249) Konig, F. B.; Schonbohm, J.; Bayles, D. *J. Comput. Chem.* **2001**, *22*, 545-559.

(250) NBO Version 3.1.; Glendening, E. D.; Reed, A. E.; Carpenter, J. E.; Weinhold, F.

(251) Spitznagel, G. W.; Clark, T.; Schleyer, P. v. R.; Hehre, W. J. *J. Comput. Chem.* **1987**, *8*, 1109-1116.

(252) Krishnan, R.; Binkley, J. S.; Seeger, R.; Pople, J. A. *J. Chem. Phys.* **1980**, *72*, 650-654.

(253) Whited, M. T.; Rivard, E.; Peters, J. C. *Chem. Commun.* **2006**, 1613-1615.

(254) Yuan, Z.; Taylor, N. J.; Sun, Y.; Marder, T. B.; Williams, I. D.; Cheng, L.-T. *J. Organomet. Chem.* **1993**, *449*, 27-37.

(255) McCortney, B. A.; Jacobson, B. M.; Vreeke, M.; Lewis, E. S. *J. Am. Chem. Soc.* **1990**, *112*, 3554-3559.

(256) Levason, W.; Reid, G. *Coord. Chem. Rev.* **2006**, *250*, 2565-2594.

(257) Levason, W.; McAuliffe, C. A. *Acc. Chem. Res.* **1978**, *11*, 363-368.

(258) Malisch, W.; Kaul, H. A.; Gross, E.; Thewalt, U. *Angew. Chem. Int. Ed.* **1982**, *21*, 549-550.

(259) Malisch, W.; Panster, P. *Angew. Chem. Int. Ed.* **1974**, *13*, 670-672.

(260) Toyota, K.; Yamamoto, Y.; Akiba, K.-y. *Organometallics* **2000**, *19*, 5134-5142.

(261) Toyota, K.; Wakisaka, Y.; Yamamoto, Y.; Akiba, K.-y. *Organometallics* **2000**, *19*, 5122-5133.

(262) Toyota, K.; Yamamoto, Y.; Akiba, K.-Y. *Chem. Lett.* **1999**, 783-784.

(263) Yamamoto, Y.; Okazaki, M.; Wakisaka, Y.; Akiba, K.-y. *Organometallics* **1995**, *14*, 3364-3369.

(264) Baracco, L.; McAuliffe, C. A. *J. Chem. Soc., Dalton Trans.* **1972**, 948-951.

(265) Dawson, J. W.; Venanzi, L. M. *J. Am. Chem. Soc.* **1968**, *90*, 7229-7233.

(266) Higginson, B. R.; McAuliffe, C. A.; Venanzi, L. M. *Inorg. Chim. Acta* **1971**, *5*, 37-40.

(267) Casares, J. A.; Espinet, P.; Martín-Alvarez, J. M.; Martínez-Ilarduya, J. M.; Salas, G. *Eur. J. Inorg. Chem.* **2005**, *2005*, 3825-3831.

(268) Jimenez-Tenorio, M.; Carmen Puerta, M.; Salcedo, I.; Valerga, P.; de los Rios, I.; Mereiter, K. *Dalton Trans.* **2009**, 1842-1852.

(269) Sharma, P.; Cabrera, A.; Sharma, M.; Alvarez, C.; Arias, J. L.; Gomez, R. M.; Hernandez, S. *Z. Anorg. Allg. Chem.* **2000**, *626*, 2330-2334.

(270) Wendt, O. F.; Scodinu, A.; Elding, L. I. *Inorg. Chim. Acta* **1998**, *277*, 237-241.

(271) Mentes, A.; Fawcett, J. *Inorg. Chim. Acta* **2005**, *358*, 1279-1283.

(272) Mentes, A.; Kemmitt, R. D. W.; Fawcett, J.; Russell, D. R. *J. Organomet. Chem.* **1997**, *528*, 59-63.

(273) Roberts, D. A.; Mason, W. R.; Geoffroy, G. L. *Inorg. Chem.* **1981**, *20*, 789-796.

(274) Solar, J. M.; Ozkan, M. A.; Isci, H.; Mason, W. R. *Inorg. Chem.* **1984**, *23*, 758-764.

(275) Bone, S. P.; Sowerby, D. B. *J. Chem. Soc., Dalton Trans.* **1979**, 1430-1433.

(276) Dawson, J. W.; Gray, H. B.; Hix, J. E.; Preer, J. R.; Venanzi, L. M. *J. Am. Chem. Soc.* **1972**, *94*, 2979-2987.

(277) Aizawa, S.-i.; Iida, T.; Funahashi, S. *Inorg. Chem.* **1996**, *35*, 5163-5167.

(278) Louw, W. J.; Dewaal, D. J. A.; Kruger, G. J. *J. Chem. Soc., Dalton Trans.* **1976**, 2364-2368.

(279) Hartley, J. G.; Venanzi, L. M.; Goodall, D. C. *J. Chem. Soc.* **1963**, 3930-3936.

(280) MacDonald, D. J.; Jennings, M. C.; Preuss, K. E. *Acta Crystallogr., Sect. C: Cryst. Struct. Commun.* **2010**, *66*, m137-140.

(281) Sheldrick, W. S.; Martin, C. *Z. Naturforsch., B: Chem. Sci.* **1992**, *47*, 919-924.

(282) Drew, D.; Doyle, J. R. *Inorg. Synth.* **1990**, *28*, 346-349.

(283) De Crisci, A. G.; Lough, A. J.; Multani, K.; Fekl, U. *Organometallics* **2008**, *27*, 1765-1779.

(284) Fernandez, E. J.; Laguna, A.; Lopez-de-Luzuriaga, J. M. *Dalton Trans.* **2007**, 1969-1981.

(285) Yam, V. W.-W.; Cheng, E. C.-C. *Chem. Soc. Rev.* **2008**, *37*, 1806-1813.

(286) Schmidbaur, H.; Schier, A. *Chem. Soc. Rev.* **2008**, *37*, 1931-1951.

(287) Schmidbaur, H.; Wohlleben, A.; Schubert, U.; Frank, A.; Huttner, G. *Chem. Ber.* **1977**, *110*, 2751-2757.

(288) Khan, M. N. I.; King, C.; Heinrich, D. D.; Fackler, J. P., Jr.; Porter, L. C. *Inorg. Chem.* **1989**, *28*, 2150-2154.

(289) Davila, R. M.; Elduque, A.; Grant, T.; Staples, R. J.; Fackler, J. P., Jr. *Inorg. Chem.* **1993**, *32*, 1749-1755.

(290) Davila, R. M.; Elduque, A.; Staples, R. J.; Harlass, M.; Fackler, J. P., Jr. *Inorg. Chim. Acta* **1994**, *217*, 45-49.

(291) Tang, S. S.; Chang, C.-P.; Lin, I. J. B.; Liou, L.-S.; Wang, J.-C. *Inorg. Chem.* **1997**, *36*, 2294-2300.

(292) Schmidbaur, H.; Mandl, J. R.; Bassett, J. M.; Blaschke, G.; Zimmer-Gasser, B. *Chem. Ber.* **1981**, *114*, 433-440.

(293) Bardaji, M.; Connelly, N. G.; Gimeno, M. C.; Jimenez, J.; Jones, P. G.; Laguna, A.; Laguna, M. *Dalton Trans.* **1994**, 1163-1167.

(294) Bardaji, M.; Gimeno, M. C.; Jones, P. G.; Laguna, A.; Laguna, M. *Organometallics* **1994**, *13*, 3415-3419.

(295) Bardaji, M.; Connelly, N. G.; Gimeno, M. C.; Jones, P. G.; Laguna, A.; Laguna, M. *Dalton Trans.* **1995**, 2245-2250.

(296) Bardaji, M.; Jones, P. G.; Laguna, A.; Laguna, M. *Organometallics* **1995**, *14*, 1310-1315.

(297) Bardaji, M.; Laguna, A.; Laguna, M. *J. Organomet. Chem.* **1995**, *496*, 245-248.

(298) Mohr, F.; Priver, S. H.; Bhargava, S. K.; Bennett, M. A. *Coord. Chem. Rev.* **2006**, *250*, 1851-1888.

(299) Bhargava, S. K.; Mohr, F.; Bennett, M. A.; Welling, L. L.; Willis, A. C. *Inorg. Chem.* **2001**, *40*, 4271-4275.

(300) Baukova, T. y. V.; Kuz'mina, L. G.; Oleinikova, N. y. A.; Lemenovskii, D. A.; Blumenfel'd, A. L. *J. Organomet. Chem.* **1997**, *530*, 27-38.

(301) Kuz'mina, L. G.; Churakov, A. V.; Howard, J. A. K. *Russ. J. Coord. Chem.* **1998**, *24*, 435-440.

(302) Meyer, N.; Lehmann, C. W.; Lee, T. K. M.; Rust, J.; Yam, V. W. W.; Mohr, F. *Organometallics* **2009**, *28*, 2931-2934.

(303) Amgoune, A.; Bourissou, D. *Chem. Commun.* **2011**, *47*, 859-871.

(304) Moret, M. E.; Peters, J. C. *Angew. Chem.-Int. Edit.* **2011**, *50*, 2063-2067.

(305) Bennett, M. A.; Bhargava, S. K.; Griffiths, K. D.; Robertson, G. B.; Wickramasinghe, W. A.; Willis, A. C. *Angew. Chem.* **1987**, *99*, 261-262.

(306) Bhargava, S. K.; Mohr, F.; Bennett, M. A.; Welling, L. L.; Willis, A. C. *Organometallics* **2000**, *19*, 5628-5635.

(307) Katz, M. J.; Sakai, K.; Leznoff, D. B. *Chem. Soc. Rev.* **2008**, *37*, 1884-1895.

(308) Contel, M.; Garrido, J.; Gimeno, M. C.; Jones, P. G.; Laguna, A.; Laguna, M. *Organometallics* **1996**, *15*, 4939-4943.

(309) Contel, M.; Jimenez, J.; Jones, P. G.; Laguna, A.; Laguna, M. *J. Chem. Soc., Dalton Trans.* **1994**, 2515-2518.

(310) Partyka, D. V.; Zeller, M.; Hunter, A. D.; Gray, T. G. *Angew. Chem., Int. Ed.* **2006**, *45*, 8188-8191.

(311) Che, C. M.; Kwong, H. L.; Yam, V. W. W.; Cho, K. C. *J. Chem. Soc., Chem. Commun.* **1989**, 885-886.

(312) Taylor, T. J.; Burress, C. N.; Gabbaï, F. P. *Organometallics* **2007**, *26*, 5252-5263.

(313) Haneline, M. R.; Tsunoda, M.; Gabbaï, F. P. *J. Am. Chem. Soc.* **2002**, *124*, 3737-3742.

(314) Heng, W. Y.; Hu, J.; Yip, J. H. K. *Organometallics* **2007**, *26*, 6760-6768.

(315) Osawa, M.; Hoshino, M.; Hashizume, D. *Dalton Trans.* **2008**, 2248-2252.

(316) Yam, V. W.-W.; Cheung, K.-L.; Yip, S.-K.; Zhu, N. *Photochem. Photobiol. Sci.* **2005**, *4*, 149-153.

(317) Partyka, D. V.; Esswein, A. J.; Zeller, M.; Hunter, A. D.; Gray, T. G. *Organometallics* **2007**, *26*, 3279-3282.

(318) Gao, L.; Peay, M. A.; Partyka, D. V.; Updegraff, J. B., III; Teets, T. S.; Esswein, A. J.; Zeller, M.; Hunter, A. D.; Gray, T. G. *Organometallics* **2009**, *28*, 5669-5681.

(319) Balch, A. L. *Struct. Bonding (Berlin, Ger.)* **2007**, *123*, 1-40.

(320) Bontemps, S.; Bouhadir, G.; Miqueu, K.; Bourissou, D. *J. Am. Chem. Soc.* **2006**, *128*, 12056-12057.

(321) Sircoglou, M.; Mercy, M.; Saffon, N.; Coppel, Y.; Bouhadir, G.; Maron, L.; Bourissou, D. *Angew. Chem., Int. Ed.* **2009**, *48*, 3454-3457.

(322) Sircoglou, M.; Bontemps, S.; Bouhadir, G.; Saffon, N.; Miqueu, K.; Gu, W.; Mercy, M.; Chen, C.-H.; Foxman, B. M.; Maron, L.; Ozerov, O. V.; Bourissou, D. *J. Am. Chem. Soc.* **2008**, *130*, 16729-16738.

(323) Neugebauer, W.; Clark, T.; Schleyer, P. v. R. *Chem. Ber.* **1983**, *116*, 3283-3292.

(324) Uson, R.; Laguna, A.; Laguna, M. *Inorg. Synth.* **1989**, *26*, 85-91.

(325) Sheldrick, G. M., *CELL_NOW*; University of Gottingen: Germany, 2006.

(326) Cooper, R. I.; Gould, R. O.; Parsons, S.; Watkin, D. J. *J. Applied Cryst.* **2002**, *35*, 168.

(327) APEX2, Bruker *Molecular Analysis Research Tool*, v. 1.27. Bruker AXS, Madison, Wisconsin, USA, 2005.

(328) Spek, A. L., *PLATON, A Multipurpose Crystallographic Tool*; Utrecht University: Utrecht, The Netherlands, 1998.

(329) ADF2010.01, ADF2010.01. SCM, Theoretical Chemistry, Vrije Universiteit, Amsterdam, The Netherlands, http://www.scm.com.

(330) Fonseca Guerra, C.; Snijders, J. G.; te Velde, G.; Baerends, E. J. *Theor. Chem. Acc.* **1998**, *99*, 391-403.

(331) te Velde, G.; Bickelhaupt, F. M.; Baerends, E. J.; Guerra, C. F.; Gisbergen, S. J. A. v.; Snijders, J. G.; Ziegler, T. *J. Comput. Chem.* **2001**, *22*, 931-967.

(332) Becke, A. D. *Phys. Rev. A* **1988**, *38*, 3098-3100.

(333) Perdew, J. P. *Phys. Rev. B* **1986**, *33*, 8822-8824.

(334) van Lenthe, E.; Baerends, E. J. *J. Comput. Chem.* **2003**, *24*, 1142-1156.

(335) van Lenthe, E.; Baerends, E. J.; Snijders, J. G. *J. Chem. Phys.* **1993**, *99*, 4597-4610.

(336) van Lenthe, E.; Baerends, E. J.; Snijders, J. G. *J. Chem. Phys.* **1994**, *101*, 9783-9792.

(337) van Lenthe, E.; Leeuwen, R. v.; Baerends, E. J.; Snijders, J. G. *Int. J. Quantum Chem.* **1996**, *57*, 281-293.

(338) van Lenthe, E.; Snijders, J. G.; Baerends, E. J. *J. Chem. Phys.* **1996**, *105*, 6505-6516.

(339) van Lenthe, E.; Ehlers, A.; Baerends, E.-J. *J. Chem. Phys.* **1999**, *110*, 8943-8953.

(340) Edmiston, C.; Ruedenberg, K. *Rev. Mod. Phys.* **1963**, *35*, 457-464.

(341) Foster, J. M.; Boys, S. F. *Rev. Mod. Phys.* **1960**, *32*, 300-302.

(342) Von Niessen, W. *J. Chem. Phys.* **1972**, *56*, 4290-4297.

(343) Hall, M. B.; Fenske, R. F. *Inorg. Chem.* **1972**, *11*, 768-775.

(344) Manson, J.; Webster, C. E.; Pérez, L. M.; Hall, M. B., Jimp 2. http://www.chem.tamu.edu/jimp2/index.html (accessed August 11, 2011).

(345) Reed, A. E.; Curtiss, L. A.; Weinhold, F. *Chem. Rev.* **1988**, *88*, 899-926.

(346) Ingleson, M. J.; Mahon, M. F.; Weller, A. S. *Chem. Commun.* **2004**, 2398-2399.

(347) Moncho, S.; Ujaque, G.; Lledos, A.; Espinet, P. *Chem.--Eur. J.* **2008**, *14*, 8986-8994.

(348) Chaplin, A. B.; Poblador-Bahamonde, A. I.; Sparkes, H. A.; Howard, J. A. K.; Macgregor, S. A.; Weller, A. S. *Chem. Commun.* **2009**, 244-246.

(349) Baratta, W.; Stoccoro, S.; Doppiu, A.; Herdtweck, E.; Zucca, A.; Rigo, P. *Angew. Chem., Int. Ed.* **2003**, *42*, 105-109.

(350) Lavallo, V.; Canac, Y.; DeHope, A.; Donnadieu, B.; Bertrand, G. *Angew. Chem., Int. Ed.* **2005**, *44*, 7236-7239.

(351) Stambuli, J. P.; Incarvito, C. D.; Buehl, M.; Hartwig, J. F. *J. Am. Chem. Soc.* **2004**, *126*, 1184-1194.

(352) Yamashita, M.; Hartwig, J. F. *J. Am. Chem. Soc.* **2004**, *126*, 5344-5345.

(353) Korshin, E. E.; Leitus, G.; Shimon, L. J. W.; Konstantinovski, L.; Milstein, D. *Inorg. Chem.* **2008**, *47*, 7177-7189.

(354) Sangtrirutnugul, P.; Stradiotto, M.; Tilley, T. D. *Organometallics* **2006**, *25*, 1607-1617.

(355) Whited, M. T.; Mankad, N. P.; Lee, Y.; Oblad, P. F.; Peters, J. C. *Inorg. Chem.* **2009**, *48*, 2507-2517.

(356) Tsay, C.; Mankad, N. P.; Peters, J. C. *J. Am. Chem. Soc.* **2010**, *132*, 13975-13977.

(357) Spokoyny, A. M.; Reuter, M. G.; Stern, C. L.; Ratner, M. A.; Seideman, T.; Mirkin, C. A. *J. Am. Chem. Soc.* **2009**, *131*, 9482-9483.

(358) Segawa, Y.; Yamashita, M.; Nozaki, K. *J. Am. Chem. Soc.* **2009**, *131*, 9201-9203.

(359) Braunschweig, H.; Green, H.; Radacki, K.; Uttinger, K. *Dalton Trans.* **2008**, 3531-3534.

(360) Braunschweig, H.; Radacki, K.; Uttinger, K. *Chem. Eur. J.* **2008**, *14*, 7858-7866.

(361) Lin, T.-P.; Wade, C. R.; Pérez, L. M.; Gabbaï, F. P. *Angew. Chem., Int. Ed.* **2010**, *49*, 6357-6360.

(362) Bojan, V. R.; Fernández, E. J.; Laguna, A.; López-de-Luzuriaga, J. M.; Monge, M.; Olmos, M. E.; Puelles, R. C.; Silvestru, C. *Inorg. Chem.* **2010**, *49*, 5530-5541.

(363) Jones, P. G. *Acta Crystallogr., Sect. C: Cryst. Struct. Commun.* **1992**, *48*, 1487-1488.

(364) Ahrland, S.; Dreisch, K.; Noren, B.; Oskarsson, A. *Acta Chem. Scand., Ser. A* **1987**, *41*, 173-177.

(365) Mathieson, T. J.; Langdon, A. G.; Milestone, N. B.; Nicholson, B. K. *J. Chem. Soc., Dalton Trans.* **1999**, 201-207.

(366) Doerrer, L. H. *Dalton Trans.* **2010**, *39*, 3543-3553.

(367) Hayoun, R.; Zhong, D. K.; Rheingold, A. L.; Doerrer, L. H. *Inorg. Chem.* **2006**, *45*, 6120-6122.

(368) Klapoetke, T. M.; Krumm, B.; Galvez-Ruiz, J.-C.; Noeth, H. *Inorg. Chem.* **2005**, *44*, 9625-9627.

(369) Elder, R. C.; Eidsness, M. K. *Chem. Rev.* **1987**, *87*, 1027-1046.

(370) Elder, R. C.; Eidsness, M. K.; Heeg, M. J.; Tepperman, K. G.; Shaw, C. F. In *ACS Symposium Series 209*; Lippard, S. J., Ed.; American Chemical Society: Washington, DC, 1984, p 385-400.

(371) Watkins, J. W.; Elder, R. C.; Greene, B.; Darnall, D. W. *Inorg. Chem.* **1987**, *26*, 1147-1151.

(372) Gardea-Torresdey, J. L.; Tiemann, K. J.; Gamez, G.; Dokken, K.; Cano-Aguilera, I.; Furenlid, L. R.; Renner, M. W. *Environ. Sci. Technol.* **2000**, *34*, 4392-4396.

(373) Messori, L.; Balerna, A.; Ascone, I.; Castellano, C.; Gabbiani, C.; Casini, A.; Marchioni, C.; Jaouen, G.; Congiu Castellano, A. *J. Biol. Inorg. Chem.* **2011**, *16*, 491-499.

(374) Braunschweig, H.; Gruss, K.; Radacki, K. *Angew. Chem., Int. Ed.* **2009**, *48*, 4239-4241.

(375) Parkin, G. *Organometallics* **2006**, *25*, 4744-4747.

(376) Hill, A. F. *Organometallics* **2006**, *25*, 4741-4743.

(377) Braunschweig, H.; Dewhurst, R. D.; Schneider, A. *Chem. Rev.* **2010**, *110*, 3924–3957.

(378) Bouhadir, G.; Amgoune, A.; Bourissou, D. *Adv. Organomet. Chem.* **2010**, *58*, 1-107.

(379) Hill, A. F.; Owen, G. R.; White, A. J. P.; Williams, D. J. *Angew. Chem., Int. Ed.* **1999**, *38*, 2759-2761.

(380) Figueroa, J. S.; Melnick, J. G.; Parkin, G. *Inorg. Chem.* **2006**, *45*, 7056-7058.

(381) Pang, K.; Quan, S. M.; Parkin, G. *Chem. Commun.* **2006**, 5015-5017.

(382) Landry, V. K.; Melnick, J. G.; Buccella, D.; Pang, K.; Ulichny, J. C.; Parkin, G. *Inorg. Chem.* **2006**, *45*, 2588-2597.

(383) Braunschweig, H.; Gruss, K.; Radacki, K. *Angew. Chem., Int. Ed.* **2007**, *46*, 7782-7784.

(384) Sircoglou, M.; Bontemps, S.; Mercy, M.; Saffon, N.; Takahashi, M.; Bouhadir, G.; Maron, L.; Bourissou, D. *Angew. Chem. Int. Ed.* **2007**, *46*, 8583-8586.

(385) Fox, B. J.; Millard, M. D.; DiPasquale, A. G.; Rheingold, A. L.; Figueroa, J. S. *Angew. Chem., Int. Ed.* **2009**, *48*, 3473-3477.

(386) Gualco, P.; Lin, T.-P.; Sircoglou, M.; Mercy, M.; Ladeira, S.; Bouhadir, G.; Pérez, L. M.; Amgoune, A.; Maron, L.; Gabbaï, F. P.; Bourissou, D. *Angew. Chem., Int. Ed.* **2009**, *48*, 9892-9895.

(387) Wagler, J.; Brendler, E. *Angew. Chem., Int. Ed.* **2010**, *49*, 624-627.

(388) Braunschweig, H.; Radacki, K.; Schwab, K. *Chem. Commun.* **2010**, *46*, 913-915.

(389) Kolpin, K. B.; Emslie, D. J. H. *Angew. Chem., Int. Ed.* **2010**, *49*, 2716-2719.

(390) Cowie, B. E.; Emslie, D. J. H.; Jenkins, H. A.; Britten, J. F. *Inorg. Chem.* **2010**, *49*, 4060-4072.

(391) Wagler, J.; Brendler, E.; Langer, T.; Poettgen, R.; Heine, T.; Zhechkov, L. *Chem.--Eur. J.* **2010**, *16*, 13429-13434.

(392) Truflandier, L. A.; Brendler, E.; Wagler, J.; Autschbach, J. *Angew. Chem., Int. Ed.* **2011**, *50*, 255-259.

(393) Derrah, E. J.; Sircoglou, M.; Mercy, M.; Ladeira, S.; Bouhadir, G.; Miqueu, K.; Maron, L.; Bourissou, D. *Organometallics* **2011**, *30*, 657-660.

(394) Becke, A. D.; Edgecombe, K. E. *J. Chem. Phys.* **1990**, *92*, 5397-5403.

(395) Schmidbaur, H.; Mitschke, K. H.; Buchner, W.; Stuehler, H.; Weidlein, J. *Chem. Ber.* **1973**, *106*, 1226-1237.

(396) Kimura, M.; Iwata, A.; Itoh, M.; Yamada, K.; Kimura, T.; Sugiura, N.; Ishida, M.; Kato, S. *Helv. Chim. Acta* **2006**, *89*, 747-783.

(397) Mann, K. R.; Lewis, N. S.; Miskowski, V. M.; Erwin, D. K.; Hammond, G. S.; Gray, H. B. *J. Am. Chem. Soc.* **1977**, *99*, 5525-5526.

(398) Heyduk, A. F.; Nocera, D. G. *Science* **2001**, *293*, 1639-1641.

(399) Esswein, A. J.; Nocera, D. G. *Chem. Rev.* **2007**, *107*, 4022-4047.

(400) Powers, D. C.; Xiao, D. Y.; Geibel, M. A. L.; Ritter, T. *J. Am. Chem. Soc.* **2010**, *132*, 14530-14536.

(401) Powers, D. C.; Geibel, M. A. L.; Klein, J. E. M. N.; Ritter, T. *J. Am. Chem. Soc.* **2009**, *131*, 17050-17051.

(402) Powers, D. C.; Ritter, T. *Nat. Chem.* **2009**, *1*, 302-309.

(403) Deprez, N. R.; Sanford, M. S. *J. Am. Chem. Soc.* **2009**, *131*, 11234-11241.

(404) Dick, A. R.; Kampf, J. W.; Sanford, M. S. *Organometallics* **2005**, *24*, 482-485.

(405) Laguna, A.; Laguna, M. *Coord. Chem. Rev.* **1999**, *193-195*, 837-856.

(406) Mohamed, A. A.; Abdou, H. E.; Fackler Jr, J. P. *Coord. Chem. Rev.* **2010**, *254*, 1253-1259.

(407) Esswein, A. J.; Dempsey, J. L.; Nocera, D. G. *Inorg. Chem.* **2007**, *46*, 2362-2364.

(408) Teets, T. S.; Lutterman, D. A.; Nocera, D. G. *Inorg. Chem.* **2010**, *49*, 3035-3043.

(409) Cook, T. R.; Esswein, A. J.; Nocera, D. G. *J. Am. Chem. Soc.* **2007**, *129*, 10094-10095.

(410) Burton, J. W. *Sci. Synth.* **2002**, *4*, 53-75.

(411) Fontaine, F. G.; Boudreau, J.; Thibault, M. H. *Eur. J. Inorg. Chem.* **2008**, 5439-5454.

(412) Gualco, P.; Mercy, M.; Ladeira, S.; Coppel, Y.; Maron, L.; Amgoune, A.; Bourissou, D. *Chem. Eur. J.* **2010**, *16*, 10808-10817.

(413) Brendler, E.; Wächtler, E.; Heine, T.; Zhechkov, L.; Langer, T.; Pöttgen, R.; Hill, A. F.; Wagler, J. *Angew. Chem. Int. Ed.* **2011**, *50*, 4696-4700.

(414) Crossley, I. R.; Hill, A. F. *Organometallics* **2004**, *23*, 5656-5658.

(415) Figueroa, J. S.; Melnick, J. G.; Parkin, G. *Inorg. Chem.* **2006**, *45*, 7056-7058.

(416) Crossley, I. R.; Hill, A. F.; Willis, A. C. *Organometallics* **2008**, *27*, 312-315.

(417) Pang, K. L.; Tanski, J. M.; Parkin, G. *Chem. Commun.* **2008**, 1008-1010.

(418) Godfrey, S. M.; Ho, N.; McAuliffe, C. A.; Pritchard, R. G. *Angew. Chem., Int. Ed. Engl.* **1996**, *35*, 2344-2346.

(419) Bontemps, S.; Bouhadir, G.; Gu, W.; Mercy, M.; Chen, C.-H.; Foxman, B. M.; Maron, L.; Ozerov, O. V.; Bourissou, D. *Angew. Chem., Int. Ed.* **2008**, *47*, 1481-1484.

(420) Holmes, R. R.; Day, R. O.; Chandrasekhar, V.; Holmes, J. M. *Inorg. Chem.* **1987**, *26*, 157-163.

(421) Cherkasov, V. K.; Grunova, E. V.; Poddel'sky, A. I.; Fukin, G. K.; Kurskii, Y. A.; Abakumova, L. G.; Abakumov, G. A. *J. Organomet. Chem.* **2005**, *690*, 1273-1281.

(422) Zhao, X.-F.; Zhang, C. *Synthesis* **2007**, 551-557.

VITA

Casey Robert Wade

c/o Prof. François Gabbaï
Department of Chemistry
Texas A&M University
College Station, TX 77843-3255

Education:
Ph.D., Chemistry, Texas A&M University, December 2011
B.S., Chemistry, University of Nebraska-Lincoln, May 2006

Publications:
Two-electron redox chemistry and reverible umpolung of a gold-antimony bond. Wade, C. R.; Gabbaï, F. P. *Angew. Chem. Int. Ed.* **2011**, *50*, 7369-7372.

Synthesis, structure, and properties of a T-shaped 14 electron stiboranyl-gold complex. Wade, C. R.; Lin, T.-P.; Nelson, R. C.; Marder, E. A.; Miller, J. T.; Gabbaï, F. P. *J. Am. Chem. Soc.* **2011**, *133*, 8948-8955.

Synthesis and structure of peri-substituted boron/pnictogen naphthalene derivatives. Wade, C. R.; Saber, M. R.; Gabbaï, F. P. *Heteroat. Chem.* **2011**, 22, 500-505.

A mercury → antimony interaction. Lin, T. P.; Wade, C. R.; Pérez, L. M.; Gabbaï, F. P. *Angew. Chem. Int. Ed.* **2010**, *49*, 6357-6360.

Stabilization of zwitterionic aryltrifluoroborates against hydrolysis. Wade, C. R.; Zhao, H.; Gabbaï, F. P. *Chem. Commun.* **2010**, 6380-6381.

Synthesis and Lewis Acidic Behavior of a Cationic 9-Thia-10-boraanthracene. Matsumoto, T.; Wade, C. R.; Gabbaï, F. P. *Organometallics* **2010**, *29*, 5490-5495.

Synthesis, structure and luminescence of 1,8-diaurionaphthalenes. Wade, C. R.; Yakovenko, A.; Gabbaï, F. P. *New J. Chem.* **2010**, *34*, 1646-1651.

Fluoride ion complexation and sensing using organoboron compounds. Wade, C. R.; Broomsgrove, A. E. J.; Aldridge, S.; Gabbaï, F. P. *Chem. Rev.* **2010**, *110*, 3958-3984.

Cyanide anion binding by a triarylborane at the outer rim of a cyclometalated ruthenium(II) cationic complex. Wade, C. R.; Gabbaï, F. P. *Inorg. Chem.* **2010**, *49*, 714-720.

Colorimetric turn-on sensing of fluoride ions in $H_2O/CHCl_3$ mixtures by pyridinium boranes. Wade, C. R.; Gabbaï, F. P. *Dalton Trans.* **2009**, 9169-9175.